Molecular Dynamics Modelling on Utilisation of Lignocellulosic Biomass Derived Biofuels

Cheng Chen

Supervisor: Prof. Xi Jiang
Dr. Yi Sui

School of Engineering and Materials Science
Queen Mary University of London

This dissertation is submitted for the degree of
Doctor of Philosophy

November 2021

Declaration

I declare that the contents of this dissertation are original and it has not been submitted in whole or in part for consideration for any other degree or qualification in this, except for those with specific reference made to the work of others. This dissertation is based on my own work and includes nothing which is the outcome of work done in collaboration, except that where specific indications have been made in the text.

Cheng Chen
November 2021

Acknowledgements

First of all, I would like to express the deepest gratitude to my supervisor Prof. Xi Jiang for his constant guidance and encouragement throughout my PhD study. The instructive advice and insightful discussion during my research have greatly inspired me on the academic pursuit.

I greatly appreciate the institutes and faculties who have provided the supercomputing services including the UK national supercomputing service of Archer, QMUL Apocrita and Barcelona Supercomputing Center. I would like to express the special thanks to Dr. Charles Moulinec of Daresbury Laboratory and Dr. Daniel Mira Martinez of Barcelona Supercomputing Center.

I would like to acknowledge the support from China Scholarship Council (CSC). Best wishes to my country.

Also, I would like to thank all my friends, Dr. Kai Zhang, Dr. Xinyu You and Prof. Qingxuan Liang, etc., for the encouragement.

Finally, I could not have completed this thesis without the support of my parents, sisters and Wei Zhou. You are the most important people in my life.

Abstract

Utilisation of renewable biofuels (rapeseed oil, soy oil, dimethyl carbonate, cyclopentanone, methyl butanoate, dimethoxymethane and ethanol) is essential to achieving net-zero carbon emission and meeting the requirement of 2 °C scenario. Deployment of biofuels derived from lignocellulosic biomass such as agricultural wastes is expected to be scaled up substantially. Molecular dynamics simulation can provide in-depth understanding of the physiochemical properties of biomass and biofuels.

Surface coking as the primary deactivation pattern of metal-based catalyst in biofuel reforming is investigated. Mass reduction of lignin pyrolysis in simulation is validated against experimental results. Mechanisms behind the effects of temperature, aromatic size and oxygen content on coke adsorption are revealed in molecular simulation considering the molecular collision dynamics, thermal dynamics and kinetics. It is identified that the modification of crystallinity of catalyst outer shell and the occurrence of seeping after coke adsorption would affect the subsequent catalyst regeneration.

Insight into the chemical mechanism of soot inception in combustion has been gained from molecular dynamics simulation with reactive force field. The hydrocarbon structures of nascent soot in molecular simulation agree well with the experimental observation. Concurrently, the mechanisms of molecular structure of the oxygenated additives, i.e. the existence of ester, alcohol, carbonyl group and ether, on soot precursor mitigation are elucidated via evaluating the early formation of CO and CO_2 quantitatively during the thermal decomposition.

Prediction of fuel transport properties in high-pressure conditions is achieved. The phase transition of biodiesel at extremely high pressure is studied via morphology evolution to elucidate the experimentally observed solidification process. Viscosity and thermal conductivity are predicted over extended ranges of temperatures and pressures. Thermophysical properties like critical temperature, critical density and critical pressure are predicted for supercritical combustion. The capability of molecular simulation on thermophysical property prediction is evaluated after comparing with the experimental results.

Table of contents

List of figures xiii

List of tables xxiii

Nomenclature xxv

1 Introduction 1

1.1 Biofuels produced from biomass . . . 1
  1.1.1 Deployment of biofuels . . . 1
  1.1.2 Technical roadmap of biofuel production . . . 2
  1.1.3 Heterogeneous catalysis in biomass thermochemical conversion . . . 5
1.2 Physicochemical properties of biofuels in combustion . . . 6
  1.2.1 Prediction of biodiesel thermophysical properties for supercritical combustion . . . 7
  1.2.2 Biofuels on soot mitigation . . . 8
1.3 Molecular dynamics simulation . . . 12
  1.3.1 Basic methodology of molecular dynamics . . . 12
  1.3.2 Classical force field . . . 19
  1.3.3 Reactive force field . . . 21
1.4 Molecular modelling of biofuel and biomass . . . 22
1.5 Knowledge gaps, motivation and thesis overview . . . 23

2 Lignin pyrolysis and catalyst deactivation 27

2.1 Modelling methodology 27
    2.1.1 Model construction 27
    2.1.2 Simulation setup procedures and details 28
2.2 Lignin pyrolysis products 32
2.3 Catalyst deactivation during thermochemical conversion of lignin 34
    2.3.1 Surface instability induced thermal degradation 34
    2.3.2 Deposition induced deactivation 37
2.4 Discussion and conclusion 42

3 Soot formation in biofuel combustion **47**

3.1 State-of-the-art soot inception model 47
3.2 Soot formation of biodiesel combustion 50
    3.2.1 Fuel molecular structure and modelling setup 50
    3.2.2 Evolution of incipient soot formation 52
    3.2.3 Mechanisms of PAH growth and nascent soot nucleation 55
    3.2.4 Comparison of biodiesel and diesel on soot formation 58
    3.2.5 Effects of biodiesel molecular structures on soot precursor mitigation 61
3.3 Soot mitigation mechanism of oxygenated fuel additive 63
    3.3.1 Modelling setup 63
    3.3.2 Incipient soot formation mechanism of fuel combustion 66
    3.3.3 Soot formation during diesel combustion with blending of oxygenates 69
    3.3.4 Quantification of oxygenated effectiveness in soot mitigation 72
3.4 Discussion and conclusion 73

4 Transport property prediction of FAMEs in high pressure conditions **77**

4.1 Green-Kubo and Einstein method 77
    4.1.1 Modelling system setup 79
    4.1.2 Pressure effect on viscosity & diffusivityy 82
    4.1.3 SE & SED relation 87

4.2 Evaluation of force field 90
  4.2.1 Hydrodynamic radius 90
  4.2.2 Physical properties 90
4.3 Breakdown of SE relation due to high pressure solidification 94
4.4 Crossing the SE relation 98
4.5 Discussion and conclusion 99

5 Comparison of biodiesel and diesel on physical property in extreme conditions 103
5.1 Modelling methodology 103
  5.1.1 Fuel composition and molecular structures 103
  5.1.2 Force fields 104
  5.1.3 MD setup 105
5.2 High pressure induced solidification 105
5.3 Critical properties and surface tension 110
5.4 Transport properties of fuel mixtures using EMD 116
  5.4.1 Density 116
  5.4.2 Viscosity 117
  5.4.3 Thermal conductivity 120
5.5 Capability of NEMD on transport properties 124
  5.5.1 Periodic perturbation-NEMD method on viscosity prediction 124
  5.5.2 Reverse NEMD method on thermal conductivity prediction 127
5.6 Discussion and conclusion 130

6 Conclusion and future recommendation 133
6.1 Summary of current work 133
6.2 Future recommendation 135
  6.2.1 Deactivation of catalyst 135
  6.2.2 Unphysical reaction condition in ReaxFF MD simulation 135
  6.2.3 Physical property prediction 136

References 139

List of figures

1.1 (a) Contributions of bioenergy to final energy demand in the years 2015 and 2060 in 2DS; (b) final energy demand of transportation in 2DS; (c) major biofuel consumption in SDS, 2015-2030; source of data: IEA bioenergy report (IEA, 2017). 2

1.2 Overview of conversion routes of first/second generation feedstock to biofuels, reproduced based on the work of Agarwal (Agarwal, 2007). 4

1.3 Pathways for the valorisation of microalgae to biofuels and high-value chemicals. 5

1.4 *P*-*T* phase diagram of SCFs with melting line, coexistence line and the newly developed thermal dynamic boundaries i.e. the Frenkel line and Widom lines. 8

1.5 Comparison of emission species on atmosphere radiative forcing, where positive forcing indicates warming the climate and NMVOC is non-methane volatile organic compound; source of data: IPCC climate change report (Blanco et al., 2014). 9

1.6 Sources of global black carbon emissions in the year 2010; source of data: Arctic Monitoring and Assessment Programme (https://www.amap.no/, 2015). 10

1.7 Computed reductions in soot precursors concentrations with the additions of selected oxygenated species: dibutyl maleate (DBM), methyl butanoate (MB), dimethyl carbonate (DMC) and methanol, which are reproduced from the work of Westbrook et al. (2006). 11

1.8 Schematic of the basic molecular dynamics simulation procedure. 13

1.9 Particle distribution: (a)-(c) are simple cubic (sc), body-cantered cubic (bcc) and face-cantered cubic (fcc); (d) random distribution 13

1.10 Periodic boundary conditions in two dimensions 15

1.11 Different intramolecular interactions between atoms of i, j , k and l. 20

2.1 (a) Schematic depiction of the cellulose, hemicellulose and lignin in plant cells of lignocellulosic biomass; (b) representative molecular structures of β-D-glucose cellulose, hemicellulose and softwood lignin fragment highlighting the most common linkages adapted from Beste (2014); (c) lignin surrogate models proposed by Faravelli et al. (2010) based on the characterization and composition of lignin structures; (d) molecular modelling of lignin decomposition over nanocatalysts. 29

2.2 Lignin molecular structure used in this study, adapted from Beste (2014). . 30

2.3 (a)-(b): Basic units of lignin and various linkage in the lignin structure; (c) atom arrangement of a 4 nm Ni nanocrystal in tridimensional view with facets indicated and the cross section with different layers (L1, L2 and L3) indicated, where the atoms are coloured according to the coordination number (CN) with cut off distance of 3.2 Å; (d) molecular structures of coke surrogate models with molecular structure, molecular mass and CAS number indicated. 31

2.4 (a) Snapshot of the equilibrated unit cell with one unimolecular ($C_{138}H_{160}O_{45}$) of the 40 lignin fragments highlighted; (b) 4 nm Ni nanocrystal centred in the box for modelling of catalyst thermal stability; (c) schematic box depicting the modelling system of coke adsorption, where Ni catalyst is fixed in centre with aromatic organics distributed around. 32

2.5 (a) Evolution of lignin mass fraction and number of species where blue solid box is mass fraction of TG experiment (temperature ramp: 2 K/min), black hollow box is mass fraction of ReaxFF MD simulation (20 K/ps), red hollow box is species of ReaxFF MD simulation; (b) snapshot of the system and the mass fraction of final composition yield, where typical molecular structures are identified. 33

2.6 (a) Potential energy per atom of nanocrystal with diameters of 2-6 nm heating from 300 K to 3000 K; (b) time evolution of the radial distribution function of the 4 nm nanocrystal heating from 300 K to 3000 K in 500 ps; (c) melting temperatures of Ni crystal with different sizes determined by potential energy evolution. 35

2.7 (a) Lindeman index of 4 nm nanocrystal at isothermal conditions, where the melting temperature of different sizes based on Lindemann index criteria is inserted, and the solid triangle is the result of nanocrystal; (b) distribution of coordination number of L3 surface at different isothermal conditions. . . . 37

2.8 Scatter plots of displacement magnitude along with atom ID of 4 nm nanocrystal at different time and the corresponding coloured maps of the overall and cross sectional snapshots, where (a): 400 K, (b): 800 K, (c): 1200 K, (d): 1600 K, (e): 2000 K, (f): 2400 K, and the numbers in bracket indicates displacement magnitude of different layers, where blue: L1, orange: L2, red: L3, and the grey area in (c) and (d) indicates atoms with displace over 3.2 Å. 38

2.9 (a) Schematic plot of the cluster recognition (coloured by green) with a cut off distance of 4 Å; (b)-(c) time evolution of overall adsorption ratio; (d)-(e) time evolution of the number of aromatic molecules, and the coloured area in (b)-(e) is the initial stage of A1O6 and A19. 40

2.10 Representative trajectories (black lines) to show the time evolution of aromatic molecule interaction with the surfaces of Ni nanocrystal, where (a)-(b): A1, (c): A19 and (d): A1O6, and green arrow in (a) indicates the movement direction of A1, (b-2) is the modified view of (b-1) to indicate the diffusion trajectory of A1 on (111) facet, (b-3) and (b-4) are part of the products after surface reaction, A19 in (c) coloured in green is trapped at the time of 40 ps and acted as subtracts for PAH stack adsorption, (d-2) to (d-5) are typical products captured after surface reaction. 41

2.11 Snapshots of the system after 800 ps isothermal simulation to demonstrate the temperature effect on adsorption of A1, A4, A19 and A1O6, where molecular formula of the cluster in (a-1), (b-1), (c-1) and (d-1), (d-2) is indicated at the bottom of the panel; (a-4), (a-5), (d-3), (d-4) and (d-5) are cross section snapshots, and intermediates seeping into catalyst are indicated in the enlarged snapshot, PAHs with its ring parallel to the particle surface are indicated by the black circle in (b-1) and (c-1), the conditions where physical nucleation occurs according to the work of Mao et al. (2017) are highlighted by the red frame and multi-layered adsorbates are indicated by black arrows. 43

2.12 Effect of coke adsorption on catalyst crystallinity of outer shell compared with the corresponding isothermal nanocrystal melting process, which is characterised by relative Lindemann index, and grey area indicates seeping occurrence. 44

3.1 Schematic diagram of soot formation process from gas phase to solid agglomerated particles in five steps. 48

3.2 Temperature effects and time evolutions of the mass and C:H ratio of the largest molecule in the simulation of biodiesel blends, where the shaded area represents the statistical uncertainty ranges determined by standard deviation. 52

3.3 Evolution of pyrolysis product distribution and incipient soot morphology of biodiesel blends, where carbon atoms from different surrogates are indicated with different colours, all the oxygen atoms in biodiesel are indicated with red sphere, and all the hydrogen atoms are indicated with silver sphere, some representative structures are enlarged. 54

3.4 Time dependence of carbon ring count statistics, where the rings are artificially coloured. 55

3.5 An indicative mechanism of soot particle formation from gaseous molecules. The process includes fuel pyrolysis to produce PAH precursors, aromatics formation, PAH growth, particle inception, evolution of the soot nuclei, together with the simulated image of soot particles with surface growth and fractal agglomeration of 200 primary particles (D_f is fractal dimension, k_f is fractal prefactor). 56

3.6 Comparison of diesel and biodiesel on incipient soot formation processes, where the fitted red line and scattered red triangles indicate the number of carbons and the C:H ratio in the largest molecule during the simulation of biodiesel, and the fitted black line and scattered black squares indicate diesel, and the dehydrogenation process is highlighted with ellipses. 58

3.7 Comparison between ReaxFF derived YSIs and experimentally measured YSIs, where the experimental values are from the unified sooting tendency database based on the work of Das et al. (2018a). 60

3.8 (a) Time evolution of the main oxygenated products during the pyrolysis of MB, EP and MC, where the shaded regions indicate the statistical uncertainty determined by the standard deviation; (b) contributions of different functional groups to nascent soot after 2ns simulation, where carbon contribution to the largest molecules is displayed. 64

3.9 Molecular structures and chemical formulas of the oxygenated fuel additives. 64

3.10 Time evolutions of major intermediates and products in diesel combustion, where the shaded area indicates the average standard deviations of five repeated simulations. 67

3.11 Time evolutions of incipient soot formation of diesel combustion, where C, H and O atoms are represented in cyan, silver and red. 68

3.12 Snapshots of the enlarged representative carbonaceous nanoparticle morphology during diesel combustion, where aliphatic side chains are coloured in yellow with direct C_2H_2 or C_2H_3 addition highlighted with red ellipse while aliphatic links between aromatic moieties in nascent soot are highlighted in green. 70

3.13 Morphological snapshots of nascent soot at 1.2 ns (above the dashed line) and final soot particles at 2 ns (below the dashed line) in diesel combustion with various additives, from left to right, (a): DMC, (b): CPO, (c): DMM, (d): MB and (e): ethanol, where the numbers of carbon atoms contributed from oxygenated fuel additives are given in purple. 71

3.14 Time evolutions of (a) CO and (b) CO_2 for diesel blending with various additives at 3000 K. 72

4.1 Equilibrium run and compression of EMD system containing 500 MDC molecules: (a) snapshot of the initial box with molecules distributed randomly; (b) snapshot of box after 500 ps simulation in NPT ensemble at 298.15 K and 0.1 MPa. 82

4.2 (a) Viscosity of MDC at 298.15 K and 0.1 MPa using GK method, where viscosity is indicated by solid black line, and the normalized ACF of P_{xy} is shown in dashed red line, the shaded region indicates the largest fluctuation range, green dotted line indicates the average value of the first plateau, the arrows indicate the corresponding axis; (b) the effect of pressure on the convergence of viscosity. 83

4.3 (a) Decomposition and fitting of PACF; (b) viscosity comparison obtained by fitting the running integral and PACF, where the solid black line is the averaged viscosity value of 40 independent replicates with standard deviation indicated in shaded area, and the red dashed line indicates the fitted value according to Equation (4.9), blue dotted line is the integration of fitted PACF, black dashed line indicates the time when standard deviation is equal to 40% of the averaged viscosity. 84

4.4 (a) Normalized VACF of MDC centre of mass at different pressures, where shaded area indicates negative values; (b) MSD of MDC centre of mass, where the shaded area is used in the linear regression. 85

4.5 System size effect on diffusion coefficient, where error bars are calculated from 40 independent trajectories and solid lines are the line fitting with linear regression. 86

4.6 (a) Normalized ACF of MDC molecule end-to-end vector, where P_1 is the first order Legendre polynomial of the angle of the vector; (b) effect of pressure on molecule reorientation using the P_1 function. 87

4.7 (a) Correlation between diffusion coefficient and the inverse of viscosity; (b) correlation between relaxation time and viscosity, where the dashed lines indicate linear fitting, pressure is also indicated by colour of the hollow square, the colour code of pressure applies to the following plots of SE relation. . . 90

4.8 (a) Effect of force field on SE relation at 348.15 K, pressure ranging 10-300 MPa, where the hollow symbols and dashed line are results of MDC while solid symbols and solid line are results of MMR; (b) effect of temperature on SE relation, where the hollow square and dashed line are results of MDC while the hollow circle and solid line are results of MMR. 91

4.9 (a) Correlation between densities of NIST and the results calculated by EMD simulation including the liquid phase, gas phase and supercritical conditions; (b) pressure effect on density of MDC and MMR at 298.15 K and 348.15 K, where lines are fitted results according to the Tait equation (Dymond and Malhotra, 1988). 92

4.10 Comparison of viscosity between MD simulation and the experimental results, where solid lines are experimental values, dashed lines are MD results fitted according to the Barus model (Dench et al., 2018). 94

4.11 (a) The SMAC parameter of MMR at different temperatures and pressures, where black dashed lines indicate transition time of 298.15 K - 100 MPa; (b) snapshots of MMR MD system at 298.15 K - 100 MPa, where grey area indicates ordered alignment of solid nuclei while red area indicates amorphous liquid phase. 96

4.12 (a) Probability distribution of MMR molecule end-to-end distance at 298.15 K, and the probability is the statistical results in the time interval, (a): 50 MPa where lines are overlapped; (b): 100 MPa where lines of [20-60] ns, [60-80] ns and [80-100] ns are overlapped, and the black dashed lines indicate the peak values. 97

4.13 Time evolution of overall diffusion coefficient of MMR at 298.15 K, where trajectories are partitioned every 2 ns and diffusion coefficient is the linear fitting of MSD between 200 ps and 1800 ps within each time interval, black dashed lines indicate the transition time of 100 MPa. 99

4.14 Correlation between viscosity from experiments and diffusion coefficient from EMD simulation at the temperature of 348.15 K, (a): MDC, (b): MMR. Solid line is the fitting of TraPPE, dashed line is the fitting of CHARMM and dotted line is the fitting of LOPLS. 100

5.1 Snapshot of initial box containing 2000 biodiesel molecules, fuel surrogate molecules are indicated with different colours, HXD and MP: purple, OTD and MS: magenta, HMN and MO: blue, DCA and ML: red, MNT and MLN: green. 106

5.2 (a) Time evolution of biodiesel morphology and molecular arrangement during nucleation at 300 K and 300 MPa, from left to right: 50 ns, 100 ns, 150 ns and 200 ns; (b) snapshots of systems after 200 ns simulation, from left to right: biodiesel at 300 K and 200 MPa, biodiesel at 300 K and 250 MPa, biodiesel at 350 K and 300 MPa, diesel at 300 K and 300 MPa. 107

5.3 (a) Time evolution of RDF of center of mass of biodiesel molecules at 300 K and 300 MPa during 200 ns simulation, RDF is averaged over each 40 ns interval; (b) RDF of systems corresponding to Figure 5.2 (b), averaged over last 40 ns trajectory, B indicates biodiesel an D indicates diesel. 108

5.4 Time evolution of relative Q_6 parameter to characterise the crystallinity of the modelling system, where the time points indicates different nucleation stages: t_1=85 ns, t_2=130 ns, t_3=40 ns, t_4=100 ns, t_5=160 ns. 109

5.5 (a) Snapshot of biodiesel box after 4 ns annealing-equilibrium simulation in semi-isotropic *NPT* ensemble at 300 K and 0.1 MPa, where the box length of diesel in the z direction is 12.49 nm; (b) and (c) are snapshots of molecule distribution of biodiesel and diesel in VLE simulation with LJ cut-off distance of 1.4 nm. 111

5.6 Equilibrium fuel density profiles and vapour-liquid coexistence curves: (a) and (b) are density profiles of biodiesel and diesel across the liquid-vapour interface as a function of the distance from the centre of liquid film, corresponding to snapshots in Figure 5.5 (b) and (c); (c) and (d) are vapour-liquid coexistence curves of biodiesel and diesel with LJ cut-off distance of 1.4 nm and LJ-PME method. Results are averaged over five independent simulations, solid symbols are gas density while hollow symbols are liquid density, error bars are immersed within the symbols. 113

5.7 Vapour-liquid surface tension of biodiesel and diesel as a function of temperature, where hollow symbols are results of LJ cut-off distance of 1.4 nm, solid symbols are results of LJ-PME, the solid and dashed lines are fitting results, green asterisk indicates biodiesel surface tension estimated using empirical equation, and the corresponding fitting equations are also listed. 117

5.8 Pressure and temperature dependence of density of biodiesel (B) and diesel (D), densities of biodiesel at 300 K - 250 MPa and 300 K - 300 MPa are not included due to the HP solidification, lines in (a) are fitting results while lines in (b) are connection between the scattered data points. 118

5.9 Viscosity of biodiesel at extreme conditions using the GK and Einstein method, coloured thin lines are results of 40 statistically independent trajectories, black thick lines are the averaged results, the slopes of MSD in (c) and (d) are viscosities. 119

5.10 Pressure and temperature dependence of viscosity of biodiesel and diesel, lines are fitting results. 120

5.11 (a) Thermal conductivity of biodiesel at extreme conditions using the GK method with simulation performed in *NVT* ensemble; (b) results of 40 independent replicated trajectories; (c) - (d) pressure and temperature dependence of thermal conductivity of biodiesel and diesel. The values are averaged over five independent trajectory, some error bars are immersed in symbols. . . . 122

5.12 Schematic plot of acceleration implementation along the z direction on each of the particles, black arrow indicates the direction and amplitude of acceleration. 124

5.13 (a) Time evolution of biodiesel viscosity using PP-NEMD method at 313.15 K and 0.1 MPa with different acceleration amplitude; (b) comparison of biodiesel viscosity between GK-EMD (red dashed line) and PP-NEMD (black dot line), viscosity is the averaged value over last 500 ps trajectories which is steady for data collection, where the shaded area indicates the values for linear regression, error bars are obtained by data blocking method. 126

5.14 Time evolution of biodiesel viscosity at extreme conditions with different acceleration amplitude: (a) biodiesel at 300 K - 200 MPa; (b) biodiesel at 5 MPa - 800 K. 127

5.15 A schematic representation of the exchange of the kinetic energy between the atoms in hot (red) slab and cold (blue) slab of a simulation box in rNEMD simulation. 128

5.16 (a) Temperature profile along the z direction in rNEMD simulation of biodiesel at 313.15 K and 0.1 MPa with different swap rate (ps^{-1}), where lines are linear fittings; (b) time evolution of temperature difference between hot side and cold side; (c) density profile along the z direction with different swap rate; (d) comparison of thermal conductivity using rNEMD (black hollow box) and GK-EMD (red dashed line). The results of rNEMD are averaged over five independent simulations. 129

5.17 Temperature gradient, temperature difference between the hot side and cold sides, density profile of biodiesel with different swap rates at extreme conditions: (a) - (c) biodiesel at 300 K - 200 MPa; (d) - (f) biodiesel at 5 MPa - 1200 K. 131

List of tables

1.1 Range of the specification of diesel and biodiesel (Lapuerta et al., 2008) . . 7

1.2 Time steps of different systems (Raabe, 2017). 14

3.1 Molecular structures, chemical formula and compositions of soy oil biodiesel. 51

3.2 Molecular structures, chemical formula and compositions of diesel. 51

3.3 The observed decomposition pathway and final oxygenated products of MB, EP, and MC in five parallel simulations, with the occasional pathways marked with star. 62

3.4 Molecular structures and the chemical formulas of diesel surrogate fuel. . . 65

3.5 Number of the molecules of diesel surrogate fuel and oxygenated additives in the simulation box. 65

3.6 The observed primary chemical reaction and relative kinetics rate of oxygenates in thermal decomposition, where the reaction leading to the direct formation of CO are marked with asterisk, the products of alkyl radicals are highlighted in blue, species facilitating the bimolecular decomposition are highlighted in green. 74

4.1 Properties of FAMEs and alkanes for comparison: molecular mass (m); phase change data of fusion or melting temperature (T_m), boiling temperature (T_b), critical temperature (T_c) and critical pressure (P_c) (NIST, 2021) (do Carmo et al., 2015). 80

4.2 Different orders of rotational relaxation time of MDC at different pressures, averaged over 5 independent trajectories. 88

4.3 The density of MDC at 298.15 K and 0.1 MPa calculated using the TraPPE force field with different system sizes, results are averaged over 5 replicated independent trajectories. 91

4.4 Comparison of diffusion coefficient with the experimental result at 298.15 K and 0.1 MPa (10^{-9} m^2/s), data was corrected over system size effect. . . . 93

5.1 Molecular names, chemical formulas, molecular structures, molecular mass and composition of rapeseed biodiesel. 104

5.2 The parameters of biodiesel surrogate fuels, taken from the work of do Carmo et al. (2015). 114

5.3 The parameters of diesel surrogate fuels, taken from the work of Lin and Tavlarides (2012). 115

5.4 Comparison between MD and empirical equation on prediction of critical properties of biodiesel and diesel. 115

Nomenclature

Roman Symbols

A	Scaling constant in YSI; fitting parameter; amplitude of acceleration
a	Acceleration of particle
B	Scaling constant in YSI; fitting parameter
C	Parameter in Ryckaert-Bellemans function; fitting parameter
c_d	Drag coefficient
c_k	Contribution of carbon type k to YSI of fuel molecule
C_p	Correlation functioin of pressure tensor
C_{Rot}	Rotational correlation function
D	Diffusion coefficient
d	Fitting parameter, width of liquid-vapor interface
D_f	Fractal dimension
E	Energy
F	Parameter in Fourier series
f	Newton force
$g(r)$	Radial distribution function
h	Specific enthalpy
i, j, k, l	Atom index of i, j, k and l; index in summation
$\boldsymbol{J}$	Species flux

k	Force parameter in bond and angle energy formula
k_B	Boltzmann constant
ke	Kinetic energy
k_f	Fractal prefactor
K_n	Kernel function
L	Length of MD box
l	Effective bond length
M	Molecular mass
N	Number of molecules/atoms in modelling system
n	Number of surrogate molecules
n_b	Number of beads
N_{df}	Number of freedom degree
n_k	Number of carbon atoms of type k
n_p	Number of particles in the soot aggregates
P	Pressure/pressure tensor
p	Momentum
P_c	Critical pressure
$P_{c,m}$	Critical pressure of mixtures
pe	Potential energy
P_n	n^{th} order of Legendre polynomial
P_{pc}	Pseudo critical pressure
Q	Steinhardt parameter
q	Partial charge on atom
$\boldsymbol{q}$	Bond-orientational order parameter; heat flux

R	Radius; gas constant
r	Distance between two atoms
$\boldsymbol{R}$	Vector between two atoms
R_{ee}	End-to-end atom distance
R_{eff}	Effective hydrodynamic radius
R_g	Gyration radius
r_p	Mean radius of the single soot monomer
S	Collective variable of SMAC; stress tensor
S_T	Soret coefficient
T	Temperature
t	Time
T_b	Boiling temperature
T_c	Critical temperature
$T_{c,m}$	Critical temperature of mixtures
T_g	Glass transtion temperature
T_m	Melting temperature
T_{pc}	Pseudo critical temperature
U	Potential energy of the system
V	Volume; velocity amplitude
v	Velocity
V_c	Critical volume
v_p	Most probable velocity
w_i	Mass fraction of component i
x_i	Mole fraction of component i

Y	Spherical harmonics

Greek Symbols

α	Fitting parameter
β	Fitting parameter
β_T	Isothermal compressibility
χ	A certain transport property
δ	Lindemann index
ε	Depth of the LJ potential well
η	Viscosity
γ	Surface tension
Γ	Gamma function; thermal dynamic factor
ι	A dimensionless constant determined by an Ewald-like summation of a periodic lattice
κ	Thermal conductivity
Λ	Onsager coefficient
λ	Velocity rescaling factor
μ	Chemical potential
ω	Frequency; acentric factor
ϕ	Torsion angle
Ψ	A switching function
ρ	Density
ρ^n	Number density
ρ_c	Critical density
σ	The distance at which the LJ potential energy is zero; switching functioin
τ	Fitting parameter

θ_i	Volumetric fraction of component i
θ	Bond angle
ε_0	Permittivity of vacuum
ξ	Improper angle
ζ	A certain physical property related to transport property

Superscripts

Fick	Fick diffusion coefficient
MS	Maxwell-Stefan diffusion coefficient

Subscripts

0	Initial state
a	Two-bond angle
α	A component of axis in Cartesian coordinates
b	Bond stretching interaction
β	A component of axis in Cartesian coordinates
d	Dihedral angle
f	Fast decay
L	Liquid state
nb	Non-bonded interactions
Rot	Rotational motion
s	Slow decay
Tra	Translational motion
V	Vapour state

Acronyms / Abbreviations

2DS	2°C Scenario

AA	All-atom
AALH	Aromatic Aliphatically Linked Hydrocarbon
AARD	Average Absolute Relative Deviation
ACF	Autocorrelation Function
ADLH	Aromatic Directly Linked Hydrocarbon
AFM	Atomic Force Microscopy
B	Biodiesel
BO	Bond Order
CGenFF	CHARMM General Force Field
CHARMM	Chemistry at Harvard Macromolecular Mechanics
CHRCR	Clustering of Hydrocarbons by Radical-Chain Reactions
CN	Coordination Number
COM	Center of Mass
CPO	Cyclopentanone
CR	Carbon Ring
CVHD	Collective Variable-Driven Hyperdynamics
DBM	Dibutyl Maleate
DCA	Decalin
DCH	*n*-Dodecylcyclohexane
D	Diesel
DDC	*n*-Dodecane
DFT	Density Functional Theory
DMC	Dimethyl Carbonate
DMM	Dimethoxymethane

EMD	Equilibrium Molecular Dynamics
EP	Ethyl Propionate
FAME	Fatty Acid Methyl Ester
FFT	Fast Fourier Transform
fs	Femtosecond
FVT	Free Volume Theory
G	Guaiacyl
GHG	Green-House Gas
GK	Green-Kubo
GROMACS	GROningen MAchine for Chemical Simulations
HACA	H-Abstraction-Carbon-Addition
H	p-Hydroxyphenyl
HMN	Heptamethylnonane
HP	High-Pressure
HTHP	High-Temperature and High-Pressure
HT	High-Temperature
HXD	*n*-Hexadecane
IEA	International Energy Agency
IPCC	Intergovernmental Panel on Climate Change
KWW	Kohlrausch-Williams-Watts
LAMMPS	Large-scale Atomic/Molecular Massively Parallel Simulator
LJ	Lennard-Jones
MB	Methyl Butanoate
MC	Methyl Crotonate

MDC	Methyl Decanoate
MD	Molecular Dynamics
ML	Methyl Linoleate
MLN	Methyl Linolenate
MMR	Methyl Myristate
MNT	1-Methylnaphthalene
MO	Methyl Oleate
MP	Methyl Palmitate
MSD	Mean Square Displacement
MS	Methyl Stearate
NEMD	Non-Equilibrium Molecular Dynamics
Ni	Nickel
NMVOC	Non-Methane Volatile Organic Compound
NOx	Nitrogen Oxides
NPT	Isothermal-Isobaric (fixed atom numbers, pressure, and temperature)
NVE	Microcanonical ensemble (fixed atom numbers, volume, and energy)
NVT	Canonical ensemble (fixed atom numbers, volume, and temperature)
OPLS	Optimized Potentials for Liquid Simulations
OTD	*n*-Octadecane
PACF	Autocorrelation Function of Pressure Tensor
PAH	Polycyclic Aromatic Hydrocarbon
PBC	Periodic Boundary Conditions
PCAH	Peri-Condensed Aromatic Hydrocarbon
PME	Particle-Mesh Ewald

PM	Particulate Matter
PP	Periodic Perturbation
PSD	Particle Size Distribution
ps	Picosecond
QEq	Charge Equilibration
RDF	Radial Distribution Function
ReaxFF	Reactive Force Field
rNEMD	reverse NEMD
RSR	Resonance-Stabilized Radical
SCF	Supercritical Fluid
SD	Standard Deviation
SDS	Sustainable Development Scenario
SE	Stokes-Einstein
SED	Stokes-Einstein-Debye
S	Syringyl
TDM	Time Decomposition Method
TEM	Transmission Electron Microscopy
TG	Thermogravimetric
TMB	1,2,4-Trimethylbenzene
TraPPE	Transferable Potentials for Phase Equilibria
UA	United-atom
UB	Urey-Bradley
VACF	Velocity Autocorrelation Function
vdW	van der Waals

VFT	Vogel-Fulcher-Tammann
VLE	Vapour Liquid Equilibrium
VMD	Visual Molecular Dynamics
XPS	X-ray Photoelectron Spectroscopy
YSI	Yield Sooting Index

Chapter 1

Introduction

1.1 Biofuels produced from biomass

1.1.1 Deployment of biofuels

Biofuels produced from biomass including wastes are renewable and regarded as alternatives to fossil fuels with the hope of achieving environmental and socioeconomic benefits such as reducing anthropogenic green-house gas (GHG) emissions, circular bioeconomy development, employment generation and energy security. According to the International Energy Agency (IEA) 2°C Scenario (2DS), modern bioenergy will meet nearly 17% of final energy demand in 2060 compared to 4.5% in 2015, growing most in the transport sector as shown in the Sustainable Development Scenario (SDS) in Figure 1.1 (a). However, the current rate of bioenergy deployment is well below these 2DS levels. In the transport sector, the present biofuel supply/consumption must be scaled up by at least 10 times, from 3 EJ to 30 EJ (2% of current global transport fuel to 27% in the year 2050 (Fairley, 2011), to keep pace with the 2DS requirements as shown in Figure 1.1 (b).

It is a consensus that liquid fuel vehicles will continue to be used for many decades particularly in the long-haul road freight transport and marine transport for international trading, even when electric vehicles are expected to become dominant for passenger cars in the global automotive market. In spite of the encouraging expectation in electrification of light-duty passenger vehicles, liquid fuels still provide over 50% of transportation energy (Lynd and de Brito Cruz, 2010), considering there is little near future prospect for battery-powered jetliners, heavy goods vehicles and marine vessels. This scenario was demonstrated clearly in the SDS as shown in Figure 1.1 (c). Presently road freight and light passenger vehicles account for the major proportion of biofuels, while there will be a sharp increase to meet the demands of 7% of international shipping and 10% of aviation fuels in 2030 although the present biofuel utilisation is minimal in both subsectors (IEA, 2017).

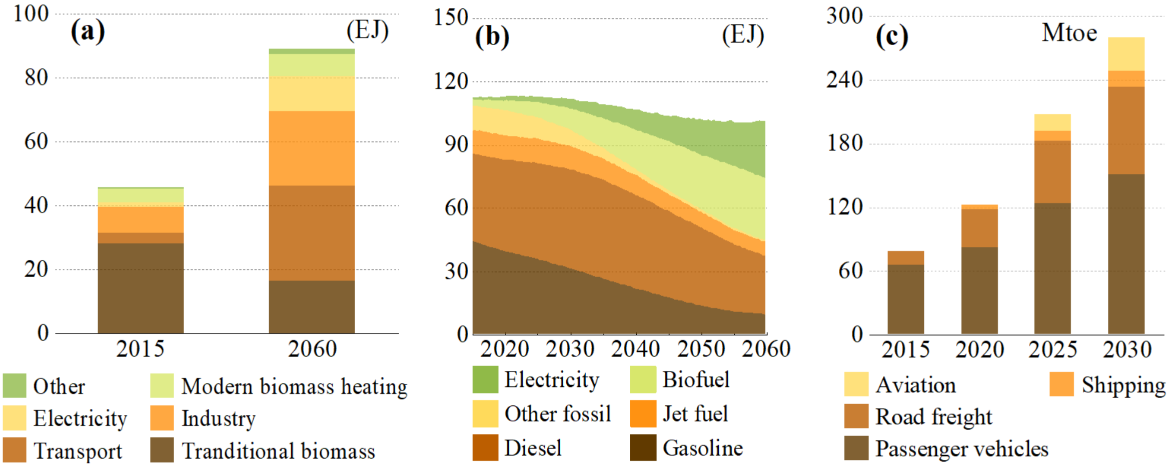

Fig. 1.1 (a) Contributions of bioenergy to final energy demand in the years 2015 and 2060 in 2DS; (b) final energy demand of transportation in 2DS; (c) major biofuel consumption in SDS, 2015-2030; source of data: IEA bioenergy report (IEA, 2017).

1.1.2 Technical roadmap of biofuel production

Biodiesel and bioethanol are currently two of the commercially available large-scale biofuels that can be produced from a variety of resources (Luque et al., 2008). Consumption share of advanced biofuels derived from lignocellulosic biomass such as agricultural and forestry wastes is expected to further scale up substantially considering sustainability of lignocellulose and massive production of 170 billion metric tons per year (Li et al., 2015). Lignocellulose comprising of cellulose, hemicellulose and lignin can be cracked and depolymerized rapidly into biofuels during pyrolytic degradation at elevated temperature.

Among the process technologies, thermochemical conversion is more suitable for industry-scale utilization compared with the biochemical methods, e.g., anaerobic and aerobic digestion (Liu et al., 2017b). Gasification is also promising and commonly used in treatment. Syngas produced from the gasification can be used as fuels directly after purification or synthesized into high-value-added chemicals like ethanol and dimethylether However, biocrude liquid fuel is a complex mixture containing aromatics, phenolics, acids, hydroxyketones, etc. The number of oxygenated compounds in a typical biofuel can be over 300 during biomass pyrolysis, resulting in undesirable attributes of high viscosity, low energy content and corrosiveness (Sharifzadeh et al., 2019). Tar formation is the main issue in gasification that can clog the downstream equipment, increase the maintenance cost and hinder biomass utilization. Tars formed inevitably during gasification refer to a series of condensed organics from single ring aromatics like toluene to heavy polycyclic aromatic hydrocarbons (PAHs) of 4-7 rings. Oxygenated aromatics like dibenzophenol also exists (Molino et al., 2016).

The third/fourth generation of biofuels producing from algae biomass is also in development. Algal biofuels do not require agricultural land and potable water resources. Algae do not compete with food or other crops and can be cultivated in shallow lagoons or raceway ponds on marginal land or closed ponds. It can be produced throughout the year unless it is limited by light irradiation, and the oil yield can even exceed that of the best oilseed crops (Dutta et al., 2014). It is estimated that algae could potentially produce 10 to 300 times more fuel than other crops (Chisti, 2007). The low content of hemicelluloses and about zero content of lignin in algal biomass results in an increased hydrolysis and/or fermentation efficiency. The road map of first/second generation biofuel production is shown in Figure 1.2. Pathways for the valorisation of microalgae are shown in Figure 1.3.

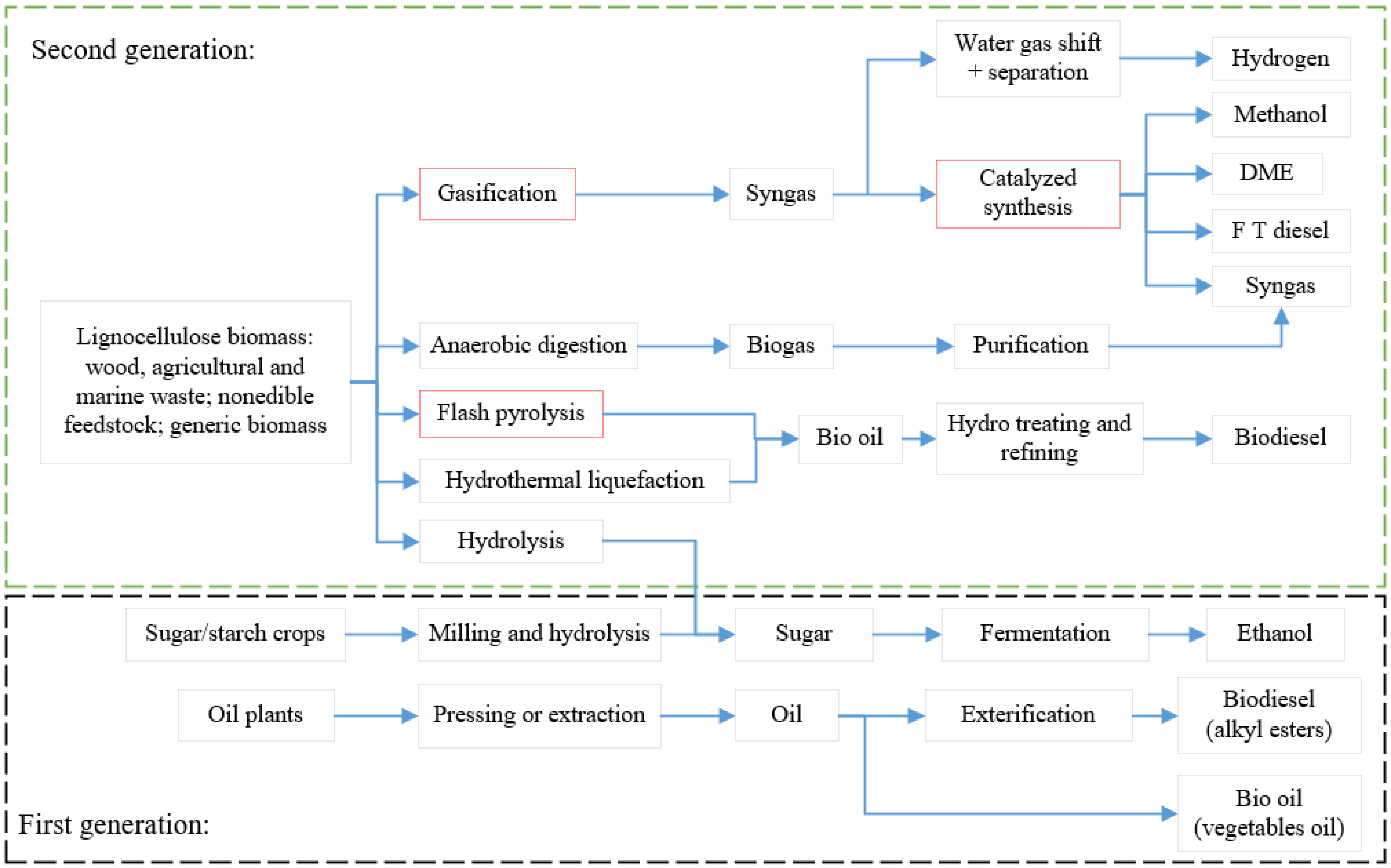
Second generation:
Lignocellulose biomass: wood, agricultural and marine waste; nonedible feedstock; generic biomass
Gasification
Anaerobic digestion
Flash pyrolysis
Hydrothermal liquefaction
Hydrolysis
Syngas
Biogas
Bio oil
Water gas shift + separation
Catalyzed synthesis
Purification
Hydro treating and refining
Hydrogen
Methanol
DME
F T diesel
Syngas
Biodiesel
First generation:
Sugar/starch crops
Milling and hydrolysis
Sugar
Fermentation
Ethanol
Oil plants
Pressing or extraction
Oil
Exterification
Biodiesel (alkyl esters)
Bio oil (vegetables oil)

Fig. 1.2 Overview of conversion routes of first/second generation feedstock to biofuels, reproduced based on the work of Agarwal (Agarwal, 2007).

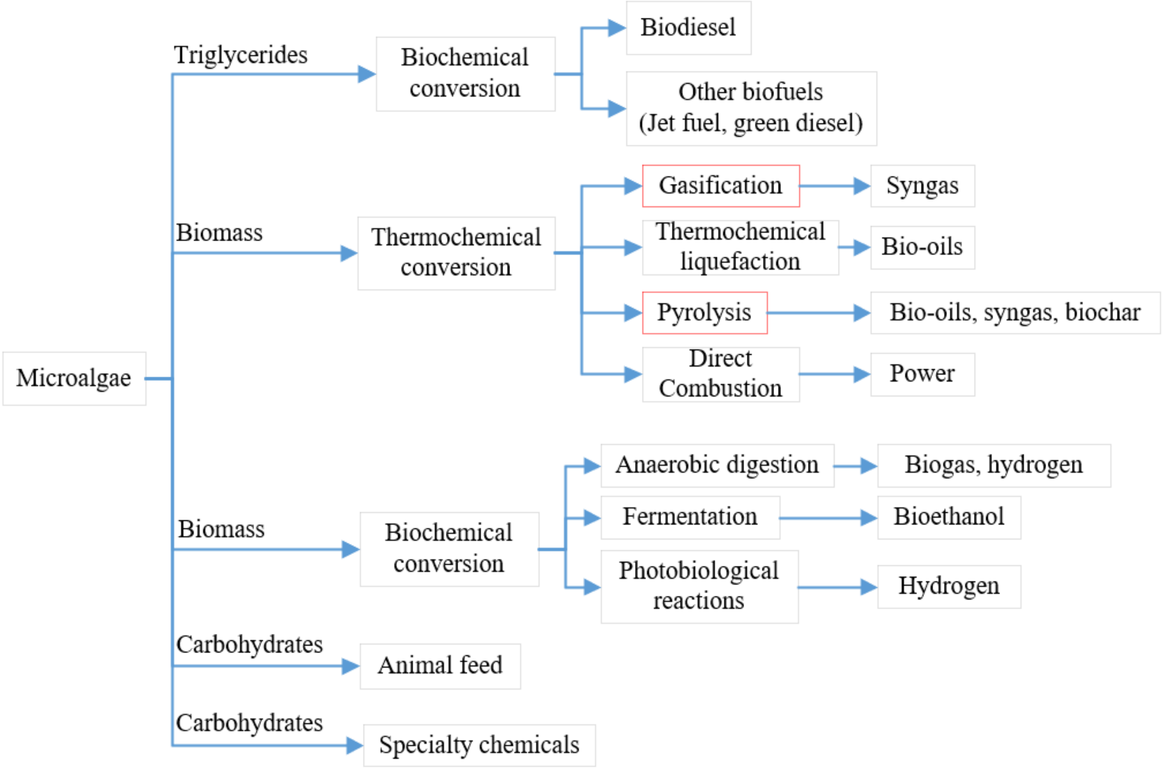
Microalgae
Triglycerides
Biochemical conversion
Biodiesel
Other biofuels (Jet fuel, green diesel)
Biomass
Thermochemical conversion
Gasification
Syngas
Thermochemical liquefaction
Bio-oils
Pyrolysis
Bio-oils, syngas, biochar
Direct Combustion
Power
Biomass
Biochemical conversion
Anaerobic digestion
Biogas, hydrogen
Fermentation
Bioethanol
Photobiological reactions
Hydrogen
Carbohydrates
Animal feed
Carbohydrates
Specialty chemicals

Fig. 1.3 Pathways for the valorisation of microalgae to biofuels and high-value chemicals.

1.1.3 Heterogeneous catalysis in biomass thermochemical conversion

It is acknowledged that catalyst can play a significant role in both biofuel reforming and tar removal. By adding appropriate catalyst like base transition metal nanoparticles into the reactors, the desirable reaction pathways can be selectively enhanced, leading to the biomass valorisation and thus achieving the optimization of the products. However, catalysts undergo deactivation temporally or permanently during their lifetime through a series of physicochemical phenomena (Hu et al., 2013) (Hervy et al., 2019) (Ochoa et al., 2020) (Cheng et al., 2020) (Li et al., 2020). Catalyst deactivation leads to secondary reactions, prohibiting the conversion rate and probably weakening the production of H_2 in gasification (Arregi et al., 2018a).

Understanding catalyst deactivation mechanisms and developing strategies to design stable catalysts are as important as research of catalytic selectivity and activity in practice, but deactivation processes are often overlooked in academic research (Murphy and Xu, 2018). For industrial application, catalyst regeneration excluding irreversible deactivation can help to control the replacement costs, and thus make the reforming process more favourable. Bartholomew (2001) classified the deactivation mechanism into six types, i.e., poisoning, fouling, sintering, crushing, catalyst surfaces reacting with gas to produce volatile compound, and inactive phase formation on catalyst surfaces after reaction with vapour, support or promoter. In terms of biofuel/tar reforming, coke deposition is the most notorious and the primary deactivation mechanism (Sharifzadeh et al., 2019) (Ochoa et al., 2020) (Gao et al., 2020). Surface coking inhibiting active sites from being available for reaction is affected by many factors, including the composition of feedstock and operating conditions like temperature, pressure and contact time, etc. Arregi et al. (2018b) studied the deactivation rate of nickel (Ni) supported catalyst in in-line steam reforming. It was observed that the increasing concentration of non-reformed oxygenated phenolic compounds in reaction medium accelerated the deactivation. Ochoa et al. (2017) showed that coke morphology mainly affected by temperature also caused a deep impact on deactivation of Ni.

1.2 Physicochemical properties of biofuels in combustion

Understanding the relations between biofuel composition & molecular structures and the physicochemical properties is essential in fuel quality evaluation and development of cleaner and more efficient engines. In comparison with conventional diesel fuels comprised of alkanes, aromatics and even sulfur, the contents of biodiesel are primarily fatty acid methyl esters (FAMEs). It has been reported widely that the oxygen atoms in FAME molecules lead to substantial reduction in emissions of particulate matter, total hydrocarbons and carbon monoxide, while the power loss is imperceptible in unmodified conventional engines when biodiesel is used (Xue et al., 2011) (Roy et al., 2013). Nevertheless, higher viscosity and worse fluidity are the major application downsides for biodiesel (Chen et al., 2018a). Injectors with common rail system always work at extremely high pressure above 100 MPa, meaning that fuel viscosity increases substantially over the atmospheric values. In general, the chemical kinetics of hydrocarbons in combustion have been the subject of numerous studies. However, fewer kinetic studies related to the oxidation of biodiesel have been performed at the experimental and modelling level. The main reason for the lack of information is the complexity in molecular structure of actual biodiesel compounds, which involves large aliphatic chains of 14-20 carbon atoms with C=C double bonds and ester groups (Coniglio et al., 2013). For the combustion kinetics, the elemental chemical reaction with rate constant, thermal dynamics parameters and transport property are the major components. Assessment of biodiesel properties and their impact is required before expanding the availability of biodiesels in the fuel market. Comparison between biodiesel and diesel on some specific properties in shown in Table 1.1.

Table 1.1 Range of the specification of diesel and biodiesel (Lapuerta et al., 2008)

Specifications	Biodiesel	Diesel
Density (15 °C) (kg/m3)	870-895	810-860
Viscosity (40 °C) (cSt)	3.5-5.5	2-3.5
Cetane Number	45-65	40-55
Cloud Point (°C)	-5 to 10	-25 to 0
Pour Point (°C)	-5 to 10	-20 to 0
Lower Heating Value (MJ/kg)	-15 to 10	-35 to 0
Water Content (mg/kg)	36.5-38	42.5-44
Acid Number (mg KOH/g)	0-500	/
Ester Content (% w/w)	0-0.6	/
Glycerin Content (% w/w)	>96	/
Sulfur Content (mg/kg)	0-0.25	15-100

1.2.1 Prediction of biodiesel thermophysical properties for supercritical combustion

Most data available in the literature encompasses the temperature dependence of biodiesel viscosity at atmospheric pressure. Fewer studies (actually only seven studies were mentioned in the latest review paper of Ferreira et al. (2020)) have dedicated to measuring and predicting the high-pressure viscosity of biodiesel (Chhetri and Watts, 2012) (Freitas et al., 2014) (Ferreira et al., 2020). Recent observation of the crystallisation and solidification process of FAMEs at room temperature and high pressure above 230 MPa makes it even more challenging to understand the rheological property of biodiesel at extremely high pressure (Tarakowski et al., 2015) (Kiełczyński et al., 2017).

The next generation clean, fuel-flexible and efficient engines will operate at considerably high pressure such as 100 bar which is above the fuel critical points, i.e., at supercritical conditions. The engine injection is thereby described as a transcritical process of subcritical liquid fuel under extremely high pressure injected into supercritical ambient gases. The fuel jet will be heated to a supercritical temperature before combustion where distinct liquid and gas phases do not exist. It is known that high-temperature and high-pressure (HTHP) supercritical fuels have properties of lower density, viscosity and higher diffusivity which is beneficial for fuel/air mixing. Prediction of fluid behaviour at HTHP supercritical conditions is a challenge. It requires new theoretical methods particularly considering the phase transition between "rigid-like", "liquid-like" and "gas-like" due to the existence of Frenkel line or Widom line (McIlroy et al., 2006) (Brazhkin et al., 2012) (Brazhkin et al., 2013) (Gallo et al., 2014) (Mallepally et al., 2018) . Direct measurements of physical properties for every encountered fluid at all conditions of interest are not only expensive and time-consuming but also extremely difficult and sometimes impossible (Baled et al., 2018). A typical *P*-*T* phase diagram of supercritical fluids (SCFs) is shown in Figure 1.4, where P_r and T_r are reduced pressure and reduced temperature normalized with respect to their critical values. Widom lines are the loci of the extrema for thermal expansion, density fluctuation and thermal capacity, which are terminated according to the disappearance of extrema (Banuti et al., 2020).

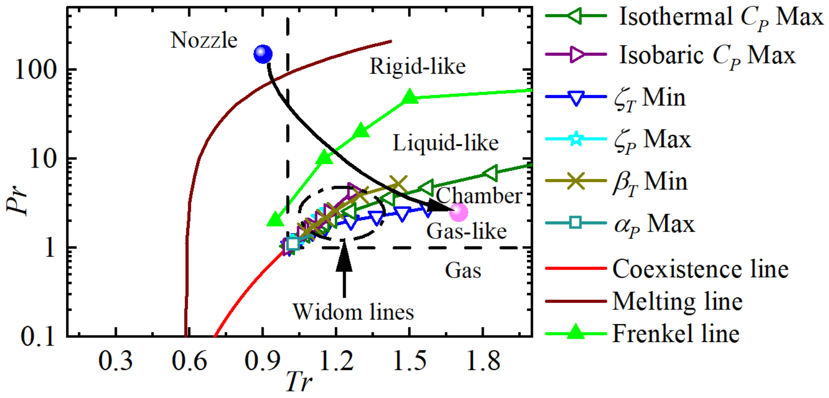

Fig. 1.4 *P*-*T* phase diagram of SCFs with melting line, coexistence line and the newly developed thermal dynamic boundaries i.e. the Frenkel line and Widom lines.

1.2.2 Biofuels on soot mitigation

Some recent studies have identified black carbon as the second largest anthropogenic contributor to global warming (Andreae and Ramanathan, 2013). Its climate impact is much higher than conventionally believed, especially in altering regional atmospheric stability. The effects of soot on climate mainly lie in its radiative influences which can be distinguished as direct, referring to scattering and absorption of radiation by soot particles themselves, and indirect, referring to the influences of soot on cloud radiative properties and cloud lifetimes (Charlson et al., 1992). According to the synthetic black-carbon climate forcing model developed by Bond et al. (2013), the best estimation of climate radiative forcing of soot is $+1.1\ \mathrm{W \cdot m^{-2}}$ with 90% uncertainty which is about twice greater than the data released by Intergovernmental Panel on Climate Change (IPCC), shown in Figure 1.5.

Any efforts on reducing soot emission can simultaneously lead to the dual benefit of mitigating near-term climate change and protecting human health. The average atmospheric lifespan of particulate carbon black is 4-12 days. Thus, cutting down the emission of diesel

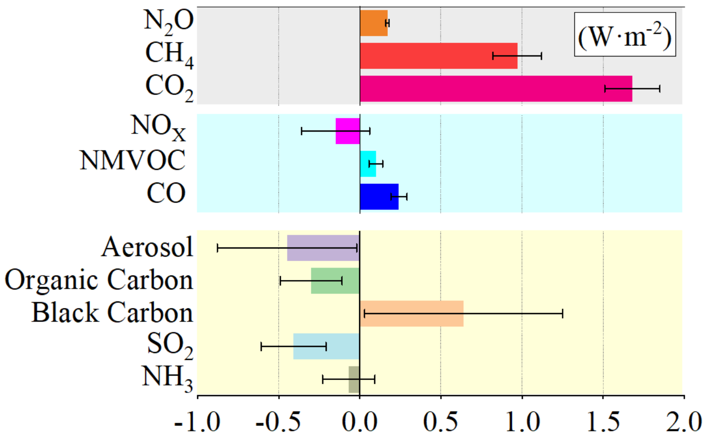

Fig. 1.5 Comparison of emission species on atmosphere radiative forcing, where positive forcing indicates warming the climate and NMVOC is non-methane volatile organic compound; source of data: IPCC climate change report (Blanco et al., 2014).

soot and organic matter is probably the most pragmatic approach to slow global warming and the fastest solution to survive Artic ice and Tibet glaciers. Some modelling studies showed that eliminating all fossil black carbon could scale down 20-45% of global net warming within 3-5 years, whereas reducing CO_2 emissions by a third was estimated to have the same effect, but after 50-200 years (Jacobson, 2002). The formation of soot depends strongly on the fuel composition. For example, compared with conventional Jet-A fuels, experiments on a NASA DC-8 aircraft at cruise conditions showed that utilisation of a 50:50 (by volume) blend of Jet- A fuel and a hydrotreated camelina oil can reduce the volatile and non-volatile particle emissions by 50% - 70% and shift the particles towards smaller size (Moore et al., 2017).

The major concern for the utilisation of diesel type of fuels is the harmful emissions of nitrogen oxides (NOx) and soot (black carbon). While NOx formation is common to combustors and the mechanisms are relatively well understood, soot formation has not been fully understood, especially when biodiesel or biodiesel/diesel blends are concerned. Soot emitted from diesel engines accounts for over 15% of total hazardous pollution in the air as shown in Figure 1.6. Soot and its co-pollutants are also the key components of fine particulate matter, i.e., $PM_{2.5}$, the leading environmental cause of cardiopulmonary mortality.

Biodiesel is considered as “carbon-neutral” fuels because combustion emissions are assumed to be offset by carbon sequestration during biomass growth. Moreover, the utilisation of biodiesel in conventional internal combustion engine resulted in particulate emission reduction appreciably under operating conditions owing to the oxygenated moiety within the primary fuel molecules which changes the rates and reaction pathways of ignition and oxidation processes (Coniglio et al., 2013). Evaluating and quantifying the effects of actual biodiesel molecular structures, e.g., chain length, unsaturation degree and oxygenated moiety

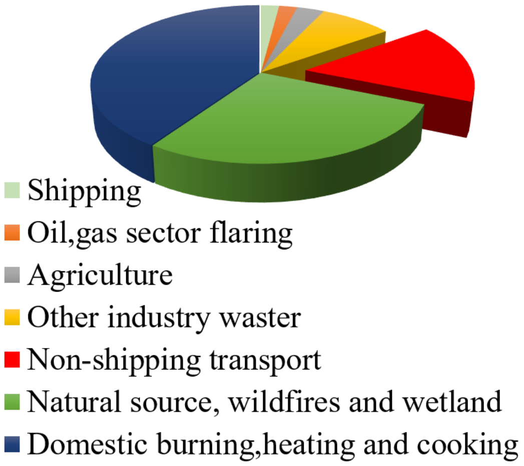

Fig. 1.6 Sources of global black carbon emissions in the year 2010; source of data: Arctic Monitoring and Assessment Programme (https://www.amap.no/, 2015).

on sooting tendency are currently lacking but essentially needed for the design of novel oxygenated biofuel additives.

For advanced biofuels, the amount of soot reduction is approximately linear to the added oxygen content, but not all oxygenated additives are of equal effectiveness. Westbrook et al. (2006) investigated how different oxygenated function groups like ester structures can have different soot-suppression efficiency of the fuel species like dibutyl maleate (DBM), methyl butanoate (MB), dimethyl carbonate (DMC) and methanol etc. It was found that when the oxygen content of the fuel reached 25-30% by mass, virtually all soot emission had disappeared, as shown in Figure 1.7. Measurements of the 75:25 blended ethylene and biofuels on soot formation in shock tube at high temperature (1700-2200 K) found that addition of ethanol, cyclopentanone, and methyl acetate reduced soot while α-diisobutylene and methyl furan produced more soot compared to the baseline (Barak et al., 2020).

Most recently, Sun et al (Sun et al., 2017a) (Sun et al., 2017b) (Sun et al., 2017c) studied several novel oxygenated fuels including carbonates, polyether and ketones. Combustion kinetics investigations were performed for typical representative compounds, including dimethyl carbonate, diethyl carbonate, cyclopentanone, 3-pentanone, 1,2-dimethocyethane and dimethoxymethane. It was found that due to the presence of the carbonate functional group, fuels of this category have special unimolecular decomposition channels, and CO_2 is easily released from their combustion processed. Therefore, one carbon atom in the fuel need to combine with two oxygen atoms to prevent from participating in the formation of soot precursors. In this way, the oxygenate atoms are not efficiently used. The carbon-oxygen double bond in the ketone fuels are tightly bounded, so carbonyl functionalities tend to be released in CO, fragmenting the carbon chains in fuel molecules, and avoiding the direct formation of larger hydrocarbon species from the fuel consumption. Meanwhile, oxygen atoms in carbonyl moieties are not able to participate in the formations of small aldehyde and ketone pollutants.

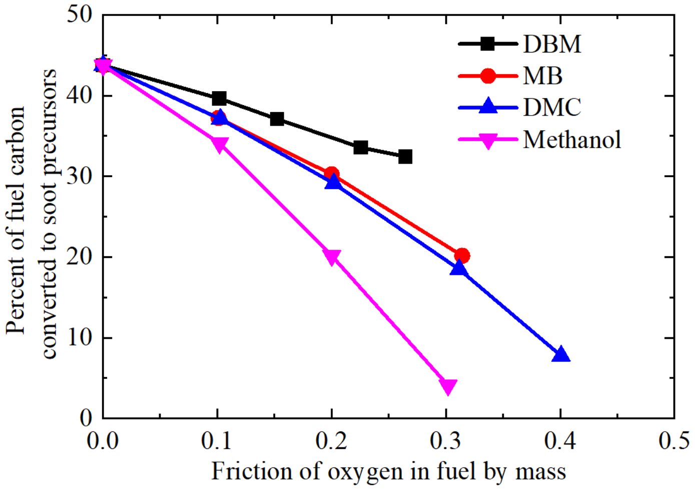

Fig. 1.7 Computed reductions in soot precursors concentrations with the additions of selected oxygenated species: dibutyl maleate (DBM), methyl butanoate (MB), dimethyl carbonate (DMC) and methanol, which are reproduced from the work of Westbrook et al. (2006).

Understanding the soot formation mechanism and thereby reducing soot emissions from combustion devices have always been a challenge with insufficient studies. It is acknowledged that soot nucleation defined as the transition from gaseous molecular precursors to condensed matter, yielding carbonaceous nanoparticles is a key step but mostly unknown (Mercier et al., 2019). Critical gaps remain between the experimental observation and mechanistic description (Wang, 2011). The widely reported soot nucleation pathways involving the dimerization of PAHs into stacks via van der Waals (vdW) force is debatable (Michelsen, 2017). It fails to explain, for example, the existence of a large amount of aliphatic C-H bonds in the shell of nascent soot (Cain et al., 2011). Irreversible process of PAH dimerization, with pyrene ($C_{16}H_{10}$) recognized as the smallest building block, is not thermodynamically favoured (Zhao et al., 2005). The binding forces (e.g., electrostatic force, dispersive force and π-π stacking interaction) of dimers with moderate-sized PAHs are too weak to allow the PAH clusters to survive in the environment above their boiling or sublimation temperatures.

The species as large as ovalene ($C_{32}H_{14}$), hexcoronene ($C_{42}H_{18}$) or circumcoronene ($C_{54}H_{18}$) may generate the dimers capable of surviving at flame temperature. The concentration of these PAH species in the gas phase during combustion is low, contradicting to the phenomenon that nascent soot was observed before the concentration peaks of these PAH species (Keller et al., 2019). The hypothesis of dimerization of PAHs with larger size in the soot nucleation process therefore appears highly unlikely. It is speculated that some stronger interactions are prerequisite for soot nucleation, such as covalent bonds combining PAH radicals and aryl radicals, but the existing theories are still inadequate to explain the rapidly persistent mass growth and the gas-to-solid nucleation process in post flame region (Wang, 2011).

1.3 Molecular dynamics simulation

1.3.1 Basic methodology of molecular dynamics

Macroscopic properties are often determined by molecular-level behaviour which can be obtained from molecular dynamics (MD) simulation of a system containing a set of N atomic particles.The basic methodology of MD simulation is shown in Figure 1.8. Each of the particles is assigned a random velocity corresponding to the Maxwell-Boltzmann distribution at the desired temperature. The interaction between the particles is described typically in the form of a suitable potential energy. The time evolution of the particles' positions is determined by integrating Newton's equations of motion with integrator like Verlet algorithm (Verlet, 1967).

The concept of ensembles plays a key role in statistical mechanics. An ensemble is a large number of microstates that all have the same constrained properties as the macroscopic system of interest. Representative ensembles include microcanonical ensemble (the system is constant in number of atoms, volume, and energy i.e, NVE), canonical ensemble (fixed atom numbers, volume, and temperature, i.e., NVT), isothermal-isobaric (fixed atom numbers, pressure, and temperature, i.e., NPT) ensemble, and the grand canonical ensemble etc. For isothermal simulation, temperature is maintained with the thermostats algorithm such as velocity rescaling (Woodcock, 1971) (Bussi et al., 2007), Andersen thermostat (Andersen and Hans, 1980), Berendsen thermostat (Berendsen et al., 1984), and Nose-Hoover thermostat (Nose, 1984), (Hoover, 1985) etc. For isobaric simulation, pressure is maintained with the barostat such as Berendsen barostat (Berendsen et al., 1984), Parrinello-Rahman barostat (Parrinello and Rahman, 1981) and Nose-Hoover barostat (Nose, 1984), (Hoover, 1985) etc. The details are introduced as:

(a) Initialisation

Initial position

The physiochemical properties at equilibrium should be insensitive to the initial conditions. Thus, an initial configuration only has to be reasonable-meaning that it should not contain non-physical overlaps between molecules that result in high-energy interactions

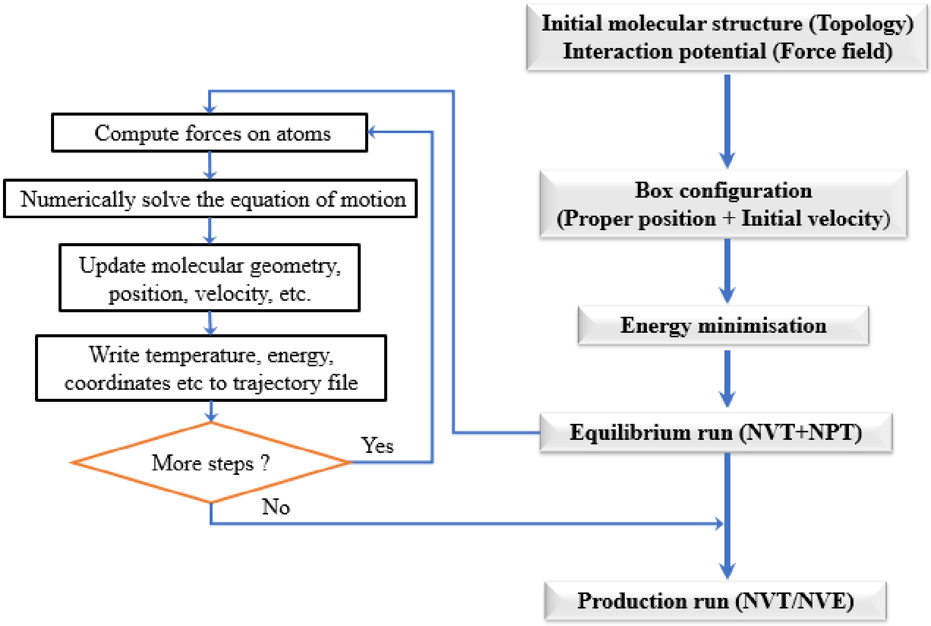
Initial molecular structure (Topology)
Interaction potential (Force field)
Box configuration
(Proper position + Initial velocity)
Energy minimisation
Equilibrium run (NVT+NPT)
Production run (NVT/NVE)
Compute forces on atoms
Numerically solve the equation of motion
Update molecular geometry, position, velocity, etc.
Write temperature, energy, coordinates etc to trajectory file
More steps ?
Yes
No

Fig. 1.8 Schematic of the basic molecular dynamics simulation procedure.

(Raabe, 2017). When simulating the solids, the initial configuration is prepared according to the experimentally determined crystal structure of the component as shown in Figure 1.9 (a)-(c). For liquids or gases, the molecules could be placed at random positions within the simulation box as shown in Figure 1.9 (d).

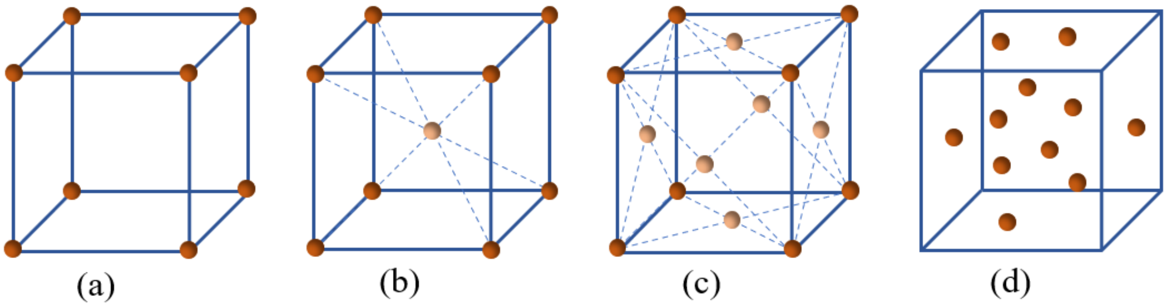

Fig. 1.9 Particle distribution: (a)-(c) are simple cubic (sc), body-cantered cubic (bcc) and face-cantered cubic (fcc); (d) random distribution

Initial velocity

In molecular dynamics studies, the set up of the simulation also comprises the assignment of initial velocities to all particles. For example, the Maxwell-Boltzmann distribution which provides a probability distribution of the velocities of particles within a system as a function of the temperature:

$$p\left(\mathbf{v}_i\right)=\sqrt{\frac{M_i}{2\pi k_B T}}\exp\left(-\frac{M_i\mathbf{v}_i^2}{2k_B T}\right) \tag{1.1}$$

where $\mathbf{v}_i$ is velocity of particle i, M_i is mass of particle i, k_B is Boltzmann constant, T is temperature.

Time step

The time step for most of MD simulations is on the femtosecond (fs) scale. For organics, the largest time step is limited by the highest frequency of chemical bond vibration, i.e., vibrations of bonds containing hydrogen atom. This is because hydrogen is the lightest atom and has the fastest bond vibration. Normally, the time step should be ten times lower that the highest frequency (Kim, 2014). Too large time step would cause the integration algorithm unstable and large truncation error. The energy of molecular system would increase rapidly, and results in the devastating atomic collisions. The repulsive forces then create a strong force that propels these atoms apart which cause the explosion of the simulation box. On the other hand, too small time step would cause very long calculation time. To solve this problem by neglecting fast vibrations, many MD simulation constrain all bonds containing hydrogen atoms. Therefore, one should select proper time step to consider both accuracy and efficiency. Time step for some typical systems is summarised in Table 1.2.

Table 1.2 Time steps of different systems (Raabe, 2017).

System	Types of Motion	Time Step (s)
Atoms	Translation	10^{-14}
Rigid molecules	Translation and Rotation	5×10^{-15}
Flexible molecules with rigid bonds	Translation, Rotation, and Torsion	2×10^{-15}
Flexible molecules with flexible bonds	Translation, Rotation, Torsion and Vibration	$5\times10^{-16}\sim10^{-15}$

(b) Boundary condition

Molecular dynamics is typically applied to systems containing several thousand atoms. If the simulation cell is bounded by real physical walls, the behaviour of a considerable fraction of particles near a solid surface are different from the particles in the bulk. The surface effects, i.e, interactions of the atoms with the container walls would distort the results. The classical way to minimize edge effects in a finite system is to apply periodic boundary conditions (PBC). The atoms of the system to be simulated are put into a space-filling box (primary cell), which is surrounded by 8 translated copies (image cell) of itself as shown in Figure 1.10. Thus the primary cell is imagined to be periodically replicated in all directions to form a macroscopic sample of the substance of interest. When a particle leaves the modelling domain, a corresponding image particle of this particle enters the simulation zone. The minimum image convention implies that the cut-off radius used to truncate non-bonded interactions can not exceed half the shortest box vector, otherwise more than one image would be within the cut-off distance of the force (Raabe, 2017). For a cubic box with a box length L and the origin of coordination located in the center of the box, the PBC is applied to the components of the position vector by:

$$\text{if } r_{i,x}{>}L/2,\ r_{i,x}^{\text{new}}{=}r_{i,x}\text{-}L$$
$$\text{if } r_{i,x}{<}{-}L/2,\ r_{i,x}^{\text{new}}{=}r_{i,x}{+}L$$

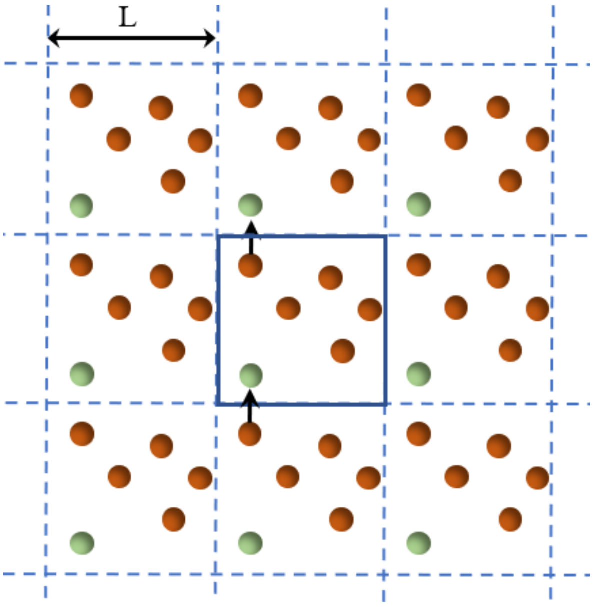

Fig. 1.10 Periodic boundary conditions in two dimensions

(c) Integrating equations of motion

The force acting on the particle is caused by its interaction with the N - 1 other particles, and can be derived from the gradient of the potential energy (U) of the system. Potential energy is a function of atom positions ($\mathbf{r}$) which is conventionally classified into intermolecular and intramolecular components. The total potential energy is summed for various contributions, such as Lennard-Jones (LJ), Coulomb, and bonded terms. The details of potential energy are introduced in the following section of 1.3.2 and 1.3.3. The force on any atom is calculated as:

$$\mathbf{f}_i = -\frac{\partial U(\mathbf{r})}{\partial \mathbf{r}_i} \tag{1.2}$$

The time-dependent particles' positions are updated by integrating Newton's equations of motion expressed as:

$$\mathbf{f}_i = m_i \mathbf{a}_i = m_i \frac{\mathrm{d}^2 \mathbf{r}_i}{\mathrm{d}t^2} \tag{1.3}$$

where $\mathbf{f}_i$ is the force on atom i, $\mathbf{a}_i$ is acceleration. As each particle interacts simultaneously with all others in the system, the motions of all particles are coupled. The analytical integration of the $3N$ (N is the number of particles in the system) second order differential equations of this many-body problems is impossible. Several finite-difference methods have been developed to solve the numerical integration of the Newton's equations of motion such as the widely used Verlet algorithm (Verlet, 1967), leap frog algorithm (Van and Berendsen, 1988), Velocity-Verlet algorithm (Swope and William, 1982), etc., in which the integration over the time t is then broken into a series of short time step Δt. The Verlet algorithm is based on a Taylor series expansion for the position $\mathbf{r}(t)$. Verlet algorithm is a two-step method as it estimates $\mathbf{r}(t+\Delta t)$ from the current position $\mathbf{r}(t)$ and the previous position $\mathbf{r}(t-\Delta t)$. The leap-frog algorithm uses positions $\mathbf{r}(t)$ at time t and velocities $\mathbf{v}$ at time $t-\frac{1}{2}\Delta t$. In velocity Verlet, positions $\mathbf{r}$ and velocities $\mathbf{v}$ at time t are used to integrate the equations of motion; velocities at the previous half step are not required.

The formulas are summarised as:

Verlet

$$\mathbf{r}_i(t+\Delta t) = 2\mathbf{r}_i(t) - \mathbf{r}_i(t-\Delta t) + \mathbf{a}_i(t)\Delta t^2 + O\left(\Delta t^4\right) \tag{1.4}$$

$$\mathbf{v}_i(t) = \frac{\mathbf{r}_i(t+\Delta t) - \mathbf{r}_i(t-\Delta t)}{2\Delta t} \tag{1.5}$$

Leap Frog

$$\mathbf{r}_i(t+\Delta t) = \mathbf{r}_i(t) + \mathbf{v}_i\left(t+\frac{1}{2}\Delta t\right) + O\left(\Delta t^2\right) \tag{1.6}$$

$$\mathbf{v}_i\left(t+\frac{1}{2}\Delta t\right) = \mathbf{v}_i\left(t-\frac{1}{2}\Delta t\right) + \mathbf{a}_i(t)\Delta t + O\left(\Delta t^2\right) \tag{1.7}$$

$$\mathbf{v}_i(t) = \frac{\mathbf{v}_i\left(t+\frac{1}{2}\Delta t\right) - \mathbf{v}_i\left(t-\frac{1}{2}\Delta t\right)}{2} \tag{1.8}$$

Velocity-Verlet

$$\mathbf{r}_i(t+\Delta t) = \mathbf{r}_i(t) + \mathbf{v}_i(t)\Delta t + \frac{1}{2}\mathbf{a}_i(t)\Delta t^2 + O\left(\Delta t^3\right) \tag{1.9}$$

$$\mathbf{v}_i\left(t+\frac{1}{2}\Delta t\right) = \mathbf{v}_i(t) + \frac{1}{2}\mathbf{a}_i(t)\Delta t + O\left(\Delta t^2\right) \tag{1.10}$$

$$\mathbf{v}_i(t+\Delta t)=\mathbf{v}_i\left(t+\frac{1}{2}\Delta t\right)+\frac{1}{2}\mathbf{a}_i(t+\Delta t)\Delta t+O\left(\Delta t^2\right) \tag{1.11}$$

(d) Temperature/pressure control

To derive thermophysical properties from MD simulations that can be compared with experimental data, it is therefore necessary to perform simulations at constant temperature and/or constant pressure, i.e. experimentally relevant conditions. In MD simulation of the N-particle system, the temperature is computed from the kinetic energy in the following equation:

$$\frac{1}{2}N_{df}k_BT(t)=E_{kin} \tag{1.12}$$

where N_{df} is number of freedom. The kinetic energy E_{kin} is in the form of:

$$E_{kin}=\frac{1}{2}\sum_{i=1}^{N}m_iv_i^2 \tag{1.13}$$

The pressure tensor is calculated from the difference between kinetic energy $\mathbf{E}_{\mathrm{kin}}$ and virial Ξ:

$$\mathbf{P}=\frac{2}{V}\left(\mathbf{E}_{\mathrm{kin}}-\Xi\right) \tag{1.14}$$

$$\mathbf{E}_{\mathrm{kin}}=\frac{1}{2}\sum_{i=1}^{N}m_i\mathbf{v}_i\otimes\mathbf{v}_i \tag{1.15}$$

$$\Xi=-\frac{1}{2}\sum_{i<j}\mathbf{r}_{ij}\otimes\mathbf{f}_{ij} \tag{1.16}$$

The straightforward way to control the temperature at a given value is to scale the velocities of particles by a factor λ , which is also the core idea of the thermostat algorithm. In velocity rescaling method, the temperature difference after velocity rescaling can be expressed as:

$$\Delta T=\sum_{i=1}^{N}\frac{m_i\left(\lambda v_i\right)^2}{N_{df}k_B}-\sum_{i=1}^{N}\frac{m_iv_i^2}{N_{df}k_B} \tag{1.17}$$

$$\Delta T=\left(\lambda^2-1\right)T(t) \tag{1.18}$$

Hence, the required scaling factor is given by:

$$\lambda=\sqrt{T_{\mathrm{new}}/T(t)} \tag{1.19}$$

Velocity rescaling method is mostly used in equilibrium simulation. It does not generate a canonical distribution, and can not reveal correctly the energy fluctuation due to the thermophysical process in the molecular system. Berendsen et al. (1984) established an algorithm to control temperature by introducing an external bath with constant temperature which is coupled with the simulation system. Meanwhile, particles' velocities are modified through a time scale τ in each time step, which is similar to the velocity rescaling scheme. The deviation of the system temperature from T_{bath} is slowly corrected according to:

$$\frac{dT(t)}{dt} = \frac{1}{\tau_T}\left(T_{\text{bath}} - T(t)\right) \tag{1.20}$$

Thus, the scaling factor λ for updating the velocity is given by:

$$\lambda = \sqrt{1 + \frac{\Delta t}{\tau_T}\left(\frac{T_{\text{bath}}}{T(t)} - 1\right)} \tag{1.21}$$

The Berendsen thermostat (Berendsen et al., 1984) suppresses the fluctuations of the kinetic energy, which indicates that it can not generate a proper canonical ensemble rigorously. Fluctuation properties like heat capacity would be affected. Andersen thermostat (Andersen and Hans, 1980) and Nose-Hoover thermostat (Nose, 1984), (Hoover, 1985) thermostat are more sophisticated approaches to control the temperature involve interactions of the system's particles with a heat bath, which can generate rigorously the correct canonical ensemble probabilities. In Andersen thermostat, temperature is controlled by stochastic collisions of its particles with imaginary heat bath particles. This can either be achieved by randomizing all the velocities simultaneously (massive collision) or by randomizing every particle with some small probability every timestep. However, it should be noted that the system dynamics by Andersen thermostat is unphysical due to a fact that stochastic collisions leave particles' velocities to decorrelate much faster than the real situation, and the true kinetics of particles are not constant. Therefore, this method can not be used to predict the transport properties by time correlation function.

The Berendsen thermostat is a weak-coupling algorithm which is extremely efficient for relaxing a system to the target temperature in initial stage, but once the system has reached equilibrium it is more important to probe a correct canonical ensemble. Nose-Hoover thermostat is an extended-ensemble approach which is first proposed by Nose (1984) and then modified by Hoover (1985). The system Hamiltonian is extended by introducing a thermal reservoir and a friction term (ζ) in the equations of motion. This friction parameter is a fully dynamic quantity with its own momentum (p) and equation of motion. It is described by the difference between the actual kinetic temperature of the system $T(t)$ and the imposed temperature T:

$$\frac{d\zeta}{dt} = \frac{N_{df} k_B}{M_{eff}} (T(t) - T) \tag{1.22}$$

where M_{eff} is the effect mass of the reservoir. The particle's motion is expressed accordingly as:

$$\frac{\mathrm{d}^2 \mathbf{r}_i}{\mathrm{d}t^2} = \frac{\mathbf{f}_i}{m_i} - \frac{p}{M_{eff}} \frac{\mathrm{d}\mathbf{r}_i}{\mathrm{d}t} \tag{1.23}$$

The effective mass is an an adjustable parameter, and a large value corresponds to a slow energy exchange between the system and the heat reservoir. The function to evolve the friction parameter is formulated according to the explicit velocity functions like leap-frog and velocity-Verlet. Nose-Hoover is the most widely used thermostat that sustains the canonical ensemble distribution both in configuration and momentum space.

A macroscopic system reacts on an imposed pressure (P) by changing its volume. Accordingly, pressure control in molecular dynamics involves volume fluctuations of the simulation box. In Berendsen algorithm, the coupling of the system to the external volume is realized by a piston that acts on the system to achieve the isotropic expansion or compression. The coordinates and box vectors are rescaled every step by the scaling factor:

$$\frac{\mathrm{d}P(t)}{\mathrm{d}t} = \frac{1}{\tau_P} \left(P_{\text{piston}} - P(t) \right) \tag{1.24}$$

$$\lambda = 1 - \beta_T \frac{\Delta t}{\tau_P} \left(P(t) - P_{\text{piston}} \right) \tag{1.25}$$

where β_T is the isothermal compressibility. It should be noted that Berendsen barostat yields a simulation with the correct average pressure, it does not yield the exact NPT ensemble. For simulations where the fluctuations in pressure or volume are important e.g. to calculate thermodynamic properties, Nose-Hoover barostat or Parrinello-Rahman barostat should be used.

1.3.2 Classical force field

During MD modelling, the forces between atoms within molecular, i.e., intramolecular interaction and also between molecules, i.e., intermolecular interaction are determined by the force field. Here, three classical force fields, i.e., Transferable Potentials for Phase Equilibria (TraPPE) (Martin and Siepmann, 1998), Chemistry at Harvard Macromolecular Mechanics (CHARMM) (Vanommeslaeghe et al., 2010) and Optimized Potentials for Liquid Simulations (OPLS) (Jorgensen et al., 1996) are selected to introduce the potential energy in MD system. The energy of non-bonded interactions between atoms are described based on Coulomb potential and the vdW interactions by 12-6 LJ function:

$$E_{nb}\left(r_{ij}\right)=\frac{q_i q_j}{4\pi\varepsilon_0 r_{ij}}+4\varepsilon_{ij}\left(\left(\frac{\sigma_{ij}}{r_{ij}}\right)^{12}-\left(\frac{\sigma_{ij}}{r_{ij}}\right)^{6}\right) \tag{1.26}$$

where r_{ij} is the distance between two atoms i and i, q_i and q_j are the partial charges on the atoms, ε_0 is the permittivity of vacuum, σ_{ij} is the vdW radius, and ε_{ij} is the well-depth for this atom pair. The LJ pair coefficients for interactions between unlike atoms can be computed using arithmetic average and geometric average: $\sigma_{ij}=\left(\sigma_{ii}+\sigma_{jj}\right)/2$ and $\varepsilon_{ij}=\left(\varepsilon_{ii}\varepsilon_{jj}\right)^{1/2}$. Apart from the non-bonded interactions, bonded interaction to maintain molecular topology is shown in Figure 1.11, with the energy functions expressed as follows:

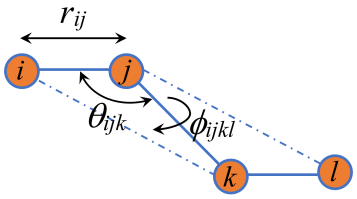

Fig. 1.11 Different intramolecular interactions between atoms of i, j , k and l.

Intramolecular interaction of bond stretching is represented by a harmonic potential:

$$E_b\left(r_{ij}\right)=\frac{1}{2}k_{ij}^{b}\left(r_{ij}-b_0\right)^2 \tag{1.27}$$

Bond-angle vibration between a triplet of atom is also represented by a harmonic potential:

$$E_a\left(\theta_{ijk}\right)=\frac{1}{2}k_{ijk}^{\theta}\left(\theta_{ijk}-\theta_0\right)^2 \tag{1.28}$$

In CHARMM force field, an Urey-Bradley correction term is also included (Vanommeslaeghe et al., 2010):

$$E_a^{UB}\left(\theta_{ijk}\right)=\frac{1}{2}k_{ijk}^{UB}\left(r_{ik}-r_{ik}^{0}\right)^2 \tag{1.29}$$

In TraPPE and OPLS force field, proper dihedral angles separated by the three bonds is represented by cosine terms of a Fourier series:

$$E_d^{F}\left(\phi_{ijkl}\right)=\frac{1}{2}\left(\sum_{n=1}^{4}F_n\left(1+(-1)^{n+1}\cos(n\phi)\right)\right) \tag{1.30}$$

Fourier function can be converted into Ryckaert-Bellemans function for computational efficiency:

$$E_d^{RB}\left(\phi_{ijkl}\right)=\sum_{n=0}^{5}C_n\left(\cos\left(\phi-180^{\circ}\right)\right)^n \tag{1.31}$$

In CHARMM force field, dihedral potential is expressed as:

$$E_d\left(\phi_{ijkl}\right) = k_\phi\left(1+\cos\left(n\phi-\phi_s\right)\right) \tag{1.32}$$

For out-of-plane improper dihedral, it is expressed as:

$$E_{id}\left(\xi_{ijkl}\right) = \frac{1}{2}k_\xi\left(\xi_{ijkl}-\xi_0\right)^2 \tag{1.33}$$

where k, F and C are the force constants. The improper dihedral angle ξ is defined as the angle between planes (i,j,k) and (j,k,l).

1.3.3 Reactive force field

To calculate chemical kinetics in MD, reactive force field (ReaxFF) developed by van Duin et al. (2001) should be used, where all connectivity dependent interactions are described based on bond order formalism. Bond order determined by interatomic distance using an empirical formula is continuous and includes contributions from σ, π and π π bonds. By updating bond order at every iteration, ReaxFF MD method is able to model the bond formation and dissociation. Nonbonded terms like vdW and Coulomb interaction are calculated independently. Charge equilibration (QEq) method is used to adjust the partial charge on individual atoms based on interactions with their neighbours. System energy associated with different forces on each atom are calculated using the following equation (van Duin et al., 2001):

$$E_{system} = E_{bond} + E_{over} + E_{under} + E_{lp} + E_{val} + E_{tor} + E_{vdW} + E_{Coulomb} \tag{1.34}$$

where E_{bond},E_{over}, E_{under}, E_{lp}, E_{val}, E_{tor}, E_{vdW}, $E_{Coulomb}$, represent bond energy, overcoordination energy penalty, undercoordination stability, lone pair energy, three-body valence angle energy, four-body torsional angle energy, vdW energy, and Coulomb energy, respectively.

Bond order is calculated directly from interatomic distance using the empirical formula:

$$\begin{aligned} BO_{ij} &= BO_{ij}^{\sigma} + BO_{ij}^{\pi} + BO_{ij}^{\pi\pi} \\ &= \exp\left[p_{bo1}\left(\frac{r_{ij}}{r_o^{\sigma}}\right)^{p_{bo2}}\right] + \exp\left[p_{bo3}\left(\frac{r_{ij}}{r_o^{\sigma}}\right)^{pbo4}\right] + \exp\left[p_{bo5}\left(\frac{r_{ij}}{r_o^{\sigma}}\right)^{pbo6}\right] \end{aligned} \tag{1.35}$$

where BO is the bond order between atoms i and j, r_{ij} is interatomic distance, r_o terms are equilibrium bond lengths, and p_{bo} terms are empirical parameters.

1.4 Molecular modelling of biofuel and biomass

MD is widely used to study the heat and mass transfer process as well as the microscopic structure evolution during phase transition. MD simulation has also been successfully used to predict the thermalphysical properties (density, enthalpy of vaporization, heat capacity, surface tension, isothermal compressibility, etc) of organics like alkane, aromatics, methyl esters, alcohols, water, ionic liquids, crude oil, etc (Wensink et al., 2003) (Caleman et al., 2012) (Bharadwaj et al., 2015) (Bedrov et al., 2019) (Chen et al., 2020). For example, Ding et al. (Ding et al., 2018a) (Ding et al., 2018b) studied the transport properties and local structure of molten alkali carbonates. Moreover, after reviewed the application of MD on calculating transport properties of working fluids at supercritical conditions, Nie et al. (2019) concluded that MD can be considered as an effective tool. Recently, Oliveira et al. (de Oliveira and Caires, 2019) (de Oliveira et al., 2020) studied the molecular arrangement in diesel/biodiesel blends and the impact of biodiesel as an additive on the stabilization of diesel/ethanol blends. It is expected that MD modelling becomes routinely used to bridge fundamental knowledge, physical insight and practical use of supercritical fluids considering that force fields (which are crucial to the simulation accuracy) and molecular simulation are more and more precise and affordable (Vega, 2018).

ReaxFF is feasible for large scale reactive systems, inheriting similar accuracy of quantum mechanics but with substantially reduced computational expenses. Besides the application of ReaxFF MD on combustion of small fuel molecules like syngas (Ashraf and van Duin, 2017), wet ethanol (Feng et al., 2019) and benzene (Dong et al., 2015), it has been successfully used to investigate the pyrolysis and oxidation of large hydrocarbon fuels like JP-10 (Chenoweth et al., 2009), diesel (Chen et al., 2019) and bio-oil (Liu et al., 2017c). Moreover, a wide range of aspects related to soot formation have also been studied, for example, incipient soot particle formation from pericondensed PAHs in the form of physical stacks or chemical carbon bridge connection and energy transfer of PAHs interacting with bath gases (Mao et al., 2017) (Wang et al., 2019).

MD simulation with classical force fields also provides an opportunity to study the three-dimensional structure of biomass components and quantification of their interactions at nanoscale level (Zhang et al., 2019) (Ciesielski et al., 2020). For example, MD simulation with all-atom force fields demonstrated the effect of hydrogen bonding on strength of crystalline cellulose nanofiber (Zhu et al., 2015). Using coarse grained force field, Lindner et al. (2013) studied the aggregation of lignin on the surface of cellulose chains in aqueous solution with the system size of 3.8 million atoms. Owing to the capability in predicting thermophysical properties and describing diffusion process in complex pores of zeolites, MD simulation can also contribute to the reactor design (Ding et al., 2018b) (Nie et al., 2019) (Keil, 2018).

In addition to the experimental methods like thermogravimetric (TG) analysis to study biomass pyrolysis, ReaxFF MD enables the identification of elementary pathways and the associated kinetic parameters of macromolecular architecture of biomass (Zheng et al., 2016) (Chen et al., 2017) (Paajanen et al., 2021). Li et al. (2021), review the utilisation of ReaxFF MD in unravelling the complex reactions and kinetics for pyrolysis and oxidation of organic systems such as lignin, coal, polymers and high-energy materials. Batuer et al. (2021) developed a ReaxFF MD simulation model of cotton cellulose pyrolysis in both non-isothermal and isothermal conditions. It was found that 80% and 100% of volatile removal ratios was the closest to the TG experimental results. The work of Monti et al. (2018) showed that the ReaxFF simulation of lignin fragmentation on a Pd catalyst was capable to reveal the surface chemistry details of adsorption dynamics of reactive oligomer and deposition dynamics of the generated fragments.

1.5 Knowledge gaps, motivation and thesis overview

Liquid biofuels are a sustainable energy source for transportation, and deployment of biofuels is important in achieving net-zero carbon. During producing biofuels from lignocellulosic biomass, improving biofuel properties by adding catalyst is essential. Deactivation will inevitably occur during this process. However, there is still a lack of investigation on the mechanism of catalyst deactivation concerning the effects of catalyst size, coke molecular structure and temperature. The properties of biofuels would affect its utilisation in engine, deployment and commercialisation. Soot formation mechanism particularly the transition form gas phase precursors to solid phase particulate matter is still controversial. It is reported that oxygenated biofuels can help reduce soot formation. However, the detailed reaction pathways in soot formation regarding the specific functional groups in biofuels is unlikely to be tracked in experiments. This results in the insufficient understanding of soot mitigation mechanism of biofuels. Moreover obtaining the physical properties of biofuels experimentally is also difficult particularly in high-temperature and high-pressure supercritical conditions which is important in developing supercritical combustion. Predicting the thermophysical properties of biofuels is still an open question which needs a reliable method.

The MD simulation can be used to fill the knowledge gaps. MD simulation as an advanced tool can be used to the study the utilisation of biomass and biofuels in atomic level, leading to much enhanced fundamental understandings of the processes involved and improved predictions of property variables. The overall aim of this study is to gain a better understanding of the key aspects of biofuel production and utilisation using MD simulations. The objectives of the study are mainly in three aspects:

- To reveal the mechanisms behind the catalyst deactivation during biomass thermochemical conversion. The effects of nanocrystal size on surface premelting and the effects of coke molecular structures on deposition will be quantified. The seeping phenomenon will be studied as it affects the catalyst regeneration after deactivation.
- To validate the soot inception model and study the nascent soot molecular structures. The specific pathways of aromatics formation from fuel pyrolysis will be identified. The soot mitigation mechanisms of biofuels will be revealed, and thus different functional groups in biofuels on soot reduction can be quantified.
- To establish reliable method to predict the thermophysical property of biodiesel at extreme and supercritical conditions. The capability of different force field on property prediction will be investigated by comparing with experimental results. Various thermophysical properties will be calculated using equilibrium and non equilibrium molecular simulation.

The thesis is organised into several chapters:

Chapter 1: The importance of biofuel production and utilisation as renewable energy in reducing GHG emission is firstly introduced. The deactivation phenomenon of catalyst are mentioned as an unsolved problem in biofuel production. The difference between biofuels and diesel in terms of physical properties like transport properties and combustion kinetics like soot formation are reviewed. The basic methodology of MD simulation is introduced and the application of MD in studying fuel properties are reviewed.

Chapter 2: The coke surrogate models are established firstly based on the distribution of lignin pyrolysis products and soot inception mechanism. Nanocatalyst surface premelting induced thermal degradation is studied via Lindemann index and atom displacement magnitude. A ReaxFF MD simulation system is established to elucidate the deactivation mechanism by demonstrating the time evolution of catalyst morphology and interactions with coke, to reveal the effect of coke size, O/C ratio and operating temperature on chemisorption/physisorption. Afterwards, the deactivation extent of catalyst is quantified via adsorption ratio and relative Lindemann index over a wide range of conditions.

Chapter 3: With the objective of developing a better understanding of sooting phenomena in nanoscale, reactive MD simulation was performed in this chapter. The role of typical building blocks and the specific chemical growth pathways on soot inception are investigated, taking advantages of the recent advance of MD force field to describe the carbon condensation chemistry. From this approach, the effects of composition and molecular structure of biodiesel blends (e.g., alkanes and aromatics in diesel, double bonds and oxygenated moieties in FAMEs) on sooting tendency are scrutinised by labelling and tracking the corresponding atoms during the simulation. The mechanisms of molecular structure of oxygenated additives, i.e. the existence ester, alcohol, carbonyl group and ether, on soot precursor mitigation are elucidated via evaluating the early formation of CO and CO_2 quantitatively during the thermal decomposition.

Chapter 4 and Chapter 5: MD simulation is employed to deal with the aforementioned challenges in transcritical injection prediction of biodiesel. In **Chapter 4**, capability of current methods on prediction of transport property of FAMEs in equilibrium MD simulation are evaluated, particularly in conditions of high pressure. **Chapter 5** is oriented to addressing a number of specific issues in three areas where there is currently a lack of understanding or reliable predictive methods, including (1) high pressure induced solidification; (2) critical property and surface tension prediction; and (3) prediction of transport properties such as density, viscosity and conductivity of the fuel mixtures using both equilibrium and nonequilibrium MD simulations.

Chapter 6: The main conclusions of the thesis are summarised, and suggestions for future work are illustrated.

Chapter 2

Lignin pyrolysis and catalyst deactivation

Surface coking is the primary deactivation pattern of metal-based catalyst in biofuel reforming, which hinders the commercial utilisation of biomass. Although significant experimental work has been performed on coke deposition induced catalyst deactivation taking place in biomass pyrolysis and upgrading, further fundamental modelling studies is required to deepen the understanding of the physiochemical phenomena. This would help to optimise the processing condition and attenuate deactivation. To the best of our knowledge, molecular modelling of catalyst surface coking in biomass utilisation has not been performed.

The schematic depiction of the catalytic thermochemical conversion process of lignin is shown in Figure 2.1. A typical lignin molecular structure is shown in Figure 2.2. Lignin pyrolysis is simulated in MD with reactive force field in Chapter 2.2, and the coke surrogate models are established accordingly. The surface instability induced thermal degradation of Ni nanocatalyst and coke deposition induced catalyst deactivation are studied in Chapter 2.3.

2.1 Modelling methodology

2.1.1 Model construction

Lignin is the third major component of lignocellulose, accounting for 10-35% by weight, up to 40% by energy in biomass (Liu et al., 2017b). Compared with semi-crystalline polysaccharide cellulose and amorphous polysaccharide hemicellulose, lignin is an amorphous aromatic polymer composed of three basic monomer units, i.e., p-hydroxyphenyl (H), guaiacyl (G) and syringyl (S) as shown in Figure 2.3 (a). The proportion of H, G and S units in lignin strongly depends on the biomass species. The exact molecular structure of lignin is difficult to characterize. The linkages of basic lignin units are complex and mainly include

C-O ether bonds (β-O-4, α-O-β', γ-O-4, α-O-β', and α-O-4 etc) and C-C bonds like α-6 as shown in Figure 2.3 (b). In this study, a simplified softwood lignin structure containing seven most common linkages proposed by Beste was adopted (Beste, 2014).

As one of the most promising active phases, Ni is widely used in reforming process (Ochoa et al., 2020). In this study, face-centred cubic (fcc) lattice of Ni nanoparticles as shown in Figure 2.3 (c) was created on a web-based crystallographic tool (Chatzigoulas et al., 2018). The minimum surface energy of corresponding Miller indices of (111), (100) and (110) was adopted from the work of Jiang et al. (2004). In order to study the surface premelting phenomena, Ni catalyst is divided into three layers, i.e., layer1 (L1) atom identities (ID) range from 1 to 369; IDs of L2 range from 370 to 1229; IDs of L3 range from 1230 to 2867.

Coke is always referred to as any unwanted carbonaceous organics depositing on the catalyst surfaces, and varies in composition depending on the reforming temperature and resident time. It is generally classified into different types based on morphology or structure, e.g., highly oxygenated encapsulating coke and aromatic filamentous coke (Ochoa et al., 2017) (Ochoa et al., 2020).

In order to simplify the complex coke composition and better understand the adsorption and decomposition mechanisms on the catalyst surfaces, surrogate coke molecular models are established as shown in Figure 2.3 (d). Peri-condensed PAHs including naphthalene (A2), pyrene (A4), coronene (A7), ovalene (A10), circumcoronene (A19) which are constituted of 2-, 4-, 7-, 10-, and 19- numbered aromatic rings respectively, are selected to represent a large range of molecular size. These PAH monomers are regarded as the key precursors and building blocks in soot formation of incomplete hydrocarbon combustion, and used widely to study the nucleation and condensation mechanism in soot inception (Mao et al., 2017) (Mao et al., 2018). The counterparts of phenolic compounds including phenol (A1O1), hydroquinone (A1O2), phloroglucinol (A1O3) and benzenehexol (A1O6) are selected to reflect the effect of O/C ratio.

2.1.2 Simulation setup procedures and details

For lignin pyrolysis simulation, 40 lignin unimolecules containing 13720 atoms are constructed into a 200 × 200 × 200 Å cubic box with a lower initial density to avoid overlapping of major functional groups. After system energy minimisation, the box is further compressed using an isobaric-isothermal *NPT* ensemble at 300 K and 100 bar with a time step of 0.25 fs until the density reduced to 1.25 g/cm^3, which is close to the value in the work of Zhang et al. (2016). Thereafter, to relax the system, 3 recycle simulation in *NPT* ensemble at atmospheric pressure with temperature annealing between 300 K and 400 K was performed for 100 ps,

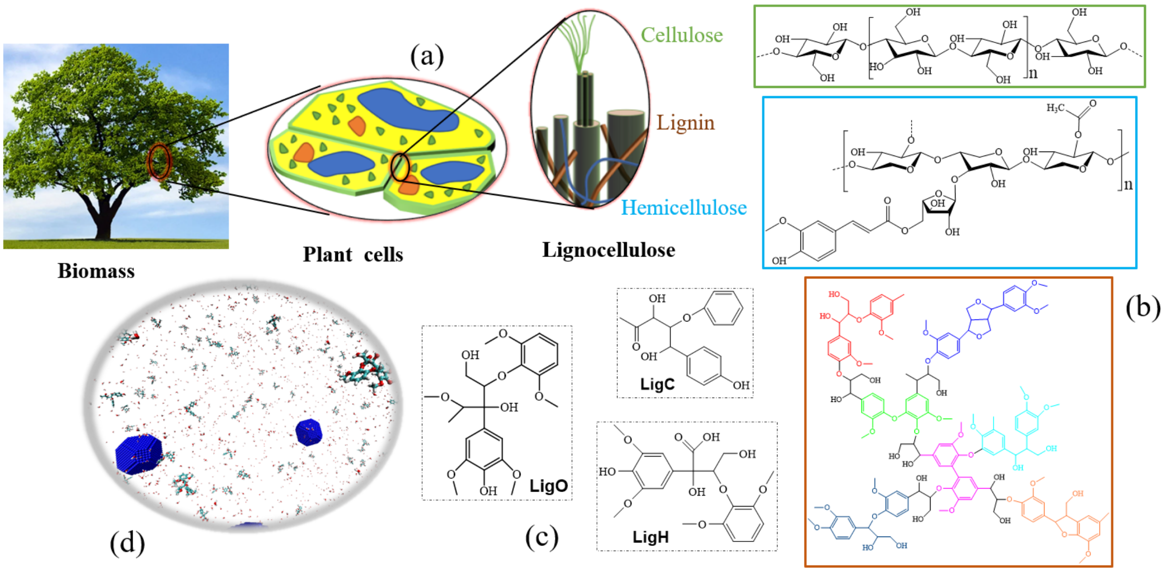

Fig. 2.1 (a) Schematic depiction of the cellulose, hemicellulose and lignin in plant cells of lignocellulosic biomass; (b) representative molecular structures of β-D-glucose cellulose, hemicellulose and softwood lignin fragment highlighting the most common linkages adapted from Beste (2014); (c) lignin surrogate models proposed by Faravelli et al. (2010) based on the characterization and composition of lignin structures; (d) molecular modelling of lignin decomposition over nanocatalysts.

followed by isochoric-isothermal *NVT* simulation at 400 K for 100 ps. The equilibrated system with a 51.1 × 51.1 × 51.1 Å cubic box is shown in Figure 2.4 (a). Production run is continued using canonical *NVT* ensemble from the equilibrated system, ramping from 300 K to 3000 K with the heating rate of 20 K/ps.

Both non-isothermal and isothermal simulations are set up using canonical *NVT* ensemble with the Ni nanocrystals placed in the centre of a 100 × 100 × 100 Å cubic box as shown in Figure 2.4 (b) to investigate the melting process of nanocatalyst. Nonisothermal simulation is performed first to study the dynamic melting with the temperature ramping from 300 K to 3000 K in 500 ps simulation. Separate isothermal simulation is then performed to study the equilibrium melting process using constant temperatures from 400 K to 2400 K with temperature interval of 400 K. For simulation of coke deposition, each of the coke surrogate molecule is duplicated 50 times and distributed randomly into the 100 × 100 × 100 Å cubic box with a 4 nm Ni nanocatalyst fixed in the centre as exhibited in Figure 2.4 (c). Isothermal simulation of 800 ps with time step of 0.25 fs is performed using canonical *NVT* ensemble. The trajectories and species information are outputted at every 400 steps. The linear and angular momentum of Ni nanocrystal is zeroed every 10 time steps.

The periodic boundary condition is applied in all directions. The velocity of molecules is assigned according to Maxwell-Boltzmann distributions of the specified temperature. The

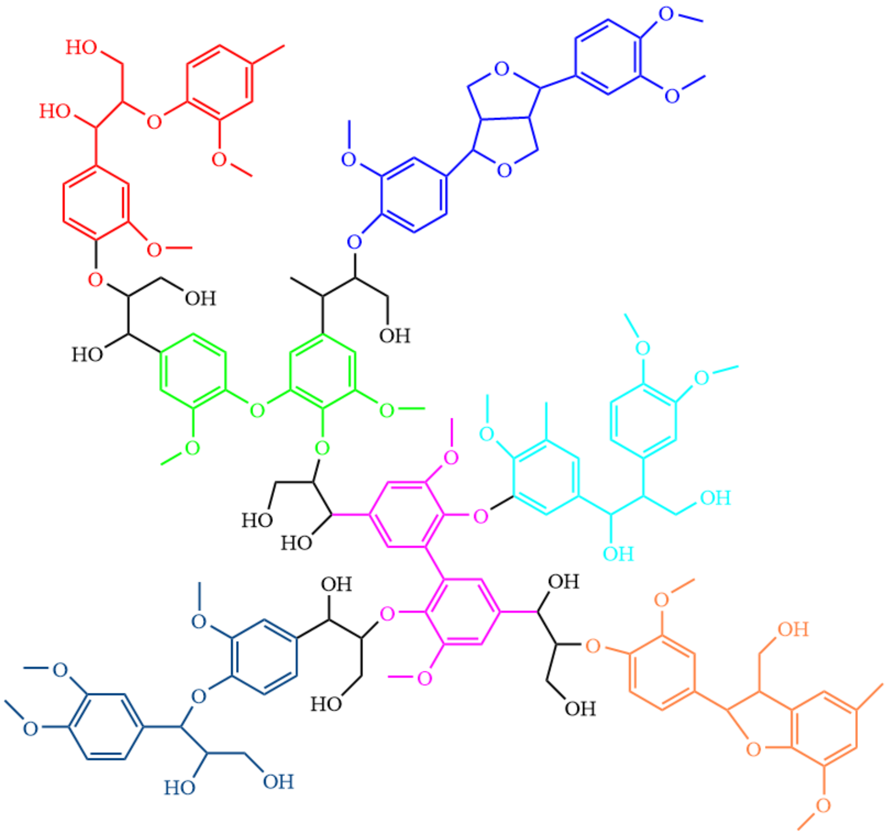

Fig. 2.2 Lignin molecular structure used in this study, adapted from Beste (2014).

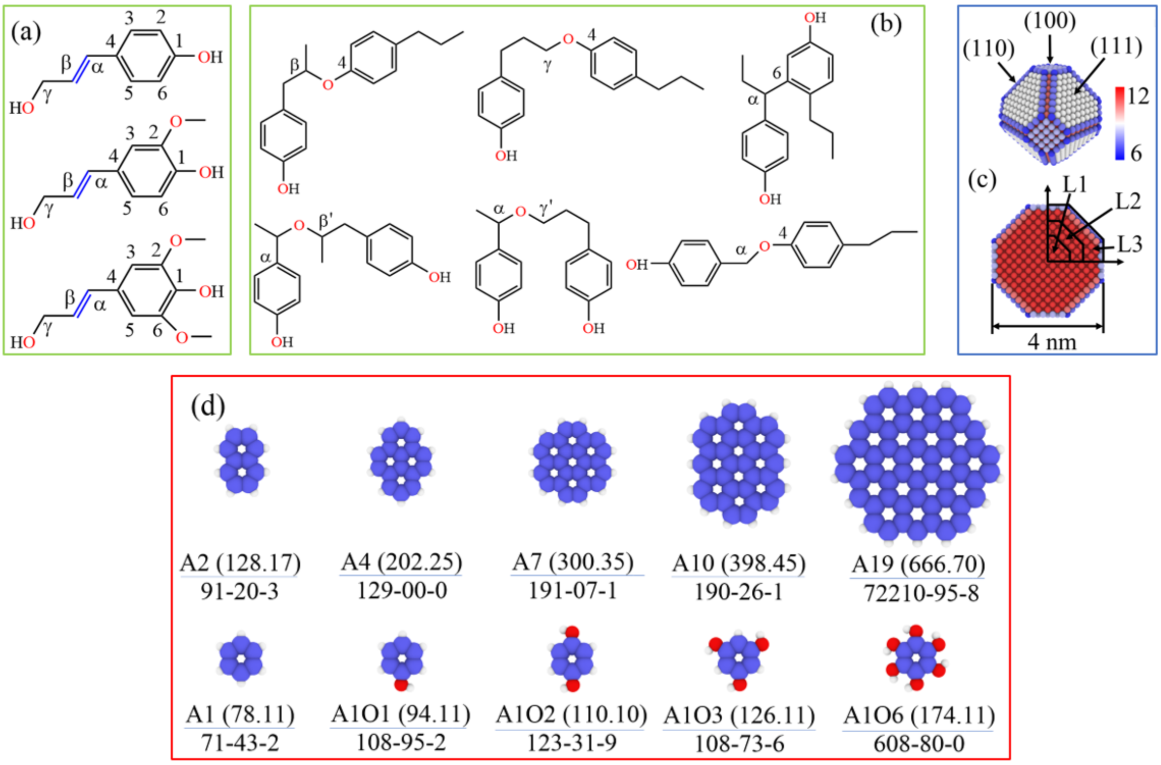
(a)
(b)
(c)
(d)
OH
HO
(100)
(110)
(111)
12
6
L1
L2
L3
4 nm
A2 (128.17)
91-20-3
A4 (202.25)
129-00-0
A7 (300.35)
191-07-1
A10 (398.45)
190-26-1
A19 (666.70)
72210-95-8
A1 (78.11)
71-43-2
A1O1 (94.11)
108-95-2
A1O2 (110.10)
123-31-9
A1O3 (126.11)
108-73-6
A1O6 (174.11)
608-80-0

Fig. 2.3 (a)-(b): Basic units of lignin and various linkage in the lignin structure; (c) atom arrangement of a 4 nm Ni nanocrystal in tridimensional view with facets indicated and the cross section with different layers (L1, L2 and L3) indicated, where the atoms are coloured according to the coordination number (CN) with cut off distance of 3.2 Å; (d) molecular structures of coke surrogate models with molecular structure, molecular mass and CAS number indicated.

Nosé-Hoover thermostat and barostat are adopted to control the system temperature and pressure with a temperature and pressure damping constant equal to 100 times and 1000 times of the time step respectively. A bond order cut off of 0.3 is employed to recognize the molecules and analyse the species forming during the simulation. The ReaxFF MD simulation is performed with REAXC package in the Large-scale Atomic/Molecular Massively Parallel Simulation (LAMMPS) (Plimpton, 1995). In this study, the latest developed C/H/O parameter set (CHO2016) (Ashraf and van Duin, 2017) was used to study lignin pyrolysis, as it improved the C1 chemistry and was widely applied to describe reaction network and kinetics during pyrolysis and oxidation of syngas, phenoxy-aromatic fuels, multicomponent diesel etc. (Ashraf and van Duin, 2017) (Chen et al., 2019) (Kwon et al., 2020b) . C/H/O/Ni parameter set (Mueller et al., 2010a) (Mueller et al., 2010b) developed for modelling hydrocarbon chemistry catalysed by Ni was adopted to study the surface coking over Ni nanocatalysts. All the visualizations are produced by OVITO (Stukowski, 2009).

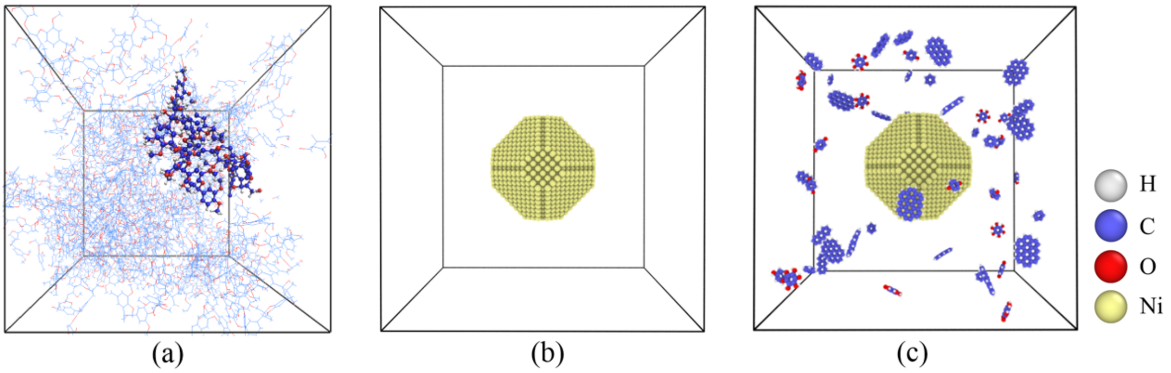

(a) (b) (c)

Fig. 2.4 (a) Snapshot of the equilibrated unit cell with one unimolecular ($C_{138}H_{160}O_{45}$) of the 40 lignin fragments highlighted; (b) 4 nm Ni nanocrystal centred in the box for modelling of catalyst thermal stability; (c) schematic box depicting the modelling system of coke adsorption, where Ni catalyst is fixed in centre with aromatic organics distributed around.

2.2 Lignin pyrolysis products

Nonisothermal simulation is performed first to study the lignin mass fraction change during pyrolysis and is compared with TG experimental results of kraft lignin (Barr et al., 2021) as shown in Figure 2.5.

Based on the species evolution in Figure 2.5 (a), the lignin pyrolysis processes can be roughly summarized into three stages. Pyrolysis at temperatures ranging from 300 K to 800 K is the initial stage where lignin molecules mainly proceed conformation adjustment with a slight mass loss. Very few small radicals like CH_3O, CH_3, and OH are observed in this stage. The second pyrolysis stage takes place when temperature ramps from 1000 K to 1800 K. The macromolecular lignin structure decomposes appreciably while number of species increases slightly in this stage. Existence of secondary reaction at temperatures from 1800 to 3000 K results in the apparent increase of species in the last pyrolysis stage. It should be pointed out that although there is a temperature difference between the experiment (423-1173 K) and simulation (800-3000 K), pyrolysis process is described well in the ReaxFF MD simulation following the consistent decreasing trend from the simulation and TG experiment as shown in Figure 2.5 (a). Relevant work (Qian et al., 2016) (Hong et al., 2020) (Batuer et al., 2021) also verified the elevated temperature strategy used in ReaxFF MD can well reproduce the pyrolysis mechanism of coal, cellulose and oil shale kerogen at higher experimental temperatures.

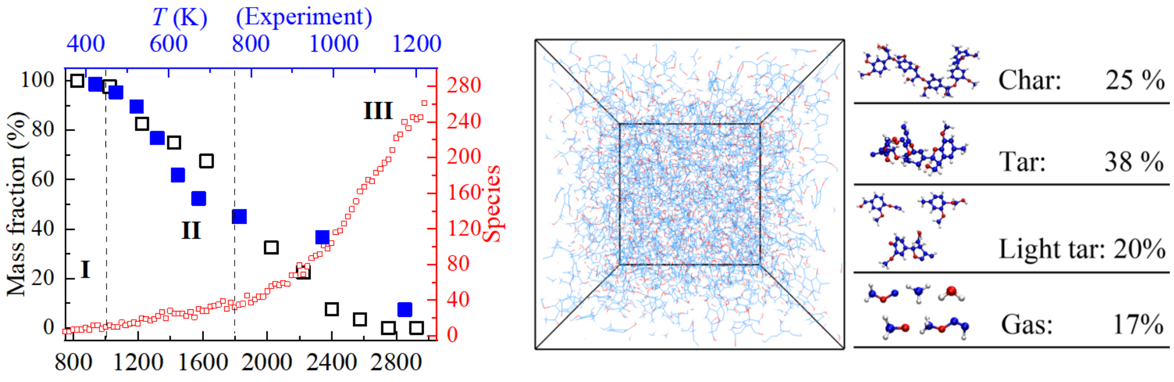

(a) T (K) (ReaxFF MD)

(b)

Fig. 2.5 (a) Evolution of lignin mass fraction and number of species where blue solid box is mass fraction of TG experiment (temperature ramp: 2 K/min), black hollow box is mass fraction of ReaxFF MD simulation (20 K/ps), red hollow box is species of ReaxFF MD simulation; (b) snapshot of the system and the mass fraction of final composition yield, where typical molecular structures are identified.

Depending on the degree of pyrolysis, the lignin macro molecular structures depolymerize into volatile compounds, monomers, oligomers, and solid bio-char. Pyrolysis products are generally classified as char, heavy tar, light tar and gases according to molecular size (Batuer et al., 2021).

Compounds containing more than 40 carbon atoms are considered as char as shown in Figure 2.5 (b). Fragments including 14-40 carbon atoms and 5-13 carbon atoms are considered as heavy tar and light tar which account for 38% and 20%, respectively. The gas molecules accounting for 17% of the products include organic gases containing 1-4 carbon atoms and inorganic gases like H_2, CO_2 and H_2O etc. Tar composition of oxygenated aromatics like phenols and m-xylene can sustain for long duration even under supercritical conditions and is supposed to proceed dehydration leading to the formation of aromatic compounds such as benzene, toluene and xylenes (Okolie et al., 2019). These coke precursors can further pyrolyze and polymerize via H-Abstraction-Carbon-Addition (HACA) soot inception mechanism [3, 44], facilitating the formation of condensed heavy PAH. For example, naphthalene, which is also recognized as the most stable and difficult-to-decompose compound among biomass-derived tars, is selected as the surrogate model to study the catalyst deactivation in tar reforming (Arregi et al., 2018a) (Cheng et al., 2020) (Gao et al., 2020).

2.3 Catalyst deactivation during thermochemical conversion of lignin

2.3.1 Surface instability induced thermal degradation

Temperature is recognised as the most common factor resulting in metal sintering during steam reforming processes. The dynamic melting temperature T_m of nanocrystal of different sizes can be obtained by the time evolution of the average potential energy, i.e., *pe* using nonisothermal temperature ramping simulation as shown in Figure 2.6 (a). The melting behaviour of the 4 nm crystal is further characterized using the atom distribution function $g(r) = dn(r)/\left(4\pi\rho^n r^2 dr\right)$ as shown in Figure 2.6 (b). It describes local number density ρ^n variation as a function of distance r from a reference atom, and can reveal the structural information of local order degree.

The *pe* curves mainly pass through three stages, taking 4 nm crystal as an example. In the first stage, a gradual linear increase of *pe* is seen between 400 K to 1550 K. The corresponding curves of $g(r)$ display a series of well-defined peaks at time before 240 ps, indicating that long-range ordered structure and crystalline arrangement are well preserved. When temperature is higher than 2000 K, i.e., after 320 ps, melting enters the third stage where the *pe* still increases linearly with temperature with a higher slop, while long-range order of atom distribution function vanishes indicating the completely amorphous liquid phase. The nonlinear sharp increase region between 1550 K and 2000 K is related to the solid-to-liquid transition, where 2000 K is always regarded as the melting point of the system as indicated by the dash lines in Figure 2.6 (a). The melting temperature depends strongly on size, and a linear decrease in melting temperature is found with increasing reciprocal of radius as shown in Figure 2.6 (c). The melting temperature of bulk Ni is obtained by extrapolating $1/R \to 0$ is 2512 K which is about 40% higher than the experimental value of 1728 K.

In order to eliminate the effect of insufficient equilibrium during the temperature ramp, a number of isothermal simulations were performed. Dimensionless Lindemann index representing the degree of atomic vibration is employed to quantify the crystallinity of

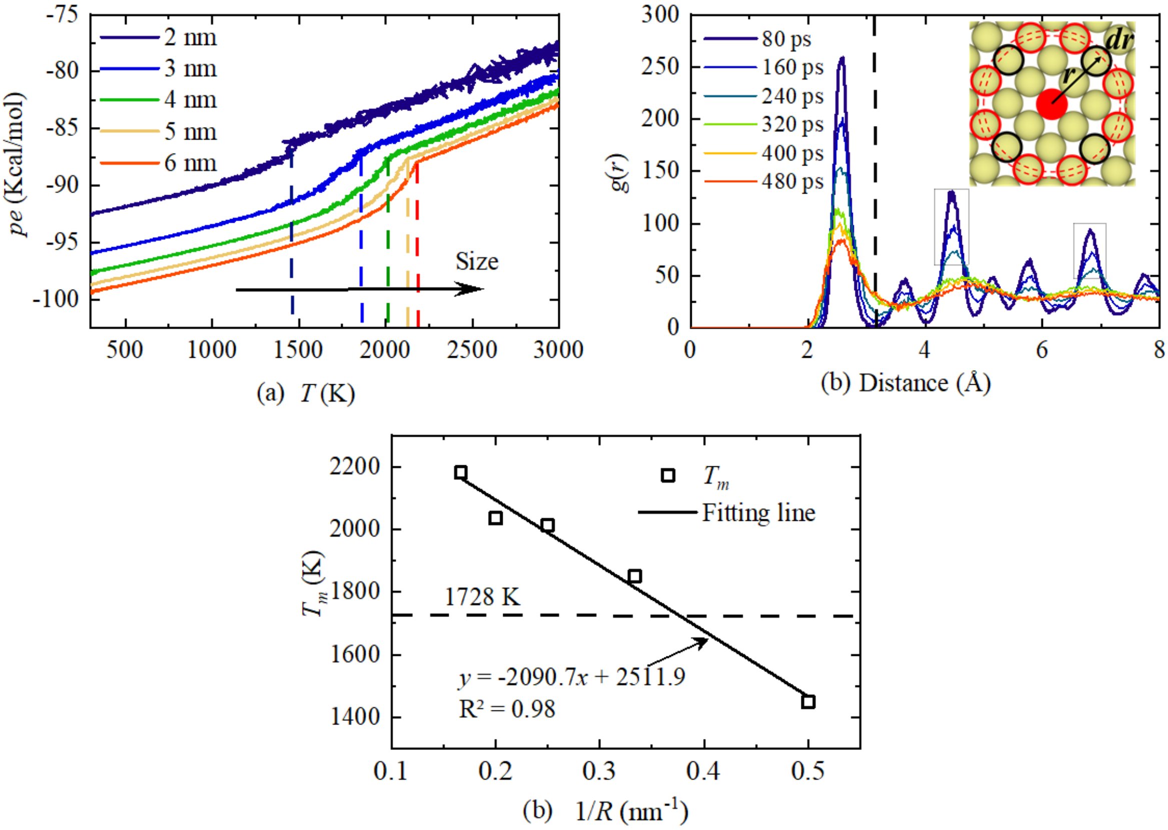

Fig. 2.6 (a) Potential energy per atom of nanocrystal with diameters of 2-6 nm heating from 300 K to 3000 K; (b) time evolution of the radial distribution function of the 4 nm nanocrystal heating from 300 K to 3000 K in 500 ps; (c) melting temperatures of Ni crystal with different sizes determined by potential energy evolution.

nanoparticles. The Lindemann index is defined as:

$$\delta_i = \frac{1}{N-1}\sum_{j\neq i}\frac{\sqrt{\left\langle r_{ij}^2\right\rangle_T - \left\langle r_{ij}\right\rangle_T^2}}{\left\langle r_{ij}\right\rangle_T} \tag{2.1}$$

$$\delta = \frac{1}{N}\sum_{i}\delta_i \tag{2.2}$$

where δ_i is the Lindemann index of the i^{th} atom, δ is the system-averaged value, N is the number of atoms in nanocrystal, r_{ij} is the interatomic distance between atom i and j, $\langle\cdots\rangle_T$ denotes the time average at temperature T.

The Lindemann index of 4nm nanocrystal at different temperatures is shown in Figure 2.7 (a). It is known that the catalyst reactivity is closely related to the number of the nearest neighbours of the surface atom, i.e., coordination number. The coordination number distribution of the Ni nanocrystal shown in Figure 2.3 (c) is determined using the first minimum of the atom distribution function, i.e., 3.2 Å as the cut-off distance. The distribution of coordination number of outer shell at different temperatures is presented in Figure 2.7 (b). Phase change of Ni nanocrystal during melting is determined at the temperature where Lindemann index δ increases to 0.08 (Neyts and Bogaerts, 2009). High Lindemann index denotes high vibrational motion of atoms and disordered structural morphology. The bulk melting temperature predicted using Lindemann index as the criterion in ReaxFF MD simulation is 2298 K, still 33% higher than the experiment result but closer to that from the potential energy method.

It is also observed that a sudden increase of Lindemann index takes place in L3 outer shell at 1600 K which corresponds to the drastic change in coordination number distribution in Figure 2.7 (b), while inner layers of L1 and L2 still persevere ordered solid state at 1600 K. Surface disordering before complete melting is regard as a general phenomenon during nanocrystal melting due to the existence of the unstable undercoordinated atoms with dangling bonds as indicated in Figure 2.3 (c). The higher values of the potential energy per atom in both solid and liquid states for the smaller nanocrystals in Figure 2.6 (a) are a reflection of the increased fraction of loosely bounded surface atoms.

It is believed that strict surface melting phenomenon defined with the formation of quasi-liquid film occurs only if the radius of nanocrystals is larger than the critical value (e.g., 2.96 nm for Ni (Chernyshev, 2009)). Surface structure instability induced deactivation of 4 nm crystal is scrutinised, considering that even slight atom modifications in crystal surfaces can affect activity and selectivity in catalysis. Generally, when temperature reaches Hüttig temperature ($0.3T_m$), i.e., around 689 K), the surface atoms located at corners, steps, and terraces with reduced coordination numbers tend to dissociate and diffuse readily over the

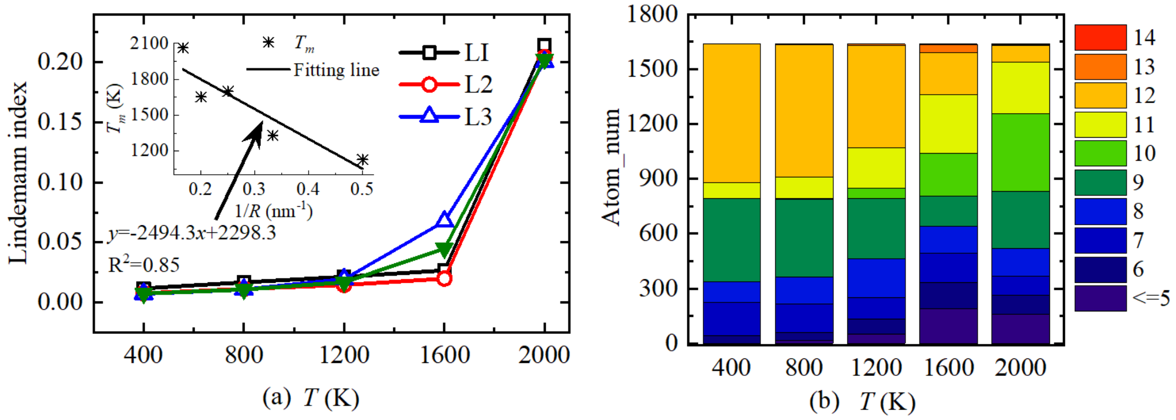

Fig. 2.7 (a) Lindeman index of 4 nm nanocrystal at isothermal conditions, where the melting temperature of different sizes based on Lindemann index criteria is inserted, and the solid triangle is the result of nanocrystal; (b) distribution of coordination number of L3 surface at different isothermal conditions.

surface. After temperature further approaches to Tamman temperature ($0.5T_m$, i.e., around 1149 K), the bulk atoms start to show mobility (Argyle and Bartholomew, 2015).

The melting behaviours are reflected via displacement magnitude as shown in Figure 2.8. The surface atoms show apparent mobility at 1200 K with the average displacement magnitude of outer shell almost 3 times greater than the core layer. The atoms with prominent mobility, i.e., those with deviation displacement from lattice position greater than 3.2 Å, present mainly at junction edges or corners of facets. These atoms also account for 39% of the out shell at 1600 K, explaining the drastic change in coordination number distribution. At temperatures of 2000 K and 2400 K, the nanocrystal becomes totally amorphous, indicating frequent change of atoms between different layers.

2.3.2 Deposition induced deactivation

Carbonaceous molecular adsorption onto catalyst surfaces is the first step to study coke deposition induced deactivation, involving coke composition, operating temperature and reaction time. In order to decouple these factors, isothermal ReaxFF MD simulation using the aromatic coke surrogate molecules (see Figure 2.3 (d)) at 1200 K was performed to investigate the time evolution of adsorption process as illustrated in Figure 2.9. Corresponding snapshots to depict the key stages during adsorption are displayed in Figure 2.10. Temperature effects on adsorption ranging from 400 K to 2000 K are confined to typical molecules of benzene (A1, minimum aromatic size), pyrene (A4, medium size PAH), circumcoronene (A19, maximum size PAH) and benzenehexol (A1O6, the highest oxygen content), as illustrated by the snapshots in Figure 2.11.

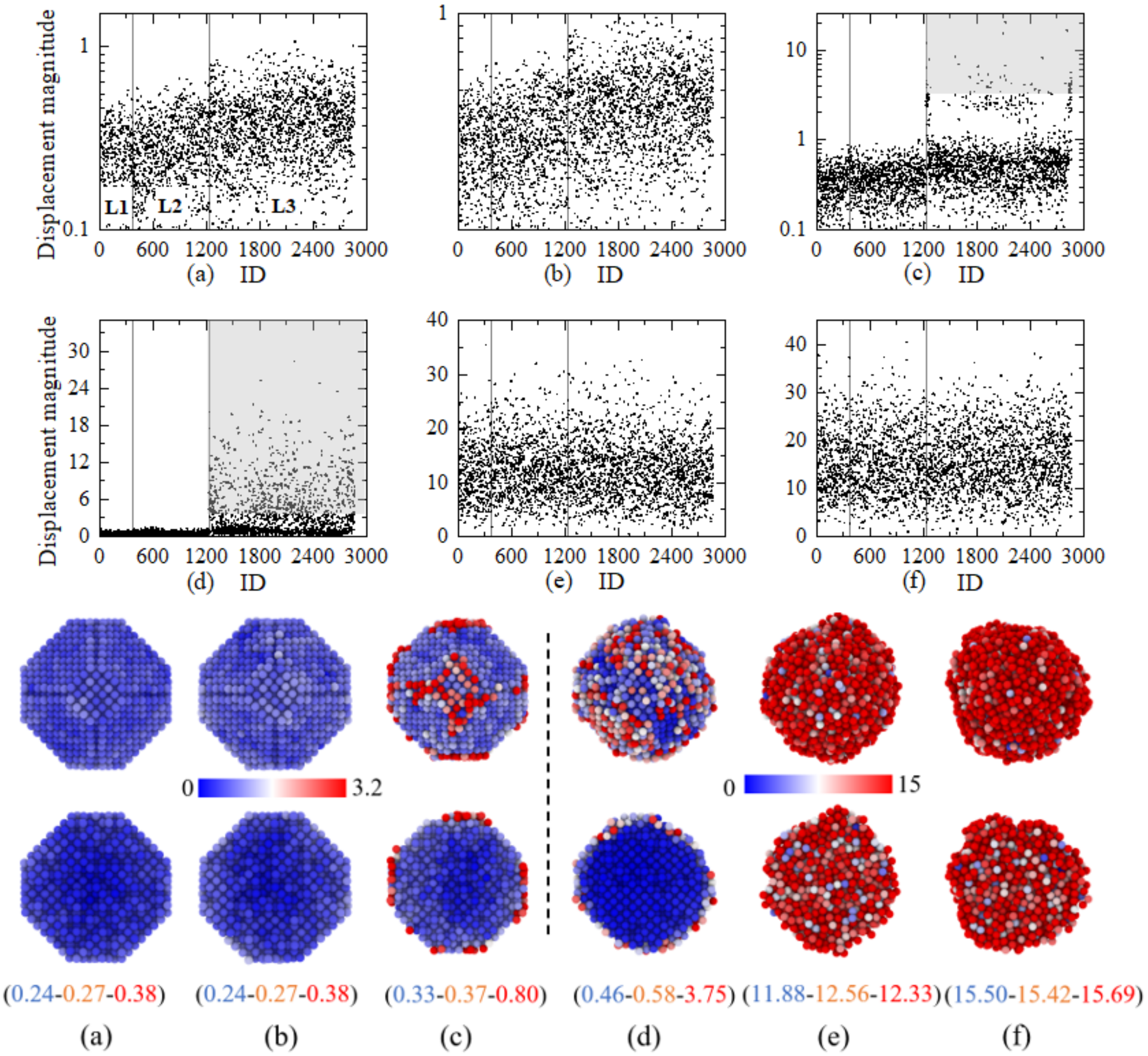

Fig. 2.8 Scatter plots of displacement magnitude along with atom ID of 4 nm nanocrystal at different time and the corresponding coloured maps of the overall and cross sectional snapshots, where (a): 400 K, (b): 800 K, (c): 1200 K, (d): 1600 K, (e): 2000 K, (f): 2400 K, and the numbers in bracket indicates displacement magnitude of different layers, where blue: L1, orange: L2, red: L3, and the grey area in (c) and (d) indicates atoms with displace over 3.2 Å.

Time evolution of molecules is obtained in ReaxFF MD simulation through the dumped information of molecular quantities and chemical formulas of species identified by the bond order criteria of 0.3. It should be noted that except for the plane-parallel monolayer adsorption onto Ni facets (Figure 2.10 (b-1)), the addition of PAH stacks with various misalignment and conformation onto Ni surfaces is also frequently observed (Figure 2.11). The analysis of the overall adsorption is extended to the recognition of the new cluster comprising Ni nanocrystal and the adsorbates. Here, an interatomic distance criteria of 4 Å adopted from the work of Mao et al. (2017), which has been used to distinguish physical nucleation PAH clusters, is employed as illustrated in Figure 2.9 (a). The adsorption ratio is thereof defined as the proportion of the adsorbate atoms. From Figure 2.9 (b)-(e), the effects of molecular size and O/C ratio on time evolution of adsorption tendency in different stages are elaborated into four aspects: initial adsorption rate, binding stability, decomposition of adsorbates and final adsorption ratio.

For benzene (A1), adsorption ratio fluctuates appreciably in all the simulation time with a low final adsorption ratio of 25%, and the number of benzene molecules reduces steadily to 35. It should be pointed out that PAH monomer constructed ReaxFF MD systems are observed to be chemically stable at 1200 K (Mao et al., 2017), and there is no decomposition occurring in our homogenous test system of A1O6 in the absence of Ni nanocatalyst. This indicates that the reduction of aromatic molecules is entirely due to the surface reaction after adsorption.

We display two typical interaction scenarios between benzene and nanocrystal in Figure 2.10 (a) and (b). The first type is that benzene is trapped at the time of 15 ps, and desorbed back immediately after 7 ps surface diffusion. Trap-diffusion-desorption is regarded as void-collision leads to the unstable physisorption which accounts for the fluctuation in adsorption ratio. The second type is that benzene diffuses on the surface for almost 399 ps after trapped by nanocrystal until decomposition occurs, e.g., dehydrogen forming C_6H_5 and aromatic ring opening. Trap-diffusion-decomposition is regarded as effective-collision, in which situation, adsorbates are able to reside on the surface for a long period due to the tuned energy exchange and momentum accommodation with the particle (Li and Wang, 2005).

Comparing the adsorption ratios, it is observed that medium size PAHs (A2, A4 and A7) show heavier fluctuation while step addition occurs in large size PAHs (A10 and A19) in late stage. This is because only A10 and A19 undergo thermally stable physical nucleation forming PAH stacks at 1200 K (Mao et al., 2017). The A19 trimers are subsequently trapped as a whole onto the aromatic subtracts at the time of 452 ps (Figure 2.10 (c)), accounting for the 6% increase of adsorption ratio (Figure 2.9 (c)). Also, it should be noted that 1200 K is the transition point for dimerization of A10. Thus, step addition of A10 is not as prominent as A19 and most A10 is monolayer adsorbates. The reduction of A10 is much more than

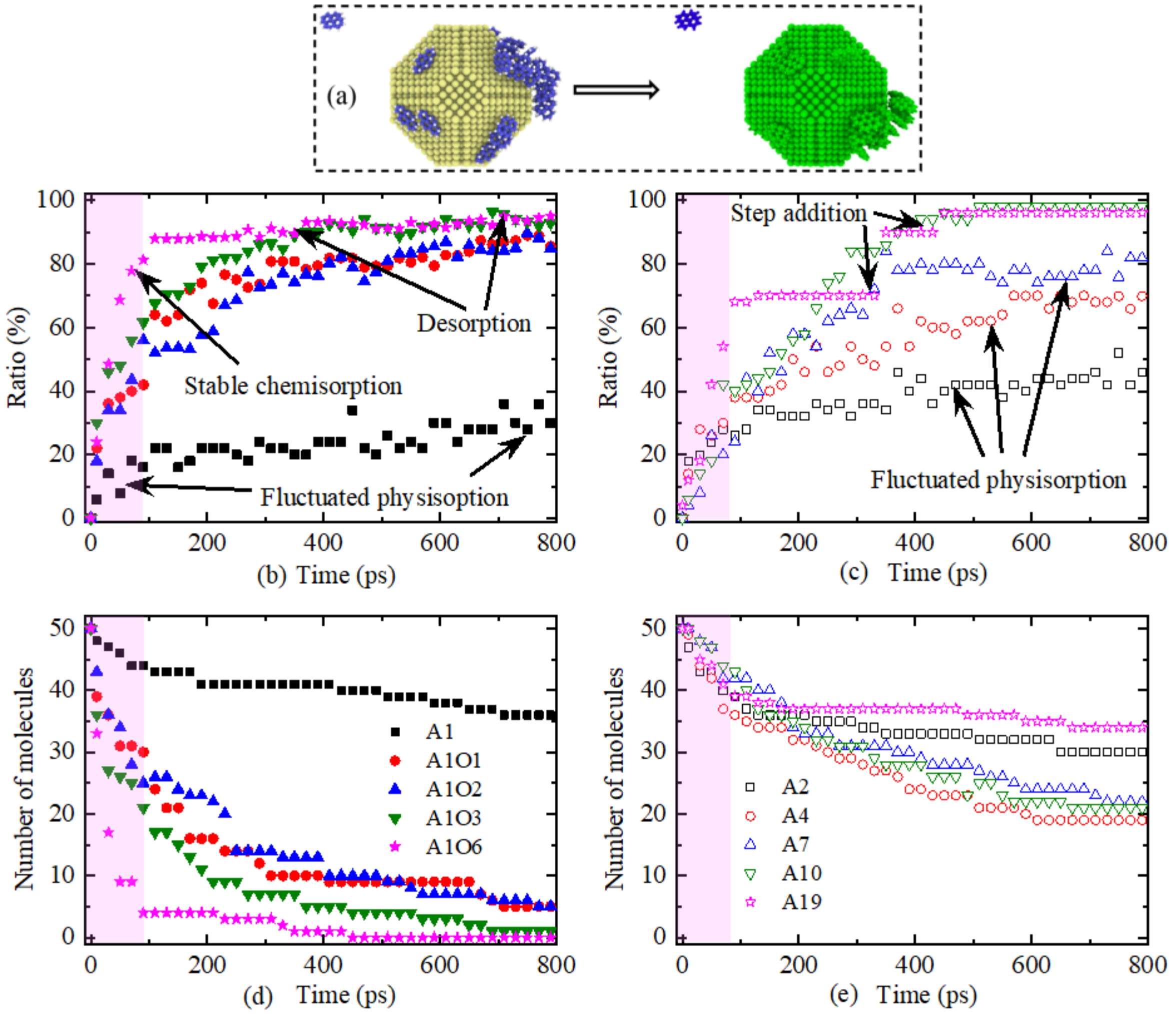

Fig. 2.9 (a) Schematic plot of the cluster recognition (coloured by green) with a cut off distance of 4 Å; (b)-(c) time evolution of overall adsorption ratio; (d)-(e) time evolution of the number of aromatic molecules, and the coloured area in (b)-(e) is the initial stage of A1O6 and A19.

A19 considering that PAH nucleation stacks result in the multi-layered adsorbates. This is described as PAH nucleation induced physisorption. A19 has the highest initial adsorption rate, and larger PAH has higher final adsorption ratio for medium PAHs, indicating that large PAH size enhances effective collision.

Aromatics with higher oxygen contents show higher initial adsorption rate and lower fluctuation (Figure 2.9 (b)). This indicates that oxygen in coke also facilitates effective collision. The substituent hydroxyl group in the benzene can lower decomposition activation energy and enhance the decomposition rate (Figure 2.9 (d)). After adsorption, benzenehexol can proceed the surface reaction like C-O bond fission, O-H bond fission and ring opening etc. (Figure 2.10 (d)). The radicals can further react into H_2O which can then desorb back into the gas phase (Figure 2.11 (d-3)), thus result in the low fluctuation of the adsorption ratio.

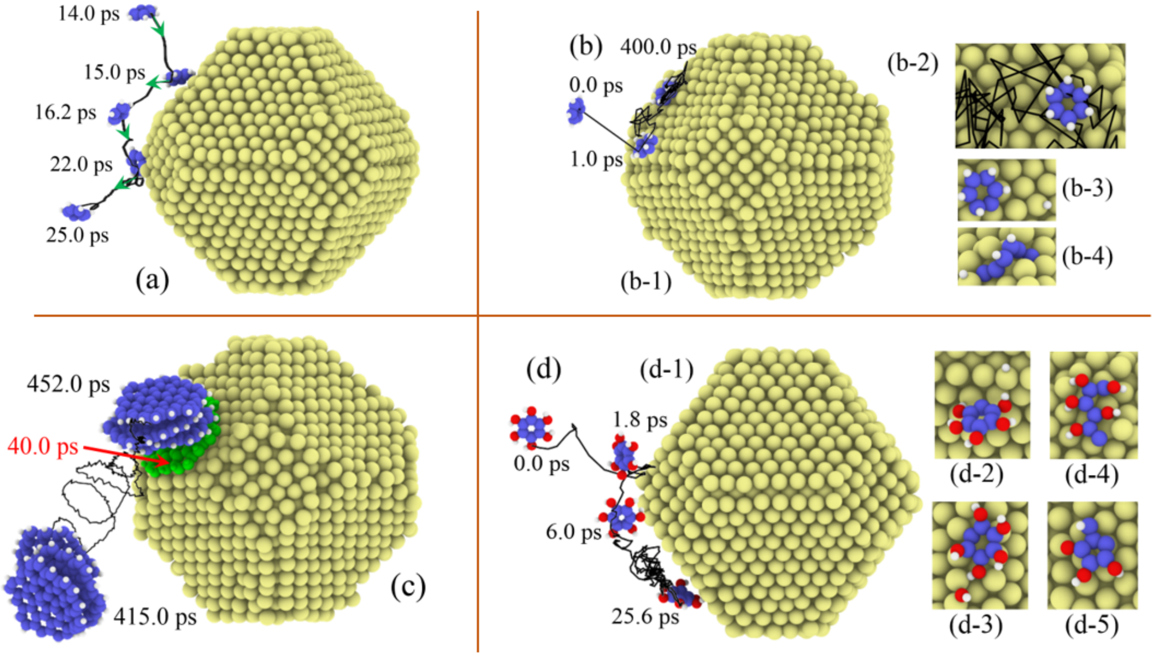

Fig. 2.10 Representative trajectories (black lines) to show the time evolution of aromatic molecule interaction with the surfaces of Ni nanocrystal, where (a)-(b): A1, (c): A19 and (d): A1O6, and green arrow in (a) indicates the movement direction of A1, (b-2) is the modified view of (b-1) to indicate the diffusion trajectory of A1 on (111) facet, (b-3) and (b-4) are part of the products after surface reaction, A19 in (c) coloured in green is trapped at the time of 40 ps and acted as subtracts for PAH stack adsorption, (d-2) to (d-5) are typical products captured after surface reaction.

Through the above analysis, it can be revealed that the mechanism of coke adsorption onto the catalyst surface includes three aspects: molecular collision dynamics, thermal dynamics and kinetics. Although both dynamics and kinetics undoubtedly depend on temperature, the effects of temperature on adsorption of different coke surrogate molecules in Figure 2.11

become complicated particularly when coupled with binding energy type between the adsorbates and the substrate, i.e., physisorption by weak vdW forces and chemisorption by covalent bonds. To be specific, at conditions where there is no surface reaction occurring, e.g., at 400 K and 800 K, the binding energy between A1O6 and Ni surface is covalent bond as the cluster is recognised as a molecule with the formula of $Ni_{2867}C_{300}H_{300}O_{300}$. This also explains that higher oxygen content facilitates effective collision. However, the binding energy is observed to depend on the posture for PAHs, i.e., only aromatic ring parallel to the catalyst surface and binding through the C-C π orbitals are identified as covalent bonding.

A1 adsorption ratios at 400 K, 800 K and 1200 K are 98%, 38% and 30% respectively. The velocity of molecules in MD accords with the Maxwell-Boltzmann distribution, i.e., $v_p = (2RT/M)^{1/2}$, where v_p is the most probable velocity, R is the gas constant and M is molar mass of the substance. A higher temperature is supposed to lead to higher probability of void-collision in physisorption due to higher momentum and kinetic energy (Li and Wang, 2005). However, when temperature is increased further to 1600 K and 2400 K, adsorption ratio increases to 40.33% and 57.67% even though desorption occurs at 2400 K. This indicates surface reaction kinetics plays a role at high temperature. Same situation also occurs for A4, where adsorption ratio decreases from 97.20% at 800 K to 70.77% at 1200 K, while increases from 54.95% at 1600 K to 58.52% at 2000 K. For the effect of thermal dynamics, it is known that PAH dimer lifetime is sensitive to molecular size, and it decreases in elevated temperature. Physical nucleation of A4 at 400 K and A19 from 400 K to 2000 K generates the PAH stacks and results in the multi-layered adsorbates.

2.4 Discussion and conclusion

Catalyst deactivation due to coke deposition is usually reversible, and the surface adsorbates can easily be removed by oxidation with O_2. The degradation of catalyst crystallinity is the real concern in regeneration. We compared the Lindemann index of nanocrystal outer shell after adsorption with the corresponding isothermal melting value at the same temperature as shown in Figure 2.12. It is clear that PAH adsorption reduces the Lindemann index at 1200 K and above, indicating more ordered crystalline structure than isothermal melting. It is assumed that the covalent bond between adsorbates and catalyst surface after chemisorption prohibits the mobility of crystal surface atoms, facilitating the preserve of crystallinity. Meanwhile, the effect of oxygen content is not as prominent as PAH size. However, it should be noted that when temperature was increased to 1600 K and 2000 K, seeping of the PAH surface reaction intermediates into the inner layer of catalyst occurs (see Figure 2.11) which indicates

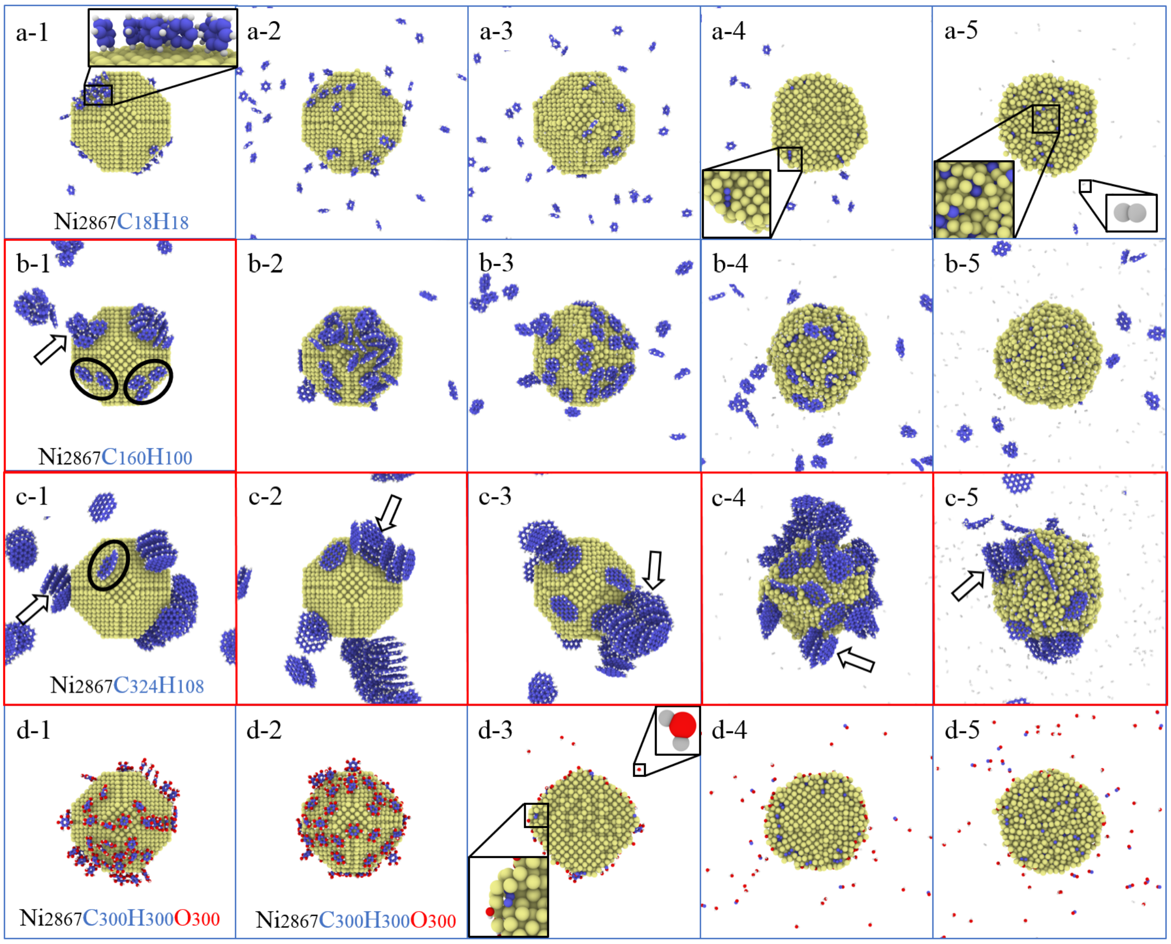
a-1
Ni2867C18H18
a-2
a-3
a-4
a-5
b-1
Ni2867C160H100
b-2
b-3
b-4
b-5
c-1
Ni2867C324H108
c-2
c-3
c-4
c-5
d-1
Ni2867C300H300O300
d-2
Ni2867C300H300O300
d-3
d-4
d-5

Fig. 2.11 Snapshots of the system after 800 ps isothermal simulation to demonstrate the temperature effect on adsorption of A1, A4, A19 and A1O6, where molecular formula of the cluster in (a-1), (b-1), (c-1) and (d-1), (d-2) is indicated at the bottom of the panel; (a-4), (a-5), (d-3), (d-4) and (d-5) are cross section snapshots, and intermediates seeping into catalyst are indicated in the enlarged snapshot, PAHs with its ring parallel to the particle surface are indicated by the black circle in (b-1) and (c-1), the conditions where physical nucleation occurs according to the work of Mao et al. (2017) are highlighted by the red frame and multi-layered adsorbates are indicated by black arrows.

the failure of conventional surface regeneration method that may result in the irreversible deactivation.

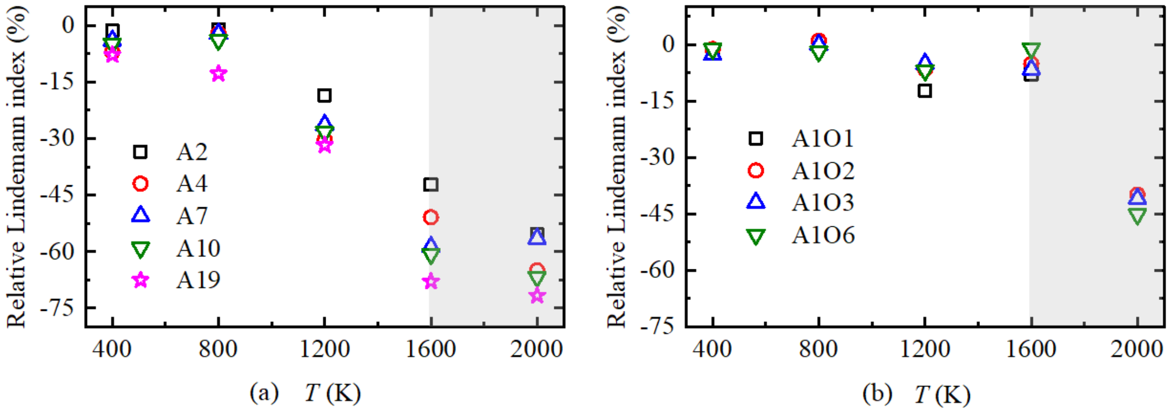

Fig. 2.12 Effect of coke adsorption on catalyst crystallinity of outer shell compared with the corresponding isothermal nanocrystal melting process, which is characterised by relative Lindemann index, and grey area indicates seeping occurrence.

The conclusions are summarised as:

The equilibrated system after 20 K/ps ratio temperature ramp (800 K-3000 K) in production run showed similarity of mass reduction trend compared with our TG experiments (423 K-1173 K). The coke surrogate models (i.e., PAH and oxygenated aromatics) are established based on the identified molecular structure to reflect the molecular size and oxygen contents in practical coke respectively.

The Ni nanocatalyst surface thermal instability is investigated via the temperature dependence of Lindeman index over different layers. Outer shell of the 4 nm nanocrystal starts to show disorder and coordination number distribution modification when temperature is higher than 1200 K.

Isothermal ReaxFF MD system of a centred Ni nanocrystal surrounded by coke surrogate molecules is constructed to reveal the mechanism behind the chemisorption and physisorption at different temperature (400 K-2000 K). It is observed that adsorption is complex process coupling the molecular collision dynamics (e.g., benzene desorbs after trapped by the nanocrystal), thermal dynamics (e.g., medium PAH like pyrene undergo dimerization and physical nucleation before adsorption at low temperature of 400 K) and kinetics (e.g., surface reaction of benzenehexol and the subsequent desorption of intermediates at high temperature above 1200 K).

In comparison with the isothermal melting of nanocrystal, surface chemisorption is observed to facilitate the preserve of nanocatalyst crystallinity owing to the covalent bond prohibiting the mobility of surface atoms. Seeping of surface reaction intermediates at 1600 K and 2000 K into the inner layer of nanocrystal is adverse to catalyst regeneration.

Chapter 3

Soot formation in biofuel combustion

Soot, not merely poses tremendous harms to public health but also causes the darkening and melting of ice glacier. The utilisation of oxygenated biofuels is believed to reduce the soot emission. In this Chapter, the soot inception model is reviewed in 3.1. The difference between biodiesel and diesel on soot inception and soot morphology are revealed using ReaxFF MD simulation in Chapter 3.2. The mechanisms of PAH growth and nascent soot nucleation are elucidated. The effect of oxygenated function groups in biofuels on soot mitigation are quantified in Chapter 3.3.

3.1 State-of-the-art soot inception model

Particle matter emissions form diesel engines are considerably high (six to ten times) than form gasoline engines. Diesel particle emissions can be divided into three main components: soot, soluble organic fraction, and inorganic fraction. More than 50% of the total PM emissions are soot that is seen as black smoke. Diesel particulate matters are typically sphere about 15–40 nm in diameter, and approximately more than 90 % of PM is smaller than 1 µm in diameter. The formation of process of PM emission as shwon in Figure 3.1 is dependent on many factors as the combustion and expansion process, fuel quality (sulfur and ash content), lubrication oil quality, and consumption, temperature, exhaust gas cooling as well as the oxygen contents, fuel components and molecular structure.

Unlike GHGs, soot formation is difficult to be precisely modelled owing to the complex process that involves gas-phase chemistry of primary fuel components, heterogeneous interactions on the surface of soot particles, and particle aerosol dynamics. Although the discussion has shifted from phenomenological possibilities to specifics of reaction pathways due to computer modelling as a scientific tool, particle nucleation, i.e., the transition of gas-phase

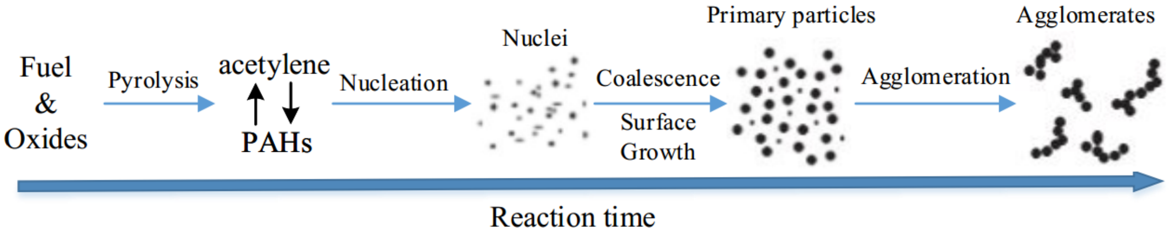

Fig. 3.1 Schematic diagram of soot formation process from gas phase to solid agglomerated particles in five steps.

two-dimensional PAH species to three-dimensional solid incipient soot particle is probably the least understood area with numerous debates. Nascent soot is generally in the size range of 1-6 nm emerging in two types, i.e., disordered incipient particle rich in aliphatics and liquid-like stacked incipient particles (Michelsen, 2017). Challenges also remain especially in the context of real fuel combustion concerning the pathways of first aromatic ring formation. Currently, supported by experimental evidence such as bimodality in nascent soot particle size distribution (PSD) of premixed flames, many numerical simulations of soot nucleation invoke the pericondensed PAH dimerization by physical binding of vdW force (Chen et al., 2014a) (Chen et al., 2014b) (Grančič et al., 2016) (Bowal et al., 2019).

Although it is generally believed that the PAH stabilomers with a central core of condensed, 6-membered aromatics rings, equal or larger than pyrene (A4) can overcome the two-three-ring thermodynamic barrier and survive from the fragmentation at flame temperature (Herdman and Miller, 2008) (Wang, 2011), these physically bonded homo/hetero molecular stacks are too volatile to achieve the thermal dynamic stability. A study by Kholghy et al. (2019) demonstrated that PAH clustering models with reduced soot nucleation reversibility by considering chemical bonds between reactive PAH dimers can predict the sooting process within experimental uncertainty for ethylene coflow diffusion flame, while PAH clustering with vdW forces only underpredicts it by more than two orders of magnitude.

Present understanding cannot fully account for the apparent irreversibility and the morphology of the covalently bonded structures in nascent soot. The previous assumption of purely chemical growth leading to fullerene-like soot nuclei has been ruled out as it greatly underpredicted the mean particle size and was too slow to account for rates in soot formation occurring in short time (1-10 ms to reach particle diameters of 50 nm) (Wang, 2011).

Combing theory and mass spectrometry experiments, Johansson et al. (2018) proposed a promising new chemical growth model referred as rapid clustering of hydrocarbons by radical-chain reactions (CHRCR) of resonance-stabilized radicals (RSRs) which may shed light on the unresolved issues of soot nucleation. In the CHRCR model, three stages are involved: initiator-RSRs growth, hydrocarbon clustering and particle-surface growth. The

CHRCR is certainly plausible to explain a range of currently unanswered sooting phenomena, such as the large amount of aliphatics, the presences of five-membered aromatic rings in young soot particles.

Further research is still needed to specify the reaction details in order to identify how these clusters achieve the gas-to-solid phase transition because lower abundance of RSRs may limit the growth rates (Frenklach and Mebel, 2020). In a recently conducted experiment to spatially resolve the molecular composition of soot, the results showed that the majority species observed in the samples are benzenoids consisting of only fused six-membered rings and do not find "seed" molecules with the morphology of aromatic islands connected by aliphatic side chains, thus challenged the CHRCR model (Jacobson et al., 2020). The controversy between these observations in soot composition and nucleation mechanisms make them important topics for continuous research.

The availability of modelling/simulation tools at the atomistic level may shed light on these unsolved issues. The multiscale model for soot inception developed by Violi et al. (2002), integrating kinetic Monte Carlo and molecular dynamics, allows the extension of the accessible time scale by orders of magnitude while retaining the full atomistic details. Application of this model to acetylene and benzene flames showed that the reaction pathways concerning the growth of incipient soot particles are dependent on the molecular structure of fuel. Some indicators were employed to evaluate the property of the three-dimensional structure of nascent soot particles including physical properties (e.g., porosity, density, radial distribution function and sphericity) and chemical properties (e.g., C:H ratio, aromatic moieties and number of cross-links) (Violi, 2004) (Violi and Venkatnathan, 2006).

MD simulation with OPLS-AA force field (Elvati and Violi, 2013) (Lowe et al., 2015) was used to quantify the impact of mass, symmetry and morphology of PCAH, AALH and aliphatics substituted PAHs on the stability of the molecular dimers. Meanwhile, the contributions from potential energy and entropy were taken into consideration simultaneously by using the free energy methods to describe the process. It was understood that the attached aliphatics increased the nucleation rate greatly due to the collision energy accommodation enhancement by the added internal degrees of freedom.

Modelling work was also performed by using replica exchange MD simulation to investigate the molecule size distributions of the heterogeneous PAH clusters in the core-shell model (Bowal et al., 2019). It was found that larger PAHs are stacked at the core while small PAHs are located on the cluster surface. Of the two main factors, the strength of intermolecular interactions played a more critical role in determining cluster partition than the molecular size difference. Another method for modelling combustion and soot formation process is reactive force field (ReaxFF) based MD simulations. For example, Mao et al. (Mao et al.,

2017) (Mao et al., 2018) (Mao et al., 2019) found that physical dimerization depended both on the temperature and PAH size while all the PAHs became chemically active at temperature above 2500 K and generated fullerene-like soot particles. It is recognized that MD-type of modelling/simulation will likely lead to high-fidelity soot models capable of simultaneously resolving particle size distribution, chemical composition, and morphology (Violi et al., 2002) (Wang, 2011) (Mao et al., 2017).

3.2 Soot formation of biodiesel combustion

3.2.1 Fuel molecular structure and modelling setup

To give an integrated description and to emulate practical fuels in the investigation of combustion properties, using surrogate models is a common strategy. In this study, diesel surrogate fuels are constructed by *n*-Dodecane (DDC, $C_{12}H_{26}$); Heptamethylnonane (HMN, $C_{16}H_{34}$); 1,2,4-Trimethylbenzene (TMB, C_9H_{12}), *n*-Dodecylcyclohexane (DCH, $C_{18}H_{36}$) with molar ratio of 20%, 20%, 30% and 30% which are in accordance with the general diesel composition, i.e., normal and iso-paraffins (ramified alkane) contributing to 25-50%, cyclo-paraffins constituting about 20-40% and the proportion of aromatics is 15-40% (Pitz and Mueller, 2011). While petrol-diesel comprises hundreds or thousands of hydrocarbon components, biodiesel fuels typically contain fewer than ten components. Soy oil biodiesel is employed in the simulation, consisting primarily of five major methyl esters, i.e., methyl palmitate (MP, C16:0), methyl stearate (MS, C18:0), methyl oleate (MO, C18:1), methyl linoleate (ML, C18:2) and methyl linolenate (MLN, C18:3) (Coniglio et al., 2013). The corresponding molecular structures and compositions are presented in Table 3.1 and Table 3.2

All the simulations are performed using LAMMPS with the latest developed CHO2016 parameters which can accurately describe C1 chemistry and carbon condense phase (Ashraf and van Duin, 2017). In order to quantify the sooting tendency consistently, each reactive system is built keeping approximately the same overall carbon number, i.e., 150 diesel molecules, 114 biodiesel molecules, and 133 biodiesel blends molecules (50%-50%) are placed randomly in the cubic box. The temperature is set up from 2500 K to 4000 K with 500 K intervals. In ReaxFF simulations, employing a high temperature and pressure to accelerate the reactions and facilitate the simulation process is a common strategy (Chenoweth et al., 2009) (Liu et al., 2017c) (Chen et al., 2019). It is also worth noting that this study is focussed on fundamental aspects of fuel chemistry leading to soot formation (rather than simulating combustion engine conditions) with special attention to renewable biodiesel fuels. The total simulation time for each system is set up as 2 ns with 0.25 fs time step. Canonical

Table 3.1 Molecular structures, chemical formula and compositions of soy oil biodiesel.

Common Name	Molecular Formula	Molecular Structure	M (g/mol)	x (mol %)
Methyl Palmitate	MP (C16:0) $C_{17}H_{34}O_2$	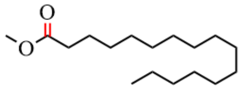	270.46	12
Methyl Stearate	MS (C18:0) $C_{19}H_{38}O_2$	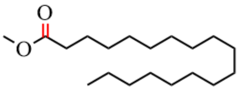	298.51	5
cis-9-Methyl Oleate	MO (C18:1) $C_{19}H_{36}O_2$	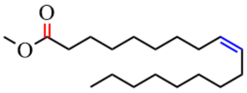	296.50	13
cis-9, 12-Methyl Linoleic	ML (C18:2) $C_{19}H_{34}O_2$	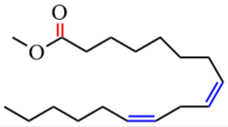	294.48	53
cis-9, 12, 15-Methyl Linolenate	MLN (C18:3) $C_{19}H_{32}O_2$	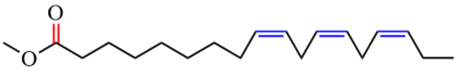	292.47	7

Table 3.2 Molecular structures, chemical formula and compositions of diesel.

Common Name	Molecular Formula	Molecular Structure	M (g/mol)	x (mol %)
n-Dodecane	DDC $C_{12}H_{26}$	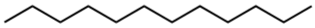	170.33	20
2,2,4,4,6,8,8-Heptamethylnonan	HMN $C_{16}H_{34}$	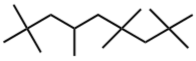	226.44	20
1,2,4-Trimethylbenzene	TMB C_9H_{12}	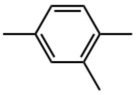	120.19	30
n-Dodecylcyclohexane	DCH $C_{18}H_{36}$	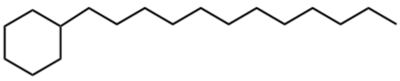	252.50	30

ensemble (NVT) is used in all the simulations in conjunction with the Nosé-Hoover thermostat employing a damping of 25 fs. The bonding formation and dynamic trajectory are recorded every 2.5 ps. For species analysis, a 0.3 bond strength cut-off is chosen in the post-processing to recognize the formation of molecules. A low cut-off value is helpful for capturing all the reactions including even short-lived intermediate species. Every case (one system at one temperature) was repeated five times with unique starting configurations to prevent uncertainties caused by the single run. The visualisations of simulation results are generated using Visual Molecular Dynamics (VMD) software (Humphrey et al., 1996).

3.2.2 Evolution of incipient soot formation

It has been understood that temperature plays important roles in modulating the initial fuel pyrolysis and the subsequent growth pathways of carbonaceous clusters. For example, peri-condensed aromatics like naphthalene, anthracene, and pyrene would experience physical stacking at temperatures below 400 K and form incipient particles, while chemical events of soot growth only take place at temperatures above 2500 K via self-assembly of fullerene-like particles connected by polyacetylenic chains (Mao et al., 2017). To investigate the temperature dependence of chemical process of nascent soot formation, the time evolutions of the average mass and C:H ratio of the largest molecule over the temperature range from 2500 K to 4000 K are presented in Figure 3.2.

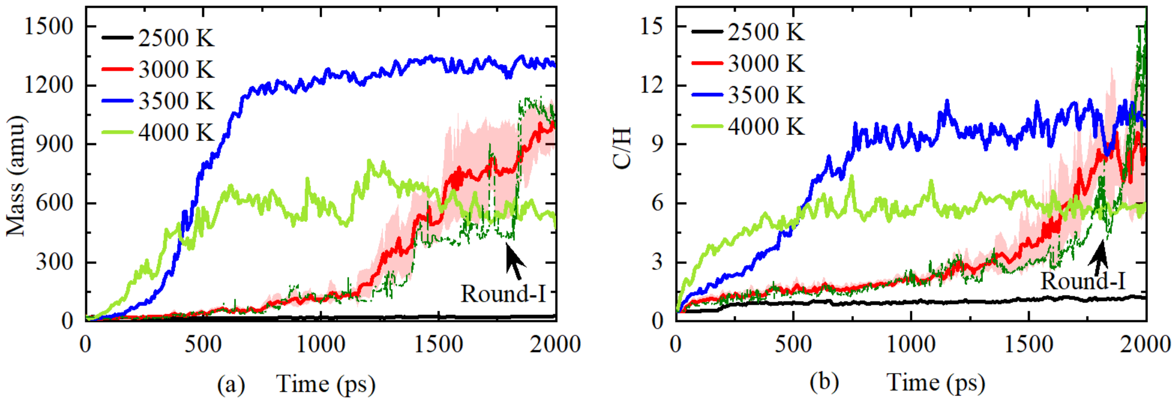

Fig. 3.2 Temperature effects and time evolutions of the mass and C:H ratio of the largest molecule in the simulation of biodiesel blends, where the shaded area represents the statistical uncertainty ranges determined by standard deviation.

Figure 3.2 (a), it is clear that 2500 K is not a favourable temperature to have nascent soot formation observed within the simulation period since the species produced only exist in the form of small polyyne-like structures. Biodiesel blends are not depleted at 2500 K with some reactants like TMB even persist the whole resident time in all five reactive systems. In

ReaxFF MD simulation, temperature accelerates fuel reaction positively by increasing the kinetic energy and collision frequency. However, this is not the pattern for soot nucleation. At 3500 K, mass of the largest molecule reached a plateau after 600 ps and stabilised at around 1200 amu.

Molecules of nascent soot precursors at 4000 K grow most rapidly yet soot particles keep fluctuating at a relatively smaller value of 600 amu after 500 ps. This is attributed to the decomposition of the formed nascent soot at higher temperature. At the initial stage of 3000 K, soot precursors increase steadily, followed by an apparent rate rise after passing the inflection point at around 1100 ps. The step-shape increment occurs several times in the first round simulation shown in Figure 3.2 (a). The rate transition indicates that the mass addition shifts from steady gas-phase PAH growth to condensed-phase soot inception by aliphatic connection. Initial mass growth of the largest molecules and the subsequent hydrocarbon clustering always accompany the continuous increment of C:H ratio as shown in Figure 3.2 (b). To have a better understanding of the formation, fragmentation and reorganisation of nascent soot, reactions at 3000 K are scrutinised in the following study. The representative molecular structures are visualised and identified in Figure 3.3.

The soot precursors comprising CR5 (carbon ring with five atoms) substituted with aliphatic branches are observed frequently in Figure 3.3. To quantify the soot formation process, the numbers of carbon rings in the reactive system ranging from triangle to octagon are counted in Figure 3.4. Before 800 ps, formation of hexagons and pentagons is relatively limited since the system would primarily go through the pyrolysis of fuels to produce PAH precursors like small unsaturated fragments as shown in Figure 3.3 (b). The decline of CR6 also occurs in this period due to the decomposition of DCH. After the occurrence of the scattered cyclopentadienyl and benzene in Figure 3.3 (c), the numbers of CR5 and CR6 increase rapidly with CR5 dominating from 800 ps to 1000 ps. During this stage, medium-sized PAHs exist in the form of peri-condensed or elongated cata-condensed aromatics.

It has been reported previously in stochastic atomistic simulation that most of the soot precursors at 202 amu and 226 amu contain penta-rings as opposed to only hexa-rings (Johansson et al., 2017). The morphology and distribution of penta-rings in molecular constituents of the incipient soot were also imaged explicitly in high-resolution atomic force microscopy (AFM) (Commodo et al., 2019). Longer time scales would stabilise these PAHs by ring reorganisation and side-chain condensation reactions. This facilitates the pentagon defect healing, leading to thermodynamically more stable PAH fragments with more hexagons. Thus, after 1000 ps, the number of CR6 overtakes CR5, and the overall quantity of carbon ring continues increasing because of continuous radical addition reaction as shown in late stages in Figure 3.3. The CR7 starts to increase at this stage along with the size expansion of PAHs,

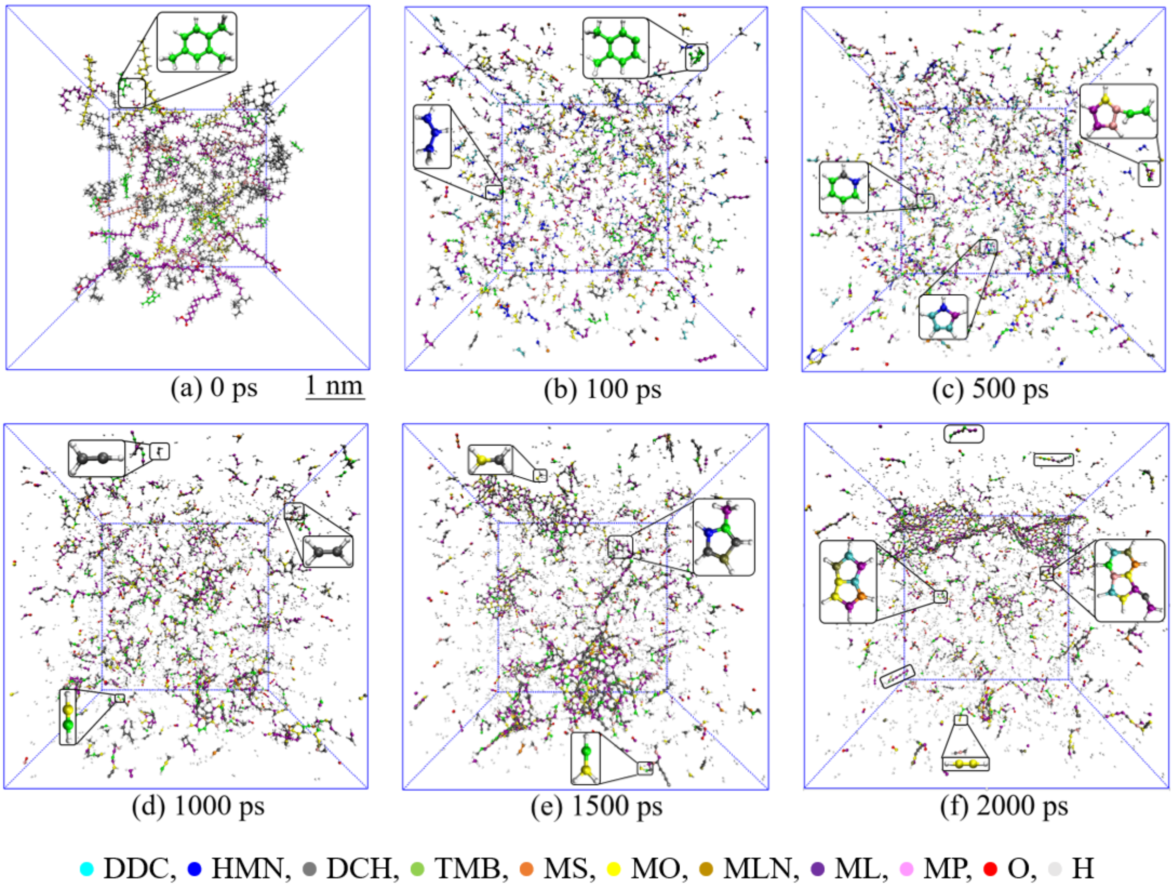

(a) 0 ps (b) 100 ps (c) 500 ps

(d) 1000 ps (e) 1500 ps (f) 2000 ps

1 nm
● DDC, ● HMN, ● DCH, ● TMB, ● MS, ● MO, ● MLN, ● ML, ● MP, ● O, ● H

Fig. 3.3 Evolution of pyrolysis product distribution and incipient soot morphology of biodiesel blends, where carbon atoms from different surrogates are indicated with different colours, all the oxygen atoms in biodiesel are indicated with red sphere, and all the hydrogen atoms are indicated with silver sphere, some representative structures are enlarged.

and mainly resides in periphery while the numbers of CR3, CR4 and CR8 are negligible during the whole process.

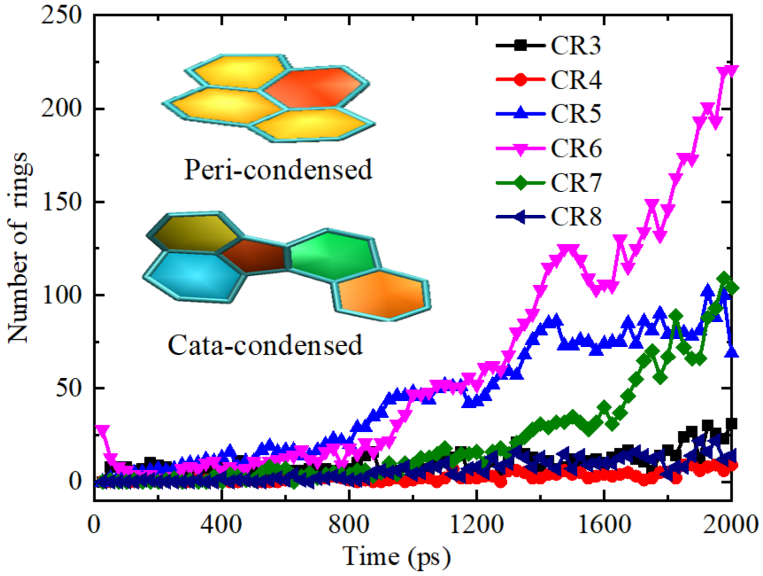

Fig. 3.4 Time dependence of carbon ring count statistics, where the rings are artificially coloured.

3.2.3 Mechanisms of PAH growth and nascent soot nucleation

The molecular details leading to the formation of solid soot particles from gaseous molecules can be revealed by examining the extensive MD results obtained. A ReaxFF-based panoramic soot formation mechanism is proposed and schematically showed in Figure 3.5. The formation can be divided into six stages: fuel pyrolysis to form gaseous precursors, initiator formation, growth of aromatics, nucleation (gas-to-solid transition), evolution of soot nuclei, particle coalescence and fractal aggregation.

Although the biodiesel blends comprising 9 components can generate massive possible reaction pathways, the predominant thermal composition pathways are C-C bond cleavage and H-atom abstraction by radical species to produce C6-C9 intermediates and C0 compounds. A series of subsequent H-abstraction reaction and β-session generate smaller unsaturated fragments like ethylene (C_2H_4), ethyne (C_2H_2) etc., and RSRs, e.g., propargyl (C_3H_3) and cyclopentadienyl, as the precursors for soot formation. The combination process of small precursors to form aromatics using MD simulation has barely been reported, which is recognized as the initial step for soot formation. Propargyl is known as the key precursor in benzene formation via $C_3H_3 + C_3H_3 \rightarrow C_6H_6$. Recently it was also recognised as the initiator in the CHRCR model for radical chain reaction via $C_3H_3 + C_2H_2 \rightarrow C_5H_5$. With unpaired electrons being delocalised over multiple C-atom sites, propargyl is stabilised by resonance and less reactive than ordinary flame radicals like methyl, ethyl and vinyl etc. This enables RSRs like propargyl and cyclopentadienyl to exist till the late stage as showed in Figure 3.3, and thus to survive the hostile flame environments. In our simulation, it has been confirmed that the penta-rings play a key role in the initial stage as showed in Figure 3.4.

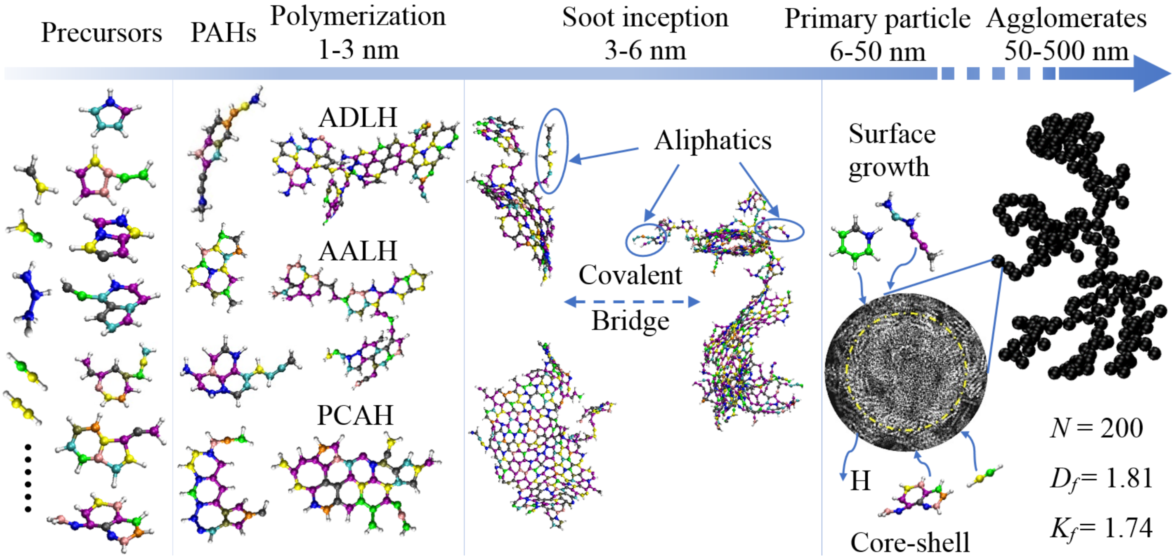

Fig. 3.5 An indicative mechanism of soot particle formation from gaseous molecules. The process includes fuel pyrolysis to produce PAH precursors, aromatics formation, PAH growth, particle inception, evolution of the soot nuclei, together with the simulated image of soot particles with surface growth and fractal agglomeration of 200 primary particles (D_f is fractal dimension, k_f is fractal prefactor).

The early soot formation model focussed on the addition of C_2H_2 to aromatics to produce the pericondensed stabilomers after H-atom abstraction from aromatics [34]. In ReaxFF MD simulation, PAH growth is initiated by the addition of C_2H_2 or C_2H_3 to cyclopentadienyl, benzyl (C_7H_7), and indenyl (C_9H_7) which agrees with the recent CHRCR model described as the addition of ethyne or vinyl to RSRs with five or seven carbon ring. At high temperatures, these adducts are able to undergo fast extension, cyclisation, and rearrangement to enlarge the PAH-like structures which are also substituted with methyl groups or unsaturated side chains. The continuous growth of PAHs proceeds through three categories of moderate-sized intermediates, i.e., ADLHs, AALHs and PCAHs to generate semi-condensed nonplanar oligomers of aromatic compound which exhibits liquid like properties. The molecular morphology of these PAHs in ReaxFF MD results are consistent with the recent AFM experimental results (Commodo et al., 2019) (Schulz et al., 2019), which confirmed the existence of aliphatically linked aromatic structures in soot.

Fully PCAH stabilomers have to be as large as coronene to attain the thermodynamic stability of dimerization through electrostatic and dispersive force which was seldom found experimentally (Sabbah et al., 2010), while the role of AALH and ADLH doped with penta-rings has been deciphered as stable components in flame via atmospheric-sampling high-resolution tandem mass spectrometry (Adamson et al., 2018).

Recently, Frenklach and Mebel (Frenklach and Mebel, 2020) updated the "HACA" model to include the nucleation mechanism by establishing the thermodynamics-kinetics coupling model. It showed that the E-bridged covalent bond with five member rings is variable to account for the soot nucleation by exciting 2 to 3 internal molecular rotors. The reversible chemical growth can also achieve the measurable nucleation flux with cluster size over 3 monomers. In this ReaxFF MD simulation, the seed molecules eventually evolve into aliphatically bridged curved three-folder cluster structure weighting approximately 1100 amu with an envelope diameter of about 5.5 nm, thus achieving the transition from gaseous PAHs to the first condensed particle nuclei. In addition to the methyl radicals or vinyl conjugated side chains, long aliphatics (C4-C10) highlighted in Figure 3.5 have also been observed. The existence of aliphatics in nascent and mature soot remains an extensively observed but not being clearly explained (Cain et al., 2010) (Cain et al., 2011). Although the controversial is revoked again recently as the mass spectrometry experiment found that the soot is composed of stabilomers mainly without aliphatics (Jacobson et al., 2020), our ReaxFF simulation results support the existence of the aliphatics in soot nuclei together with the AFM images which also confirmed the existence of long aliphatics in nascent soot directly (Frenklach, 2002) (Commodo et al., 2019) (Schulz et al., 2019).

The MD results are processed to indicate the morphological evolution of primary particles. The amorphous clustering structures are arranged in a core surrounded by ordered graphite at a specific distance. Graphitisation during soot maturing at high temperature always results in ordered outer shell structure with interplaying distance at around 0.35 nm (Michelsen, 2017).

To reveal the turbostratic structure in soot nuclei, a schematic core-shell model (randomly oriented multiple amorphous inner core surrounded by regular aligned outer shell) is constructed which is then simulated into TEM (Transmission Electron Microscopy)-like image. It provides a way to build large scale artificial atomic models of soot particles by mimicking the fringe lattice parameters in high resolution TEM experiments, e.g., distributions of fringe length, tortuosity and separation distance. Most soot particles have complex fractal aggregation, affecting the nature of the particles. In this study, the fractal morphology is quantified by the scaling law given as $n_p = k_f \cdot (R_g/r_p) \cdot D_f$, where n_p is the number of particles in the aggregate, D_f its fractal dimension, k_f is the fractal prefactor, R_g is the radius of gyration of the aggregate and r_p is the mean radius of the single monomers. The fractal parameters in this study are based on the experimental result of the biodiesel blends (Lapuerta et al., 2017).

3.2.4 Comparison of biodiesel and diesel on soot formation

The comparison between diesel and biodiesel fuels on soot formation at the atomic level is achieved for the first time, as that demonstrated in Figure 3.6, with different stages divided based on the mass growth of the largest molecules. Components of real biodiesel are large FAMEs comprising methyl esters and the attached saturated paraffin or unsaturated olefin chains of 16-18 carbon atoms. Detailed kinetics of real biodiesel is insufficiently understood and is always constructed by analogy with two kinds of moieties. The differences between diesel and biodiesel on soot formation lies in several aspects: C:H ratio of the largest molecules during soot formation, size, composition and morphology of the nascent soot.

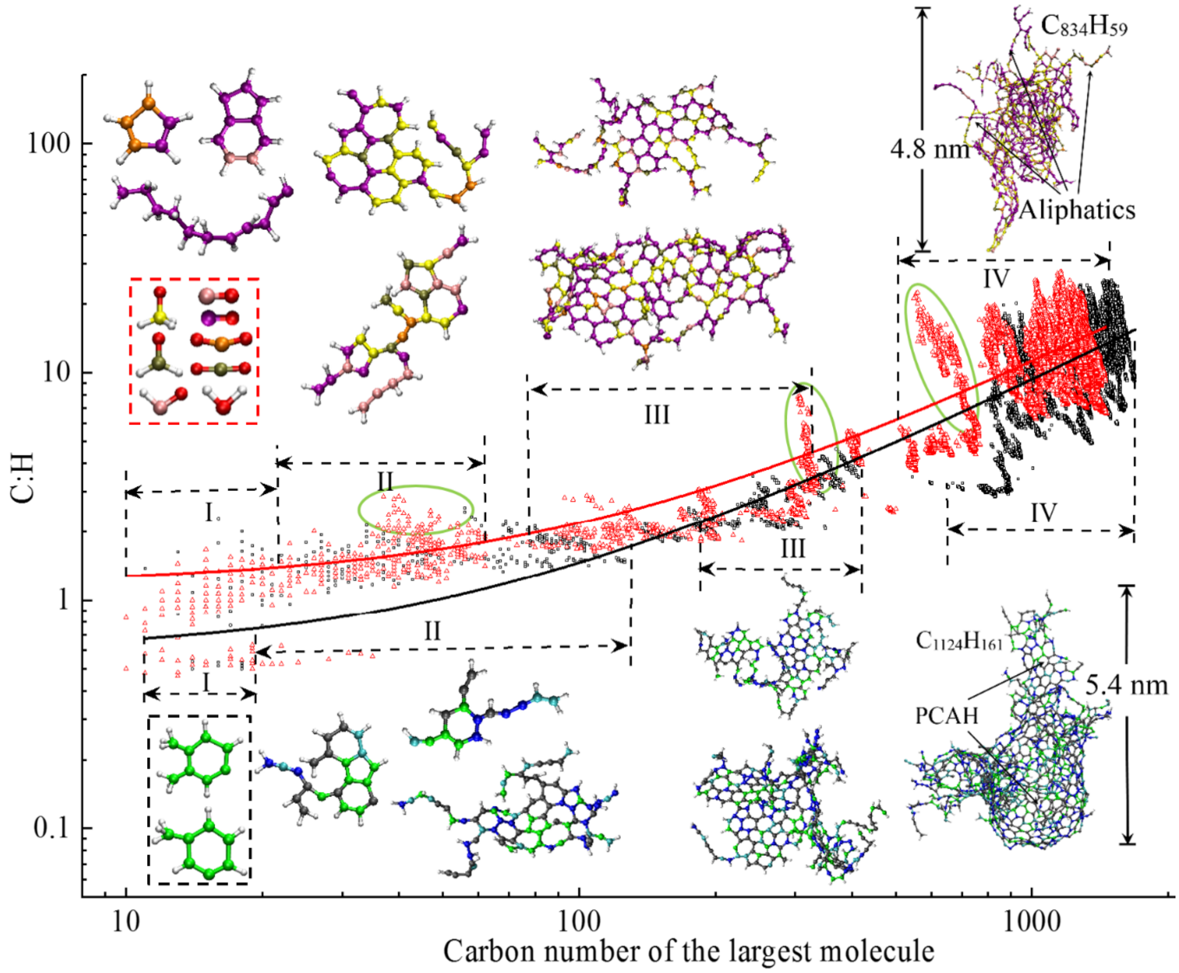

Fig. 3.6 Comparison of diesel and biodiesel on incipient soot formation processes, where the fitted red line and scattered red triangles indicate the number of carbons and the C:H ratio in the largest molecule during the simulation of biodiesel, and the fitted black line and scattered black squares indicate diesel, and the dehydrogenation process is highlighted with ellipses.

As shown in Figure 3.6, the methyl ester functional group results in the higher C:H ratio in biodiesel soot inception, because dehydrogenation via H-atom abstraction from PAH precursors and nascent soot formation are enhanced at all growth stages due to the early formation of hydroxyl and methoxy radicals. In addition, the fuel-bonded oxygen causes the removal of C-atoms from soot precursors, suppressing the PAH and soot surface growth and leading to smaller primary particles. It was also reported that smaller primary soot particles always have higher reactive surface area, which in turn would increase the availability of active sites for oxidation and thereby enhance the particle size reduction (Zhang et al., 2017).

The fuel composition and the molecular structure particularly the oxygen content in biodiesel determines the soot formation pathways, which are the underlying reason for the observed differences in the resulting soot particles between diesel and biodiesel. For diesel, the bond strength of cycloalkyl ring in DCH is similar to the bonds in non-cyclic alkanes, thus the mechanisms of soot precursor formation from cycloalkanes and non-cyclic alkane are similar after the ring opening. In comparison with n-alkanes, highly branched paraffin like HMN tends to produce large alkenes, because the C-C fission produces alkyl radicals with methyl substitution at the β C-atoms. The methyl C-H or C-C bond fission of TMB would generate trimethylbenzyl radicals, methylbenzyl and dimethylbenzyl radicals directly, circumventing the cyclisation steps that are necessary for soot formation from aliphatic hydrocarbons. Therefore, nascent soot of diesel has more organised fullerene-like structures and is aromatics dominated while final nascent soot of biodiesel appears to be amorphous in structure with a considerable amount of long aliphatic branches.

The morphological differences in Figure 3.6 help to elucidate the fundamental mechanisms behind XPS (X-ray Photoelectron Spectroscopy) experimental results that internal nanostructures of the primary particles generating from fuels with higher biodiesel contents exhibit pronounced C-C sp^3 hybridization signals indicating higher degree of structural disorder (Savic et al., 2016).

To quantitatively compare the sooting propensity of diesel and biodiesel, yield sooting index (YSI) is employed as a metric. Experimental YSI is based on converting the maximum soot concentration in a fuel-doped methane/air coflow laminar flame into an apparatus-independent index, and effects of combustion conditions e.g., pressure, temperature and dopant concentration can be factored out to highlight the effect of fuel composition and molecular structure on sooting behaviour. Kwon et al. (2020b) has developed the framework to predict the YSI in ReaxFF MD simulation. In this study, four reference fuels including benzene, *n*-dodecane, methyl octanoate and ethyl formate are selected specifically after test.

The following equation is used to estimate the YSIs of the test fuels:

$$\mathrm{YSI}_{\mathrm{ReaxFF}} = A \times \sum_i w_i + B \tag{3.1}$$

where w_i is the mass fraction of fragment i including the nascent soot and the corresponding unsaturated fragments like PAH precursors which would contribute to the surface growth, A and B are scaling constants chosen so that the ReaxFF-estimated YSIs for ethyl formate and benzene are equal to 9.2 and 100.3 respectively on a unified scale (Das et al., 2018a). The comparison between ReaxFF-derived YSIs and experimental YSIs is shown in Figure 3.7. It is apparent that for the selected fuels ReaxFF-derived YSI is able to reproduce the experimentally-measured YSI reasonably. The YSIs of diesel and biodiesel are calculated using the same scaling constants as the simulation conditions remain the same (Kwon et al., 2020b). The ReaxFF-derived YSI of diesel is equal to 79.36 ± 6.43, higher than that of biodiesel which is equal to 68.61 ± 4.23.

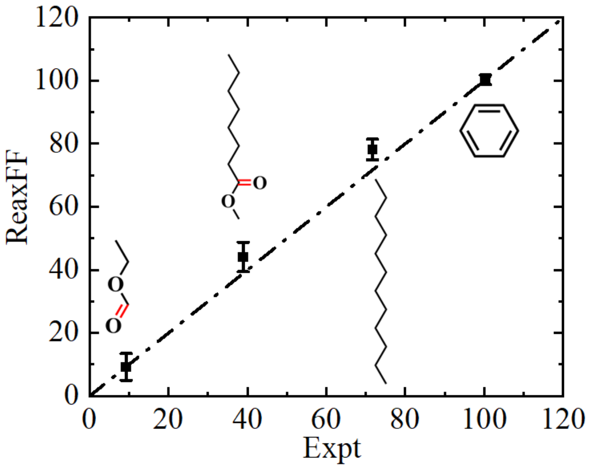

Fig. 3.7 Comparison between ReaxFF derived YSIs and experimentally measured YSIs, where the experimental values are from the unified sooting tendency database based on the work of Das et al. (2018a).

It has been demonstrated that the sooting tendency of the mixtures of surrogate fuels can be predicted accurately (4%-5% of average error) via the predictive mixing rules (Das et al., 2017) given as follows:

$$\mathrm{YSI}_{\mathrm{Mix}} = \sum_{i=1}^{n} w_i \times \mathrm{YSI}_{\mathrm{Sur}} + \sum_{j=1}^{m} w_j \times \left(\sum_{k=1}^{11} n_k \times c_k \right)_j \tag{3.2}$$

where w_i is the mass fraction of surrogate fuel i, n is the number of surrogate fuels with experimentally measured YSI values available while m is the number of surrogate fuels without experimental YSIs, n_k is the number of carbon atoms of type k in surrogate fuel

j, and c_k is the contribution of each carbon type to the YSI. The YSIs of the surrogate compounds are obtained either using the measured YSIs or by lumping up the contribution from the C-atom types present in the fuel molecules via group-additivity approach when YSIs are not experimentally available. To compare with the ReaxFF-derived YSI directly, the predicted YSI should be converted into the unified value by using the following formula, as the predictive model is in "low scale" (Das et al., 2018a).

$$\mathrm{YSI}_{\mathrm{Unified}} = 0.64^{[\pm 0.03]} \times \mathrm{YSI}_{\mathrm{Low}} + 30.4^{[\pm 1.9]} \tag{3.3}$$

As a consequence, the predicted unified YSI value of the mixtures of diesel surrogate fuels in current study is equal to 79.05 ± 4.27. Thus, ReaxFF-derived YSI is feasible to evaluate sooting tendency of diesel and biodiesel fuels quantitatively.

3.2.5 Effects of biodiesel molecular structures on soot precursor mitigation

The simplest biodiesel surrogate fuels, i.e., methyl butanoate (MB), ethyl propionate (EP) and methyl crotonate (MC) are selected to interpret the effect of unsaturation and isomerisation of fuel molecular structure on soot suppression, as they contain structural functional groups expected to account for fuel-specific effects observed in combustion of practical biodiesel fuels. The specific fuel destruction pathways are captured and listed in Table 3.3 using Chemical Trajectory AnalYzer scripts (Dontgen et al., 2015).

From the observed pathways shown in Table 3.3, pyrolysis of fuels is accomplished mainly via unimolecular decomposition by direct C-C and C-O bond cleavage, yielding aliphatic radicals and oxygenated radicals. H-atom abstraction via methoxy radical attack (R4) also occurs occasionally in MB pyrolysis since the C-H bond in CH_2 group alongside the carbonyl group in alkyl esters is considerably weaker compared with the secondary C-H bonds in conventional hydrocarbons, which makes it a more vulnerable site for radical attack by H-atom abstraction [49]. Time history of stable oxygenated products like CO and CO_2 in Figure 3.8 (a) quantifies the capability of the ester groups on capturing and removing C-atoms from soot precursor pool. Early formation of CO and CO_2 moieties increases instantly in MB and EP with initial number of CO_2 more than twice greater than CO in MB, whereas negligible amount of CO_2 is produced in MC decomposition.

The radicals like $CH_3(CH_2)_2(CO^\cdot)$, $CH_3CH_2(CO^\cdot)$, $CH_3CH_2O^\cdot$ and $CH_3(CH)_2CO^\cdot$ formed by C-O bond fission inside ester groups via R1, R5 and R9 generates CO moiety rapidly, while methoxy radicals react into CO via aldehyde intermediates: $CH_2O \rightarrow CHO \rightarrow CO$

Table 3.3 The observed decomposition pathway and final oxygenated products of MB, EP, and MC in five parallel simulations, with the occasional pathways marked with star.

ID	Reaction	Final products
R1	$MB \rightarrow CH_3O^{\bullet} + CH_3(CH_2)_2(CO^{\bullet})$	CO
R2	$MB \rightarrow CH_3^{\bullet} + CH_3(CH_2)_2(CO)O^{\bullet}$	CO_2
R3	$MB \rightarrow CH_3CH_2CH_2^{\bullet} + CH_3O(CO^{\bullet})$	CO, CO_2
R4☆	$MB + CH_3O^{\bullet} \rightarrow CH_4O + CH_3CH_2CH^{\bullet}(CO)OCH_3$	CO
R5	$EP \rightarrow CH_3CH_2(CO^{\bullet}) + CH_3CH_2O^{\bullet}$	CO
R6	$EP \rightarrow CH_3CH_2^{\bullet} + CH_3CH_2O(CO^{\bullet})$	CO, CO_2
R7	$EP \rightarrow CH_3CH_2^{\bullet} + CH_3CH_2(CO)O^{\bullet}$	CO_2
R8☆	$EP \rightarrow CH_3^{\bullet} + CH_3CH_2(CO)OCH_2^{\bullet}$	CO
R9	$MC \rightarrow CH_3O^{\bullet} + CH_3(CH)_2(CO^{\bullet})$	CO
R10☆	$MC \rightarrow CH_3CHCH^{\bullet} + CH_3O(CO^{\bullet})$	CO, CO_2
R11☆	$MC \rightarrow CH_3^{\bullet} + CH_3(CH)_2(CO)O^{\bullet}$	CO_2

(Ashraf and van Duin, 2017). Formaldehyde decreases immediately after reaching peak which accounts for the steady increase of CO at the later stage. Reactions of methoxycarbonyl ($CH_3O(CO^{\cdot})$) and ethoxycarbonyl ($CH_3CH_2O(CO^{\cdot})$) radicals both proceed in two competitive channels yielding CO and CO_2. In addition, MB, EP and MC produce a small amount of H_2O indicating the additional dehydrogen of nascent soot by O-atoms.

Aliphatic counterparts tend to produce soot precursors of high unsaturation. For example, the recombination of methyl radicals in R2, R8 and R11 generates ethane. The subsequent H-atom abstraction and dehydrogen of ethane would produce ethylene. Compared with the propyl radical in MB pyrolysis, the presence of C=C double bond leads to resonant stabilised propenyl radical in MC decomposition via R10. In this study, a site-specific method as shown in Figure 3.8 (b) is proposed by colouring and labelling each C-atom so as to track and quantify the carbon from different sites to nascent soot. C-atoms in all carbonyl structures contribute almost zero to nascent soot as C=O seems to never be broken even at high temperature while the C-atoms connecting with the ester O-atoms contribute the second to last but still considerably. The C=C double bond in MC has the highest sooting tendency, whereas the site sooting tendency of alkyl C-atoms is effectively the same in MB, EP and MC. From a combined consideration of the oxygenated product trend and carbon site contribution to soot in Figure 3.8, it can be seen that the influence of unsaturation on sooting behaviour is more prominent than isomerisation regarding the fuel molecular structures.

3.3 Soot mitigation mechanism of oxygenated fuel additive

3.3.1 Modelling setup

A recently proposed 5-components diesel surrogate fuel by Qian et al. (2018) is employed to simulate diesel soot formation, which can accurately reproduce gaseous emissions of the target diesel fuel in the actual engine combustion conditions. The surrogate fuel shown in Table 3.4 includes 21.6% *n*-Hexadecane (*n*-HXD, $C_{16}H_{34}$), 15.5% *n*-Octadecane (*n*-OTD, $C_{18}H_{38}$), 26.0% heptamethylnonane (HMN, $C_{16}H_{34}$), 20.7% 1-methylnaphthalene (1-MNT, $C_{11}H_{10}$) and 16.2% decalin (DCA, $C_{10}H_{18}$) by mol. Five representative oxygenates, i.e, dimethyl carbonate (DMC, $C_3H_6O_3$), cyclopentanone (CPO, C_5H_8O), methyl butanoate (MB, $C_5H_{10}O_2$), dimethoxymethane (DMM, $C_3H_8O_2$) and ethanol (C_2H_6O) shown in Figure 3.9 are selected to blend with diesel surrogates so as to evaluate the effects of ketones, esters, ethers and alcohols on soot precursor mitigation.

The reactive systems studied are shown in Table 3.5. System 1 is established as a baseline containing 149 pure diesel surrogate molecules with 150 oxygen molecules to model the

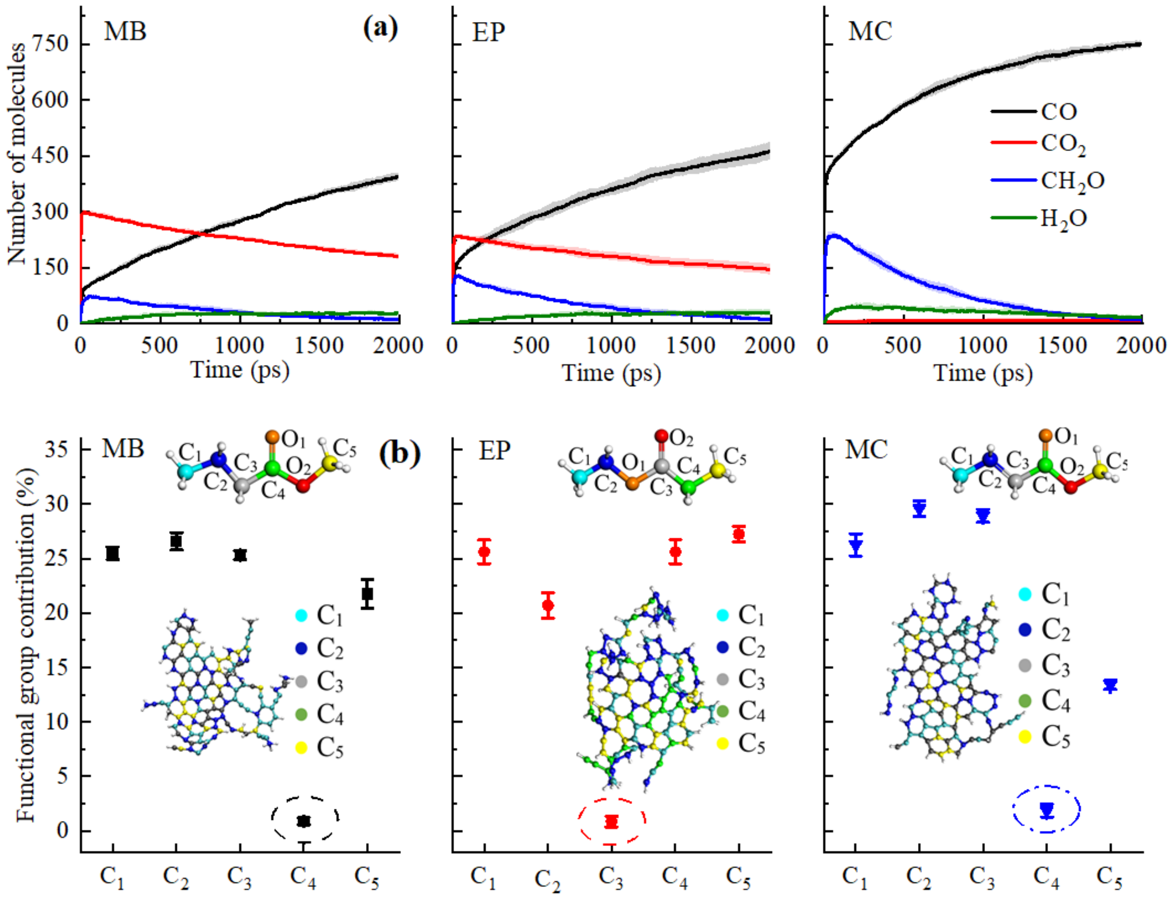

Fig. 3.8 (a) Time evolution of the main oxygenated products during the pyrolysis of MB, EP and MC, where the shaded regions indicate the statistical uncertainty determined by the standard deviation; (b) contributions of different functional groups to nascent soot after 2ns simulation, where carbon contribution to the largest molecules is displayed.

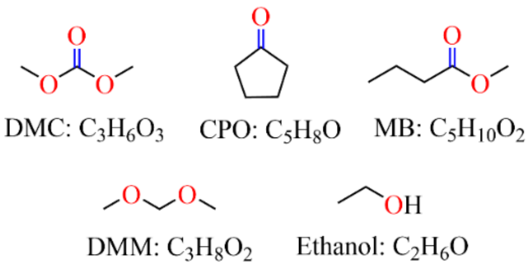
DMC: $C_3H_6O_3$
CPO: C_5H_8O
MB: $C_5H_{10}O_2$
DMM: $C_3H_8O_2$
Ethanol: C_2H_6O
O
OH

Fig. 3.9 Molecular structures and chemical formulas of the oxygenated fuel additives.

Table 3.4 Molecular structures and the chemical formulas of diesel surrogate fuel.

Common Name	Molecular Formula	Molecular Structure	M (g/mol)	x (mol %)
n-Hexadecane	*n*-HXD $C_{16}H_{34}$	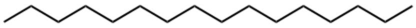	226.44	21.6
n-Octadecane	*n*-OTD $C_{18}H_{38}$	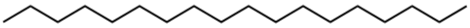	254.49	15.5
2,2,4,4,6,8,8-Heptamethylnonan	HMN $C_{16}H_{34}$	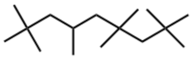	226.44	26.0
trans-Decalin	DCA $C_{10}H_{18}$	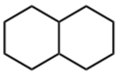	138.25	16.2
1-Methyl Naphthalene	1-MNT $C_{11}H_{10}$	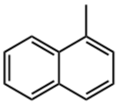	142.20	20.7

Table 3.5 Number of the molecules of diesel surrogate fuel and oxygenated additives in the simulation box.

System No.	*n*-HXD	HMN	1-MNT	Decalin	*n*-OTD	Additives
1	32	39	31	24	23	O_2: 150
2	27	34	27	21	20	DMC: 100
3	9	12	9	7	7	CPO: 300
4	25	31	24	19	18	DMM: 150
5	21	25	20	16	15	MB: 150
6	23	28	22	17	17	Ethanol: 300

fuel-rich combustion. To study the effect of fuel additives, oxygenate fuel molecules are doped into the simulation boxes containing the diesel model. A rule is adopted in which systems 2-6 are setup by adjusting the number of diesel molecules in the box so that these systems have approximately the same carbon and oxygen numbers as system 1. This could highlight the influence of the molecular structure of the additive instead of the amount of oxygen. The density of system 1 is set to be 0.1 $g \cdot cm^{-3}$, and the edge length of the cubic box is 82.5 Å. The size of the simulation boxes in systems 2-6 is adjusted accordingly to have the same density as system 1.

3.3.2 Incipient soot formation mechanism of fuel combustion

The time evolutions of the regular products of diesel combustion, e.g., CO, CO_2, H_2O and formaldehyde (CH_2O) are shown in Figure 3.10 (a), followed by those of the typical C1-C3 intermediates like methyl radical (CH_2), ethylene (C_2H_4), ethyne (C_2H_2), vinyl (C_2H_3) and propargyl (C_3H_3) displayed in Figure 3.10 (b). Visualisation and identification of the representative molecular structures are captured and presented in Figure 3.11. In the fuel-rich combustion, O_2 is consumed at an extremely high rate at the initial stage accompanying with the acute increase of CO molecules. The formation of CO_2 occurs around 1.8 ps later than CO, because of its dependence on the production of C1 species like CO, HCO, and CH_2O. Only around 6 CO_2 molecules are produced, rather small volume compared with CO. The amount of CO_2 molecules remained almost constant in this period, manifesting that no CO has been further converted into CO_2. H_2O production takes place earlier than CO_2 with appreciable quantity. Formaldehyde molecule is also found to be an important intermediate and it reaches a maximum number of 92 at 29.1 ps. The existence of formaldehyde peak is the feature of low-temperature combustion of large alkanes. At temperature as high as 3000 K it is unstable and would decompose to CO easily which explains the steady increase of CO at the late stage.

In Figure 3.10 (b), the number of ethylene decreases immediately after reaching its maxima at around 80.8 ps while the peaks of ethyne and vinyl radical are relatively inconspicuous. Ethyne, vinyl radical and propargyl radical can persist the whole process whereas methyl radical and ethylene deplete almost completely at the late stage. This is mainly because that paraffins like n-HXD and n-OTD accounting for the largest proportion of the diesel composition, would experience H-abstraction and consecutive unimolecular C-C fission to produce alkyl radical like C_4H_9, C_7H_{15}, C_8H_{17} and $C_{13}H_{27}$, etc., releasing ethylene at the same time (Chen et al., 2019). A series of β-scission reactions of these C4-C13 fragments take place subsequently to form alkenes. HMN tends to produce more of the large alkenes as it is more likely to dissociate to alkyl radicals with substitution at the β C-atom. Ethylene mainly reacts into ethyne and vinyl radical while propargyl radical is from the dehydrogen of propene via a serial of H-abstractions with H-atom as the primary abstractor (McEnally et al., 2006). Propargyl radical is a kind of resonantly-stabilized radicals (RSRs) which would undergo decomposition and oxidation at much lower rates than nonresonant radicals do. These C2 and C3 unsaturated hydrocarbons play crucial roles in cyclopentadienyl and benzene formation whilst the specific pathways vary considerably. Another observation is the large aliphatics repolymerized by a wide variety of these precursors and alkenes after the depletion of the initial diesel alkanes, and the relevant molecular structures are captured and illustrated in Figure 3.11 (d).

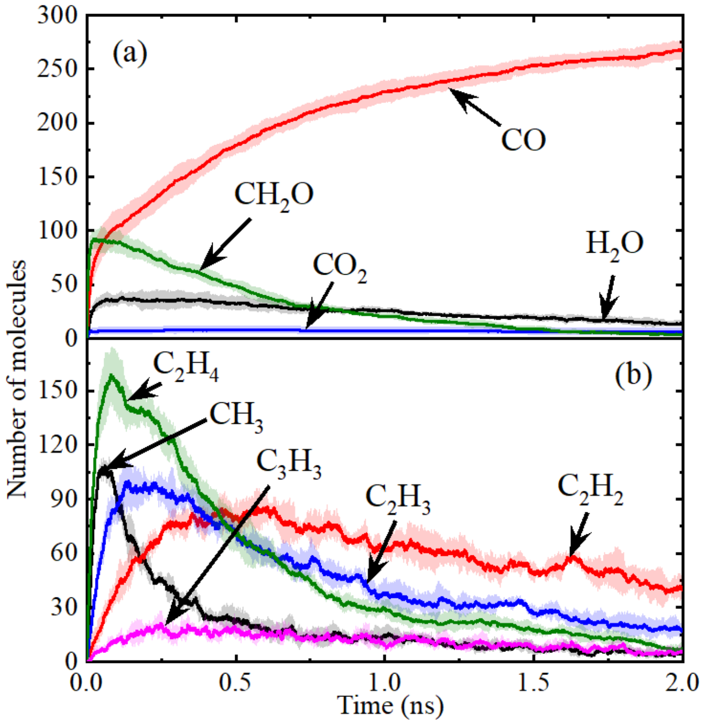

Fig. 3.10 Time evolutions of major intermediates and products in diesel combustion, where the shaded area indicates the average standard deviations of five repeated simulations.

Hydrocarbon combustion is kicked off either by unimolecular C-C bond dissociation or the oxidative reaction by abstraction of a hydrogen free radical from the substrate. In this study, the earliest reaction of 1-MNT detected is the H-abstraction reaction by O_2 through cleavage of the C-H bond in methyl group at 0.3 ps, producing hydroxyl radical and the corresponding 1-naphthylmethyl radical. This is ascribed to the relatively low dissociation energy of the methyl C-H bond, 85.1 Kcal/mol (Kalpathy et al., 2015). The aromatics is generally stable and can survive a long time to ring-opening reactions. In this period, it is possible to break the methyl-aryl C-C bond and the aryl C-H bond. These decomposition reactions would favour the formation of 1-MNT radical and naphthalene radical. Moreover, 2-methylindene radical with a pentagonal ring is also observed. The early formation of these aryl groups, with molecular structures and highlighted radical sites displayed in Figure 3.12 (a), was also observed experimentally by Shaddix et al. (1997). They are regarded as potential building blocks with high propensity to produce nascent soot by reacting with additional benzenoid rings. Thus, soot precursor formation mechanism is closely correlated with the fuel molecular structures, particularly the large hydrocarbons existing in practical fuels which can decompose in a wide range of pathways.

The initial mass growth is found to be triggered by the addition of C_2H_2 or C_2H_3 to cyclopentadienyl and benzene. The newly generated RSRs are constructed by five-, six- or

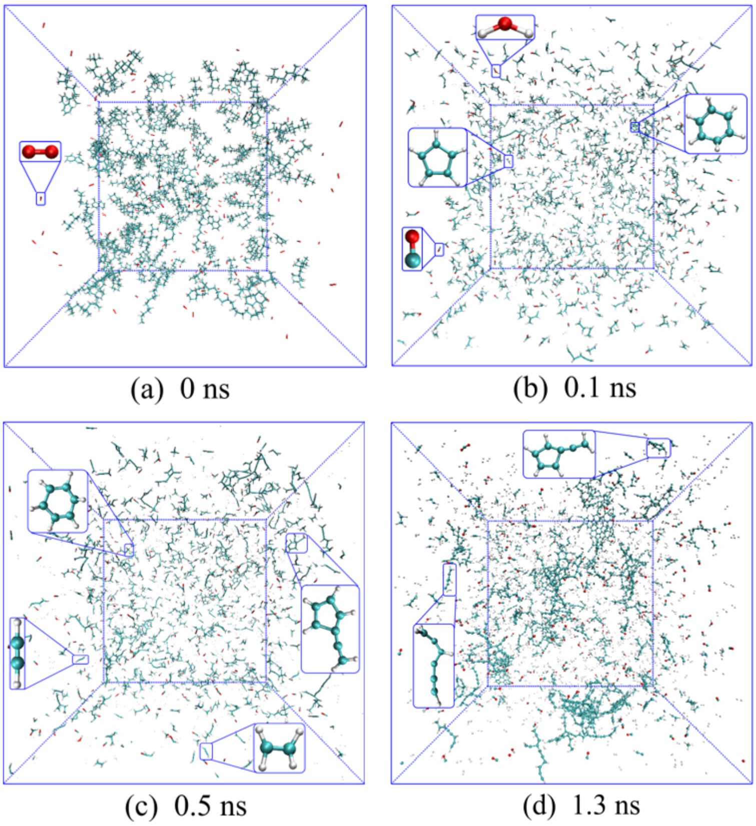
(a) 0 ns
(b) 0.1 ns
(c) 0.5 ns
(d) 1.3 ns

Fig. 3.11 Time evolutions of incipient soot formation of diesel combustion, where C, H and O atoms are represented in cyan, silver and red.

seven-membered carbon rings substituted with unsaturated aliphatics, as shown in Figure 3.11 (c) and Figure 3.12 (b). More recently, the aliphatic-substituted aromatics in nascent soot particles were observed and visualized directly by high-resolution atomic force microscopy (Schulz et al., 2019). The small aliphatics would connect the RSRs by chemical covalent bond, dimerizing into cross-linked three-dimensional AALH structures as shown in Figure 3.12 (d).

The unstable AALH structures further evolve into a peri-condensed plane through rearrangement and ring closure (Keller et al., 2019), leading to aromatic peri-condensed polycyclic hydrocarbon structures at 1.5 ns. Structure of ADLH is also observed at around 1.6 ns. In this period, addition reactions also take place in the hydrocarbon flame, generating the elongated aliphatic side chains, e.g., C8 alkene in Figure 3.12 (e). The flat size of incipient soot can have a length of 6.03 nm as shown in Figure 3.12 (f). At high temperature, it would undergo cyclization and condensation, resulting in branched fullerene/ellipsoid structure. The morphology of the nascent soot at 1.6 ns is an amorphous structure, around 3.7 nm in diameter and 998 amu in mass, rich in aliphatics, with a C:H ratio of 6-10. The ratio of C-H groups presented in aliphatics to that in aromatic rings is around 1.2 at 1.6 ns and 2.3 at 2 ns, respectively. In addition, it can be assumed that aliphatic-substituted aromatics can also act as building blocks to stack into the outer shell when the temperature becomes somewhat lower. RSR moieties on shell surfaces could provide sites for small hydrocarbons in flames to attach. This pathway could potentially explain recent experimental results showing that the soot shell surface is abundant with alkyl or alkenyl functionalities in the range of C2-C8 (Wang, 2011).

3.3.3 Soot formation during diesel combustion with blending of oxygenates

The blending ratio was configured properly to unify the oxygen contents and the overall carbon quantity to highlight the effect of oxygenate molecular structure on soot formation process. Some insights to the soot inception of diesel with oxygenates can be gained from the detailed morphological development comparison, as shown in Figure 3.13 at the time instants of 1.2 ns and 2 ns, respectively. The C-atoms contributed from the oxygenates are quantified and highlighted in the nascent soot.

From Figure 3.13, both morphology of the nascent soot and the number of C-atoms from oxygenates vary in different cases, among which C-atoms from DMC only account for 5.9% (calculated from 18/304) and 5.7% (from 46/814) at 1.2 ns and 2 ns, respectively as shown in Figure 3.13 (a), while almost 73.8% and 67.0% of the C-atoms are from CPO at 1.2 ns and 2 ns as shown in Figure 3.13 (b). This is mainly attributed to the initial configuration which was determined by the C:O ratio of the oxygenate molecular structures. It is more

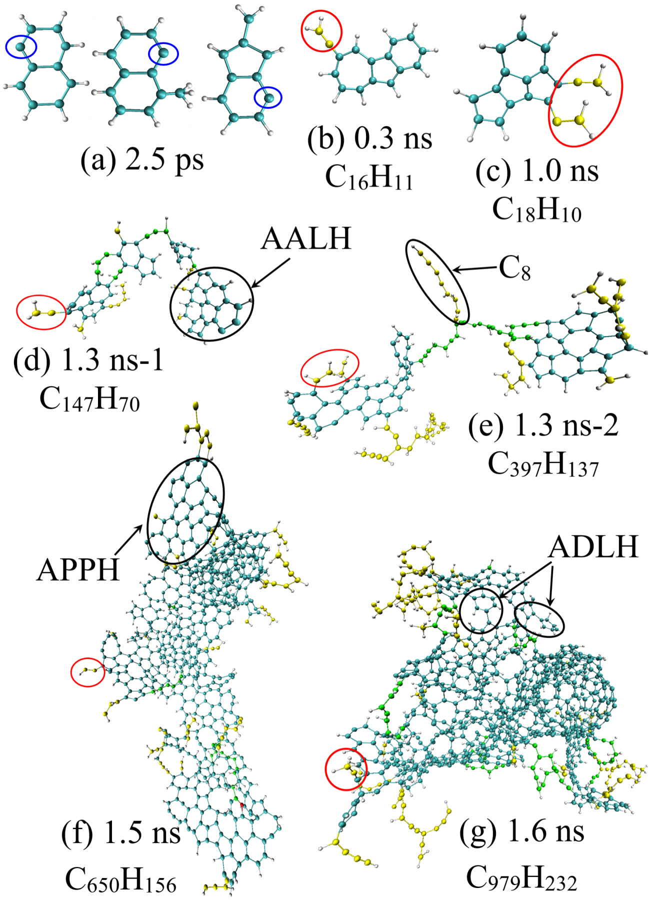
(a) 2.5 ps

(b) 0.3 ns $C_{16}H_{11}$

(c) 1.0 ns $C_{18}H_{10}$

(d) 1.3 ns-1 $C_{147}H_{70}$

(e) 1.3 ns-2 $C_{397}H_{137}$

(f) 1.5 ns $C_{650}H_{156}$

(g) 1.6 ns $C_{979}H_{232}$

Fig. 3.12 Snapshots of the enlarged representative carbonaceous nanoparticle morphology during diesel combustion, where aliphatic side chains are coloured in yellow with direct C_2H_2 or C_2H_3 addition highlighted with red ellipse while aliphatic links between aromatic moieties in nascent soot are highlighted in green.

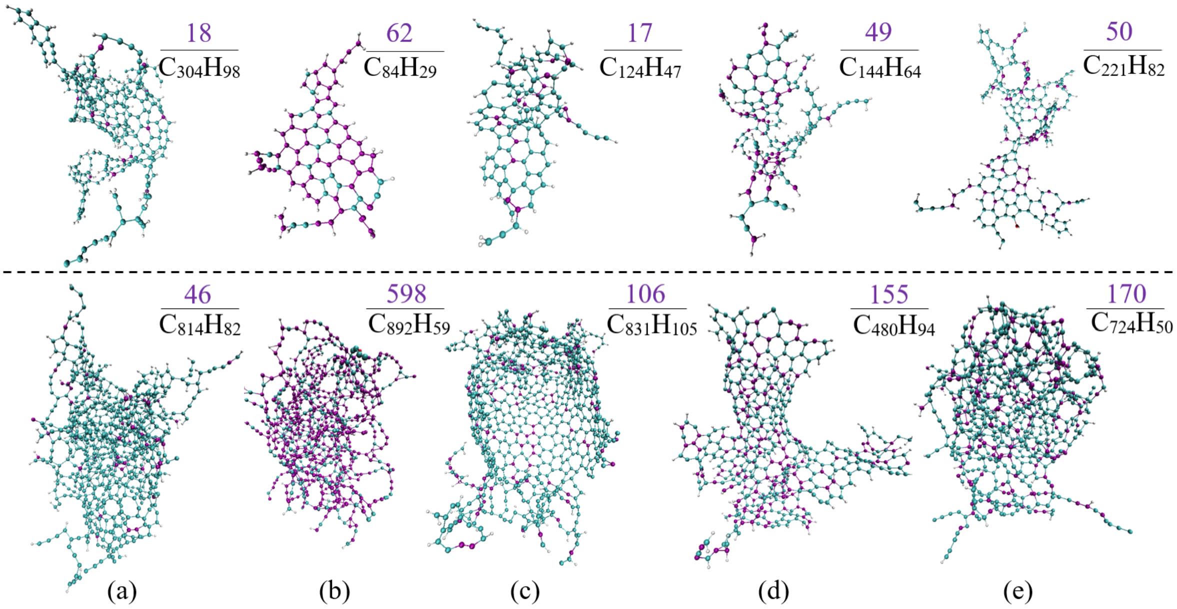

Fig. 3.13 Morphological snapshots of nascent soot at 1.2 ns (above the dashed line) and final soot particles at 2 ns (below the dashed line) in diesel combustion with various additives, from left to right, (a): DMC, (b): CPO, (c): DMM, (d): MB and (e): ethanol, where the numbers of carbon atoms contributed from oxygenated fuel additives are given in purple.

meaningful to compare the C-atom ratio originated from oxygenated additives in nascent soot with the corresponding initial stoichiometric configuration to evaluate the sooting propensity of oxygenates. For the cases of diesel blending with DMC and DMM, the C-atom contribution ratios at 2 ns are 5.7% and 12.8% respectively, both of which are much smaller than the C-atom ratio between oxygenates and fuel mixtures in the initial box, 14.0% and 21.2% respectively. This means that DMC and DMM are much less likely to form the nascent soot compared with diesel surrogate molecules.

The ratios for cases blending with CPO and ethanol are 67.0% and 23.5% in nascent soot, both of which are lower but at almost the same level as the initial ratio, 70.4% and 28.1%, respectively. It is thus indicated that the CPO and ethanol have similar sooting propensities to diesel. This also occurs for fuel mixtures blending with MB, 35.1% of the C-atoms are from MB in the initial box but the contribution is 32.3% in the final nascent soot. These observations can be ascribed to the consecutive C-C bond in the molecular structures of CPO, MB and ethanol which would lead to soot formation. However, C-atoms in DMC and DMM are separate and each of them is bound to a different O-atom, avoiding significant levels of the products such as ethylene, acetylene or unsaturated radicals which are known to be PAH precursors.

3.3.4 Quantification of oxygenated effectiveness in soot mitigation

The effectiveness of oxygenates on soot suppression is not well understood and is drawing increasing interests (Farooq et al., 2012) (Sun et al., 2017a) (Sun et al., 2019). In the kinetics modelling performed by Westbrook et al. (2006) for premixed fuel-rich combustion of *n*-Heptane and oxygenate blends, it was observed that all oxygenates tested reduced the emission of soot precursors, but with different effectiveness. In the previous experimental study by Farooq et al. (2012), the effectiveness was represented by the number of C-atoms captured by CO and CO_2. The time histories of CO and CO_2 for thermal decomposition of oxygenates blending with diesel are presented in Figure 3.14. The capability of ReaxFF on capturing chemical reaction pathways and predicting Arrhenius parameters quantitatively has been validated extensively against experiments and continuum methods (Ashraf and van Duin, 2017) (Ashraf et al., 2019). It is a common practice to normalize the absolute rate constants using the slowest reaction obtained from ReaxFF simulation, that is, the rate constant of the slowest reaction is set to be 1 (Chen et al., 2018b). The thermal pyrolysis pathways of the oxygenates and the relative kinetics rates are summarized in Table 3.6.

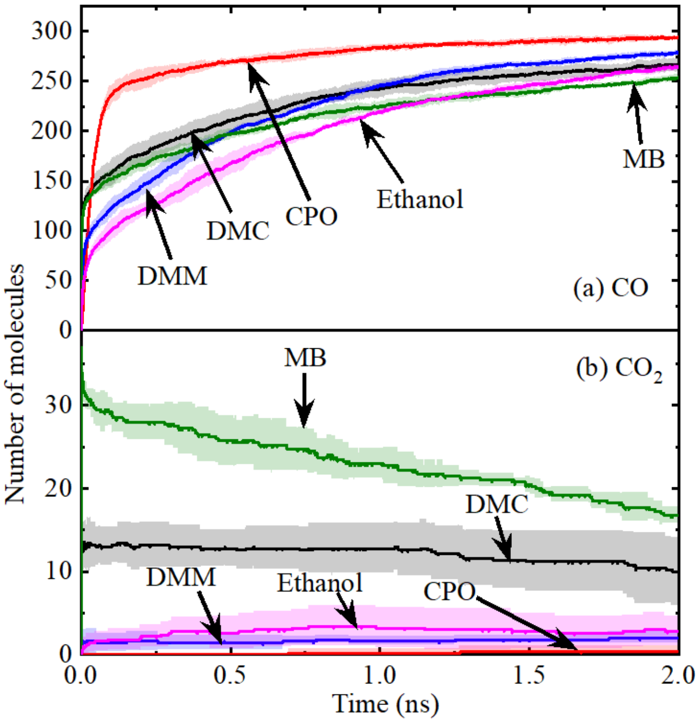

Fig. 3.14 Time evolutions of (a) CO and (b) CO_2 for diesel blending with various additives at 3000 K.

Among the additives, CPO shows the best performance with 294 oxygen atoms used to fix C-atoms while MB has the lowest quantity. This is because the scission of the C=O double bonds in CPO carbonyl group hardly occurs even at 3000 K, and double bonds maintain all the way to CO formation through the unimolecular decomposition, i.e., R3* with rapid kinetic rate. This also explains the steep increase of CO in the initial stage of Figure 3.14 (a) before the turning point at around 0.12 ns. In contrast, MB has the lowest plateau value for CO but with a fair amount of CO_2 as demonstrated in Figure 3.14 (b), indicating that CO_2 moieties in esters tend to result in the direct formation of CO_2 molecules considerably. In this way, two O-atoms together captured only one C-atom from species pool. The oxygen initially present in esters is therefore less effective. As a carbonate ester, the early formation of CO_2 was also observed in DMC. Specifically, pyrolysis of DMC and MB by R1 and R11 respectively, can produce a considerable amount of methoxycarbonyl radical, i.e., $CH_3O(C^{\cdot}O)$, which has two competitive decomposition pathways to produce CO_2 or CO + CH_3O. However, both $CH_3O(CO)O^{\cdot}$ in DMC by R2 and $CH_3(CH_2)(CO)O^{\cdot}$ in MB by R10 are more likely to produce CO_2 directly via β-scission (Farooq et al., 2012).

Unimolecular decomposition plays a leading role in pyrolysis of oxygenates while H-abstraction by H-atom, methoxy and hydroxyl radical also accounts for a certain proportion in the consumption of oxygenates. Relevant pathways in DMM and ethanol produce H2O which affects the effectiveness of O-atom on combining C-atoms to some extent and should not be ignored. Form Table 3.6, it can be summarized that although oxygenates decompose primarily into oxygenated intermediates, they also produce methyl, ethyl, propyl and some biradicals, which in turn are likely to favour the soot precursor production. For example, three of the MB pyrolysis pathways produce the alkyl radicals whereas in the case of DMC and DMM, only one methyl radical formation pathway is observed. In this manner, the consumption patterns of the additive can be expressed in two aspects, removing C-atoms from the soot precursor pool via combination with O-atoms in functional groups while contributing to soot precursor formation due to the alkyl chains simultaneously.

3.4 Discussion and conclusion

A series of reactive molecular dynamics simulation was performed to provide molecular details of the nascent soot formed from the utilisation of multicomponent diesel/biodiesel blends and diesel/oxygenated additives. Effects of each unique surrogate fuel molecule structure on sooting behaviour were thereupon investigated particularly the functional groups in biofuels on soot mitigation. The ReaxFF force field with CHO2016 parameters identified the complex sequence of soot formation pathways involving the fuel pyrolysis, formation of unsaturated precursors, PAH growth, and gas-to-solid transition of the nascent soot, together with the predictive core-shell model of the soot nuclei.

Table 3.6 The observed primary chemical reaction and relative kinetics rate of oxygenates in thermal decomposition, where the reaction leading to the direct formation of CO are marked with asterisk, the products of alkyl radicals are highlighted in blue, species facilitating the bimolecular decomposition are highlighted in green.

ID	Reaction	Relative rate
R1	$\mathrm{DMC} \rightarrow \mathrm{CH_3O^{\bullet} + CH_3O(C^{\bullet}O)}$	(1.01±0.09)E+04
R2	$\mathrm{DMC} \rightarrow \mathrm{CH_3^{\bullet} + CH_3O(CO)O^{\bullet}}$	(2.44±0.14)E+02
R3*	$\mathrm{CPO} \rightarrow \mathrm{CO + CH_2^{\bullet}\ (CH_2)_2CH_2^{\bullet}}$	(7.99±0.73)E+03
R4	$\mathrm{CPO} \rightarrow \mathrm{CH_2^{\bullet}CH_2^{\bullet} + (C^{\bullet}O)CH_2CH_2^{\bullet}}$	(1.84±0.12)E+03
R5	$\mathrm{CPO} \rightarrow \mathrm{CH_2^{\bullet}CH_2CH_2^{\bullet} + (C^{\bullet}O)CH_2^{\bullet}}$	(4.66±0.24)E+02
R6	$\mathrm{DMM} \rightarrow \mathrm{CH_3^{\bullet} + CH_3OCH_2O^{\bullet}}$	(5.22±0.31)E+03
R7	$\mathrm{DMM + HO^{\bullet} \rightarrow H_2O + CH_2^{\bullet}OCH_2OCH_3}$	(1.27±0.16)E+03
R8	$\mathrm{DMM + CH_3O^{\bullet} \rightarrow CH_3OCH^{\bullet}OCH_3 + HOCH_3}$	(2.50±0.17)E+01
R9	$\mathrm{MB} \rightarrow \mathrm{CH_3O^{\bullet} + CH_3(CH_2)_2(C^{\bullet}O)}$	(1.78±0.15)E+03
R10	$\mathrm{MB} \rightarrow \mathrm{CH_3^{\bullet} + CH_3(CH_2)_2(CO)O^{\bullet}}$	(5.00±0.27)E+02
R11	$\mathrm{MB} \rightarrow \mathrm{CH_3CH_2CH_2^{\bullet} + CH_3O(C^{\bullet}O)}$	(1.54±0.11)E+02
R12	$\mathrm{MB} \rightarrow \mathrm{CH_3O(CO)CH_2^{\bullet} + CH_3CH_2^{\bullet}}$	(2.51±0.15)E+01
R13	$\mathrm{MB + H^{\bullet} \rightarrow CH_3CH_2CH^{\bullet}(CO)OCH_3 + H_2}$	(3.77±0.20)E+00
R14	$\mathrm{Ethanol} \rightarrow \mathrm{{}^{\bullet}OH + CH_3CH_2^{\bullet}}$	(4.71±0.41)E+01
R15	$\mathrm{Ethanol} \rightarrow \mathrm{CH_2^{\bullet}OH + CH_3^{\bullet}}$	(9.39±0.51)E+00
R16	$\mathrm{Ethanol + {}^{\bullet}OH \rightarrow H_2O + CH_3CH_2O^{\bullet}}$	(0.99±0.09)E+00
R17	$\mathrm{Ethanol} \rightarrow \mathrm{{}^{\bullet}H + CH_2^{\bullet}CH_2OH}$	(4.02±0.23)E+00

The time history of the carbon rings in reactive systems revealed that PAH growth by chemistry is substantially more complicated than the previous model described, as addition of gaseous ethynes to radical sites and the subsequent ring closures forming peri-condensed aromatics with primarily fused six-membered carbon rings. Specifically, five-membered rings are also identified to be prevalent and even dominant among PAH species induced by the radical chain reaction of the RSRs. The variety of PAHs increased dramatically with size, forming typical intermediate structures like ADLH, AALH and PCAH. The curved semi-condensed oligomers of aromatics of high molecular mass served as the key particle seeds to achieve the soot inception transition of gas to solid. Given the frequent appearance of aliphatics in reactive systems, the formation of carbonaceous particles would involve the attachment and elongation of aliphatic side chains both in the amorphous core and outer shell surface which helped to explain the experimental aliphatic signals.

Diesel and biodiesel show distinct nascent soot morphologies due to their different fuel compositions. The nascent soot of diesel was aromatics dominated and more organised than that of biodiesel which contains a considerable amount of aliphatics. ReaxFF MD-based simulation was extended to quantify the sooting tendency of the fuel mixtures by adopting the YSIs. It was observed that the YSI of diesel is about 15.67% higher than biodiesel. As the consequence of the methyl ester functional groups in biodiesel, the underlying soot reduction mechanism was elucidated by the early formation of oxygenated products, e.g., CO and CO_2 during fuel thermal decomposition, which was also confirmed by the proposed site specific method that the C-atoms in carbonyl contributed almost zero to nascent soot.

Effects of oxygenate molecular structures on soot formation are quantified and reflected in two aspects: removing C-atoms from the soot precursor pool through combination with the O-atoms, and contributing to soot precursor formation due to the existence of C-C bonds simultaneously. Regarding the soot propensity, C-atoms from DMC and DMM are less likely than diesel to appear in incipient soot particles while MB, CPO and ethanol show similar tendencies to diesel. C=O double bond in carbonyl group is sufficiently stable to survive in the high-temperature condition and in favour of the formation of CO while the production of CO_2 in DMC and MB is mainly due to C-O fission between ester moiety and methyl group and the subsequent β-scission. The effect of oxygenated additives on diesel blends sooting propensity should be the combined factors of oxygenated moiety and the aliphatic counterparts.

Chapter 4

Transport property prediction of FAMEs in high pressure conditions

This Chapter presents equilibrium molecular dynamics (EMD) simulation results of FAMEs, including transport property prediction, evaluation of the force field which plays a key role in MD simulations, together with analyses of the dynamics of molecular structure. The formulas of Green-Kubo (GK) and Einstein method on calculation of viscosity and diffusivity are introduced in Chapter 4.1. The applicability of Stokes-Einstein (SE) relation and Stokes-Einstein-Debye (SED) relation are studied. The capability of force fields on property prediction is evaluated in Chapter 4.2. The mechanism behind the breakdown of SE relation due to high pressure induced solidification is revealed in Chapter 4.3. The focus of Chapter 4.4 is on a new predictive method that can be used to estimate experimental viscosity at high temperature and high pressure conditions provided that Stokes-Einstein relation applies.

4.1 Green-Kubo and Einstein method

The transport property (χ) can be calculated from an equilibrium MD simulation, via correlation with specific variable ζ by Einstein equation or its time derivation $\dot{\zeta}$ by the Green-Kubo (GK) equation (Maginn et al., 2018). In the GK method, transport property is related to the running integral of the autocorrelation function (ACF) for $\dot{\zeta}(t)$:

$$\chi = \int_0^\infty \left\langle \dot{\zeta}\left(t_0\right) \dot{\zeta}\left(t_0+t\right) \right\rangle_{t_0} dt \tag{4.1}$$

An equivalent expression for χ is known as the Einstein formula via mean-square of variable ζ:

$$\chi = \lim_{t\to\infty} \frac{\left\langle \left(\zeta\left(t_0\right) - \zeta\left(t_0+t\right)\right)^2 \right\rangle_{t_0}}{2t} = \frac{1}{2} \lim_{t\to\infty} \frac{d}{dt} \left\langle \left(\zeta\left(t_0\right) - \zeta\left(t_0+t\right)\right)^2 \right\rangle_{t_0} \tag{4.2}$$

Although the simulation setup and computational cost are essentially the same for these two approaches, in practice one method is often preferred depending on the properties being estimated. For viscosity, the GK method is related to the autocorrelation function of pressure tensor (PACF):

$$\eta = \frac{V}{k_B T} \int_0^\infty \left(\langle P_{\alpha\beta}(t) P_{\alpha\beta}(0) \rangle\right) dt \tag{4.3}$$

where V is volume, k_B is Boltzmann constant, T is temperature, $P_{\alpha\beta}$ represents the $\alpha\beta$ components of the pressure tensor, α, β is any two of the x, y or z Cartesian coordinates. Shear viscosity is a collective property as the GK formulation consolidates the contributions of all the atoms into a single autocorrelation function. To improve the convergence, it is common to include multiple terms from the pressure tensor:

$$\eta = \frac{V}{10 k_B T} \int_0^\infty \left(\left\langle \sum_{\alpha\beta} P_{\alpha\beta}(t) P_{\alpha\beta}(0) \right\rangle \right) dt \tag{4.4}$$

where the factor of 10 results from assigning weighting factor of 3/3 and 4/3 for each of the six off-diagonal ($\alpha \neq \beta$) terms and the three diagonal terms (Mondello and Grest, 1997) (It should be noted that the ACFs of the three off-diagonal elements of the pressure tensor are expected to be equivalent/dependent, attributed to the isotropy of the system). The pressure tensor is calculated from the following equation:

$$P_{\alpha\beta}(t) = \frac{1}{V} \left(\sum_{i=1}^{N} \mathrm{m}_i v_{i_\alpha} v_{i_\beta} + \sum_{i=1}^{N-1} \sum_{j>1}^{N} r_{ij_\alpha} f_{ij_\beta} \right) \tag{4.5}$$

where m_i is the mass of a molecule i, N is the number of molecules, v_{i_α} and v_{i_β} are the velocity components of a molecule i in the α and β-directions, and r and f represent the displacement and force between two molecules, respectively.

Einstein equation connects the self-diffusivity to the particle displacement and can average over the number of the particles. Diffusion coefficient of particles in three dimensional systems is calculated using:

$$D_{\mathrm{self}} = \lim_{t\to\infty} \frac{1}{6 N_i t} \left\langle \sum_{j=1}^{N_i} \left(r_{j,i}(t) - r_{j,i}(0)\right)^2 \right\rangle \tag{4.6}$$

where $r_{j,i}(t)$ is the position of the j^{th} molecule of species i at time t, and N_i is the number of molecules of species i in the system. The particle mean square displacement (MSD) grows linearly with the time for sufficient large value of t (Pranami and Lamm, 2015). In homogeneous system, D_{xx}=D_{yy}=D_{zz} (Maginn et al., 2018).

Besides the translational diffusivity, molecular motions also lead to changes in molecular orientations. Rotational motion and reorientation of molecules can be characterised by an end-to-end vector, i.e., $\boldsymbol{R}$ defined by the coordinates of the terminal carbon atoms. Relaxation time is determined by the ACF of angle θ between the end-to-end vector of a given molecule:

$$t_{Rot}(t) = \int_0^{\infty} (\langle P_n(\cos\angle(\boldsymbol{R}(t),\boldsymbol{R}(0))\rangle)\, dt \tag{4.7}$$

where P_n is n^{th} order Legendre polynomial.

4.1.1 Modelling system setup

The physical properties of alkanes have been studied extensively in past decades using the EMD simulation (Mondello and Grest, 1997) (Ungerer et al., 2007) (Yang et al., 2021)]. However, there are few MD studies on FAMEs which contain the ester function group. The molecular structure of two typical FAMEs of different chain lengths, i.e., methyl decanoate (MDC) and methyl myristate (MMR) are selected in this study. Changes in molecular structure are reflected in changes in macroscopic properties of materials. Basic physical properties of molecular mass, fusion temperature and boiling temperature of corresponding *n*-alkanes and branched alkanes are listed in Table 4.1 for comparison. FAMEs and *n*-alkanes with the same chain length have approximated fusion temperature, which is 20% higher than that of branched alkanes. Boiling point of FAMEs is higher than that of normal alkane and branched alkanes. Both FAMEs and alkanes with longer chain length have higher fusion temperature and boiling temperature. Moreover, a wide range of properties of FAMEs such as density, viscosity, oxidative stability etc., show strong correlation with molecular structure configurations like the chain length, degree of unsaturation and the position of double bonds (Gopinath et al., 2015).

Table 4.1 Properties of FAMEs and alkanes for comparison: molecular mass (m); phase change data of fusion or melting temperature (T_m), boiling temperature (T_b), critical temperature (T_c) and critical pressure (P_c) (NIST, 2021) (do Carmo et al., 2015).

FAMEs and alkanes	M (g/mol)	T_m (K)	T_b (K)	T_c (K)	P_c (MPa)
Methyl Decanoate (MDC: $C_{11}H_{22}O_2$)	186.29	260.40	497.20	689.05	1.97
n-Dodecane (DDC: $C_{12}H_{26}$)	170.33	263.50	489.00	658.10	1.82
2,2,4,6,6-pentamethylheptane (PMH: $C_{12}H_{26}$)	170.33	206.00	451.00	-	-
n-Decane (DCN: $C_{10}H_{22}$)	142.29	245.25	447.27	617.70	2.10
n-Octane (OTN: C_8H_{18})	114.23	216.60	398.77	569.32	2.50
Methyl Myristate (MMR: $C_{15}H_{30}O_2$)	242.40	291.24	596.20	747.00 [8]	1.57 [8]
n-Hexadecane (HXD: $C_{16}H_{34}$)	226.44	291.00	554.00	722.00	1.40
2,2,4,4,6,8,8-Heptamethylnonane (HMN: $C_{16}H_{34}$)	226.44	-	513.20	692.00	1.57

Three different force fields, i.e., TraPPE (Martin and Siepmann, 1998), CHARMM (Vanommeslaeghe et al., 2010) and OPLS (Jorgensen et al., 1996) are selected to predict the transport properties of FAMEs. The OPLS all-atom (AA) force field was parameterized for simulation of organic molecules and peptides. The pair potential for atoms separated by three bonds or more within a molecule, i.e., 1-4 interactions are scaled down by the "fudge factor" of 0.5. In this study, optimised OPLS parameters for esters and long alkanes (LOPLS) are adopted (Siu et al., 2012) (Pluhackova et al., 2015). CHARMM is an all-atom force field which is widely used in biochemistry applications, in particular simulation of lipid membranes for which dedicated membrane builder tools are available. Force field parameters of CHARMM36 (Huang and MacKerell Jr, 2013) are used and topology files are generated from CHARMM General Force Field (CGenFF) (Vanommeslaeghe et al., 2010). TraPPE-UA is a united-atom (UA) potential, which is computationally more efficient than LOPLS-AA and CHARMM-AA. In TraPPE force field, all bond length is fixed, and intramolecular nonbonded 1-4 interactions are already considered in torsion energy. The parameters of ester function group are adopted from the work of Kamath et al. (2006).

All EMD simulations are performed in the GROningen MAchine for Chemical Simulations (GROMACS) molecular simulation package (Van Der Spoel et al., 2005). The initial boxes are constructed by distributing molecules randomly in a relative larger box to avoid overlap as shown in Figure 4.1 (a). MD systems are relaxed via steepest descent energy minimization to ensure the system has no steric clashes or inappropriate geometry. Minimization is converged when the maximum force on any atom is less than 1000 KJ$\cdot$mol^{-1}. Equilibration run is performed for 500 ps in NPT ensemble to compress the system to the desired pressure and density as shown in Figure 4.1 (b). The Parrinello-Rahman barostat is used for pressure coupling with the compressibility set as 4.5e-5$\cdot$bar^{-1}. Temperature is coupled using velocity rescaling method. Production run of 0.5-100 ns in NVT ensemble is then followed for data collection.

The initial velocity of molecule is generated according to Maxwell distribution of temperature with random seed. Neighbour searching was performed using the Verlet scheme, with a list created every one step using a length of 1.4 nm. The cut-off distance of LJ potential is 1.4 nm. The long-range electrostatic interactions were calculated using the fourth order particle-mesh Ewald (PME) algorithm (Darden et al., 1993) with a cut-off distance of 1.4 nm in real space. The size of FFT (fast Fourier transform) grid in reciprocal space of PME is 0.12 nm. The periodical boundary conditions in all direction are used in all simulations. The time step is set as 1 fs for all simulations. LINCS constraint-algorithm (Hess et al., 1997) is used to fix all the bonds in TraPPE force field and C-H bonds in LOPLS and CHARMM force field.

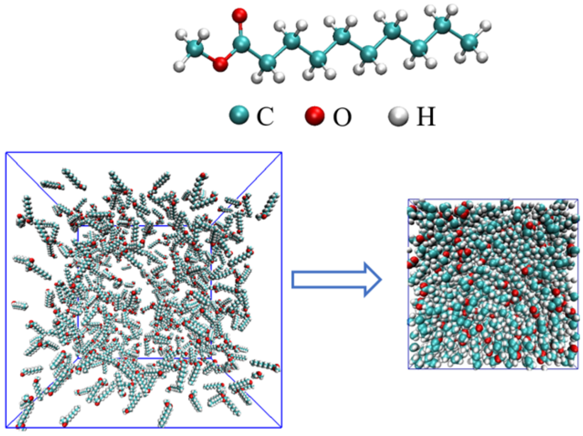

(a) (b)

Fig. 4.1 Equilibrium run and compression of EMD system containing 500 MDC molecules: (a) snapshot of the initial box with molecules distributed randomly; (b) snapshot of box after 500 ps simulation in *NPT* ensemble at 298.15 K and 0.1 MPa.

4.1.2 Pressure effect on viscosity & diffusivityy

Systems configured in Figure 4.1 with TraPPE force field are used to study the pressure effect on viscosity and diffusivity at 298.15 K. Normalized PACF and time evolution of viscosity at 0.1 MPa are shown in Figure 4.2 (a). Pressure effect on viscosity is shown in Figure 4.2 (b). Pressure tensor is dumped every 5 fs which is frequent enough to accurately calculate the time integration. In Figure 4.2 (a), normalized PACF decays rapidly, reaching minimum at 0.04 ps followed by the fluctuation around zero. Shear viscosity reaches the first plateau at 74 ps, and sustains until 178 ps during which it remains stable with an average value of 1.26 cP. In the time period of 200-500 ps, viscosity shows apparent rise and fall with maximum value of 1.77 cP at 270 ps and minimum value of 0.87 cP at 391 ps. It was recommended that the estimation of viscosity should be made at the time shortly after $\eta(t)$ reaches the plateau instead of longer correlation times (Zhang and Greenfield, 2007) (Zhang and Greenfield, 2010) (Fanourgakis et al., 2012) (Li and Greenfield, 2014). It is not applicable to use this criteria to distinguish the effect of pressure on viscosity. The plateau value of $\eta(t)$ at 0.1 MPa is higher than that at 1 MPa and 10 MPa. There is no identifiable plateau for $\eta(t)$ at 100 MPa, as it reaches the local maximum value at 60 ps and decrease directly. It inevitably results in uncertainty if plateau values are identified manually.

Identifying the plateau region of running integration without introducing the artificial deviation is often hampered by the noisy tail of the ACF. To eliminate the tail, one can decompose the PACF by fitting it to the Kohlrausch-Williams-Watts (KWW) stretched exponential

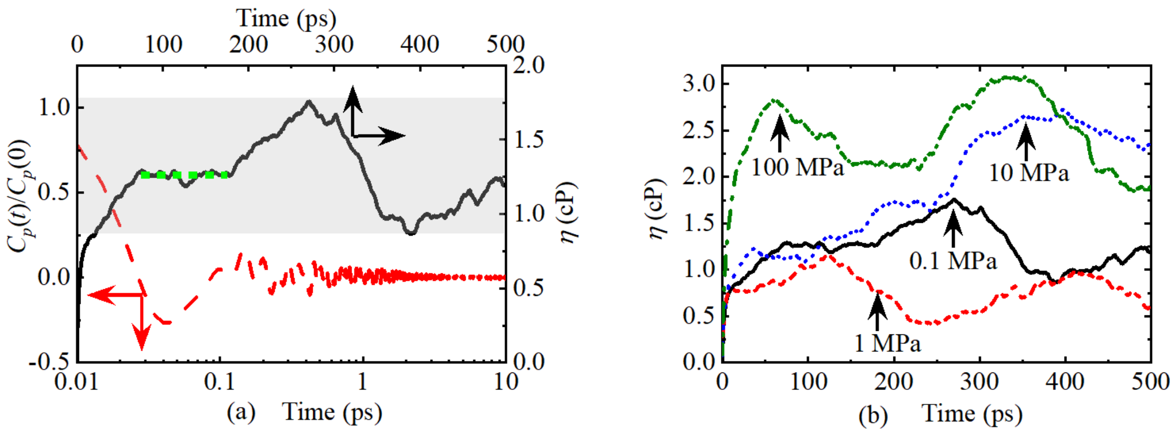

Fig. 4.2 (a) Viscosity of MDC at 298.15 K and 0.1 MPa using GK method, where viscosity is indicated by solid black line, and the normalized ACF of P_{xy} is shown in dashed red line, the shaded region indicates the largest fluctuation range, green dotted line indicates the average value of the first plateau, the arrows indicate the corresponding axis; (b) the effect of pressure on the convergence of viscosity.

function (Maginn et al., 2018):

$$\frac{C_p(t)}{C_p(0)} = A\mathrm{e}^{-(t/\tau_s)^{\beta_s}} + (1-A)\cos(\omega t)e^{-(t/\tau_f)^{\beta_f}} \tag{4.8}$$

where ω is the frequency of rapid pressure oscillations (mainly due to bonded forces in molecular simulations), τ_f and β_f are the time constant and exponent of fast relaxation, τ_s and β_s are constants for slow relaxation. Parameter A is the pre-factor that determines the weight between fast and slow relation. The results from the fitting are shown in Figure 4.3 (a). The running integral of the fitting function can be used to compute the viscosity.

For highly viscous liquids, another approach to improve convergence is time decomposition method (TDM) proposed by Zhang et al. (2015) by fitting the running integral. In TDM, a series of independent and shorten trajectories are obtained in NVT simulation with the same system configuration but different random seeds for the initial velocity distribution. The averaged running integral as a function of time is also fitted to a double stretched exponential functions express as:

$$\eta(t) = A\alpha\tau_1\left(1-\mathrm{e}^{-t/\tau_1}\right) + A(1-\alpha)\tau_2\left(1-\mathrm{e}^{-t/\tau_2}\right) \tag{4.9}$$

where A, α, τ_1, and τ_2 are fitting parameters. When the standard deviation of the replicated running integral is equal to 40% of the averaged $\eta(t)$, it is the time range over which the running integration should be fitted.

The mean value of 40 independent replicated running integrals is shown in Figure 4.3 (b), with the fitted viscosity equal to 1.45 cP. Averaged viscosity reached the plateau at 300 ps with the value of 1.41 cP. The minimum value of the averaged viscosity is 1.14 cP in 852 ps. The fluctuation of the averaged viscosity in the late stage still exists but behaves much better than the noisy $\eta(t)$ curve in Figure 4.2. Although the result of viscosity obtained by fitting PACF shows more rapid and stable convergence compared with the result obtained by fitting to running integral, significant underestimation is demonstrated. Standard deviation as shown in Figure 4.3 (b) increases as a power function of time due to the accumulation of the random noise at long times in correlation function. The averaged plateau value of single run in Figure 4.2 (a) is close to the TDM result. It should be noted that the standard deviation between 74 ps and 178 ps ranges from 0.24 cP to 0.44 cP which indicates significant randomness of the value derived from the single run. In the following study, all viscosities are calculated using the TDM method with 40 statistically independent trajectories.

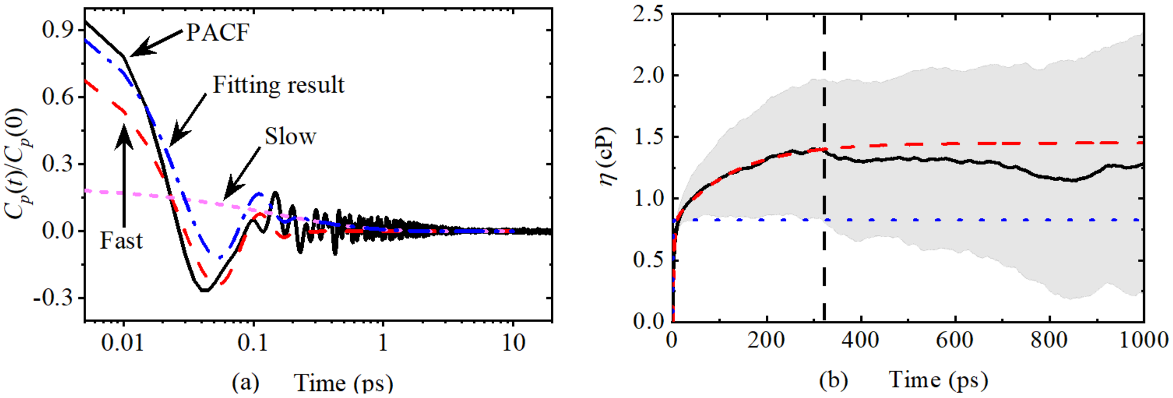

Fig. 4.3 (a) Decomposition and fitting of PACF; (b) viscosity comparison obtained by fitting the running integral and PACF, where the solid black line is the averaged viscosity value of 40 independent replicates with standard deviation indicated in shaded area, and the red dashed line indicates the fitted value according to Equation (4.9), blue dotted line is the integration of fitted PACF, black dashed line indicates the time when standard deviation is equal to 40% of the averaged viscosity.

Unlike viscosity, diffusion coefficient has less intrinsic uncertainties (Kim et al., 2018). It is much easier to obtain accurate self-diffusivity as it describes the motion of individual molecules and the accuracy of statistics is improved by averaging over all particles in the system. The velocity autocorrelation function (VACF) and MSD of molecule centre of mass (COM) is shown in Figure 4.4. Oscillatory behaviour of VACF of monatomic LJ fluid is used to identify the Frenkel line of dynamic cross-over between gas-like and liquid-like regime in supercritical conditions (Brazhkin et al., 2013). VACF of gas decays monotonically in an exponential function. VACF of solids and liquids near melting temperature has both oscillatory and decaying components due to the cage effect described in cell theory (Scalliet et al., 2015) (Bellissima et al., 2017). The negative region of VACF is typical for liquids and dense gases when rebounding collisions are more frequent than scattering collisions (Kondratyuk et al., 2016) (Maginn et al., 2018). With pressure increases, the minimum of VACF deepens and shifts to smaller times. Same as the GK method in calculation of viscosity, tail effect would introduce considerable noise in integration of VACF, it is a trade-off in determining the simulation length of VACF (Maginn et al., 2018). Diffusion coefficient using Einstein method by linear regression of MSD is used more widely in MD simulations. In order to avoid the influence of anomalous ballistic diffusion in the initial stage which shows a non-linear relationship between MSD and time, the linear fit is performed in middle region between 100 ps and 900 ps. Atom position data is dumped every 0.1 ps for the observation of the initial ballistic diffusion process.

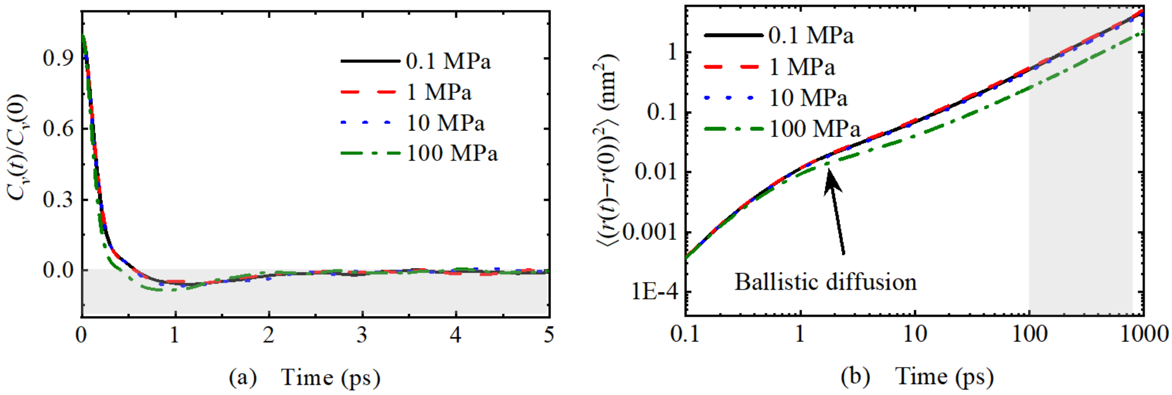

Fig. 4.4 (a) Normalized VACF of MDC centre of mass at different pressures, where shaded area indicates negative values; (b) MSD of MDC centre of mass, where the shaded area is used in the linear regression.

The scaling law of system size must be taken into account to achieve accurate estimates of self-diffusivity (Yeh and Hummer, 2004) (Moultos et al., 2016) (dos Santos et al., 2020) (Celebi et al., 2021). Finite size effect of self-diffusivity depends on the hydrodynamic radius of diffusing molecule with respect to the size of the simulation box (Celebi et al., 2021). Diffusion coefficients of MD systems with different configurations of molecular numbers are shown in Figure 4.5. Linear dependence of self-diffusion coefficient on $1/N^{1/3}$ (N is the number of molecules in system) was observed. Self-diffusion coefficient of infinite system size, i.e., D^{∞} is obtained by the linear fitting and extrapolation. D^{∞} is 5-10% higher than self-diffusion coefficient of system with 500 molecules. Applying analytic correction term using the following equation derived by Yeh and Hummer (Yeh and Hummer, 2004) is also a feasible approach for to obtain D^{∞}:

$$D_{\text{self}}^{\infty} = D_{\text{self}}^{\text{MD}} + \frac{k_B T \iota}{6\pi\eta L} \tag{4.10}$$

where ι is a dimensionless constant equal to 2.837297 for periodic lattice, L is box length. It was verified that Yeh-Hummer correction results have excellent consistency with the extrapolated infinite self-diffusion coefficient (Yeh and Hummer, 2004) (Moultos et al., 2016) (dos Santos et al., 2020). Finite-size effect on viscosity is generally negligible (Maginn et al., 2018). It was conformed that there was no dependence on the system size for the shear viscosity of glymes at 400 K and 30 bar using TDM (Moultos et al., 2016).

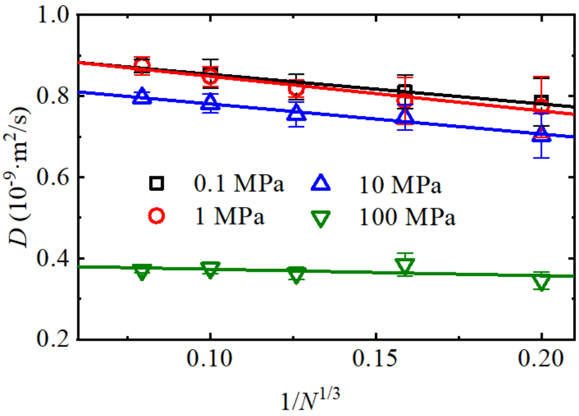

Fig. 4.5 System size effect on diffusion coefficient, where error bars are calculated from 40 independent trajectories and solid lines are the line fitting with linear regression.

The result of normalized rotational correlation function using different orders of Legendre polynomial of the angle between end-to-end vector is shown in Figure 4.6 (a). Different orders of rotational dynamics of P_1, P_2 and P_3 correlation function correspond to different experimental measurement techniques like spectral band shapes measured in infrared absorption, nuclear magnetic resonance and polarized Raman spectra (Li and Greenfield, 2014). The rotational correlation function of P_1, P_2 and P_3 decays to zero at time of 512 ps, 185 ps and 96 ps respectively. The longest orientation relaxation time is often employed to determine the duration length of trajectory for accurate viscosity estimate in single run and the plateau region for data interception in viscosity curve (Mondello and Grest, 1997) (Gordon, 2003b). The effect of pressure on molecular reorientation is shown Figure 4.6 (b). The rotational correlation function decays slower in higher pressure conditions indicating longer relaxation time. To evaluate the molecule relaxation time, rotational correlation function was approximated by the sum of two stretched exponential function which corresponds separately to the conformational dynamics and reorientation of overall molecules as a rigid body (Zhang and Greenfield, 2007) (Zhang and Greenfield, 2010) (Li and Greenfield, 2014) (Falk et al., 2020):

$$\frac{C_{Rot}(t)}{C_{Rot}(0)} = A\mathrm{e}^{-(t/\tau_s)^{\beta_s}} + (1-A)\mathrm{e}^{(t/\tau_f)} \tag{4.11}$$

After integrating from t=0 to t=∞, we obtain the correlation time which is given analytically by the gamma function Γ:

$$t_{Rot} = A\tau_s \frac{1}{\beta_s}\Gamma\left(\frac{1}{\beta_s}\right) + (1-A)\tau_f \tag{4.12}$$

The results of relaxation time are listed in Table 4.2. Relaxation time increased significantly when pressure was increased to 100 MPa. The characteristic decay times for different values of n can be related by the Debye rule as $t_{Rot\_n}/t_{Rot\_n+1}=(n+2)/n$ (Zhang and Greenfield, 2007). Therefore, in the case of isotropic rotational diffusion, a value of 3 for ratio of t_{Rot_1}/t_{Rot_2} and value of 6 for ratio of t_{Rot_1}/t_{Rot_3} is expected. Our results in Table 4.2 agree well with this relation, indicating that polynomials of correlation functions with different orders will lead to comparable results. The correction term for system-size scaling effect on rotational diffusion should be extremely small as it is in linear relationship with the inverse value of box volume (Celebi et al., 2021). So, the system size effect on rotational relaxation time is ignored in the following study.

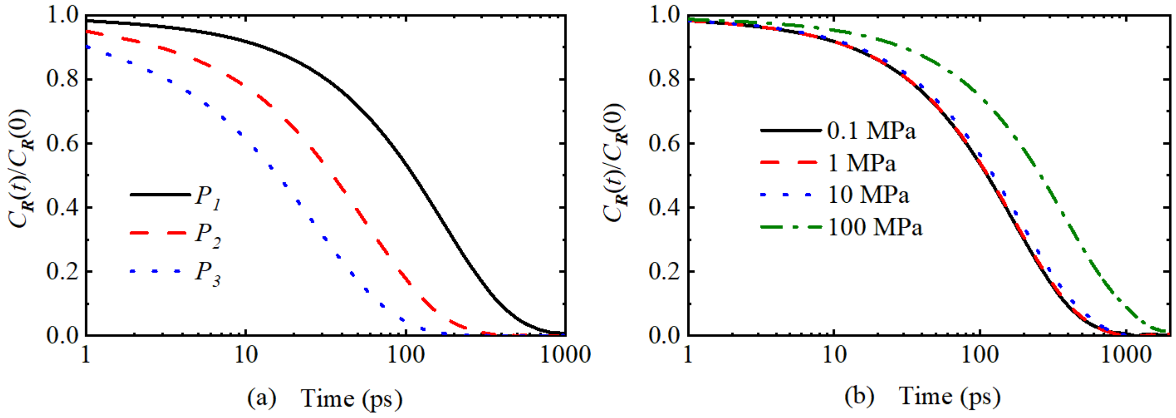

Fig. 4.6 (a) Normalized ACF of MDC molecule end-to-end vector, where P_1 is the first order Legendre polynomial of the angle of the vector; (b) effect of pressure on molecule reorientation using the P_1 function.

4.1.3 SE & SED relation

To achieve the same level of statistical precision with diffusion coefficient, it is estimated that almost two orders of magnitude of trajectory duration are needed in viscosity calculation (Mondello and Grest, 1997) (Zhang et al., 2015). Kinetic theory in liquid state which relate the diffusivity and viscosity by microscopic form of friction coefficient has been regarded as a promising approach to obtain viscosity from diffusion coefficient efficiently (Bedrov et al., 2000) (Zhang and Greenfield, 2007) (Koddermann et al., 2008) (Zhang and Greenfield, 2010)

Table 4.2 Different orders of rotational relaxation time of MDC at different pressures, averaged over 5 independent trajectories.

P (MPa)	t_{Rot_1} (ps)	t_{Rot_2} (ps)	t_{Rot_3} (ps)	t_{Rot_1}/t_{Rot_2}	t_{Rot_1}/t_{Rot_3}
0.1	166.03 ± 3.25	56.39 ± 1.94	27.39 ± 0.36	2.95 ± 0.13	6.06 ± 0.15
1	167.82 ± 10.69	57.55 ± 2.23	27.86 ± 0.60	2.92 ± 0.27	6.03 ± 0.42
10	202.56 ± 19.47	63.57 ± 0.80	30.66 ± 0.29	3.19 ± 0.32	6.61 ± 0.64
100	387.75 ± 17.17	139.75 ± 10.47	69.19 ± 3.65	2.79 ± 0.24	5.61 ± 0.14

(Li and Greenfield, 2014):

$$D = \frac{k_B T}{c_d} \tag{4.13}$$

where c_d is the drag coefficient of molecule. In SE relation of molecule translational motion, $c_d = n\pi R_{eff}\eta$. In SED relation of molecule rotation motion, $c_d = n(\frac{4}{3}\pi R_{eff}^3)\eta$. Parameter n is equal to 4 or 6 based on slip or stick hydrodynamic boundary condition (Gordon, 2003b) (Moultos et al., 2016) (Moultos et al., 2016) (dos Santos et al., 2020) (Falk et al., 2020), R_{eff} is effective molecule hydrodynamic radius.

Molecular rotation motion is characterised by molecular reorientation relaxation time t_{Rot}, and D will only indicate self-diffusion coefficient of molecular translational motion in the following study. Elongated normal alkanes or polymer with Gaussian chain can be described by Rouse model where the molecular strucutre is treated as a collection of beads connected with a harmonic spring. Conformational dynamics of molecule described by longest relaxation time is in the form of:

$$t_{Rot} = \frac{c_d {n_b}^2 l^2}{3\pi^2 k_B T} \tag{4.14}$$

SE and SED relation evolve into the following equations (Doi et al., 1988) (Kremer and Grest, 1990) (Mondello and Grest, 1997) (Mondello et al., 1998) (Yang et al., 2021).

$$D = \frac{k_B T}{n_b c_d} \tag{4.15}$$

$$t_{Rot} = \frac{12M\eta}{\pi^2 \rho RT} \tag{4.16}$$

Here, c_d is the translational fractional drag coefficient of monomer, n_b is number of beads, l is effective bond length, R is gas constant, M is molecular mass. For Gaussian polymer with linear chain, molecular geometry has the relation of $\langle {R_{ee}}^2\rangle$=6$\langle {R_g}^2\rangle$=$n_b l^2$ where R_{ee} is end-to-end distance, R_g is gyration radius (Mondello et al., 1998). Combing Equations

(4.14)-(4.16), eliminating c_d and subscribing l with R_{ee} or R_g, the viscosity via SE relation can be expressed as:

$$\eta\left(R_{ee}\right)=\frac{\rho RT\left\langle R_{ee}^2\right\rangle}{36MD} \tag{4.17}$$

$$\eta\left(R_g\right)=\frac{\rho RT\left\langle R_g^2\right\rangle}{6MD} \tag{4.18}$$

Viscosity via SED relation is the direct inversion of Equation (4.16) and is rewritten in the following form:

$$\eta\left(t_{Rot}\right)=\frac{\pi^2\rho RT t_{Rot}}{12M} \tag{4.19}$$

It was verified that normal alkane like HXD was too short to be regarded as Gaussian chain (Mondello and Grest, 1997) (Mondello et al., 1998). Moreover, the ester function group in MDC and MMR also reduce the Gaussianity indicating the breakdown of Rouse model on methyl esters selected in this study. To use SE and SED relation in viscosity prediction of component with complexed molecular structure, obtaining R_{eff} is crucial. For Gaussian polymer, hydrodynamic radius can be obtained from ensemble-averaged estimates of the radius of gyration via R_{ee} =0.6647$\left\langle {R_g}^2\right\rangle^{1/2}$ (Haydukivska et al., 2020). In temperature dependent transport property prediction, some previous studies on complexed non-Gaussian molecules like asphalt, ionic liquid or short alkane employed a linear regression between viscosity with single molecule property of translational diffusion coefficient or relaxation time, i.e., $1/\eta \sim D/T$ or $t_{Rot}T \sim \eta$ (Mondello and Grest, 1997) (Zhang and Greenfield, 2007) (Koddermann et al., 2008) (Zhang and Greenfield, 2010) (Li and Greenfield, 2014).

More recently, R_{eff} is obtained by averaging molecule cross section over ensemble in EMD simulation. In conjunction with free volume theory (FVT) of molecular diffusion, a parameter free and nonempirical method was proposed subsequently and was applied to predict viscosity of alkane lubricants over extreme pressure of 0.7 GPa. This indicates the applicability of SE relation in pressure dependent transport property prediction. The correlation of viscosity, translational diffusion and relaxation time is demonstrated in Figure 4.7 in terms of MDC at 298.15 K. The linear scaling of transport property data is well-behaved, indicating the preservation of SE relation. Compared with the previous study by Shi et al. (2013) on coupling of instantaneous shear stress relaxation time with reorientation relaxation time, statistical error was eliminated significantly in this study due to the replicated trajectories. If we consider $\eta \sim t_{\mathrm{Rot}} \sim 1/D$ overall, the product of relaxation time and diffusion coefficient, i.e. $t_{\mathrm{Rot}} \cdot D$, should be constant if translation and rotation equally reflect viscosity (Zhang and Greenfield, 2007) (Zhang and Greenfield, 2010) (Li and Greenfield, 2014). The relative standard deviation of translation-rotation diffusion product is also a small value of 5.06% at pressure ranging 1-100 MPa.

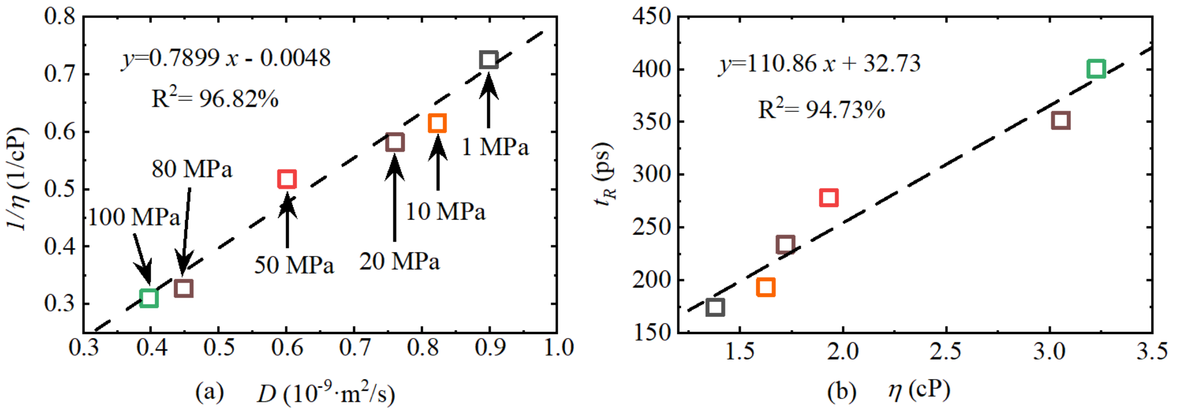

Fig. 4.7 (a) Correlation between diffusion coefficient and the inverse of viscosity; (b) correlation between relaxation time and viscosity, where the dashed lines indicate linear fitting, pressure is also indicated by colour of the hollow square, the colour code of pressure applies to the following plots of SE relation.

4.2 Evaluation of force field

4.2.1 Hydrodynamic radius

In previous EMD study on obtaining R_{eff} either via SE linear correlation or averaging molecular cross section over ensemble, it is observed that R_{eff} remains universal with different force fields of AA and UA models (Kondratyuk et al., 2020a), and R_{eff} is only weakly dependent on density and temperature (Falk et al., 2020). Data of $1/\eta \sim D/T$ with pressure range of 10-300 MPa in isothermal conditions was plotted in Figure 4.8. Viscosities of TDM results are used in the Yeh-Hummer term of Equation (4.10) to correct system size effect on diffusion coefficient. The linear regression worked well with different force fields and various isothermal temperatures. Compared with the SE linear fitting in Figure 4.7, widen pressure range increased the goodness-of-fit. Slip boundary conditions are employed in calculation of R_{eff}, which is the same boundary condition as Falk et al. (2020). The conformation difference between MDC and MMR reflects merely the chain length difference. Comparing the R_{eff} in Figure 4.8, effect of molecular structure on R_{eff} difference is distinguished. This indicates that R_{eff} in EMD simulation is an intrinsic property of molecular structure and is insensitive to the modelling configurations (Gordon, 2003a) (Gordon, 2005).

4.2.2 Physical properties

The capability of selected force fields was evaluated over density prediction of n-alkanes, considering the availability of the NIST data for comparison as shown in Figure 4.9 (a). The

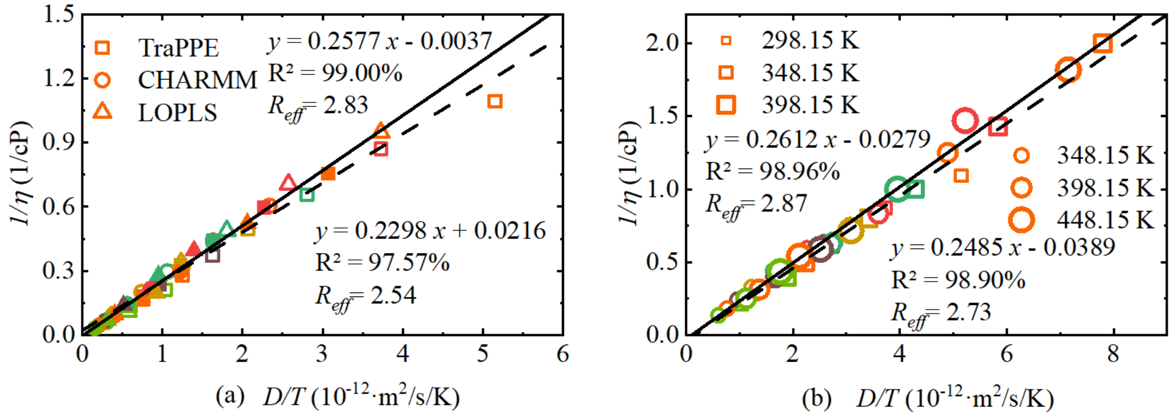

Fig. 4.8 (a) Effect of force field on SE relation at 348.15 K, pressure ranging 10-300 MPa, where the hollow symbols and dashed line are results of MDC while solid symbols and solid line are results of MMR; (b) effect of temperature on SE relation, where the hollow square and dashed line are results of MDC while the hollow circle and solid line are results of MMR.

densities of OTN, DCN and DDC are predicted at pressures ranging from 4MPa to 100 MPa, and temperatures ranging from 300 K to 700 K. Densities of 361 phase points are calculated in total for each force field. Based on phase change data listed in Table 4.1, these conditions cover the gas phase, liquid phase and supercritical state. As shown in Table 4.3, there is no scaling effect of system size on density prediction, and statistical error is negligible. The simulation is performed in *NPT* ensemble containing 500 molecules, running 500 ps with density averaged over the last 200 ps trajectory.

Table 4.3 The density of MDC at 298.15 K and 0.1 MPa calculated using the TraPPE force field with different system sizes, results are averaged over 5 replicated independent trajectories.

Molecule number	125	250	500	1000	2000
ρ (g/ml)	0.8716	0.8714	0.8715	0.8714	0.8714
SD (g/ml)	5.67E-4	4.75E-4	2.08E-4E	3.09E-4	6.97E-5

Among the three force fields, TraPPE reproduces densities most accurately with an average absolute relative deviation (AARD) of 1.44%, which is in agreement with previous MD simulations (AARD of 1% and 2% for DDC and *n*-Octacosane, respectively) (Papavasileiou et al., 2019). Results of LOPLS has the largest AARD of 8.90%, despite that LOPLS parameters have been optimised over the dihedral energy profile and LJ interaction in gas phase (Siu et al., 2012). Both CHARMM and LOPLS force fields show underestimation at low density conditions, particularly LOPLS which deviates around 10%-50% at low density conditions ranging from 0.5 g/ml to 0.3 g/ml. The prediction of these three force fields is accurate at liquid phase and high pressure condensed phase at supercritical conditions.

Using TraPPE force field for prediction, the densities of MDC and MMR at high pressure up to 300 MPa are shown in Figure 4.9 (b). At 298.15 K, densities of MDC and MMR are limited up to 150 MPa and 50 MPa respectively to avoid the high-pressure induced liquid-solid transition (Kouakou et al., 2013). The fitted density model itself is useful as a guide for the molecular modelling. The pressure dependence of density ρ is fitted by the Tait equation (Dymond and Malhotra, 1988).

$$\frac{\rho - \rho_{10}}{\rho} = A \log\left(\frac{B+P}{B+10}\right) \tag{4.20}$$

where ρ_{10} is the density at pressure of 10 MPa, A and B are the fitting parameters. From Figure 4.9 (b), the density difference between MDC and MMR at 348.15 K appears at high pressure above 150 MPa.

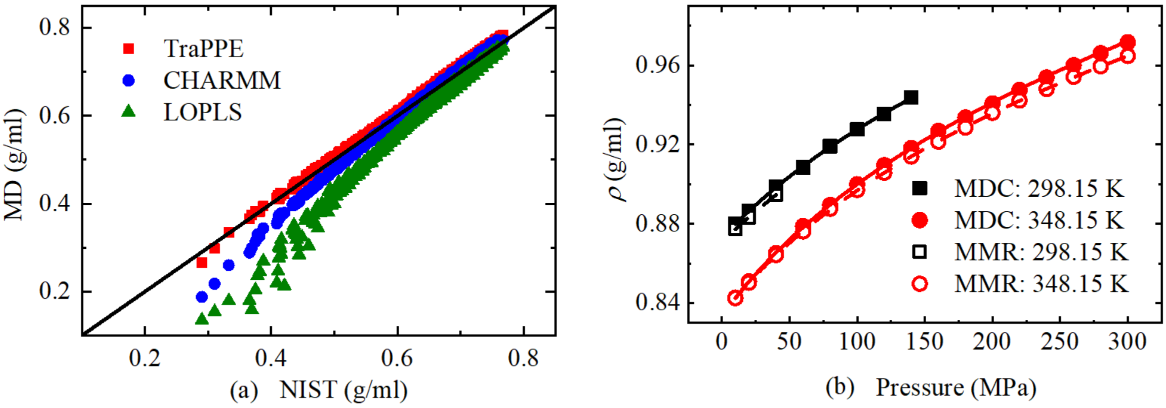

(a) NIST (g/ml) (b) Pressure (MPa)

Fig. 4.9 (a) Correlation between densities of NIST and the results calculated by EMD simulation including the liquid phase, gas phase and supercritical conditions; (b) pressure effect on density of MDC and MMR at 298.15 K and 348.15 K, where lines are fitted results according to the Tait equation (Dymond and Malhotra, 1988).

Diffusivity is difficult to obtain experimentally, with data rarely available. According to a previous study (Siu et al., 2012), the LOPLS force field exhibits improved accuracy on prediction of diffusion. This is also reflected in our simulation results shown in Table 4.4, i.e. LOPLS has the smallest deviation among the three force fields, with the value of -25.16% and -17.28% for DCN and DDC respectively. All atom molecular models of LOPLS and CHARMM tend to underestimate diffusion. Diffusion coefficient predicted by CHARMM was underestimated substantially by a factor of 0.63 and 0.54 for DCN and DDC respectively. Conversely, the united atom model of TraPPE overestimates the diffusion because the absence of hydrogen atoms increases the molecule free volume (Kondratyuk et al., 2016). Diffusion constant is dependent on molecular size, while all these three force fields followed exactly the scaling law of diffusivity over molecular size, i.e., $D \propto M^{-2}$ (Von Meerwall et al., 1998) (Freed et al., 2005). Scaling factors of D_{DDC}/D_{CCN} are equal to 0.63, 0.57, and 0.58 respectively for TraPPE, CHARMM and LOPLS.

Table 4.4 Comparison of diffusion coefficient with the experimental result at 298.15 K and 0.1 MPa (10^{-9} m^2/s), data was corrected over system size effect.

	Expt.	TraPPE	CHARMM	LOPLS
DCN	1.55	2.35 ± 0.15	0.83 ± 0.062	1.16 ± 0.047
DDC	0.81	1.47 ± 0.059	0.47 ± 0.019	0.67 ± 0.030

Considering the temperature range in the experimental result, viscosities of MDC and MMR are calculated at isotherms of 298.15 K and 348.15 K via TDM. The comparison of viscosity-pressure results is shown in Figure 4.10. The corresponding experimental values are adopted from the work of Habrioux et al. (Habrioux et al., 2015) (Habrioux et al., 2016), where isothermal viscosities are correlated according to the modified Tait equation:

$$\ln\left(\frac{\eta}{\eta_{0.1}}\right) = A(P-0.1) + B\ln\left(\frac{C+(P-0.1)}{C}\right) \tag{4.21}$$

where A, B and C are fitting parameters. A is temperature independent, B and C are fluid-specific parameters dependent on the temperature (Habrioux et al., 2015) (Habrioux et al., 2016) (Baled et al., 2018), $\eta_{0.1}$ is the viscosity at 0.1 MPa for each isothermal temperature which can be obtained by fitting Vogel-Fulcher-Tammann (VFT) correlation in the form of

$$\eta_{0.1}(T) = \mathrm{A}\exp\left(\frac{\mathrm{B}}{T-C}\right) \tag{4.22}$$

where A,B and C are fitting parameters.

For MD simulation, the viscosity-pressure relation is described by the single exponential Barus model (Dench et al., 2018) given as:

$$\eta = \eta_0 \exp(AP) \tag{4.23}$$

where η_0 is zero pressure viscosity, A is fitting parameter. Equation (4.23) has been used to successfully describe the rheology of 1-diphenylethane at high pressure up to 400 MPa (Kondratyuk et al., 2020a).

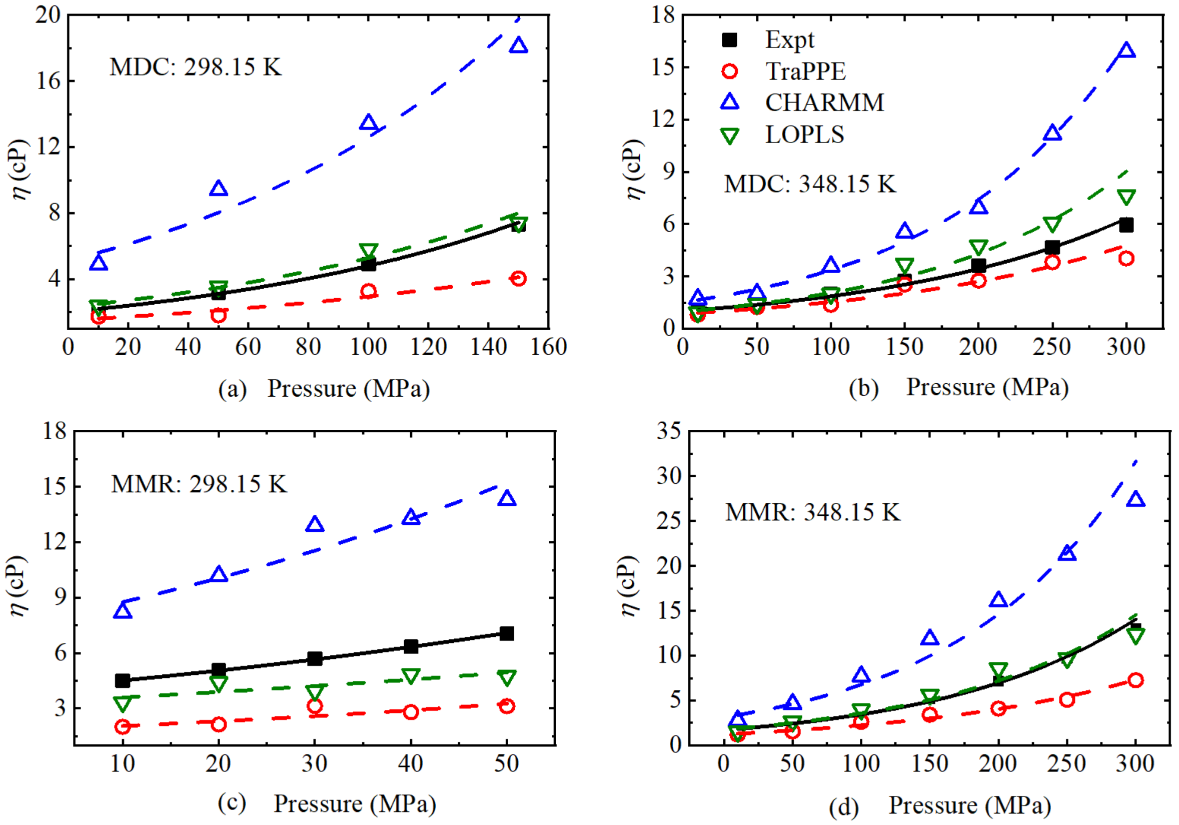

Fig. 4.10 Comparison of viscosity between MD simulation and the experimental results, where solid lines are experimental values, dashed lines are MD results fitted according to the Barus model (Dench et al., 2018).

All these three force fields can describe the viscosity-pressure trend. It is observed that CHARMM overestimates viscosity substantially in all conditions, and TraPPE underestimates viscosity. The deviation is more prominent at high pressure compressed condition. LOPLS exhibits the best agreement with experimental values. The evaluation of force field performance using EMD-TDM method is consistent with the previous observation using non-equilibrium MD simulation (NEMD) with periodic perturbation method (Papavasileiou et al., 2019).

4.3 Breakdown of SE relation due to high pressure solidification

A violation or breakdown of SE relation has been observed in viscous liquids due to occurrence of glass-formation instead of normal crystallization when liquid is cooled sufficiently fast (Debenedetti and Stillinger, 2001) (Kumar, 2006) (Kawasaki and Kim, 2017). Decoupling between D and η and between t_{Rot} and D would occur in supercooled liquids when temperature is below approximately $1.2T_g$ (T_g is glass transition temperature) (Debenedetti and Stillinger, 2001) (Kumar, 2006) (Lombardo et al., 2006) (Kawasaki and Kim, 2017). There have been studies on higher order phase transition and thermodynamic property inhomogeneity when crossing Frenkel line and Widom lines on $P-T$ diagram of monatomic gas and water (Brazhkin et al., 2013) (Bolmatov et al., 2013) (Bryk et al., 2017) (Bryk et al., 2017) (Yoon et al., 2018). Some experimental studies conformed the liquid-solid transition of polyatomic organic components, i.e., solidification of biodiesel mixtures (up to 350 MPa) (Tarakowski et al., 2015), n-Octane ($\sim$0.9 GPa) (Takekiyo et al., 2020), pure FAMEs (Kouakou et al., 2013) (up to 80 MPa), n-Tetradecane (302.8 MPa) (Jian and Zheng, 2009), and the crystallisation of Methyl Stearate (0.2 GPa) (Liu et al., 2019). The observations of the HP glass formation of water (Andersson, 2011) (Handle et al., 2012), ionic liquid (Ribeiro et al., 2014) (Yoshimura et al., 2018) and crude oil (Kutcherov et al., 2017), raise question whether SE remains valid for liquids which are densified by high pressure instead of cooling (Falk et al., 2020).

To scrutinise the HP induced phase transition of FAMEs, we firstly tracked the morphology evolution of the modelling system in 100 ns trajectory. Molecular alignment was quantified by using a collective variable named SMAC (Giberti et al., 2015a), in which the relative orientation is characterised by torsion angle between internal molecule vector. The SMAC variable describes the local order in the neighbourhood of a molecule, and has been used to study the phase transition such as the nucleation process of urea (Giberti et al., 2015a) and the crystallisation of paraffin in cooling condition (da Silva et al., 2021). SMAC is expressed as:

$$S_i = \frac{\left\{1-\psi\left(\sum_{j\neq i}^{N}\sigma\left(r_{ij}\right)\right)\right\}\sum_{j\neq i}^{N}\sigma\left(r_{ij}\right)\sum_n K_n\left(\phi_{ij}\right)}{\sum_{j\neq i}^{N}\sigma\left(r_{ij}\right)} \tag{4.24}$$

where r_{ij} is the distance between centre of vector of molecule i and j, ϕ_{ij} is torsion angle between the molecular vectors, $\sigma\left(r_{ij}\right)$ is a switching function to ensure that only molecules within the cut-off distance are considered, ψ is also switching function, K_n is kernel function consisted of two Gaussian functions with standard deviation of 0.48 and reference angles of zero and π (Giberti et al., 2015a) (Tribello et al., 2017) (da Silva et al., 2021). $K_n\left(\phi_{ij}\right)$ converts torsion angles close to zero and π to a number close to one which corresponds to ordered arrangement of molecules in MD system (Tribello et al., 2017). $\sigma\left(r_{ij}\right)$ is a rational function expressed as:

$$\sigma = \frac{1-\left(\frac{r-d_0}{r_0}\right)^n}{1-\left(\frac{r-d_0}{r_0}\right)^m} \tag{4.25}$$

where d_0=0.0, n=6, m=2n, r_0 is cut-off distance equal to 8.6 Å which is the radius of second coordination sphere obtained by radial distribution function (RDF) of COM of molecule.

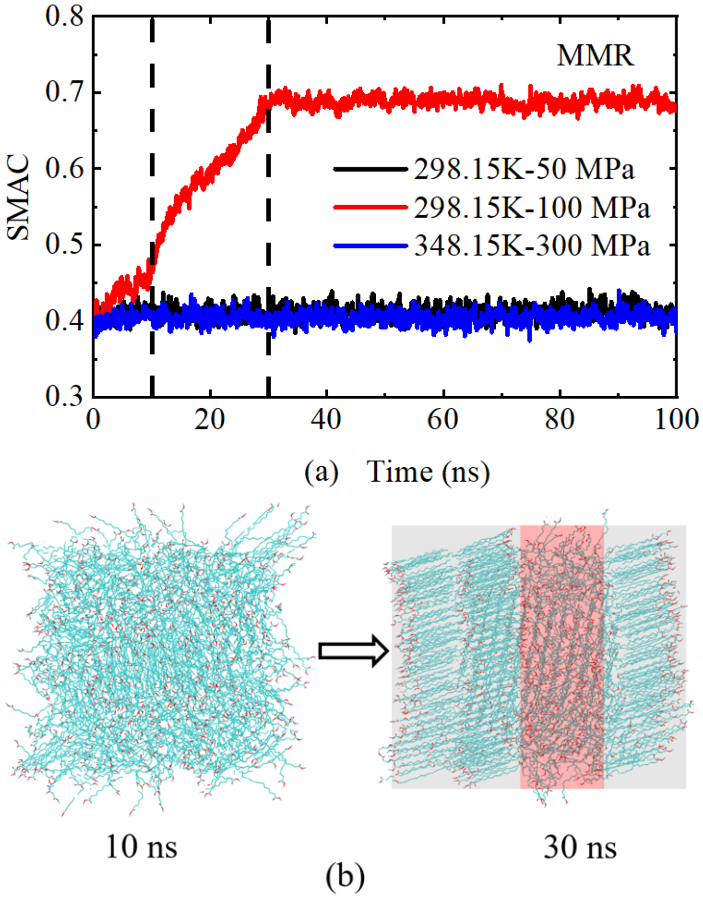

Fig. 4.11 (a) The SMAC parameter of MMR at different temperatures and pressures, where black dashed lines indicate transition time of 298.15 K - 100 MPa; (b) snapshots of MMR MD system at 298.15 K - 100 MPa, where grey area indicates ordered alignment of solid nuclei while red area indicates amorphous liquid phase.

Compared with MDC and alkanes in Table 4.1, MMR has the highest melting temperature of 291.24 K, and was selected in favour of liquid-solid transition in MD simulation. The time evolution of the collective variable and typical morphology snapshots of MMR are shown in Figure 4.11.

Normally, FAMEs melting temperature increases with increasing pressure (Kouakou et al., 2013). At conditions of 298.15 K - 50 MPa and 348.15 K - 300 MPa, collective variables keep stable and have relatively low values as shown in Figure 4.11 (a). The time invariance indicates the unchanged amorphous liquid states at these conditions. Solidification process of MMR at 298.15 K - 100 MPa can be described by three different stages. Molecular rearrangement takes place before 10 ns with SMAC increasing from 0.42 to 0.47, which is followed by accelerated solidification process with SMAC increasing further to 0.7 in 20 ns. After 30 ns, SMAC resides at the plateau and remains stable with MD system changed into the heterogeneous structure as shown in Figure 4.11 (b). It should be noted that time evolution of SMAC in Figure 4.11 (a) shows the approximate trend with the nucleation of pure paraffin under harsh subcooling conditions (da Silva et al., 2021). This indicates that HP is supposed to have the equivalent effect on FAME crystallisation behaviour with the cooling process.

The mechanism of SE violation of liquids has been attributed to the attained solidity upon supercooling, which is in accord with the growth of non-Gaussianity and spatially heterogeneous dynamics (Lombardo et al., 2006) (Kawasaki and Kim, 2017). The HP induced heterogeneity is reflected in the spatial distribution of solid-liquid phase as shown in Figure 4.11 (b). Pressure effect on MMR molecular conformation is characterised by end-to-end distance probability distribution as shown in Figure 4.12. There are two peak values of probability, at 1.67 nm and 1.89 nm, corresponding to liquid and solid state respectively. The probability at 50 MPa liquid state is not exact normal distribution because MMR is not ideal Gaussian polymer chain. After crystallisation at 100 MPa, the peak value shift to 1.89 nm and probability increases with solidification degree accordingly. This indicates that HP solidification can also enhance the non-Gaussian behaviour of MMR.

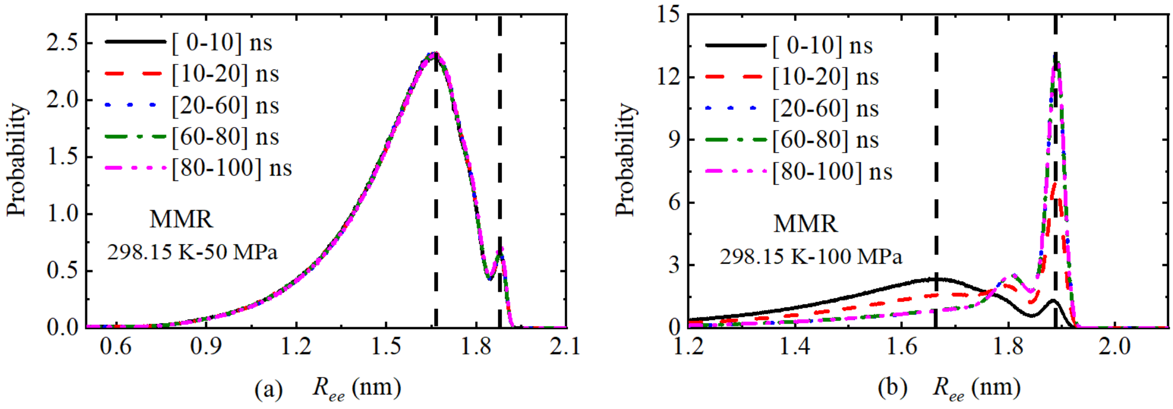

Fig. 4.12 (a) Probability distribution of MMR molecule end-to-end distance at 298.15 K, and the probability is the statistical results in the time interval, (a): 50 MPa where lines are overlapped; (b): 100 MPa where lines of [20-60] ns, [60-80] ns and [80-100] ns are overlapped, and the black dashed lines indicate the peak values.

In glass transition of supercooled liquids, dynamics like structural relaxation time in different regions only a few manometers away can differ orders of magnitude (Ediger, 2000) (Koddermann et al., 2008) (Kawasaki and Kim, 2017). In HP solidified systems displayed in Figure 4.11 (b), molecule in solid phase is stretched while in liquid phase it is flexible. The heterogeneous spatial distribution of molecule conformation indicates the structure relaxation dynamics and molecular mobility is also highly spatially correlated. The time evolution of overall diffusion coefficient is shown in Figure 4.13. Different with the stable values at 50 MPa, diffusion coefficient at 100 MPa shows an inverse relation with the solidification degree. It reached an extremely low average value of 9.68×10^{-11} m^2/s at final stage where stretched molecule at solid region would slide in preferred direction along the main chain

(Kondratyuk et al., 2020a). Once diffusion falls below the cut-off value (5×10^{-11} m^2/s for argon), pressure-induced glass transition occurs (Shumway et al., 1995).

Viscosity becomes large due to the extraordinary slow-down of stress relaxation when temperature gets close to T_g (Debenedetti and Stillinger, 2001) (Ediger and Harrowell, 2012). For solidified HP system, it is impracticable to obtain the viscosity directly using TDM, because at least 30 ns equilibrium run is needed before data collection. Moreover, the feasibility of GK method is questionable in heterogeneous system. Previous MD modelling study on 1-methylnaphthalene implied that the HP induced vitrification would occur above 300 MPa which explained the observation of faster-than-exponential growth of viscosity with pressure (Kondratyuk et al., 2020b). Viscosity becomes large due to the extraordinary slow-down of stress relaxation when temperature gets close to T_g (Debenedetti and Stillinger, 2001) (Ediger and Harrowell, 2012). For solidified HP system, it is impracticable to obtain the viscosity directly using TDM, because at least 30 ns equilibrium run is needed before data collection. Moreover, feasibility of the GK method is questionable in heterogeneous system. Previous MD modelling study on 1-methylnaphthalene implied that the HP induced vitrification would occur above 300 MPa which explained the observation of faster-than-exponential growth of viscosity with pressure (Kondratyuk et al., 2020b).

To investigate phase transition in cooling of pure and spatially unconfined liquids, it is necessary to perform simulation with long time scale due to the large number of possible network configurations (Matsumoto et al., 2002). Considerable long time trajectory is also needed to study the violation/preservation of SE relation (Kawasaki and Kim, 2017). The application of EMD has been common in studying tribology of lubricants at HP conditions up to 1 GPa (Kondratyuk and Pisarev, 2019) (Falk et al., 2020), where the appearance of solid nuclei is possible. It should be stressed that identifying the conditions where spatial heterogeneities occur is vital for the reliability in predicting HP transport property.

4.4 Crossing the SE relation

In general, viscosity is a mesoscopic property which is experimentally measurable while diffusion coefficient is a microscopic description of molecular motion which can be readily obtained in EMD simulation. However, direct viscosity measurements for every fluid at all conditions of interest are not only expensive and time-consuming but also extremely difficult and sometimes impossible to obtain especially at high-temperature, high-pressure (HTHP) conditions. The work of Gordon (Gordon, 2003a) (Gordon, 2005), Falk et al. (2020) and Kondratyuk et al. (2020a) proved that R_{eff} is a constant parameter over wide range of HTHP conditions. It demonstrated that predicting viscosity through diffusion coefficient via scaling

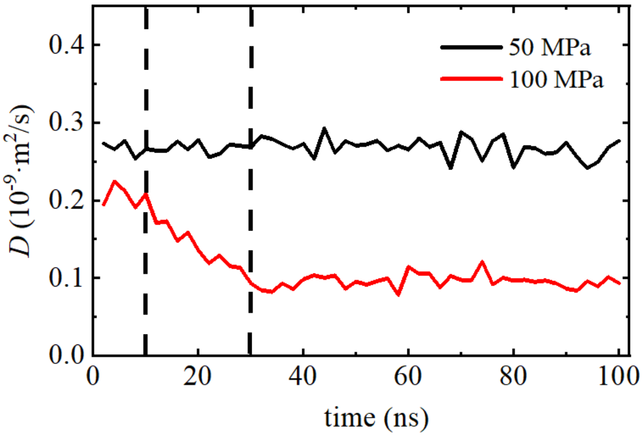

Fig. 4.13 Time evolution of overall diffusion coefficient of MMR at 298.15 K, where trajectories are partitioned every 2 ns and diffusion coefficient is the linear fitting of MSD between 200 ps and 1800 ps within each time interval, black dashed lines indicate the transition time of 100 MPa.

behaviour of SE relation is promising in both reducing computational cost and keeping the ultimate accuracy.

Hereon, we develop a predictive method via the crossing linkage between experimentally available viscosities and corresponding EMD diffusion coefficients in any force field as shown in Figure 4.14. Using the hybrid R_{eff} via liner regression, the viscosity can be estimated in HTHP region after extrapolation provided SE relation preserves. The predicted value should have experimental-level accuracy. Among these three force fields, TraPPE is supposed to be robust even in extreme conditions considering the overall capability in density prediction over wide range of HTHP conditions. The demonstrated correlations between viscosity and diffusion coefficient can be exploited in the determination of transport properties of new fluids such as new fuels or those of existing fluids/fuels in unexplored HTHP supercritical conditions.

4.5 Discussion and conclusion

In this Chapter, equilibrium molecular modelling with three force fields (TraPPE, CHARMM and LOPLS) has been performed to comprehensively study the properties of FAMEs in high pressure conditions up to 300 MPa, which is very challenging for other methods such as experimental measurements. This study provided a new methodological approach to fuel property predictions in extreme conditions using molecular dynamics simulation, with results given in terms of transport property predictions, together with analyses of the dynamics

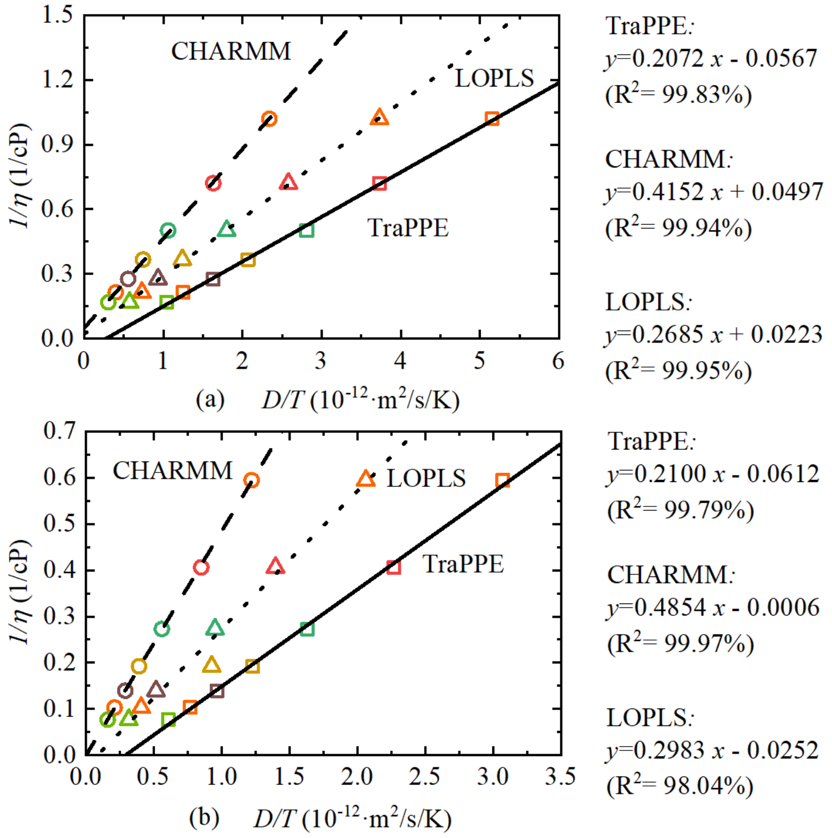

Fig. 4.14 Correlation between viscosity from experiments and diffusion coefficient from EMD simulation at the temperature of 348.15 K, (a): MDC, (b): MMR. Solid line is the fitting of TraPPE, dashed line is the fitting of CHARMM and dotted line is the fitting of LOPLS.

of molecular structure and Stokes-Einstein relation. There are several observations from the simulation and the methodological approach.

Determining plateau time for FAME viscosity is a trade-off due to the increasing statistical error with longer running integral. Averaging over replicated independent trajectories with subsequent fitting is a feasible solution to obtain viscosity rigorously in spite of the increased computational cost. Translational diffusion coefficient obtained via Einstein method is statistically accurate, and scaling effect of system size should be considered. Rotational diffusion is characterised via reorientation relaxation time of end-to-end vector.

Accuracy of density, diffusion coefficient and viscosity prediction varies among the three force fields. TraPPE force field shows exact agreement with experimental density over wide range of conditions. All-atom models tend to underestimate diffusion and overestimate viscosity, vice versa for united atom model. LOPLS force field has performed better than CHARMM on diffusion coefficient and viscosity.

The Stokes-Einstein relation holds for most conditions where diffusion coefficient, relaxation time and viscosity are correlated, except at temperature close to melting point with high pressure. There is need to pay special attention on this when using EMD to predict transport properties at extreme high pressures. Because high pressure induced solidification requires simulation with long time scale for the nuclei to appear, the consequent spatial heterogeneity results in the breakdown of Stokes-Einstein relation.

A hybrid effective hydrodynamic radius is obtained by the cross-correlation of experimental viscosities and EMD diffusion coefficients. The predictive method established in this chapter can be used to estimate experimental viscosity at high temperature and high pressure conditions from the corresponding EMD diffusion coefficient provided Stokes-Einstein relation applies.

Chapter 5

Comparison of biodiesel and diesel on physical property in extreme conditions

During the injection and subsequent spray, atomisation and droplet evaporation, fuel would go through a wide range of temperature and pressure from the fuel nozzle to the combustion chamber. A typical operating condition in diesel spray combustion is "Spray-A" of n-Dodecane where fuel starts from nozzle condition of 363 K - 150 MPa to ambient condition of 900 K - 6 MPa (Pickett et al., 2010). Common rail injection system has been tested under ultra-high injection pressure above 300 MPa (Natti et al., 2013) (Zhao et al., 2020). Therefore, high pressure induced solidification of biodiesel and diesel is studied in Chapter 5.2. Critical property is calculated in Chapter 5.3. The application of EMD on prediction of density, viscosity and thermal conductivity at wide range of HTHP conditions (up to 300 MPa and 1500 K) is introduced in Chapter 5.4. The performance and capability of NEMD on viscosity and thermal conductivity prediction at extreme conditions are discussed in Chapter 5.5.

5.1 Modelling methodology

5.1.1 Fuel composition and molecular structures

In this chapter, the rapeseed biodiesel is selected as the research object with the molecular structure and composition adopted from the work of Herbinet et al. (2008). The five-component diesel surrogate fuels developed by Qian et al. (2018) are employed. The details of rapeseed biodiesel are listed in Table 5.1.

Table 5.1 Molecular names, chemical formulas, molecular structures, molecular mass and composition of rapeseed biodiesel.

Common Name	Molecular Formula	Molecular Structure	M (g/mol)	x (mol %)
Methyl Palmitate	MP (C16:0) $C_{17}H_{34}O_2$	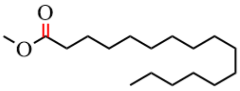	270.46	4.3
Methyl Stearate	MS (C18:0) $C_{19}H_{38}O_2$	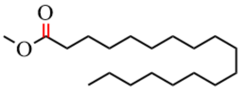	298.51	1.3
cis-9-Methyl Oleate	MO (C18:1) $C_{19}H_{36}O_2$	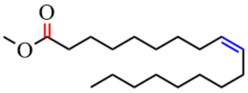	296.50	59.9
cis-9, 12-Methyl Linoleic	ML (C18:2) $C_{19}H_{34}O_2$	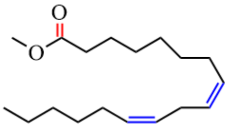	294.48	21.1
cis-9, 12, 15-Methyl Linolenate	MLN (C18:3) $C_{19}H_{32}O_2$	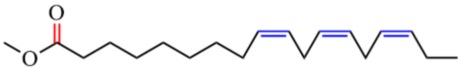	292.47	13.2

5.1.2 Force fields

Simulations of liquid-solid phase change in MD typically require long time scale trajectories due to the energy barrier associated with nucleation events. TraPPE-UA force field is developed for simulation of phase equilibrium in which carbon and bonded hydrogen atoms are treated as a "pseudo-atom" for computational efficiency. The force field parameters of alkanes, cycloalkanes & aromatics and FAMEs are taken from the work of Martin and Siepmann (1998), Kamath et al. (2006) and Yiannourakou et al. (2019) respectively.

In this study, simulation of thermal conductivity using both the Green-Kubo (GK) EMD and reverse NEMD are performed in LAMMPS package (Plimpton, 1995). The remaining simulation are performed in GROMACS package (Van Der Spoel et al., 2005). In the TraPPE force field, bond length is fixed. This can be achieved in GROMACS by using the LINCS algorithm to constrain all bonds. In LAMMPS, there is no corresponding algorithm to fix all bonds of the large molecules in fuels. A practical trade-off is to treat bond as flexible with parameters constraining bond stretching adopted from other force fields (Keasler et al., 2012). For example, in TraPPE force field of alcohols (Chen et al., 2001), force constant of angle bending of C-C-O and C-O-H were taken from AMBER94 force field, and some torsion parameters are taken from OPLS-UA force field. Yiannourakou et al. (2019) developed TraPPE-UA force field to study vapour-liquid equilibrium (VLE) of polycyclic compounds, with bond stretching parameters borrowed from OPLS. Gong et al. (Gong et al., 2021a) (Gong et al., 2021b) studied the diesel droplet evaporation under sub- and supercritical conditions with bond stretching force constant taking from NERD model. In this study, the bond stretching force parameters are adopted from OPLS force field (Jorgensen et al., 1996).

5.1.3 MD setup

Three ensembles are used depending on different scenarios, i.e., NPT, NVT and NVE (microcanonical ensemble). In LAMMPS, the Nose-Hoover thermostat and barostat are used to control the temperature and pressure with the damping constants equal to 100 and 1000 times of the time step respectively. In GROMACS, temperature is maintained by rescaling velocity with a stochastic term to ensure the correct kinetic energy distribution, and pressure is controlled by Parrinello-Rahman barostat (Parrinello and Rahman, 1981).

The cut-off radius of vdW interactions and Coulombic interactions are set to be 1.4 nm. For thermal conductivity simulation in LAMMPS, PPPM solver (Hockney and Eastwood, 2021) is used for the calculation of long-range electrostatic interactions in reciprocal space with the desired relative force error of 1.0e-5. In GROMACS, PME solver (Darden et al., 1993) is used for long-range electrostatic interactions. PME calculations are performed using a fourth-order spline interpolation with grid spacing of 0.12 nm. All simulations were performed with initial energy minimisation before the equilibrium run and production run. Periodical boundary condition is used in all directions in the simulation.

5.2 High pressure induced solidification

Occurrence of solid-like phase of fuel could be harmful for common rail injector which should be avoided (Tarakowski et al., 2015). The liquid-to-solid phase transition of FAMEs under high pressure (HP) remains much less studied than crystallisation under hash cooling conditions. To investigate the high pressure induced solidification in molecular level, the modelling system is constructed with 2000 biodiesel (or diesel) molecules randomly distributed in a box as shown in Figure 5.1. Nie et al. (2019) reviewed the MD study on transport properties of supercritical working fluids. And most MD simulation (both EMD and NEMD) to compute transport properties like viscosity and thermal conductivity contains around 500 - 2000 molecules. Recently, Yang et al. (2021) studied the viscosity and thermal conductivity of *n*-alkanes like *n*-decane, *n*-undecane and *n*-dodecane with 250 molecules in simulation box. The edge length of box is set at a relatively large value of 20 nm to avoid atom overlap. A steepest descent energy minimization simulation is performed to relax the molecular geometry. Equilibrium run of 2 ns in NPT ensemble is followed with a time step of 2fs to compress the system to the target temperature and density. A final 200 ns production run is performed in NVT ensemble with atom trajectory dumped every 100 ps. The effect of temperature, pressure and composition on phase transition is evaluated according to the morphology shown in Figure 5.2.

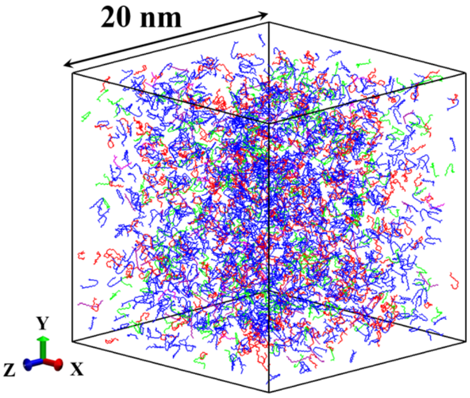

Fig. 5.1 Snapshot of initial box containing 2000 biodiesel molecules, fuel surrogate molecules are indicated with different colours, HXD and MP: purple, OTD and MS: magenta, HMN and MO: blue, DCA and ML: red, MNT and MLN: green.

In a previous experimental study, it was reported that phase transition of rapeseed methyl ester occurred at pressure above 230 MPa in room temperature (Tarakowski et al., 2015). A visual inspection of the molecular trajectory at 300 K and 300 MPa is used to confirm the formation of solid phase as shown in Figure 5.2. The nucleation is initiated from the chain straightening of molecular conformation and orientation adjustment. This results in the parallel alignment of molecules and the increase of local density which facilitates the formation of critical nucleus before 50 ns. Prentice et al. (2020) observed that the squalene undergoes the crossover to an amorphous and metastable solid-like state without crystallisation at conditions up to 1 GPa, which was then validated by MD simulation. After 100 ns, the molecules in biodiesel show apparent crystalline structure of ordered arrangement. It should be pointed out that nucleation is a rare event and complex molecules do not often crystallize spontaneously during simulation, thus extreme long-time scale trajectory is needed (Matsumoto et al., 2002) (Giberti et al., 2015b). FAME molecules can be regarded as the combination of ester function group and linear chain hydrocarbons as shown in Table 5.1. The crystalline system of biodiesel shows similar morphology in analogy with cooling induced nucleation of n-alkane (C8, C10, C20 and C30) (Zerze et al., 2013) (Luo et al., 2015) (Xu et al., 2020) and waxy crude oil (Chen et al., 2020), which have been described as crystalline blocks and are spatially segregated with different nucleus sizes and chain orientations.

When pressure is reduced to 250 MPa, the system has single bundle-like nuclei with stretched chains packed densely and oriented in the same direction. At conditions of 300

K-200 MPa and 350 K-300 MPa, there are no nucleus appear. Biodiesel has higher tendency in solidification than diesel at HP conditions as there is no nucleus appearing in diesel at 300 K and 300 MPa. HP solidified fluids are non-hydrostatic medium which has a sharply increased viscosity and ceased of diffusion (Prentice et al., 2020). Condensed fuels shift from liquid-like viscous fluid to solid-like elastic matter inside the nozzle indicating the occurrence of phase transition which will inevitably affect the subsequent spray and droplet breakup in a combustor chamber.

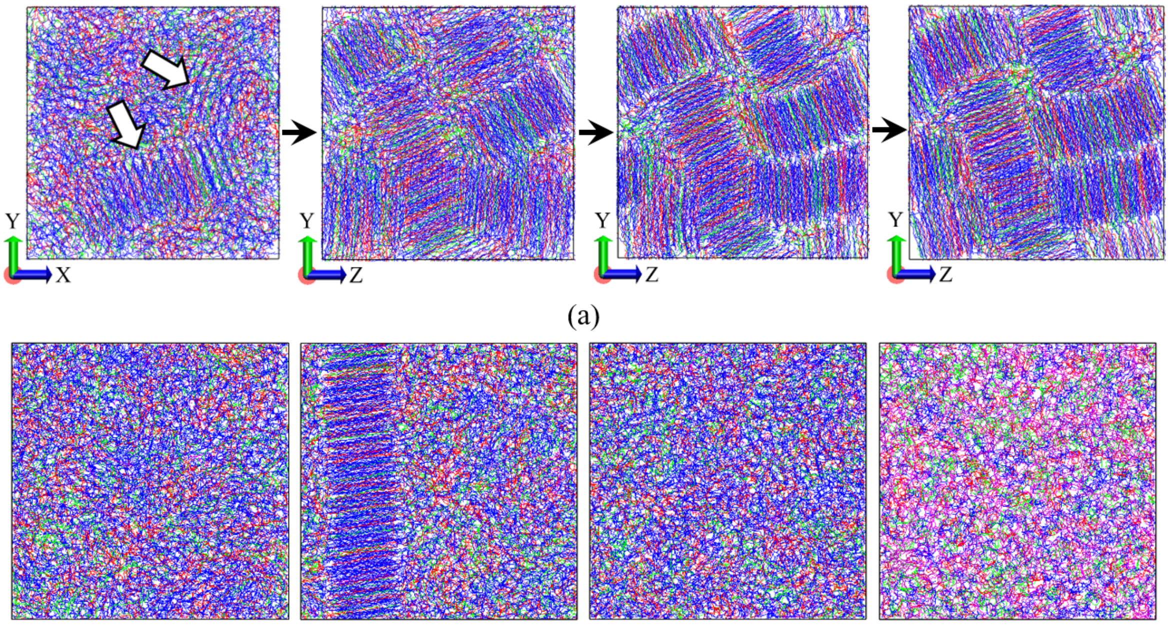

(a)

(b)

Fig. 5.2 (a) Time evolution of biodiesel morphology and molecular arrangement during nucleation at 300 K and 300 MPa, from left to right: 50 ns, 100 ns, 150 ns and 200 ns; (b) snapshots of systems after 200 ns simulation, from left to right: biodiesel at 300 K and 200 MPa, biodiesel at 300 K and 250 MPa, biodiesel at 350 K and 300 MPa, diesel at 300 K and 300 MPa.

RDF is widely used to quantify the local strucutre during phase transition. RDF is the probability of finding a particle at a separation distance r from the centre of the reference particle. In order to study the time evolution of modelling system during solidification, the sub-block average method is applied where the trajectory is divided into consecutive blocks and RDF is statistically averaged over the frames in the interval. The RDFs of centre of mass (COM) of fuel molecules distributed in Figure 5.2 are shown in Figure 5.3. Crystals are typically characterized by long-range order. For example, discrete peaks of RDF emerge at multiple coordination spheres with radial distance of σ, $\sqrt{2}\sigma$, $\sqrt{3}\sigma$, etc in reduced units in solid phase of monoatomic gas. For completely uniform distribution of particles, the local density is equal to the bulk density with RDF equal to 1 for all radial distances. Accumulation of particles leads to RDF > 1, while depletion makes RDF < 1. For biodiesel mixtures, the system stays amorphous in initial 40 ns and the RDF increases gradually to 1 at radial distance equal to 0.5 nm. During nucleation process between 40-80 ns, the first peak value of RDF is 2.17 at 0.47 nm, which then jumped to 4.48 between 80-120 ns. When crystallization terminates gradually after 100 ns, the first peak value still increases slowly to 6.01. The second and third peaks also emerge at 0.81 nm and 0.92 nm with small values due to the imperfect crystalline strucutre. RDF can also characterize the crystalline morphology with single nucleus of biodiesel at 300 K-200 MPa, which has a peak value of 2.78, smaller than biodiesel system at 300 K-300 MPa.

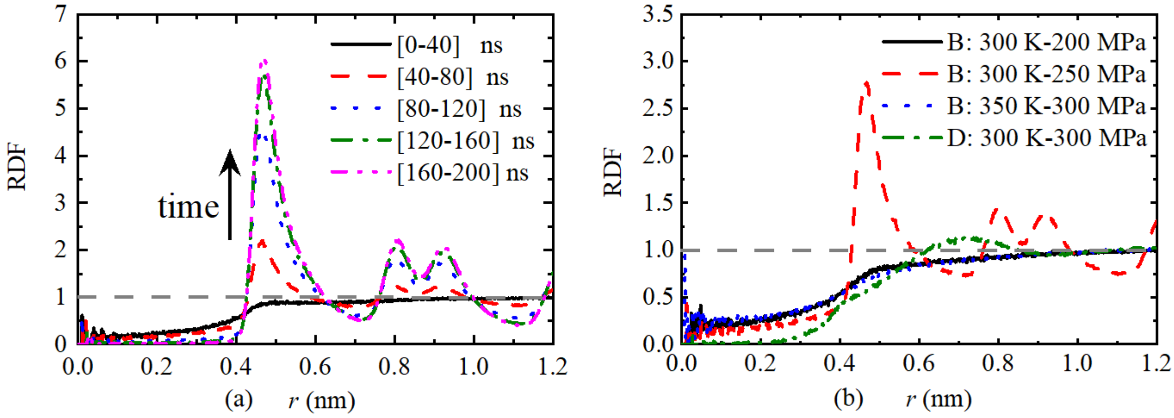

Fig. 5.3 (a) Time evolution of RDF of center of mass of biodiesel molecules at 300 K and 300 MPa during 200 ns simulation, RDF is averaged over each 40 ns interval; (b) RDF of systems corresponding to Figure 5.2 (b), averaged over last 40 ns trajectory, B indicates biodiesel an D indicates diesel.

RDF can be used to distinguish the evolution of local crystalline strucutre but not instantly. Collective variables like coordination numbers, SMAC and Steinhardt parameter, etc., are developed to enhance the sampling with metadynamics and to drive the phase separation process during nucleation (Giberti et al., 2015b) (Tribello et al., 2017) (Liu et al., 2020). They are also used to identify the molecular structures possessing a crystalline arrangement by analysing MD trajectories. Among collective variables, Steinhardt parameter (Steinhardt et al., 1983) is more applicable for biodiesel mixtures as it is a bond-based parameter. A set of nominal bonds, i.e., $\boldsymbol{R}_{ij}$ between central atom i and atoms within its coordination spheres is defined. The local environment around particle i can be characterised by the bond-orientational order parameter of $\boldsymbol{q}_{nm}(i)$ which is expressed as:

$$\boldsymbol{q}_{nm}(i) = \frac{\sum_{j \neq i}^{N} \sigma\left(r_{ij}\right) Y_{nm}\left(\boldsymbol{R}_{ij}\right)}{\sum_{j \neq i}^{N} \sigma\left(r_{ij}\right)} \tag{5.1}$$

where r_{ij} is the distance between atoms i and j, Y_{nm} is the n^{th} order spherical harmonics, m is a number that runs from $-n$ to $+n$, $\sigma\left(r_{ij}\right)$ is a switching function in rational form that acts on

r_{ij}. After averaging vector $\boldsymbol{q}_{nm}$ over all the harmonics with the given n value, the Steinhardt parameter in below equation can be used to measure the order degree of the coordination sphere. To compare the overall nucleation process between different systems, Steinhardt parameter is averaged over all particles.

$$Q_n(i) = \left(\frac{4\pi}{2n+1} \sum_{m=-n}^{n} |\boldsymbol{q}_{nm}(i)|^2 \right)^{1/2} \tag{5.2}$$

In general, Q_n is small when the coordination shell is disordered and large when the coordination shell is ordered. The sixth order Steinhardt parameter has been used to study the crystal growth process in MD system of n-Octant (C8) (Xu et al., 2020) and n-Eicosane (C20) (Anwar et al., 2013). The time evolution of relative Q_6 parameter of different system is shown in Figure 5.4, which is in accordance with the nucleation process in Figure 5.2. For amorphous system without nucleation, Q_6 parameters keep constant value at 1.0 while crystalline systems have higher value which corresponds to both the intra- bond orderings and inter- chain orderings. Comparing the crystallisation process of biodiesel at 300 MPa and 250 MPa, it is observed that after the long quiescent induction period, there is a linear increase period which corresponds to the free growth of crystals without impediment (Paajanen et al., 2019). As expected, biodiesel at 300 MPa has faster growth rate which is 1.74 times of the rate at 250 MPa. The difference the nucleation processes is that there is a transition period (t_4 - t_5) at 300 MPa which shows gradually reduced growth rate until termination. This is because the multiple nuclei limit each other's further growth in this stage.

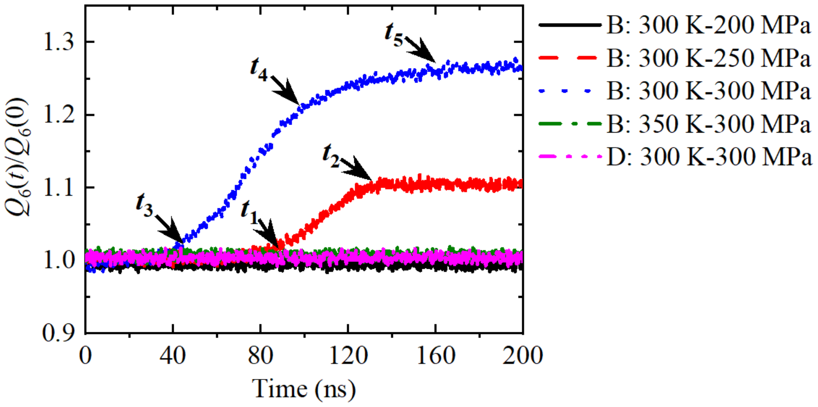

Fig. 5.4 Time evolution of relative Q_6 parameter to characterise the crystallinity of the modelling system, where the time points indicates different nucleation stages: t_1=85 ns, t_2=130 ns, t_3=40 ns, t_4=100 ns, t_5=160 ns.

5.3 Critical properties and surface tension

For prediction of critical property and surface tension based on VLE modelling, 2000 biodiesel (or diesel) molecules are distributed randomly in a rectangular box of $8 \times 8 \times 32$ nm in the x, y and z directions. After energy minimisation, annealing simulation is performed in semi-isotropic NPT ensemble with 1 fs time step. Pressure and compressibility in the x and y directions are set up as zero, while in the z direction, they are set up as 1 bar and 4.5e-5/bar respectively. The box is compressed in the z direction in cooling condition of 250 K for 0.5 ns and then expanded by increasing temperature to 300 K linearly in 1.5 ns. After that, system is maintained for 2 ns at 300 K for equilibrium. The liquid film generated is shown in Figure 5.5 (a). The second step is VLE simulation in NVT ensemble with 1fs time step. The z edge of box is scaled up 3 times based on the average length of the z edge during the last 1 ns trajectory in NPT simulation. The liquid film is then placed in the centre of the elongated box. The liquid film is heated from 300 K to the targeted temperature with a rate of 0.1 K/ps and then maintained for 10 ns at the temperature for production run. At each temperature, five statically independent simulations are replicated by setting the initial velocities randomly. Results are averaged over the final 5 ns of each individual trajectory. Snapshots of biodiesel and diesel after 10 ns NVT simulation are shown in Figure 5.5 (b) and (c).

As shown in Figure 5.5 (b) and (c), the vacuum space on both side of liquid films during VLE simulation makes the system inhomogeneous. Ignoring long-range dispersion force affects the modelling of vapour-liquid interfaces significantly, and leads to incorrect estimation of surface tension (mostly underestimate) (Ismail et al., 2007) (Fischer et al., 2015) (Morrow and Harrison, 2019) (Papavasileiou et al., 2019). The tail corrections for the two-phase simulation can range 50% - 7% as the cut-off radius changes from 2.1σ to 6.4σ in reduced unit (Ghoufi et al., 2016). In order to compensate the truncation of dispersion forces, one can increase the cut-off distance to 2-3 times of its normal value (Feria et al., 2020), or apply Ewald summation method for LJ interactions like PME (Fischer et al., 2015) (Morrow and Harrison, 2019) (Papavasileiou et al., 2019) or PPPM (in't Veld et al., 2007) (Isele-Holder et al., 2012). Mesh-based Ewald solvers were shown to be faster and more accurate than incorporating extremely large cut-off distances (Isele-Holder et al., 2013) (Morrow and Harrison, 2019). The geometric combination rules rather than Lorentz-Berthelot mixing is adopted for LJ interaction in the reciprocal space, so as to gain a significant increase in computational efficiency with a minor loss in accuracy (Isele-Holder et al., 2013). The same Fourier grid and interpolation order are used for both LJ-PME and electrostatic PME. The modelling of systems where dispersion interactions are simply truncated with cut-off distance of 1.4 nm is also performed in comparison with the LJ-PME method.

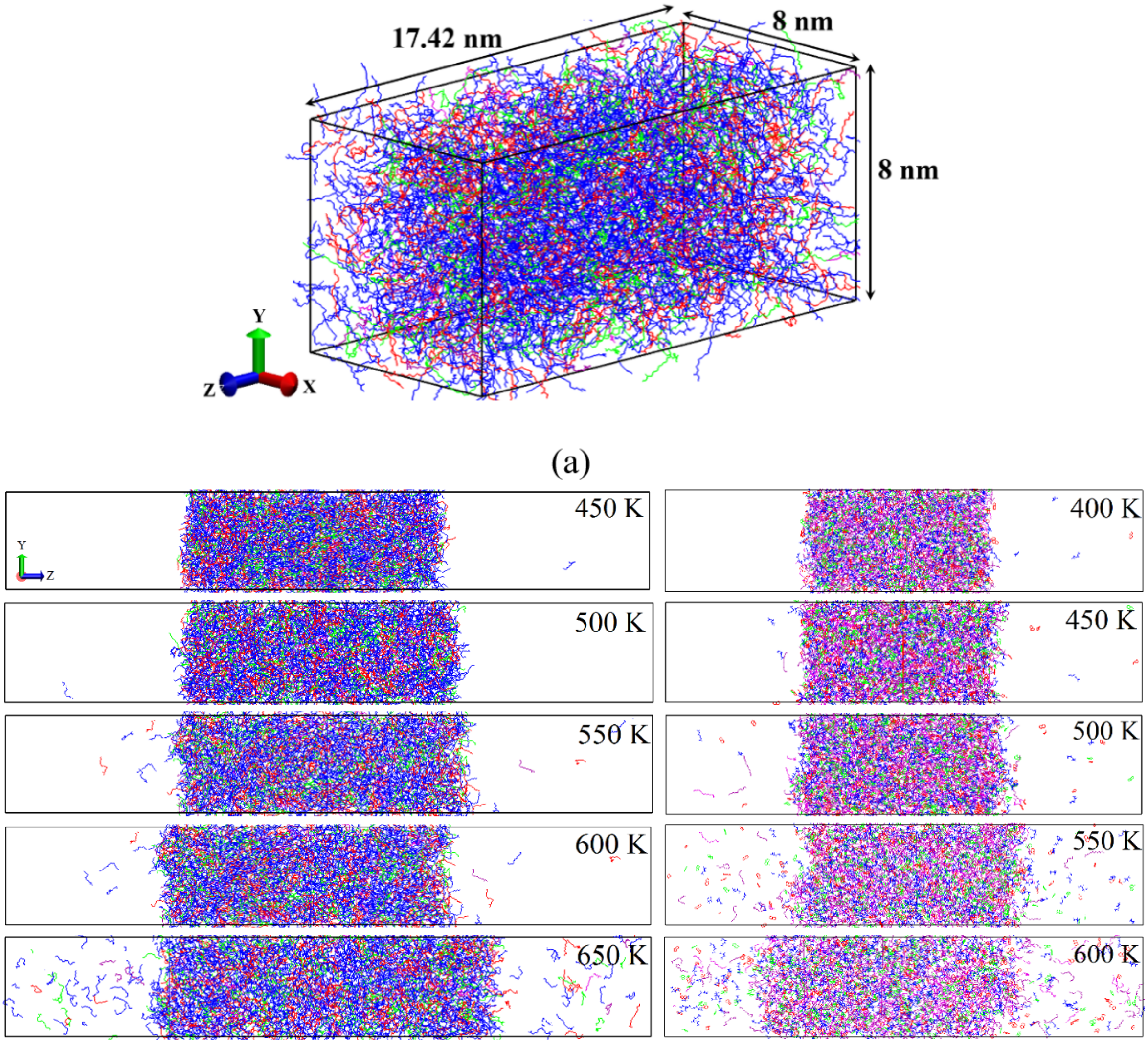
17.42 nm
8 nm
8 nm
Y
Z
X
Y
Z
450 K
500 K
550 K
600 K
650 K
400 K
450 K
500 K
550 K
600 K

(a)

(b)

(c)

Fig. 5.5 (a) Snapshot of biodiesel box after 4 ns annealing-equilibrium simulation in semi-isotropic *NPT* ensemble at 300 K and 0.1 MPa, where the box length of diesel in the z direction is 12.49 nm; (b) and (c) are snapshots of molecule distribution of biodiesel and diesel in VLE simulation with LJ cut-off distance of 1.4 nm.

The density profile of biodiesel and diesel along the z direction is shown in Figure 5.6 (a) - (b). To obtain the critical properties, the density of liquid and vapour phase, i.e. ρ_L and ρ_V, in VLE are obtained by fitting the density profile to the equation expressed as:

$$\rho(z) = \frac{1}{2}(\rho_L + \rho_V) - \frac{1}{2}(\rho_L - \rho_V)\tanh\left(\frac{2(z - z_0)}{d}\right) \tag{5.3}$$

where z_0, and d are the fitting parameters related to the position where the density is half between ρ_L and ρ_V, d is the width of the liquid-vapor interface.

Densities of fuel in liquid and gas phase are plotted in Figure 5.6 (c) - (d). Critical temperature (T_c) and critical density (ρ_c) are extrapolated using the density scaling law and the law of rectilinear diameters. Critical pressure (P_c) is estimated using ρ_L in the Rackett equation proposed by Messerly et al. (2016). The equations are expressed as:

$$\rho_L - \rho_V = A(T_c - T)^{\beta} \tag{5.4}$$

$$\frac{1}{2}(\rho_L + \rho_V) = \rho_c + B(T_c - T) \tag{5.5}$$

$$P_c = \frac{RT_c\rho_c}{M}\left(\frac{\rho_c}{\rho_L}\right)^{\left(1-\frac{T}{T_c}\right)^{\iota}} \tag{5.6}$$

where A and B are fitting parameters, β is the critical exponent with a universal value of 0.325 (Kamath et al., 2006) (Morrow and Harrison, 2019), R is the gas constant, M is the molecular mass, and ι is an empirical constant equal to 2/7 (Morrow and Harrison, 2019).

Critical properties of mixtures depend on molecular structure and composition. T_c increases with the number of carbons in the fatty acid chain, while P_c decreases with the chain length (do Carmo et al., 2015) (Evangelista et al., 2018). A theoretical method based on empirical equations developed by Kay and B. (1969) and Li (1971) is used to estimate critical temperatures and critical pressures of multicomponent fuels (Gong et al., 2021b) (Lin and Tavlarides, 2012). The equation for critical temperature of mixtures, $T_{c,m}$ is expressed as:

$$T_{c,m} = \sum_{i=1}^{n} \theta_i T_{c,i} \tag{5.7}$$

where n is the number of surrogate molecules, θ_i is the volumetric fraction of component i expressed as:

$$\theta_i = \frac{x_i V_{c,i}}{\sum_{i=1}^{n} x_i V_{c,i}} \tag{5.8}$$

where x_i and $V_{c,i}$ are the mole fraction and critical molar volume of component i.

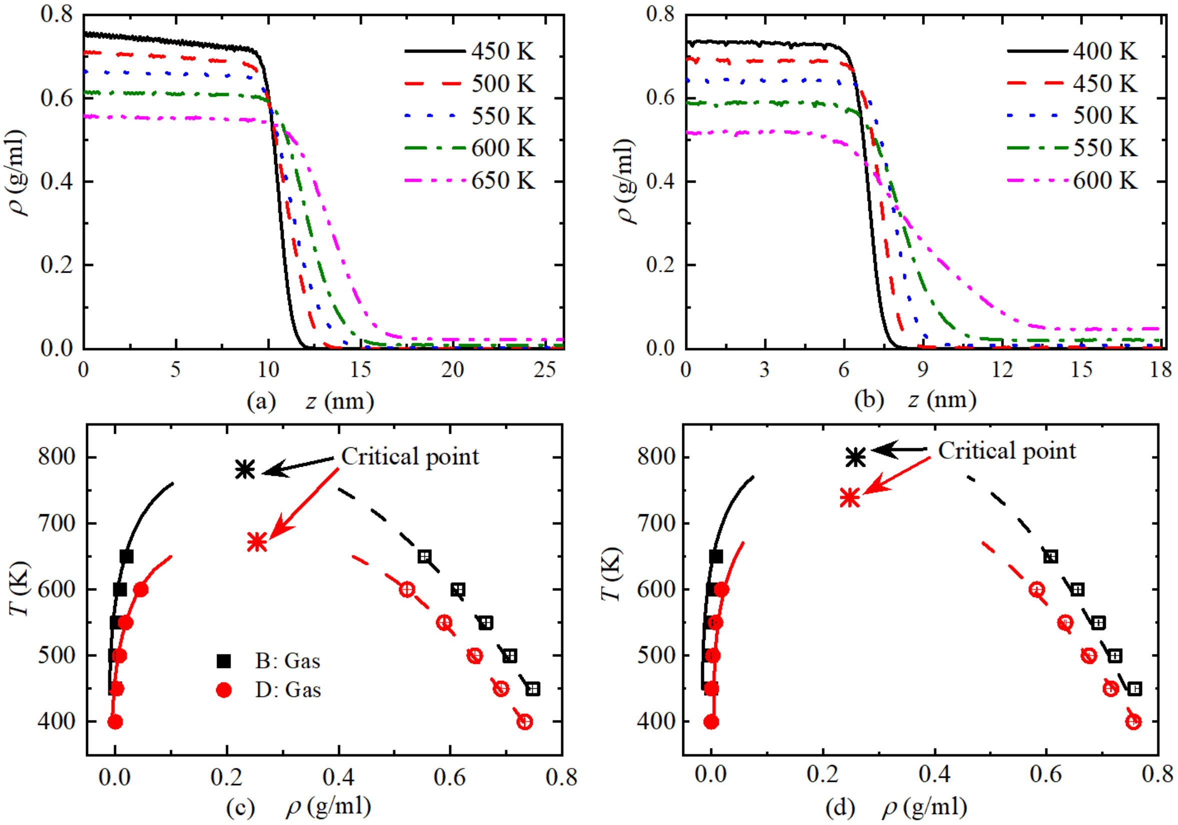

Fig. 5.6 Equilibrium fuel density profiles and vapour-liquid coexistence curves: (a) and (b) are density profiles of biodiesel and diesel across the liquid-vapour interface as a function of the distance from the centre of liquid film, corresponding to snapshots in Figure 5.5 (b) and (c); (c) and (d) are vapour-liquid coexistence curves of biodiesel and diesel with LJ cut-off distance of 1.4 nm and LJ-PME method. Results are averaged over five independent simulations, solid symbols are gas density while hollow symbols are liquid density, error bars are immersed within the symbols.

The equation for critical pressure $P_{c,m}$ of mixtures can be described as:

$$P_{c,m} = P_{pc}\left(1 + (5.808 + 4.93\omega_m)\frac{T_{c,m} - T_{pc}}{T_{pc}}\right) \tag{5.9}$$

where P_{pc} and T_{pc} are pseudo critical pressure and temperature, ω_m is the mean acentric factor. They can be expressed as the molar averages of all individual components:

$$T_{pc} = \sum_{i=1}^{n} x_i T_{c,i} \quad P_{pc} = \sum_{i=1}^{n} x_i P_{c,i} \quad \omega_m = \sum_{i=1}^{n} x_i \omega_i \tag{5.10}$$

The values of these parameters of biodiesel and diesel surrogate fuels are listed in the supplementary material as Table 5.2 and Table 5.3. The predicted critical properties of biodiesel and diesel are listed in Table 5.4. Biodiesel has higher critical temperature and lower critical pressure in all methods. For critical temperature, although overestimated slightly, LJ-PME can reproduce critical temperature better than simply truncated LJ interaction. Critical pressures estimated using Equation (5.6) show positive correlation with temperature, and are higher than theoretical results by a factor around 2. Compared with the results of Morrow and Harrison (2019) on critical property prediction of pure surrogate hydrocarbons of diesel, using MD-VLE simulation to predict the critical pressure of fuel mixtures is far from satisfactory.

Table 5.2 The parameters of biodiesel surrogate fuels, taken from the work of do Carmo et al. (2015).

FAME	T_c (K)	P_c (MPa)	V_c (cm^3/mol)	ω
MP	769	1.379	1022	0.8341
MS	790	1.257	1135	0.8870
MO	792	1.278	1115	0.8475
ML	793	1.305	1094	0.8094
MLN	794	1.332	1073	0.7639

For supercritical combustion, the disappearance of surface tension of droplet will change the conventional two-phase evaporation to diffusion dominated mixing process. The primary method to compute surface tension in MD simulation was developed by Tolman (Tolman, 1948) and then refined by Kirkwood and Buff (Kirkwood and Buff, 1949). It computes the surface tension as an integral of the difference between the normal and tangential pressures:

$$\gamma = \frac{1}{2}\int_{-\infty}^{\infty} \left(P_{\perp}(z) - P_{\parallel}(z)\right) dz \tag{5.11}$$

Table 5.3 The parameters of diesel surrogate fuels, taken from the work of Lin and Tavlarides (2012).

Hydrocarbons	T_c (K)	P_c (MPa)	V_c (cm^3/mol)	ω
n-HXD	723	1.40	1034	0.7180
n-OTD	747	1.29	1189	0.8000
HMN	693	1.57	863	0.5480
DCA	687	3.20	480	0.3030
1-MNT	772	3.60	462	0.3480

Table 5.4 Comparison between MD and empirical equation on prediction of critical properties of biodiesel and diesel.

	T_c (K)		P_c (MPa)		ρ_c (g/ml)
	Theoretical results	MD	Theoretical results	MD	MD
Biodiesel	792	782*	1.32	[2.06-3.05]*	0.23*
		800#		[2.50-3.44]#	0.26#
Diesel	722	672*	2.15	[3.15-4.87]*	0.25*
		739#		[3.13-4.50]#	0.25#

*: LJ cut-off distance of 1.4 nm, #: LJ-PME

where $P_{\perp}(z)$ is the pressure component normal to the surface and $P_{||}(z)$ is the pressure component parallel to the surface. In the case of an interface between two fluid phases, the integral in equation (14) can be replaced with an ensemble average of the difference between the normal and tangential pressures (in't Veld et al., 2007), using the equation expressed as:

$$\gamma = \frac{1}{2} L_z \left(\langle P_{zz} \rangle - \frac{1}{2} \left(\langle P_{yy} \rangle + \langle P_{xx} \rangle \right) \right) \tag{5.12}$$

where L_z is the length of the box in z axis, P_{ii} is the diagonal component of the pressure tensor, $\langle \cdots \rangle$ in is an average over the canonical ensemble.

Both the chain length and unsaturation degree affect the surface tension of pure FAMEs. Generally, the surface tension of FAMEs increases with the increase in unsaturation degree and molecular mass (Thangaraja et al., 2016). Phankosol et al. (2014) developed an empirical equation to estimate surface tension of biodiesel mixtures at temperatures between 30 and 80 °C according to FAME composition.

$$\gamma = 60.211 - 0.4307 N_C - 0.1125 T + 0.00207 N_C T + 3.676 N_= - 0.00893 N_= T \tag{5.13}$$

where N_C and $N =$ are average numbers of carbon atoms and double bonds of biodiesel mixtures.

The surface tension of biodiesel and diesel at different temperatures is shown in Figure 5.7. The surface tensions decrease linearly with increase of temperature (Chhetri and Watts, 2013) (Thangaraja et al., 2016) (Das et al., 2018b). The surface tension obtained from MD-VLE simulation with LJ cut-off distance of 1.4 nm can be 28.78%-70.37% lower than results of LJ-PME, and the absolute relative deviation increases with temperature. Surface tension of biodiesel estimated from LJ-PME approximates closer to the results from empirical method. The surface tension of biodiesel is significantly higher than fossil diesel and hence causes poor atomization characteristics when injected into the combustion chamber.

5.4 Transport properties of fuel mixtures using EMD

5.4.1 Density

Fuel density is the main property that affects the injection process, such as total mass injected and pressure wave in the common-rail system (Boudy and Seers, 2009). The predicted density of biodiesel and diesel is shown in Figure 5.8. After comparing with different force field like LOPLS, Lipid14 and MARTINI, it was observed that the TraPPE can reproduce the

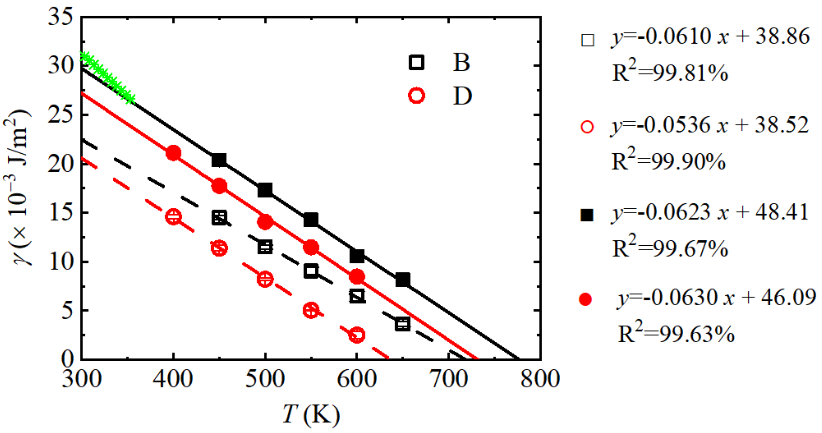

Fig. 5.7 Vapour-liquid surface tension of biodiesel and diesel as a function of temperature, where hollow symbols are results of LJ cut-off distance of 1.4 nm, solid symbols are results of LJ-PME, the solid and dashed lines are fitting results, green asterisk indicates biodiesel surface tension estimated using empirical equation, and the corresponding fitting equations are also listed.

density of alkanes exactly (only 1% deviation from experiments) (Papavasileiou et al., 2019). MD systems with 2000 biodiesel (or diesel) molecules are equilibrated in *NPT* ensemble for 500 ps, and densities are the averaged results over the last 200 ps trajectories. For fuels at isothermal conditions, density is fitted according to the Tait correlation (Dymond and Malhotra, 1988) expressed as:

$$\frac{\rho-\rho_0}{\rho}=A\log\left(\frac{B+P}{B+P_0}\right) \tag{5.14}$$

where ρ_0 is a density at P_0 which is 10 MPa here, A and B are fitting parameters.

At isothermal conditions, density of biodiesel is 5.39% and 5.43% higher than diesel as a whole at 300 K and 400 K respectively. The effect of pressure on relative difference of biodiesel and diesel is weaker with increase of pressure. The relative difference between biodiesel and diesel at isobaric condition of 5 MPa increases sharply from 6.69% at 400 K to 86.55% at 900 K and then decrease gradually to 42.17% at 1500 K. However, at 15 MPa, the relative difference increases gradually from 6.13% at 400 K to 25.68% at 1500 K.

5.4.2 Viscosity

There are basically two equivalent methods on viscosity prediction in EMD, i.e., the Green-Kubo and Einstein equations. In analogy with the diffusion coefficient in the Einstein equation, viscosity can be expressed as the mean-square “displacement” (MSD) of the time

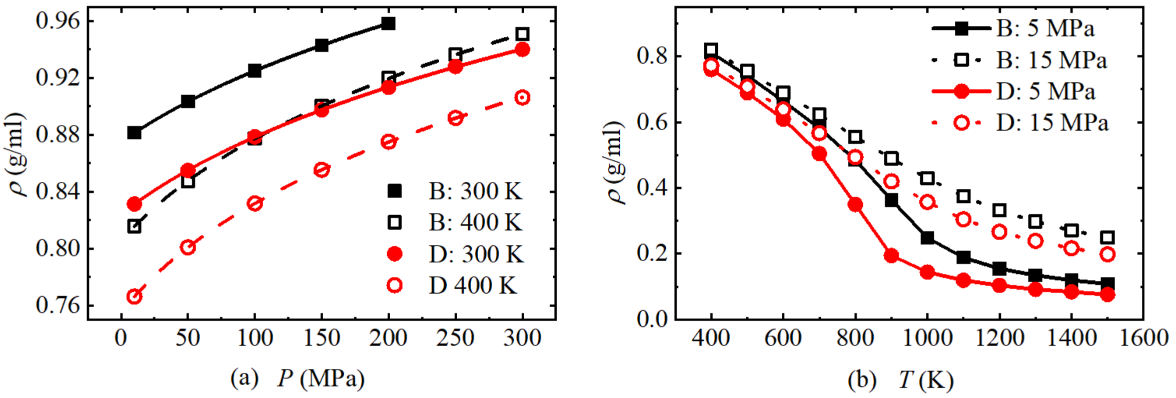

(a) P (MPa) (b) T (K)

Fig. 5.8 Pressure and temperature dependence of density of biodiesel (B) and diesel (D), densities of biodiesel at 300 K - 250 MPa and 300 K - 300 MPa are not included due to the HP solidification, lines in (a) are fitting results while lines in (b) are connection between the scattered data points.

integral of the pressure tensor (Chen et al., 2009) (Mondello and Grest, 1997):

$$\eta = \frac{V}{2k_BT} \lim_{t\to\infty} \frac{d}{dt} \left(\left\langle \sum_{\alpha\beta} \left(L_{\alpha\beta}(t) - L_{\alpha\beta}(0)\right)^2 \right\rangle \right) \tag{5.15}$$

where $L_{\alpha\beta}$ is expressed as:

$$L_{\alpha\beta}(t) = \int_0^t P_{\alpha\beta}\left(t'\right) dt' \tag{5.16}$$

It was observed that there was no dependence on system size when calculating viscosity and thermal conductivity in EMD simulation (Moultos et al., 2016) (Yang et al., 2019). MD systems containing 2000 fuel molecules are equilibrated in *NPT* ensemble for 500 ps at targeted conditions. Production run of 2ns simulation in *NVT* ensemble is followed. According to previous studies, both methods converge very slowly, because of the heavy pressure fluctuation during the simulation (Hess, 2002) (Hess, 2002).

To better understand the convergence of viscosity, 40 statistically independent trajectories are replicated with molecules in each system having different initial velocity distribution. The viscosity of biodiesel at extreme conditions using the GK and Einstein method is shown in Figure 5.9. Each viscosity curve using the GK equation shows the same time evolution pattern of increasing at initial stage and then reaching the plateau with severe noise. The deviation between each viscosity curves escalate dramatically with time, and the standard deviation would increase with integration time in a power law function (Zhang et al., 2015). The deviation between the "MSD" curves also increases with time in the Einstein method. The averaged viscosity curves in GK methods show good convergence with stable flat regions in late stage. Viscosity is a collective property, and sufficient independent trajectories are

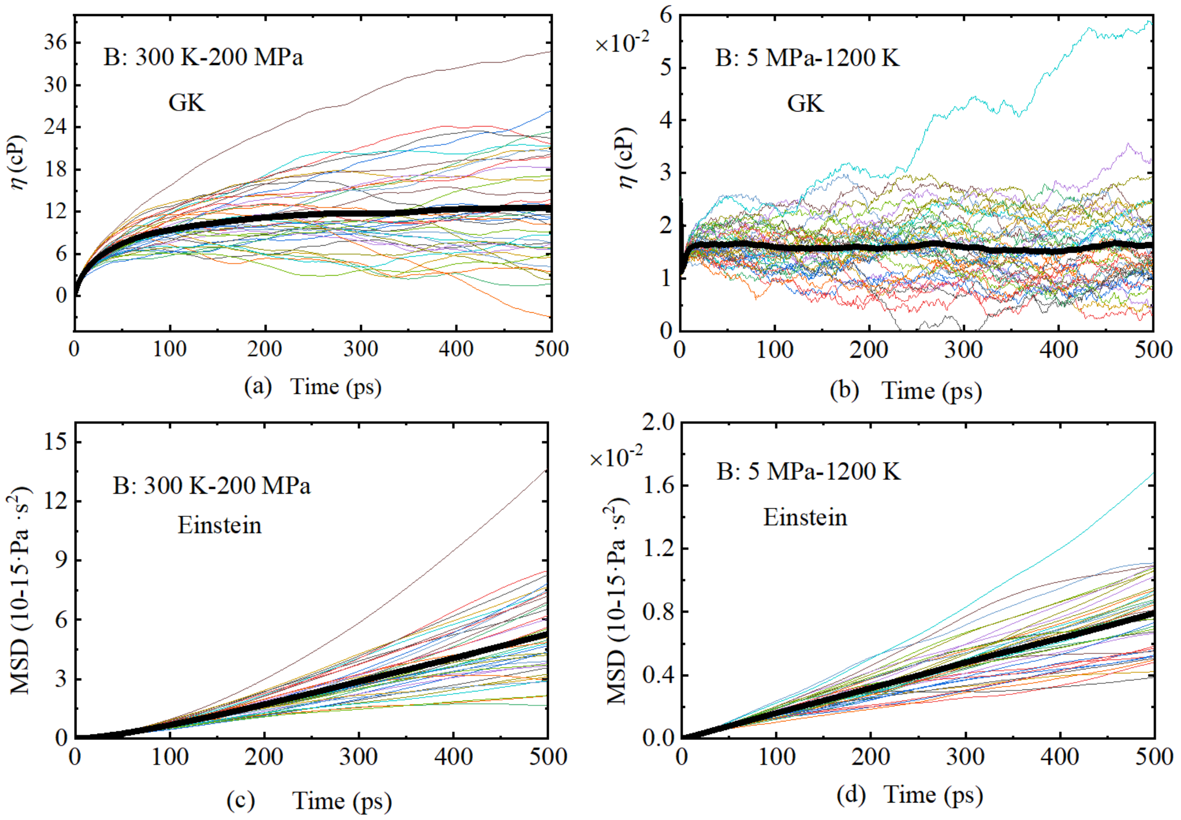

Fig. 5.9 Viscosity of biodiesel at extreme conditions using the GK and Einstein method, coloured thin lines are results of 40 statistically independent trajectories, black thick lines are the averaged results, the slopes of MSD in (c) and (d) are viscosities.

indispensable when estimating viscosity from the averaged values of running integrals in EMD simulation.

To calculate the viscosity rigorously (instead of identifying the plateau region manually), the averaged running integral is fitted a double exponential function developed by Zhang et al. (2015), i.e.,the time decomposed method (TDM). The viscosity of biodiesel and diesel as a function of temperature and pressure are calculated using the GK-TDM method, with the results shown in Figure 5.10. The 2ns trajectory is long enough for time integration in all conditions. The pressure dependence of GK viscosity is then fitted according to equation developed by Kashiwagi and Makita (Kashiwagi and Makita, 1982):

$$\ln \frac{\eta(P)}{\eta_0} = A \ln \left(\frac{B+P}{B+P_0} \right) \tag{5.17}$$

where η_0 is the shear viscosity at pressure P_0 = 10 MPa, A and B are the fitting parameters.

The temperature dependence of viscosity are fitted according to the following equations by Das et al. (2018b):

$$\eta(T) = \exp\left(\frac{A}{T-B}\right) - C \tag{5.18}$$

where A, B and C are fitting parameters.

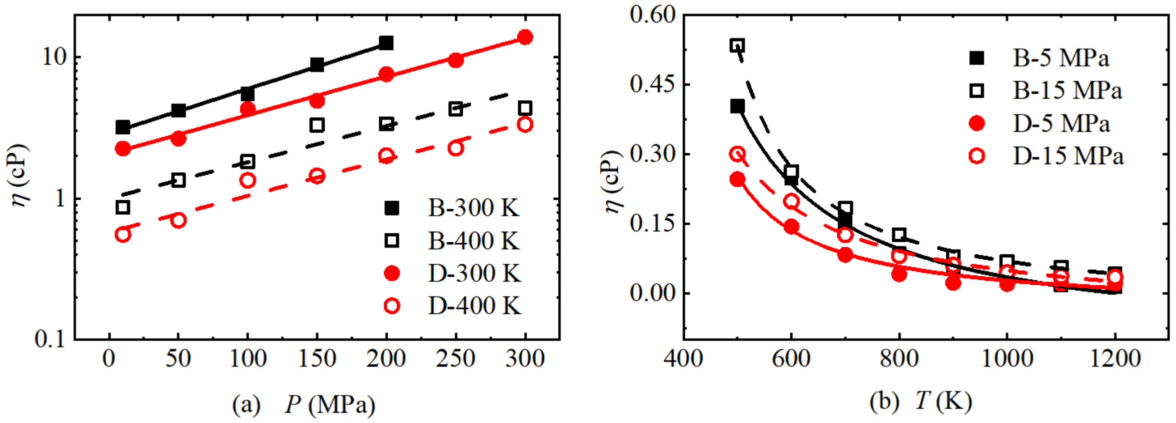

Fig. 5.10 Pressure and temperature dependence of viscosity of biodiesel and diesel, lines are fitting results.

At isothermal conditions of 300 K and 400 K, the viscosity of biodiesel is higher than diesel by a factor of 1.3-2.3. Viscosity is also greatly affected by temperature. Although absolute difference between biodiesel and diesel diminished rapidly at isobaric conditions, the relative difference at 15 MPa is still among 20.43%-52.81% at temperature above 900 K. Molecular configurations of FAMEs affect viscosity in terms of unsaturation degree, cis-trans isomerism, and location of double bond. FAMEs with higher unsaturation have lower viscosity, and trans-configuration will lead to higher viscosity than cis-configuration, while the location of double bond has the least effect (Hoekman et al., 2012). It is desired for a fuel to possess optimum kinematic viscosity. Fuel with excessive viscosity will have poor cold flow property, narrow injection angle, poor atomization characteristics and large droplet sizes, thus ultimately results in the incomplete combustion and high emissions (Hoekman et al., 2012). Fuel with lower viscosity fails to provide sufficient lubrication and leads to the increased wear.

5.4.3 Thermal conductivity

The thermal conductivity (κ) of fuel is calculated according to the GK method, which is expressed as the ensemble average of auto correlation function of the heat flux:

$$\kappa = \frac{V}{k_B T^2}\int_0^\infty \langle q_x(0)\cdot q_x(t)\rangle\, dt = \frac{V}{3k_B T^2}\int_0^\infty \langle \boldsymbol{q}(t)\cdot \boldsymbol{q}(0)\rangle \mathrm{d}t \tag{5.19}$$

where $\boldsymbol{q}$ is heat flux computed from per-atom kinetic energy, potential energy and stress tensor by the following equations:

$$\boldsymbol{q} = \frac{1}{V}\left(\sum_{i=1}^{N}(ke_i + pe_i)\,v_i - \sum_{i=1}^{N} S_i v_i\right) \tag{5.20}$$

where the first term inside the bracket corresponds to the kinetic and potential energy of atom i, N is the total number of atoms in the system, and S_i is the per-atom stress tensor, the term v_i multiplying the energy contributions is the atom velocity vector (Aimoli et al., 2014). It should be noted that the second term in Equation (5.20) includes contributions that come from the non-bonded interactions of vdW and Coulomb, as well as contributions from the bond stretching, angle bending and dihedral (Nazarychev et al., 2021). The recently observed corrections on heat flux was not considered in this study in terms of the deficiency of current atomic stress approximation in dealing with the contributions from many-body interactions like angle and dihedral (Surblys et al., 2019) (Boone et al., 2019).

The convergence of thermal conductivity of biodiesel at extreme conditions and the effect of pressure and temperature on thermal conductivity are shown in Figure 5.11. The running integral shows high frequency and heavy fluctuation in initial stage which is negligible in viscosity. Similar to viscosity, the convergence time of running integral of heat flux in HP condition is at around 200 ps which is longer than that of HT condition which is at around 10 ps. However, unlike viscosity, thermal conductivity can converge steadily at both HP condensed condition and supercritical gas phase. This indicates that averaging the running integral of massive multiple independent trajectories can be avoided. Thermal conductivity is the averaged value over the last 200 ps correlation time in each trajectory.

At isothermal conditions with pressure ranging 10-300 MPa, pressure dependence of fuel thermal conductivity is not prominent. The difference between biodiesel and diesel at isothermal condition mainly exists at pressure below 200 MPa, where biodiesel has lower thermal conductivity than diesel. At isobaric condition with temperature ranging 500-1200 K, thermal conductivity correlates strongly with temperature, which decreases almost linearly with the increase of temperature. Diesel has higher thermal conductivity than biodiesel with the range of 30.48% - 59.63% at 5 MPa and 41.68% - 50% at 15 MPa. At supercritical dense gas phase above 800 K, fuel thermal conductivity at 15 MPa is clearly higher than that at 5 MPa.

The difference between biodiesel and diesel on thermal conductivity would affect the mixing process in supercritical combustion due to the coupling effects between thermal conductivity, temperature gradient and thermal diffusion (i.e., Soret effect). Different transport processes (heat flux and species flux) induced by different thermodynamic forces interfere

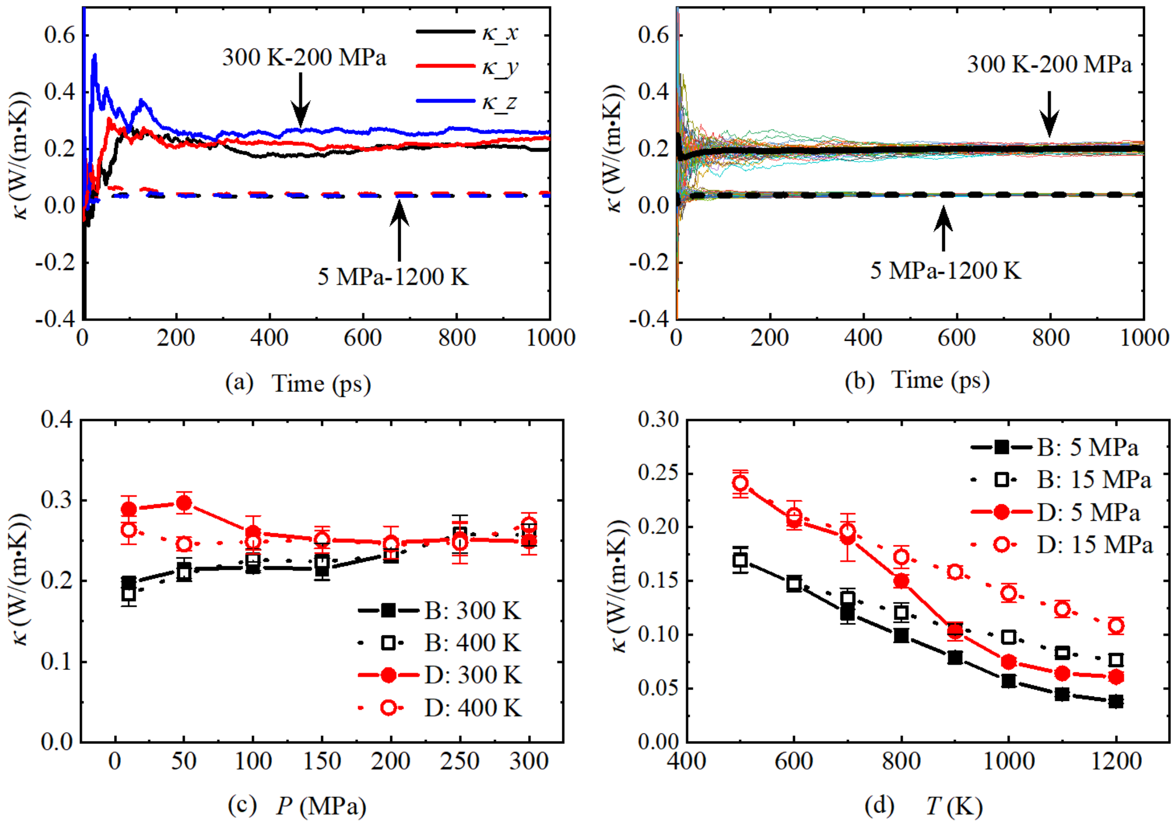

Fig. 5.11 (a) Thermal conductivity of biodiesel at extreme conditions using the GK method with simulation performed in NVT ensemble; (b) results of 40 independent replicated trajectories; (c) - (d) pressure and temperature dependence of thermal conductivity of biodiesel and diesel. The values are averaged over five independent trajectory, some error bars are immersed in symbols.

with one another in irreversible thermodynamics and Onsager reciprocal relations (Jofre and Urzay, 2021). For instance, in addition to causing heat conduction, temperature gradients also induce mass transport through the Soret effect.

The standard heat flux is expressed as:

$$\boldsymbol{q} = -\frac{\Lambda_{q,q}}{T^2}\nabla T + \sum_{i=1}^{N-1}(h_i - h_N)\boldsymbol{J}_i - \sum_{k=1}^{N-1}\frac{\Lambda_{q,k}}{T}\nabla_T(\mu_k - \mu_N) \tag{5.21}$$

The standard species diffusion flux is expressed as:

$$\boldsymbol{J}_i = -\sum_{k=1}^{N-1}\frac{\Lambda_{i,k}}{T}\nabla_T(\mu_k - \mu_N) - \frac{\Lambda_{q,i}}{T^2}\nabla T \tag{5.22}$$

where $\boldsymbol{J}$ is species flux, h is specific enthalpy, μ is specific chemical potential, Λ represents Onsager coefficient, $\Lambda_{q,q} = \kappa T^2$ participates in heat transfer in Fourier function of first term in Equation (5.21), $\Lambda_{q,i}$ is involved in the computation of the Soret and Dufour effect. For binary mixtures, $\Lambda_{q,i}$ is related to binary diffusion coefficient via thermal-diffusion ratio of k_T.

Soret effect is known to be important, particularly when large ratio of the molecular mass of pure compounds are present in fluids. Typically, Soret effect tends to drive lighter molecules towards hot regions and heavier molecules towards cold regions of the flow.

The effect is not only restricted in diffusion of H and H_2 in H_2/air flames. Rosner et al. (2000), Dworkin et al. (2009) and Liu et al. (2017a) demonstrated the importance of Soret effect in describing flame properties concerning its transport effects on heavy fuels and combustion intermediates including soot precursors like PAHs. A modelling study on $C_{12}H_{26}/N_2$ mixtures observed that although the effect is only fractional compared with species flux contributed from composition gradients, the positive value of k_T indicates that $C_{12}H_{26}$ tends to migrate towards cold flow zones, thereby sharpening the transcritical interfaces (Jofre and Urzay, 2021). In supercritical combustion, the effect of thermal diffusion should be re-examined. It is recognised as quantitatively significant because of the vanishing of Fickian diffusion in first part of Equation (5.22) (Bellan, 2000) (Palle and Miller, 2007) (Xin et al., 2012).

5.5 Capability of NEMD on transport properties

5.5.1 Periodic perturbation-NEMD method on viscosity prediction

NEMD method can potentially avoid the high computational cost associated with the replicated trajectories in EMD simulation. In general, a perturbation is needed which can be generated by imposing a linear velocity gradient along the shear direction or applying a momentum flux (Papavasileiou et al., 2019). In periodic perturbation (PP) method adopted in this study, external force is applied to the particles in MD system and then the viscosity from the perturbation of the induced momentum is measured (Hess, 2002). PP-NEMD method has been used to predict the shear viscosity of alkanes, alcohols and sulfur compounds, etc., in various force field and shown promising performance (Zhao et al., 2007) (Zhao et al., 2008) (Papavasileiou et al., 2019) (Zhu et al., 2021).

A periodic external force characterized by acceleration a is applied in the x direction on each particle, which is a function of the z coordinate as shown in Figure 5.12. The external forces in the y and z direction, a_y and a_z, are zero. Since v_y and v_z are zero, and there is no pressure gradient in the x direction, for a Newtonian liquid adding a small force will result in a velocity gradient as expressed in the following equation:

$$a_x(z) + \frac{\eta}{\rho}\frac{\partial^2 v_x(z)}{\partial z^2} = 0 \tag{5.23}$$

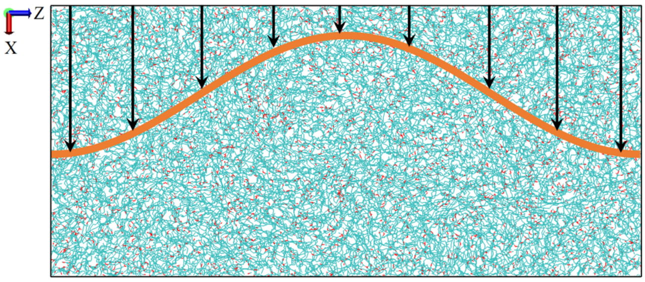

Fig. 5.12 Schematic plot of acceleration implementation along the z direction on each of the particles, black arrow indicates the direction and amplitude of acceleration.

In simulation with a periodic boundary condition, the acceleration a and velocity v should also be periodic. To satisfy both conditions mentioned above, the cosine function was applied. The acceleration profile is described as:

$$a_x(z) = A\cos\left(\frac{2\pi z}{L_z}\right) \tag{5.24}$$

where A is the amplitude of the periodic profile, L_z is box length in the z direction and $2\pi/L_z$ is the wavelength. The generated velocity profile is expressed as:

$$v_x(z) = V\cos\left(\frac{2\pi z}{L_z}\right) \tag{5.25}$$

where the amplitude V can be readily evaluated from the simulated velocity profiles:

$$V = A\frac{\rho}{\eta}\left(\frac{L_z}{2\pi}\right)^2 = \frac{\sum_{i=1}^{N} m_i v_{i,x} 2\cos\left(\frac{2\pi z}{L_Z}\right)}{\sum_{i=1}^{N} m_i} \tag{5.26}$$

Subsequently, the shear viscosity is obtained using the following formula:

$$\eta = \frac{A}{V}\rho\left(\frac{L_Z}{2\pi}\right)^2 \tag{5.27}$$

It is suggested that elongated box length in the z direction can reduce the wavelength dependence of the viscosity (Hess, 2002) (Papavasileiou et al., 2019) (Boone et al., 2019). To this end, initial box is built using same methodology with the generation of liquid film in VLE simulation. A series of 1 ns - NVT production run with time step of 1fs is performed. The time for liquids to build-up the desired velocity profile from the initial equilibrium state is of the order of the molecular relaxation time (Hess, 2002). For example, molecular rotation correlation time of alkanes like n-Hexadecane ($C_{16}H_{34}$) at ambient condition is around 300 ps (Mondello and Grest, 1997). The heat generated through the viscous friction is removed by coupling to the Nose-Hoover thermostat.

The capability of PP-NEMD is tested on system at ambient condition of 313.15 K - 0.1 MPa. Seven NVT simulations were performed with acceleration amplitude A ranging from 0.002 to 0.03 $\mathrm{nm \cdot ps^{-2}}$. The results of viscosity are shown in Figure 5.13. For very small acceleration amplitudes of 0.002 $\mathrm{nm \cdot ps^{-2}}$, the viscosity shown heavy fluctuation with high frequency and even unphysical negative values, while for large force with 0.02 $\mathrm{nm \cdot ps^{-2}}$ and 0.03 $\mathrm{nm \cdot ps^{-2}}$, viscosity reduces gradually in initial 100 ps and then reach steady response region with extreme low values. Viscosity fluctuation is weakened with increase of acceleration amplitudes. It is essential to determine the appropriate acceleration amplitudes. On the one hand, acceleration amplitudes should be small enough so that the perturbation does not disturb the equilibrium of the system. On the other hand, if the external force is too weak to develop a stable drift-velocity profile, the consequent signal-to-noise ratio will be too low (Zhao et al., 2007) (Zhao et al., 2008) (Papavasileiou et al., 2019). Too large amplitude will cause the system to move far from equilibrium (Papavasileiou et al., 2019).

Statistical uncertainty in viscosity prediction is quantified by block averaging method, where time-serial data set is divided in a number of blocks and averages are calculated for each block. The standard deviation among the block averages is used to estimate the overall standard deviation. As the block length increases, block averages are expected to be uncorrelated. The blocking procedure is performed iteratively from an initial very short block length until the blocked standard deviation reaches its plateau (Hess, 2002) (Grossfield and Zuckerman, 2009). Heavy fluctuation in viscosity with low force perturbation shows high statistical uncertainty as indicated in Figure 5.13 (b).

To determine the viscosity, a linear dependence of the calculated shear viscosities with respect to the applied perturbation forces is identified. Extrapolation of the linear fitting to zero perturbation force is the shear viscosities for the "undisturbed" fluids (Zhao et al., 2007) (Zhao et al., 2008) (Papavasileiou et al., 2019). Viscosity of PP-NEMD is 3.14 cP which is 16.49% lower than 3.76 cP estimated by the GK-EMD method. The PP-NEMD result is not closer to experimental results considering that the TraPPE force field underestimates viscosity intrinsically in the GK-EMD results (Kondratyuk et al., 2020a).

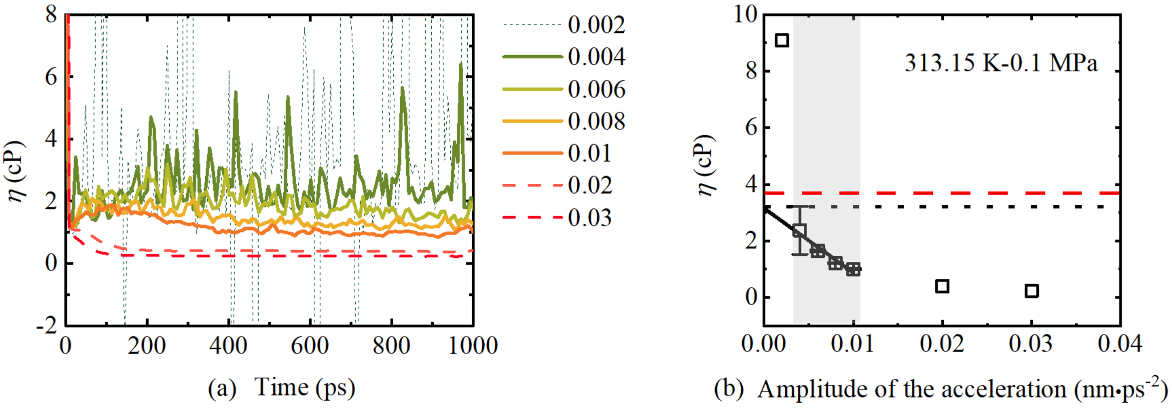

(a) Time (ps) (b) Amplitude of the acceleration (nm•ps^{-2})

Fig. 5.13 (a) Time evolution of biodiesel viscosity using PP-NEMD method at 313.15 K and 0.1 MPa with different acceleration amplitude; (b) comparison of biodiesel viscosity between GK-EMD (red dashed line) and PP-NEMD (black dot line), viscosity is the averaged value over last 500 ps trajectories which is steady for data collection, where the shaded area indicates the values for linear regression, error bars are obtained by data blocking method.

Prediction of biodiesel viscosity using the PP-NEMD method at extreme conditions is shown in Figure 5.14. Both molecular transverse relaxation time and rotational relaxation time correlate with pressure following the free-volume theory (Freed, 2007) (Freed, 2009) (Falk et al., 2020), which means that biodiesel at HP compressed condition takes longer time to reach steady state. For biodiesel at 300 K - 200 MPa, even applying high amplitude of 0.01 $\mathrm{nm \cdot ps^{-2}}$, heavy fluctuation still exits apparently with negative values. When increasing the amplitude further to the values above 0.015 $\mathrm{nm \cdot ps^{-2}}$, the force is too large to maintain the system equilibrium, and viscosity decreases to extremely low value after 600 ps. An

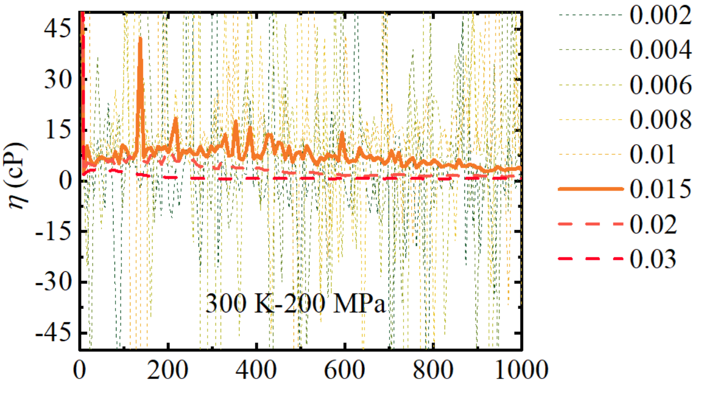

(a)

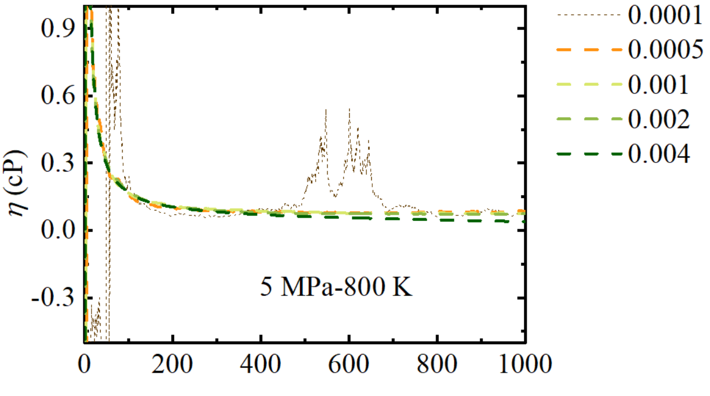

(b)

Fig. 5.14 Time evolution of biodiesel viscosity at extreme conditions with different acceleration amplitude: (a) biodiesel at 300 K - 200 MPa; (b) biodiesel at 5 MPa - 800 K.

appropriate amplitude should exist between 0.01 and 0.015 $\mathrm{nm \cdot ps^{-2}}$. The same behavior also occurs at HT dense gas phase, with an appropriate amplitude existing between 1e-4 and 5e-4 $\mathrm{nm \cdot ps^{-2}}$. It should be noted that too narrow an amplitude range would also lead to the unreliable fitted results.

5.5.2 Reverse NEMD method on thermal conductivity prediction

To calculate thermal conductivity κ in the NEMD simulation according to Fourier's law, i.e., $\boldsymbol{q} = -\kappa \nabla T$, one can impose temperature gradient in a simulation box and then measure the resulting heat flux. Or using the reverse NEMD (rNEMD) approach by Müller-Plathe (Müller-Plathe, 1997), in which the heat flux is created in a system by exchanging the kinetic energy between atoms located in different regions of a simulation box as shown in Figure 5.15. rNEMD has been applied to predict the thermal conductivity of paraffin, benzene and cyclohexane, etc. (Zhang et al., 2005) (Nazarychev et al., 2021). To be specific, a simulation box is divided into 20 bins in the z direction. The first slab is set to be the cold layer, while the central 11^{th} slab is set to be the hot layer. By exchanging the velocity of hottest atom in cold slab with that of coldest atom in hot slab, an artificial energy transfer from the cold slab to the hot slab is imposed. After reaching steady state, the heat flux from hot side to cold side is balanced with the total kinetic energy transferred by these swaps. The thermal conductivity is the ratio of heat flux to the slope of the temperature profile:

$$\kappa = \frac{\sum_{transfer} ke}{2L_x L_y \Delta t} \left(\frac{\mathrm{d}T}{\mathrm{d}z} \right)^{-1} \tag{5.28}$$

where heat flux is equal to the transferred total energy divided by time and the cross-sectional area of the simulation box, the temperature gradient is determined by calculating the temperature T of each bin:

$$T = \frac{1}{3N_b k_B} \left\langle \sum_{i=1}^{N_b} m_i v_i^2 \right\rangle \tag{5.29}$$

where N_b is the number of atoms in each slab.

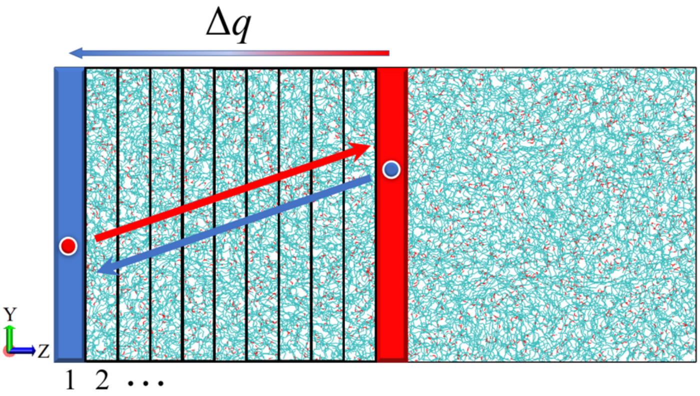

Fig. 5.15 A schematic representation of the exchange of the kinetic energy between the atoms in hot (red) slab and cold (blue) slab of a simulation box in rNEMD simulation.

Simulation box of liquid film is established in LAMMPS by specifying the pressure tensor of the z component only, and the volume in the z direction is varied independently during simulation. Simulations are performed in NPT ensemble for 2 ns where pressure and temperature ramp from 250 K and 1 bar to the targeted temperature and pressure in 1ns, and then followed by a second 1ns simulation at constant temperature and constant pressure. The box length in the z direction is scaled to the mean length in last 500 ps trajectories. The simulation is then continued in NVT ensemble for 1 ns equilibrium before being changed into microcanonical ensemble for rNEMD simulation. Time step is 1fs in all simulations.

The temperature gradient and amount of the heat flux are determined by the swap rate (inverse value of the time interval between exchange). The thermal conductivity of biodiesel at ambient condition with different swap rate is shown in Figure 5.16. All swap rates from

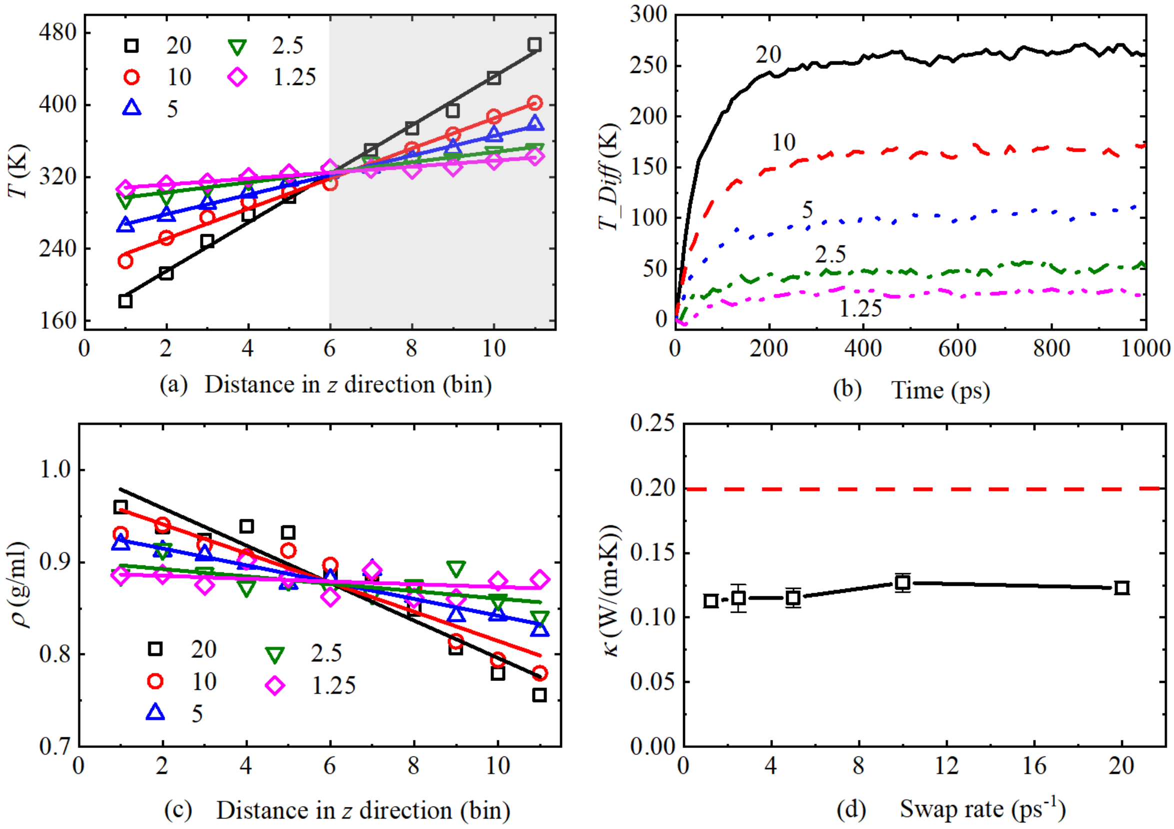

Fig. 5.16 (a) Temperature profile along the z direction in rNEMD simulation of biodiesel at 313.15 K and 0.1 MPa with different swap rate (ps^{-1}), where lines are linear fittings; (b) time evolution of temperature difference between hot side and cold side; (c) density profile along the z direction with different swap rate; (d) comparison of thermal conductivity using rNEMD (black hollow box) and GK-EMD (red dashed line). The results of rNEMD are averaged over five independent simulations.

1.25 ps^{-1} to 20 ps^{-1} produce temperature profile with good linearity. And the magnitude of the temperature gradient increases with the increase of swap rate. The temperature different between the hot slab and the cold slab converges after 200 ps, which means the system reaches its steady state and the generated temperature gradient is stable. The concomitant density gradient as a function of the position along the heat flux direction would result in the inhomogeneity of the system. Also, the temperature in cold slab can be as low as 181.46 K at swap rate of 20 ps^{-1}, which is below the melting point of FAMEs and can result in the anisotropy of conduction. Both the density inhomogeneity and the possible phase transition can introduce the deviation or even invalidation. Effect of phase transition can be avoided by doing the linear regression of the slabs with temperature higher than melting point, i.e, the shaded area in Figure 5.16 (a). The thermal conductivity calculated with higher swap rate is a bit larger than that with lower swap rate. Overall, the thermal conductivity predicted from rNEMD is smaller than that of GK-EMD method with an approximate factor of 0.5.

The capability of rNEMD on thermal conductivity predication at extreme condition is shown in Figure 5.17. At HP compressed condition with swap rates of 2.5, 5 and 10 ps^{-1}, the results show good linearity, temperature difference stabilisation and negligible density inhomogeneity. Liner regression should also be performed using the slabs in the shaded area in Figure 5.17 (a), to avoid the possible occurrence of HP induced solidification. For dense gas state of supercritical condition, the effect of density gradient is apparent at swap rate of 1 ps^{-1}. Density at the cold slab is 3.35 times higher than that at the hot slab. When the swap rate is reduced to 0.25 ps^{-1}, an extended simulation length of more than 2000 ps is needed to ensure the stabilisation of the temperature difference and to generate the identifiable temperature gradient.

5.6 Discussion and conclusion

In this chapter, thermal physical properties of biodiesel in a wide range of conditions are predicted using equilibrium and nonequilibrium molecular dynamics, and the corresponding results are compared with fossil diesel. Extreme conditions include condensed solid phase at 300 K - 300 MPa and dense gas phase of supercritical conditions at 5 MPa - 1200 K. The properties investigated include high pressure induced solidification, critical properties, surface tension and transport properties like density, viscosity and thermal conductivity. The capability of nonequilibrium molecular dynamics on viscosity and thermal conductivity calculation at extreme conditions is also studied.

At 300 K, solidification of biodiesel occurs at pressure above 200 MPa, which corresponds to the working condition of future high pressure common rail injector. It is identified that biodiesel is more likely to solidify than diesel. Bond-orientational order parameter of Q_6 is used to characterise the degree of crystallinity during the simulation.

Biodiesel has higher critical temperature, lower critical pressure and higher surface tension than diesel. The long-range dispersion interaction is essential in accurately predicting surface tension. The performance of vapour-liquid equilibrium simulation on critical pressure prediction of fuel mixtures is not as good as pure component.

Equilibrium molecular dynamics are employed to build the database of transport properties over wide ranges of temperatures and pressures without restriction. Compared with thermal conductivity, multiple independent replicated simulation is necessary to eliminate the statistical uncertainty in viscosity calculation using the Green-Kubo method. The resulting sharp increase in computation resource thus hampers its application in building large scale database directly. Obtaining the parameters in empirical equation by fitting the limited viscosity data points can deal with this issue. The density and viscosity difference between biodiesel

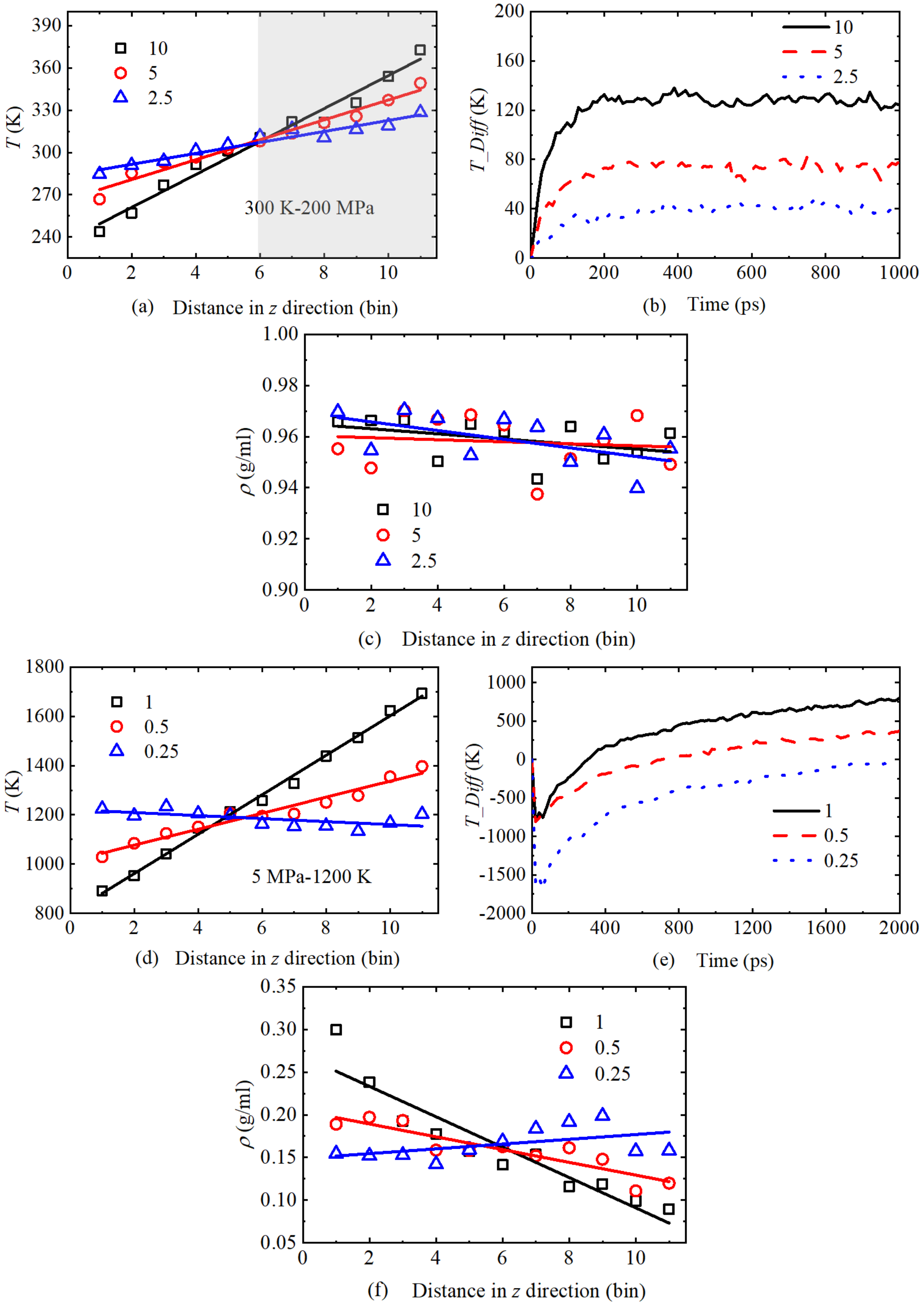

Fig. 5.17 Temperature gradient, temperature difference between the hot side and cold sides, density profile of biodiesel with different swap rates at extreme conditions: (a) - (c) biodiesel at 300 K - 200 MPa; (d) - (f) biodiesel at 5 MPa - 1200 K.

and diesel on injection, spray and atomization is explicit. The effect of thermal conductivity difference is highlighted due to the importance of Soret effect in supercritical combustion.

Unlike the transferability of equilibrium method, nonequilibrium method requires additional adjustments in different conditions, such as choosing appropriate strength of external force in periodical perturbation method and optimum swap rate in reverse nonequilibrium method.

Chapter 6

Conclusion and future recommendation

6.1 Summary of current work

A number of topics have been investigated in this thesis, including the physiochemical properties of biomass and biofuels from the aspects of deactivation of catalyst during biomass conversion, soot formation and mitigation mechanism of oxygenated biofuel additives, and thermophysical property prediction of biodiesel. MD simulation was performed with reactive force field and classical force fields like OPLS, TraPPE and CHARMM according to whether chemical reaction takes place or not. Besides equilibrium MD simulation in which properties are well-distributed across the computational box, nonequilibrium MD simulation was also applied by imposing appropriate external perturbation artificially so that a detectable microscale response can be produced.

The pyrolysis of lignin in ReaxFF MD simulation (800 K - 3000 K with ramp ratio of 20 K/ps) demonstrated a comparable trend with experimental results (423 K - 1173 K with ramp ratio of 2 K/min) in mass reduction. The molecular structures of tar and char were identified, and therefrom the coke surrogates were established, i.e., PAHs and oxygenated aromatics. The Ni catalyst deactivation mechanisms amid thermochemical conversion of lignin were attributed to surface premelting and coke deposition. Surface premelting was caused by higher mobility of atoms with lower coordination number at outer layer. The mechanisms behind the coke-catalyst interaction patterns (desorption, chemisorption and physisorption) were attributed to molecular collision dynamics, thermal dynamics and kinetics. The deactivation patterns were dependent on the temperature, PAH size and oxygen contents. The surface premelting induced deactivation is non-reversible while the catalyst deactivated due to coke deposition can be regenerated except in the simulations where seeping occurred at high temperature above 1600 K. The ReaxFF force field with the latest CHO2016 parameters was employed to study the combustion of diesel with addition of oxygenated biofuels. Soot formation mechanisms were scrutinized in time evolution of PAH growth pathways and incipient soot morphology. The nascent soot demonstrated structures of aromatics linked by aliphatics which were in consistent with the CHRCR model rather than PAH nucleation mechanism and HACA growth mechanism. The effects of biodiesel and oxygenated additives on soot mitigation were quantified by tracking the specific function groups in early formation of CO and CO2.

For viscosity prediction of FAMEs, running integral of time correlation function of pressure tensor using the GK-EMD method was subject to significant statistical error. Because it represents the collective response to naturally occurring fluctuations which are relatively small and highly uncertain in single run. Fitting the averaged value of sufficient independent running integral by the double exponential function is a reliable method despite of the increased computational cost. Diffusivity using Einstein method is a property averaged over each particle, thus converges easily. The rotational dynamics was characterised by reorientation relaxation time. Diffusion coefficient demonstrated system size scaling effect while it is negligible in viscosity and rotational relaxation time. A predictive model was established based on the observation that the correlation between experimental viscosity and EMD diffusion coefficient was in accordance with SE relation. The precondition should be stressed when applying the predictive method at extreme conditions considering that the high pressure induced solidification can result in the breakdown of the SE relation. Classical force fields like TraPPE-UA, LOPLS-AA and CHARMM-AA have different performance on accuracy and efficiency regarding property prediction of density, viscosity and diffusivity.

Nonequilibrium MD simulation is not necessarily more accurate than GK-EMD method on estimating viscosity and thermal conductivity. The limitation of nonequilibrium MD simulation on building large scale data set of fuel properties lies in the identification of the fitting regime which needs prior adjustment of perturbation amplitude at each condition so as to obtain optimum signal-to-noise ratio.

The emission from biodiesel utilisation was examined in MD simulation in two aspects. Compared with fossil diesel, biodiesel has the advantage of lower yield sooting index due to ester functional group. However, larger molecular size makes biodiesel more vulnerable to solidification in common-rail injector working at hundreds of megapascal pressure. Biodiesel also has higher viscosity and surface tension over broad range of conditions which would mainly deteriorate its injection and atomisation, and ultimately result in poorer combustion.

6.2 Future recommendation

6.2.1 Deactivation of catalyst

The modelling of interface chemistry between coke surrogates and nanocrystal facets can also be achieved using density functional theory (DFT) or *ab initio* molecular dynamics. Crucial steps concerning the effect of coke molecular structures on deposition can be understood deeply in atomic level using the quantum chemistry based method.

The interaction between coke surrogates and nanocrystals can be studied from the perspective of energy transfer and momentum accommodation during the collision. The effects of factors like the PAH size, rigidity and initial velocity orientation as well as nanocrystal size etc. on the transition between different deactivation patterns of permanent adsorption, trapping-desorption and intermediate reflection can be explored.

The evaluation of deactivation degree on kinetics of lignin catalytic fragmentation can be quantified by Arrhenius parameters in a more direct way.

6.2.2 Unphysical reaction condition in ReaxFF MD simulation

In order to accelerate the reaction, the temperature and pressure are increased manually in ReaxFF MD simulation. This is the main weakness of the application of ReaxFF and results in the controversial comments on its reliability. Accelerated MD simulation techniques have been implemented with ReaxFF to deal with this issue, though still in development. For example, collective variable-driven hyperdynamics (CVHD) method has been used to study combustion of *n*-Dodecane at realistic temperature as low as 700 K (Bal and Neyts, 2016). Bond boost method has been used to study the crossing-linking of polymers (Vashisth et al., 2018). However, previous studies using CVHD method (Bal and Neyts, 2016) (Ashraf et al., 2019) (Kwon et al., 2020a) (Lele et al., 2021) were restricted to bond scission process and has not been applied on the simulation of PAH growth and soot inception.

Machine learning force fields like deep potential or neural network potential provide another promising method (Botu et al., 2017) (Meuwly, 2021) (Behler, 2021) (Unke et al., 2021) (Poltavsky and Tkatchenko, 2021). The ACM Gordon Bell Prize of 2020 was awarded to Jia et al. (2020) for their work on pushing the limit of molecular dynamics with *ab initio* accuracy to 100 million atoms with the deep potential. Most importantly, deep potential was implemented with ReaxFF in LAMMPS, i.e., DeepMD (Zhang et al., 2018). Recently, Zeng et al. (2020) has used DeepMD package to investigate the chemical reaction networks of methane in combustion. Therefore, the soot formation mechanism in real combustion conditions by using deep potential ReaxFF MD simulation can be explored. The panoramic scenario can be established to include the initial fuel pyrolysis, PAH formation and soot inception as plotted in **Chapter 3-Figure 3.5**.

6.2.3 Physical property prediction

Viscosity prediction

In calculation of transport properties, the most difficult one is viscosity. The reasons lie in (1) inaccurate description of molecular model, i.e., force field; (2) considerable uncertainty induced by insufficient statistics.

To enhance the statistics, a concept of space partition methodology is established based on the fact that accuracy of viscosity in GK-EMD is independent of the system size. The MD box can be partitioned into chunks with equal size (e.g., 4×4×4 in x, y and z axis) and the correlation function can be calculated within each chunk. The viscosity of the whole box obtained by averaging over the time integral of the 64 chunks can be fitted to the stretched exponential function in TDM method. It is expected that the improved statistical accuracy can be achieved in single run of 500 ps instead of massive independent replicated simulation.

Zhu et al. (2021) established a framework to enhance viscosity prediction by adaptively varying the non-bonded vdW interaction and torsion potential parameters (VaFF) according to be deviation between PP-NEMD results and experimental results. Qiu et al. (2021) and Boothroyd et al. (2021) developed the workflow (names as OpenFF toolkit) of training the vdW parameters and assessing the classical force fields so as to improve the prediction of physical property beyond viscosity. These two force fields cover a diversity of compounds besides hydrocarbons and FAMEs.

By combing the aforementioned space partition method with the high-quality force fields like VaFF and OpenFF, a database of viscosity of various fuels can be built in a wide range of conditions. According to the quantitative structure-property relationship (QSPR), a machine learning based predictive method can be established to predict the thermophysical properties of new fuels with molecular structures as inputs that can be quantified by the molecular descriptor.

Binary diffusion and Soret effect

The importance of diffusive mixing process and Soret effect on supercritical combustion has been discussed in **Chapter 5.4.3**. Both the binary diffusion coefficient and thermal diffusion coefficient of fuel molecules in N_2 can be obtained in MD simulation.

It is more convenient to use Maxwell-Stefan (MS) diffusion coefficient in modeling the multicomponent transport process in liquids. The chemical potential is the driving force for diffusion, and the binary MS diffusion coefficient is expressed as (Liu et al., 2013) (Jamali et al., 2019) (Zhao et al., 2021):

$$D_{ij}^{\mathrm{MS}} = \frac{x_j}{x_i}\Lambda_{ii} + \frac{x_i}{x_j}\Lambda_{jj} - 2\Lambda_{ij} \tag{6.1}$$

where Λ_{ij} is Onsager coefficient which is expressed as the cross correlation of the displacements of species i and j:

$$\Lambda_{ij} = \lim_{t\to\infty}\frac{1}{6Nt}\left\langle\left(\sum_{k=1}^{N_i}\left(r_{k,i}(t) - r_{k,i}(0)\right)\right)\times\left(\sum_{l=1}^{N_j}\left(r_{l,j}(t) - r_{l,j}(0)\right)\right)\right\rangle \tag{6.2}$$

The Fick diffusion coefficient (D^{Fick}) describes the diffusion of molecules in a multicomponent mixture as a result of the gradient in the concentration of constituent species. For a binary mixture, the following relation holds:

$$D^{\mathrm{Fick}} = \Gamma D^{\mathrm{MS}} \tag{6.3}$$

where Γ is thermal dynamic factor, which can be obtained by Kirkwood and Buff coefficient (Zhao et al., 2021):

$$\Gamma = 1 - x_i\frac{\rho_j^n\left(G_{ii} + G_{ij} - 2G_{ij}\right)}{1 + \rho_j^n x_i\left(G_{ii} + G_{jj} - 2G_{ij}\right)} \tag{6.4}$$

$$G_{ij}^{\infty} = 4\pi\int_0^{\infty}\left(g_{ij}(r) - 1\right)r^2 dr \tag{6.5}$$

where $g_{ij}(r)$ is RDF between species i and j, and ρ_j^n is the number density of species j.

Soret coefficient (S_T) can be obtained in NEMD simulation with the implementation of enhanced heat exchange algorithm (eHEX) (Antoun et al., 2018a) (Antoun et al., 2018b) .

$$S_T = \frac{D_T}{D_{ij}} = \frac{\nabla x_i}{x_i\left(1 - x_i\right)\nabla T} \tag{6.6}$$

where ∇T is the temperature gradient, ∇x_i is the mole fraction gradient of component i, which can be measured in NEMD simulation at stationary state when the temperature and composition gradients are well developed in the liner regime.

Solidification

Plotting the solidification line of alkanes or FAMEs on the phase diagram is not only helpful to guide the design of common-rail injector but also to evaluate the property of hydrocarbon lubricants, which even work at high pressure conditions up to GPa. The pressure dependence of melting temperature can be fitted to Simon-Glatzel equation (Rzoska, 2017):

$$T_m(P) = T_0 \left(1 + \frac{P}{A}\right)^{1/B} \tag{6.7}$$

where T_0, A and B are fitting parameters. The effect of pressure on vitrification can be estimated by fitting to the equation which is analogous to Simon-Glatzel type relation (Holt et al., 2019):

$$T_g(P) = T_g(0) \left(1 + \frac{A}{B}P\right)^{1/A} \tag{6.8}$$

where $T_g(0)$, A and B are empirical and adjustable parameters. To collect the pressure-dependent phase transition temperatures of alkanes and FAMEs, enhanced sampling technique like metadynamics in conjunction with collective variables can be employed to address the nucleation problem of long timescale simulation without losing the characteristic atomistic resolution (Giberti et al., 2015b).

References

Adamson, B., Skeen, S., Ahmed, M., and Hansen, N. (2018). Detection of aliphatically bridged multi-core polycyclic aromatic hydrocarbons in sooting flames with atmospheric-sampling high-resolution tandem mass spectrometry. *The Journal of Physical Chemistry A*, 122(48):9338–9349.

Agarwal, A. K. (2007). Biofuels (alcohols and biodiesel) applications as fuels for internal combustion engines. *Progress in Energy and Combustion Science*, 33(3):233–271.

Aimoli, C. G., Maginn, E. J., and Abreu, C. R. (2014). Transport properties of carbon dioxide and methane from molecular dynamics simulations. *The Journal of Chemical Physics*, 141(13):134101.

Andersen and Hans, C. (1980). Molecular dynamics simulations at constant pressure and/or temperature. *The Journal of Chemical Physics*, 72(4):2384–2393.

Andersson, O. (2011). Glass–liquid transition of water at high pressure. *Proceedings of the National Academy of Sciences*, 108(27):11013–11016.

Andreae, M. O. and Ramanathan, V. (2013). Climate's dark forcings. *Science*, 340(6130):280–281.

Antoun, S., Saghir, M. Z., and Srinivasan, S. (2018a). Composition effect on thermophobicity of ternary mixtures: An enhanced molecular dynamics method. *The Journal of Chemical Physics*, 149(3):034502.

Antoun, S., Saghir, M. Z., and Srinivasan, S. (2018b). An improved molecular dynamics algorithm to study thermodiffusion in binary hydrocarbon mixtures. *The Journal of Chemical Physics*, 148(10):104507.

Anwar, M., Turci, F., and Schilling, T. (2013). Crystallization mechanism in melts of short n-alkane chains. *The Journal of Chemical Physics*, 139(21):214904.

Argyle, M. D. and Bartholomew, C. H. (2015). Heterogeneous catalyst deactivation and regeneration: a review. *Catalysts*, 5(1):145–269.

Arregi, A., Amutio, M., Lopez, G., Bilbao, J., and Olazar, M. (2018a). Evaluation of thermochemical routes for hydrogen production from biomass: A review. *Energy Conversion and Management*, 165:696–719.

Arregi, A., Lopez, G., Amutio, M., Artetxe, M., Barbarias, I., Bilbao, J., and Olazar, M. (2018b). Role of operating conditions in the catalyst deactivation in the in-line steam reforming of volatiles from biomass fast pyrolysis. *Fuel*, 216:233–244.

Ashraf, C., Shabnam, S., Jain, A., Xuan, Y., and van Duin, A. C. (2019). Pyrolysis of binary fuel mixtures at supercritical conditions: A ReaxFF molecular dynamics study. *Fuel*, 235:194–207.

Ashraf, C. and van Duin, A. C. (2017). Extension of the ReaxFF combustion force field toward syngas combustion and initial oxidation kinetics. *The Journal of Physical Chemistry A*, 121(5):1051–1068.

Bal, K. M. and Neyts, E. C. (2016). Direct observation of realistic-temperature fuel combustion mechanisms in atomistic simulations. *Chemical Science*, 7(8):5280–5286.

Baled, H. O., Gamwo, I. K., Enick, R. M., and McHugh, M. A. (2018). Viscosity models for pure hydrocarbons at extreme conditions: A review and comparative study. *Fuel*, 218:89–111.

Banuti, D., Raju, M., and Ihme, M. (2020). Between supercritical liquids and gases-Reconciling dynamic and thermodynamic state transitions. *The Journal of Supercritical Fluids*, 165:104895.

Barak, S., Rahman, R. K., Neupane, S., Ninnemann, E., Arafin, F., Laich, A., Terracciano, A. C., and Vasu, S. S. (2020). Measuring the effectiveness of high-performance co-optima biofuels on suppressing soot formation at high temperature. *Proceedings of the National Academy of Sciences*, 117(7):3451–3460.

Barr, M. R., Volpe, R., and Kandiyoti, R. (2021). Identifying synergistic effects between biomass components during pyrolysis and pointers concerning experiment design. *ACS Sustainable Chemistry & Engineering*, 9(16):5603–5612.

Bartholomew, C. H. (2001). Mechanisms of catalyst deactivation. *Applied Catalysis A: General*, 212(1-2):17–60.

Batuer, A., Chen, D., He, X., and Huang, Z. (2021). Simulation methods of cotton pyrolysis based on ReaxFF and the influence of volatile removal ratio on volatile evolution and char formation. *Chemical Engineering Journal*, 405:126633.

Bedrov, D., Piquemal, J.-P., Borodin, O., MacKerell Jr, A. D., Roux, B., and Schroder, C. (2019). Molecular dynamics simulations of ionic liquids and electrolytes using polarizable force fields. *Chemical Reviews*, 119(13):7940–7995.

Bedrov, D., Smith, G. D., and Sewell, T. D. (2000). Temperature-dependent shear viscosity coefficient of octahydro-1, 3, 5, 7-tetranitro-1, 3, 5, 7-tetrazocine (HMX): A molecular dynamics simulation study. *The Journal of Chemical Physics*, 112(16):7203–7208.

Behler, J. (2021). Four generations of high-dimensional neural network potentials. *Chemical Reviews*.

Bellan, J. (2000). Supercritical (and subcritical) fluid behavior and modeling: drops, streams, shear and mixing layers, jets and sprays. *Progress in Energy and Combustion Science*, 26(4-6):329–366.

Bellissima, S., Neumann, M., Guarini, E., Bafile, U., and Barocchi, F. (2017). Density of states and dynamical crossover in a dense fluid revealed by exponential mode analysis of the velocity autocorrelation function. *Physical Review E*, 95(1):012108.

Berendsen, H., Postma, J., Van Gunsteren, W., Di, N. A., and Haak, J. (1984). Molecular dynamics with coupling to an external bath. *The Journal of Chemical Physics*, page 3684–3690.

Beste, A. (2014). ReaxFF study of the oxidation of lignin model compounds for the most common linkages in softwood in view of carbon fiber production. *The Journal of Physical Chemistry A*, 118(5):803–814.

Bharadwaj, V. S., Eagan, N. M., Wang, N. M., Liberatore, M. W., and Maupin, C. M. (2015). Molecular simulations of fatty-acid methyl esters and representative biodiesel mixtures. *ChemPhysChem*, 16(13):2810–2817.

Blanco, G., Gerlagh, R., Suh, S., Barrett, J., de Coninck, H. C., Morejon, C. D., Mathur, R., Nakicenovic, N., Ahenkorah, A. O., and Pan, J. (2014). Drivers, trends and mitigation. *Climate Change 2014: Mitigation of Climate Change-Contribution of Working Group III to the Fifth Assessment Report of the Intergovernmental Panel on Climate Change*.

Bolmatov, D., Brazhkin, V., and Trachenko, K. (2013). Thermodynamic behaviour of supercritical matter. *Nature Communications*, 4(1):1–7.

Bond, T. C., Doherty, S. J., Fahey, D. W., Forster, P. M., Berntsen, T., DeAngelo, B. J., Flanner, M. G., Ghan, S., Kärcher, B., and Koch, D. (2013). Bounding the role of black carbon in the climate system: A scientific assessment. *Journal of Geophysical Research: Atmospheres*, 118(11):5380–5552.

Boone, P., Babaei, H., and Wilmer, C. E. (2019). Heat flux for many-body interactions: corrections to LAMMPS. *Journal of Chemical Theory and Computation*, 15(10):5579–5587.

Boothroyd, S., Wang, L.-P., Mobley, D., Chodera, J., and Shirts, M. (2021). The open force field evaluator: An automated, efficient, and scalable framework for the estimation of physical properties from molecular simulation.

Botu, V., Batra, R., Chapman, J., and Ramprasad, R. (2017). Machine learning force fields: construction, validation, and outlook. *The Journal of Physical Chemistry C*, 121(1):511–522.

Boudy, F. and Seers, P. (2009). Impact of physical properties of biodiesel on the injection process in a common-rail direct injection system. *Energy Conversion and Management*, 50(12):2905–2912.

Bowal, K., Martin, J. W., and Kraft, M. (2019). Partitioning of polycyclic aromatic hydrocarbons in heterogeneous clusters. *Carbon*, 143:247–256.

Brazhkin, V., Fomin, Y. D., Lyapin, A., Ryzhov, V., and Trachenko, K. (2012). Two liquid states of matter: A dynamic line on a phase diagram. *Physical Review E*, 85(3):031203.

Brazhkin, V., Fomin, Y. D., Lyapin, A., Ryzhov, V., Tsiok, E., and Trachenko, K. (2013). “Liquid-gas” transition in the supercritical region: Fundamental changes in the particle dynamics. *Physical Review Letters*, 111(14):145901.

Bryk, T., Gorelli, F., Mryglod, I., Ruocco, G., Santoro, M., and Scopigno, T. (2017). Behavior of supercritical fluids across the “Frenkel line”. *The Journal of Physical Chemistry Letters*, 8(20):4995–5001.

Bussi, G., Donadio, D., and Parrinello, M. (2007). Canonical sampling through velocity rescaling. *The Journal of Chemical Physics*, 126(1):014101.

Cain, J. P., Camacho, J., Phares, D. J., Wang, H., and Laskin, A. (2011). Evidence of aliphatics in nascent soot particles in premixed ethylene flames. *Proceedings of the Combustion Institute*, 33(1):533–540.

Cain, J. P., Gassman, P. L., Wang, H., and Laskin, A. (2010). Micro-FTIR study of soot chemical composition-evidence of aliphatic hydrocarbons on nascent soot surfaces. *Physical Chemistry Chemical Physics*, 12(20):5206–5218.

Caleman, C., van Maaren, P. J., Hong, M., Hub, J. S., Costa, L. T., and van der Spoel, D. (2012). Force field benchmark of organic liquids: density, enthalpy of vaporization, heat capacities, surface tension, isothermal compressibility, volumetric expansion coefficient, and dielectric constant. *Journal of Chemical Theory and Computation*, 8(1):61–74.

Celebi, A. T., Jamali, S. H., Bardow, A., Vlugt, T. J., and Moultos, O. A. (2021). Finite-size effects of diffusion coefficients computed from molecular dynamics: a review of what we have learned so far. *Molecular Simulation*, 47(10-11):831–845.

Charlson, R. J., Schwartz, S., Hales, J., Cess, R. D., Coakley, J. J., Hansen, J., and Hofmann, D. (1992). Climate forcing by anthropogenic aerosols. *Science*, 255(5043):423–430.

Chatzigoulas, A., Karathanou, K., Dellis, D., and Cournia, Z. (2018). Nanocrystal: A web-based crystallographic tool for the construction of nanoparticles based on their crystal habit. *Journal of Chemical Information and Modeling*, 58(12):2380–2386.

Chen, B., Potoff, J. J., and Siepmann, J. I. (2001). Monte carlo calculations for alcohols and their mixtures with alkanes. transferable potentials for phase equilibria. 5. united-atom description of primary, secondary, and tertiary alcohols. *The Journal of Physical Chemistry B*, 105(15):3093–3104.

Chen, C., Zhao, L., Wang, J., and Lin, S. (2017). Reactive molecular dynamics simulations of biomass pyrolysis and combustion under various oxidative and humidity environments. *Industrial & Engineering Chemistry Research*, 56(43):12276–12288.

Chen, D., Totton, T. S., Akroyd, J., Mosbach, S., and Kraft, M. (2014a). Phase change of polycyclic aromatic hydrocarbon clusters by mass addition. *Carbon*, 77:25–35.

Chen, D., Totton, T. S., Akroyd, J. W., Mosbach, S., and Kraft, M. (2014b). Size-dependent melting of polycyclic aromatic hydrocarbon nano-clusters: A molecular dynamics study. *Carbon*, 67:79–91.

Chen, H., He, J., Chen, Y., and Hua, H. (2018a). Performance of a common rail diesel engine using biodiesel of waste cooking oil and gasoline blend. *Journal of the Energy Institute*, 91(6):856–866.

Chen, T., Smit, B., and Bell, A. T. (2009). Are pressure fluctuation-based equilibrium methods really worse than nonequilibrium methods for calculating viscosities? *The Journal of Chemical Physics*, 131(24):246101.

Chen, X., Hou, L., Wei, X., and Bedrov, D. (2020). Transport properties of waxy crude oil: A molecular dynamics simulation study. *ACS Omega*, 5(30):18557–18564.

Chen, Z., Sun, W., and Zhao, L. (2018b). Combustion mechanisms and kinetics of fuel additives: A ReaxFF molecular simulation. *Energy & Fuel*, 32(11):11852–11863.

Chen, Z., Sun, W., and Zhao, L. (2019). Initial mechanism and kinetics of diesel incomplete combustion: ReaxFF molecular dynamics based on a multicomponent fuel model. *The Journal of Physical Chemistry C*, 123(14):8512–8521.

Cheng, L., Wu, Z., Zhang, Z., Guo, C., Ellis, N., Bi, X., Watkinson, A. P., and Grace, J. R. (2020). Tar elimination from biomass gasification syngas with bauxite residue derived catalysts and gasification char. *Applied Energy*, 258:114088.

Chenoweth, K., van Duin, A. C., Dasgupta, S., and Goddard Iii, W. A. (2009). Initiation mechanisms and kinetics of pyrolysis and combustion of JP-10 hydrocarbon jet fuel. *The Journal of Physical Chemistry A*, 113(9):1740–1746.

Chernyshev, A. (2009). Effect of nanoparticle size on the onset temperature of surface melting. *Materials Letters*, 63(17):1525–1527.

Chhetri, A. and Watts, K. (2012). Viscosities of canola, jatropha and soapnut biodiesel at elevated temperatures and pressures. *Fuel*, 102:789–794.

Chhetri, A. and Watts, K. (2013). Surface tensions of petro-diesel, canola, jatropha and soapnut biodiesel fuels at elevated temperatures and pressures. *Fuel*, 104:704–710.

Chisti, Y. (2007). Biodiesel from microalgae. *Biotechnology Advances*, 25(3):294–306.

Ciesielski, P. N., Pecha, M. B., Lattanzi, A. M., Bharadwaj, V. S., Crowley, M. F., Bu, L., Vermaas, J. V., Steirer, K. X., and Crowley, M. F. (2020). Advances in multiscale modeling of lignocellulosic biomass. *ACS Sustainable Chemistry Engineering*, 8(9):3512–3531.

Commodo, M., Kaiser, K., De Falco, G., Minutolo, P., Schulz, F., D'Anna, A., and Gross, L. (2019). On the early stages of soot formation: Molecular structure elucidation by high-resolution atomic force microscopy. *Combustion and Flame*, 205:154–164.

Coniglio, L., Bennadji, H., Glaude, P. A., Herbinet, O., and Billaud, F. (2013). Combustion chemical kinetics of biodiesel and related compounds (methyl and ethyl esters): experiments and modeling–advances and future refinements. *Progress in Energy and Combustion Science*, 39(4):340–382.

da Silva, G. C., Oliveira, F. G., de Souza, W. F., de Oliveira, M. C., Esteves, P. M., and Horta, B. A. (2021). Effects of paraffin, fatty acid and long alkyl chain phenol on the solidification of n-hexadecane under harsh subcooling condition: A molecular dynamics simulation study. *Fuel*, 285:119029.

Darden, T., York, D., and Pedersen, L. (1993). Particle mesh Ewald: An N·log (N) method for Ewald sums in large systems. *The Journal of Chemical Physics*, 98(12):10089–10092.

Das, D. D., John, P. C. S., McEnally, C. S., Kim, S., and Pfefferle, L. D. (2018a). Measuring and predicting sooting tendencies of oxygenates, alkanes, alkenes, cycloalkanes, and aromatics on a unified scale. *Combustion and Flame*, 190:349–364.

Das, D. D., McEnally, C. S., Kwan, T. A., Zimmerman, J. B., Cannella, W. J., Mueller, C. J., and Pfefferle, L. D. (2017). Sooting tendencies of diesel fuels, jet fuels, and their surrogates in diffusion flames. *Fuel*, 197:445–458.

Das, M., Sarkar, M., Datta, A., and Santra, A. K. (2018b). Study on viscosity and surface tension properties of biodiesel-diesel blends and their effects on spray parameters for CI engines. *Fuel*, 220:769–779.

de Oliveira, I. P. and Caires, A. R. L. (2019). Molecular arrangement in diesel/biodiesel blends: A molecular dynamics simulation analysis. *Renewable Energy*, 140:203–211.

de Oliveira, I. P., Caires, A. R. L., Baskar, K., Ponnusamy, S., Lakshmanan, P., and Veerappan, V. (2020). Biodiesel as an additive for diesel-ethanol (diesohol) blend: physical-chemical parameters and origin of the fuels' miscibility. *Fuel*, 263:116753.

Debenedetti, P. G. and Stillinger, F. H. (2001). Supercooled liquids and the glass transition. *Nature*, 410(6825):259–267.

Dench, J., Di Mare, L., Morgan, N., and Wong, J. (2018). Comparing the molecular and global rheology of a fluid under high pressures. *Physical Chemistry Chemical Physics*, 20(48):30267–30280.

Ding, J., Du, L., Pan, G., Lu, J., Wei, X., Li, J., Wang, W., and Yan, J. (2018a). Molecular dynamics simulations of the local structures and thermodynamic properties on molten alkali carbonate K_2CO_3. *Applied Energy*, 220:536–544.

Ding, J., Pan, G., Du, L., Lu, J., Wang, W., Wei, X., and Li, J. (2018b). Molecular dynamics simulations of the local structures and transport properties of na2co3 and k2co3. *Applied Energy*, 227:555–563.

do Carmo, F. R., Evangelista, N. S., Fernandes, F. A., and de Sant'Ana, H. B. (2015). Evaluation of optimal methods for critical properties and acentric factor of biodiesel compounds with their application on soave–redlich–kwong and peng–robinson equations of state. *Journal of Chemical & Engineering Data*, 60(11):3358–3381.

Doi, M., Edwards, S. F., and Edwards, S. F. (1988). *The Theory of Polymer Dynamics*, volume 73. oxford university press.

Dong, X., Fan, X., Fan, Y., and Wen, Y. (2015). Reactive molecular dynamics simulation of the pyrolysis and combustion of benzene: ultrahigh temperature and oxygen-induced enhancement of initiation pathways and their effect on carbon black generation. *RSC Advances*, 5(54):43695–43704.

Dontgen, M., Przybylski-Freund, M.-D., Kroger, L. C., Kopp, W. A., Ismail, A. E., and Leonhard, K. (2015). Automated discovery of reaction pathways, rate constants, and transition states using reactive molecular dynamics simulations. *Journal of Chemical Theory and Computation*, 11(6):2517–2524.

dos Santos, T. J., Abreu, C. R., Horta, B. A., and Tavares, F. W. (2020). Self-diffusion coefficients of methane/n-hexane mixtures at high pressures: An evaluation of the finite-size effect and a comparison of force fields. *The Journal of Supercritical Fluids*, 155:104639.

Dutta, K., Daverey, A., and Lin, J.-G. (2014). Evolution retrospective for alternative fuels: First to fourth generation. *Renewable Energy*, 69:114–122.

Dworkin, S., Smooke, M., and Giovangigli, V. (2009). The impact of detailed multicomponent transport and thermal diffusion effects on soot formation in ethylene/air flames. *Proceedings of the Combustion Institute*, 32(1):1165–1172.

Dymond, J. and Malhotra, R. (1988). The tait equation: 100 years on. *International Journal of Thermophysics*, 9(6):941–951.

Ediger, M. and Harrowell, P. (2012). Perspective: Supercooled liquids and glasses. *The Journal of Chemical Physics*, 137(8):080901.

Ediger, M. D. (2000). Spatially heterogeneous dynamics in supercooled liquids. *Annual Review of Physical Chemistry*, 51(1):99–128.

Elvati, P. and Violi, A. (2013). Thermodynamics of poly-aromatic hydrocarbon clustering and the effects of substituted aliphatic chains. *Proceedings of the Combustion Institute*, 34(1):1837–1843.

Evangelista, N. S., do Carmo, F. R., and de Sant'Ana, H. B. (2018). Estimation of physical constants of biodiesel-related fatty acid alkyl esters: normal boiling point, critical temperature, critical pressure, and acentric factor. *Industrial & Engineering Chemistry Research*, 57(25):8552–8565.

Fairley, P. (2011). Introduction: next generation biofuels. *Nature*, 474(7352):S2–S5.

Falk, K., Savio, D., and Moseler, M. (2020). Nonempirical free volume viscosity model for alkane lubricants under severe pressures. *Physical Review Letters*, 124(10):105501.

Fanourgakis, G. S., Medina, J., and Prosmiti, R. (2012). Determining the bulk viscosity of rigid water models. *The Journal of Physical Chemistry A*, 116(10):2564–2570.

Faravelli, T., Frassoldati, A., Migliavacca, G., and Ranzi, E. (2010). Detailed kinetic modeling of the thermal degradation of lignins. *Biomass & Bioenergy*, 34(3):290–301.

Farooq, A., Ren, W., Lam, K. Y., Davidson, D. F., Hanson, R. K., and Westbrook, C. K. (2012). Shock tube studies of methyl butanoate pyrolysis with relevance to biodiesel. *Combustion and Flame*, 159(11):3235–3241.

Feng, M., Jiang, X. Z., Zeng, W., Luo, K. H., and Hellier, P. (2019). Ethanol oxidation with high water content: A reactive molecular dynamics simulation study. *Fuel*, 235:515–521.

Feria, E., Algaba, J., Míguez, J. M., Mejía, A., Gómez-Álvarez, P., and Blas, F. J. (2020). Vapour–liquid phase equilibria and interfacial properties of fatty acid methyl esters from molecular dynamics simulations. *Physical Chemistry Chemical Physics*, 22(9):4974–4983.

Ferreira, A. G., Talvera-Prieto, N. M. C., Portugal, A. A., and Moreira, R. J. (2020). Models for predicting viscosities of biodiesel fuels over extended ranges of temperature and pressure. *Fuel*, page 119544.

Fischer, N. M., van Maaren, P. J., Ditz, J. C., Yildirim, A., and van der Spoel, D. (2015). Properties of organic liquids when simulated with long-range Lennard-Jones interactions. *Journal of Chemical Theory and Computation*, 11(7):2938–2944.

Freed, D. E. (2007). Dependence on chain length of NMR relaxation times in mixtures of alkanes. *The Journal of Chemical Physics*, 126(17):174502.

Freed, D. E. (2009). Temperature and pressure dependence of the diffusion coefficients and NMR relaxation times of mixtures of alkanes. *The Journal of Physical Chemistry B*, 113(13):4293–4302.

Freed, D. E., Burcaw, L., and Song, Y.-Q. (2005). Scaling laws for diffusion coefficients in mixtures of alkanes. *Physical Review Letters*, 94(6):067602.

Freitas, S. V., Segovia, J. J., Martín, M. C., Zambrano, J., Oliveira, M. B., Lima, A. S., and Coutinho, J. A. (2014). Measurement and prediction of high-pressure viscosities of biodiesel fuels. *Fuel*, 122:223–228.

Frenklach, M. (2002). Reaction mechanism of soot formation in flames. *Physical Chemistry Chemical Physics*, 4(11):2028–2037.

Frenklach, M. and Mebel, A. (2020). On the mechanism of soot nucleation. *Physical Chemistry Chemical Physics*, 22(9):5314–5331.

Gallo, P., Corradini, D., and Rovere, M. J. N. c. (2014). Widom line and dynamical crossovers as routes to understand supercritical water. *Nature Communications*, 5(1):1–6.

Gao, X., Wang, Z., Ashok, J., and Kawi, S. (2020). A comprehensive review of anti-coking, anti-poisoning and anti-sintering catalysts for biomass tar reforming reaction. *Chemical Engineering Science: X*, 7:100065.

Ghoufi, A., Malfreyt, P., and Tildesley, D. J. (2016). Computer modelling of the surface tension of the gas–liquid and liquid–liquid interface. *Chemical Society Reviews*, 45(5):1387–1409.

Giberti, F., Salvalaglio, M., Mazzotti, M., and Parrinello, M. (2015a). Insight into the nucleation of urea crystals from the melt. *Chemical Engineering Science*, 121:51–59.

Giberti, F., Salvalaglio, M., and Parrinello, M. (2015b). Metadynamics studies of crystal nucleation. *IUCrJ*, 2(2):256–266.

Gong, Y., Luo, K. H., Ma, X., Shuai, S., and Xu, H. (2021a). Atomic-level insights into transition mechanism of dominant mixing modes of multi-component fuel droplets: From evaporation to diffusion. *Fuel*, 304:121464.

Gong, Y., Xiao, G., Ma, X., Luo, K. H., Shuai, S., and Xu, H. (2021b). Phase transitions of multi-component fuel droplets under sub-and supercritical conditions. *Fuel*, 287:119516.

Gopinath, A., Sairam, K., Velraj, R., and Kumaresan, G. (2015). Effects of the properties and the structural configurations of fatty acid methyl esters on the properties of biodiesel fuel: a review. *Proceedings of the Institution of Mechanical Engineers, Part D: Journal of Automobile Engineering*, 229(3):357–390.

Gordon, P. A. (2003a). Characterizing isoparaffin transport properties with Stokes-Einstein relationships. *Industrial & Engineering Chemistry Research*, 42(26):7025–7036.

Gordon, P. A. (2003b). Influence of simulation details on thermodynamic and transport properties in molecular dynamics of fully flexible molecular models. *Molecular Simulation*, 29(8):479–487.

Gordon, P. A. (2005). Extrapolation of rheological properties for lubricant components with Stokes-Einstein relationships. *Industrial & Engineering Chemistry Research*, 44(15):5828–5835.

Grančič, P., Martin, J. W., Chen, D., Mosbach, S., and Kraft, M. (2016). Can nascent soot particles burn from the inside? *Carbon*, 109:608–615.

Grossfield, A. and Zuckerman, D. M. (2009). Quantifying uncertainty and sampling quality in biomolecular simulations. *Annual Reports in Computational Chemistry*, 5:23–48.

Habrioux, M., Bazile, J.-P., Galliero, G., and Daridon, J. L. (2015). Viscosities of fatty acid methyl and ethyl esters under high pressure: methyl caprate and ethyl caprate. *Journal of Chemical & Engineering Data*, 60(3):902–908.

Habrioux, M., Bazile, J.-P., Galliero, G., and Daridon, J. L. (2016). Viscosities of fatty acid methyl and ethyl esters under high pressure: methyl myristate and ethyl myristate. *Journal of Chemical & Engineering Data*, 61(1):398–403.

Handle, P. H., Seidl, M., and Loerting, T. (2012). Relaxation time of high-density amorphous ice. *Physical Review Letters*, 108(22):225901.

Haydukivska, K., Blavatska, V., and Paturej, J. (2020). Universal size ratios of gaussian polymers with complex architecture: radius of gyration vs hydrodynamic radius. *Scientific Reports*, 10(1):1–11.

Herbinet, O., Pitz, W. J., and Westbrook, C. K. (2008). Detailed chemical kinetic oxidation mechanism for a biodiesel surrogate. *Combustion and Flame*, 154(3):507–528.

Herdman, J. D. and Miller, J. H. (2008). Intermolecular potential calculations for polynuclear aromatic hydrocarbon clusters. *The Journal of Physical Chemistry A*, 112(28):6249–6256.

Hervy, M., Weiss-Hortala, E., Minh, D. P., Dib, H., Villot, A., Gerente, C., Berhanu, S., Chesnaud, A., Thorel, A., and Le Coq, L. (2019). Reactivity and deactivation mechanisms of pyrolysis chars from bio-waste during catalytic cracking of tar. *Applied Energy*, 237:487–499.

Hess, B. (2002). Determining the shear viscosity of model liquids from molecular dynamics simulations. *The Journal of Chemical Physics*, 116(1):209–217.

Hess, B., Bekker, H., Berendsen, H. J., and Fraaije, J. G. (1997). LINCS: a linear constraint solver for molecular simulations. *Journal of Computational Chemistry*, 18(12):1463–1472.

Hockney, R. W. and Eastwood, J. W. (2021). *Computer simulation using particles*. crc Press.

Hoekman, S. K., Broch, A., Robbins, C., Ceniceros, E., and Natarajan, M. (2012). Review of biodiesel composition, properties, and specifications. *Renewable and Sustainable Energy Reviews*, 16(1):143–169.

Holt, A., Fragiadakis, D., Wollmershauser, J., Feigelson, B., Tyagi, M., and Roland, C. (2019). Stability limits of pressure densified polycarbonate glass. *Macromolecules*, 52(11):4139–4144.

Hong, D., Si, T., and Guo, X. (2020). Insight into the calcium carboxylate release behavior during zhundong coal pyrolysis and combustion. *Proceedings of the Combustion Institute*.

Hoover, W. G. (1985). Canonical dynamics: Equilibrium phase-space distributions. *Physical review A*, 31(3):1695–1697.

https://www.amap.no/ (2015). Summary for policy-makers: Arctic climate issues 2015. *Arctic Monitoring and Assessment Programme*.

Hu, X., Lievens, C., Mourant, D., Wang, Y., Wu, L., Gunawan, R., Song, Y., and Li, C.-Z. (2013). Investigation of deactivation mechanisms of a solid acid catalyst during esterification of the bio-oils from mallee biomass. *Applied Energy*, 111:94–103.

Huang, J. and MacKerell Jr, A. D. (2013). CHARMM36 all-atom additive protein force field: Validation based on comparison to NMR data. *Journal of Computational Chemistry*, 34(25):2135–2145.

Humphrey, W., Dalke, A., and Schulten, K. (1996). VMD: visual molecular dynamics. *Journal of Molecular Graphics*, 14(1):33–38.

IEA (2017). Technology roadmap: Delivering sustainable bioenergy. *International Energy Agency*.

in't Veld, P. J., Ismail, A. E., and Grest, G. S. (2007). Application of ewald summations to long-range dispersion forces. *The Journal of Chemical Physics*, 127(14):144711.

Isele-Holder, R. E., Mitchell, W., Hammond, J. R., Kohlmeyer, A., and Ismail, A. E. (2013). Reconsidering dispersion potentials: Reduced cutoffs in mesh-based ewald solvers can be faster than truncation. *Journal of Chemical Theory and Computation*, 9(12):5412–5420.

Isele-Holder, R. E., Mitchell, W., and Ismail, A. E. (2012). Development and application of a particle-particle particle-mesh ewald method for dispersion interactions. *The Journal of Chemical Physics*, 137(17):174107.

Ismail, A. E., Tsige, M., Veld In't, P. J., and Grest, G. S. (2007). Surface tension of normal and branched alkanes. *Molecular Physics*, 105(23-24):3155–3163.

Jacobson, M. Z. (2002). Control of fossil-fuel particulate black carbon and organic matter, possibly the most effective method of slowing global warming. *Journal of Geophysical Research: Atmospheres*, 107(D19):ACH 16–1–ACH 16–22.

Jacobson, R. S., Korte, A. R., Vertes, A., and Miller, J. H. (2020). The molecular composition of soot. *Angewandte Chemie*, 132(11):4514–4520.

Jamali, S. H., Wolff, L., Becker, T. M., De Groen, M., Ramdin, M., Hartkamp, R., Bardow, A., Vlugt, T. J., and Moultos, O. A. (2019). OCTP: A tool for on-the-fly calculation of transport properties of fluids with the order-n algorithm in LAMMPS. *Journal of Chemical Information and Modeling*, 59(4):1290–1294.

Jia, W., Wang, H., Chen, M., Lu, D., Lin, L., Car, R., Weinan, E., and Zhang, L. (2020). Pushing the limit of molecular dynamics with ab initio accuracy to 100 million atoms with machine learning. In *SC20: International Conference for High Performance Computing, Networking, Storage and Analysis*, pages 1–14. IEEE.

Jian, X. and Zheng, H. (2009). Raman scattering spectroscopic study of n-tetradecane under high pressure and ambient temperature. *Spectrochimica Acta Part A: Molecular and Biomolecular Spectroscopy*, 72(1):214–217.

Jiang, Q., Lu, H., and Zhao, M. (2004). Modelling of surface energies of elemental crystals. *Journal of Physics: Condensed Matter*, 16(4):521.

Jofre, L. and Urzay, J. (2021). Transcritical diffuse-interface hydrodynamics of propellants in high-pressure combustors of chemical propulsion systems. *Progress in Energy and Combustion Science*, 82:100877.

Johansson, K., Head-Gordon, M., Schrader, P., Wilson, K., and Michelsen, H. (2018). Resonance-stabilized hydrocarbon-radical chain reactions may explain soot inception and growth. *Science*, 361(6406):997–1000.

Johansson, K. O., Dillstrom, T., Elvati, P., Campbell, M. F., Schrader, P. E., Popolan-Vaida, D. M., Richards-Henderson, N. K., Wilson, K. R., Violi, A., and Michelsen, H. A. (2017). Radical–radical reactions, pyrene nucleation, and incipient soot formation in combustion. *Proceedings of the Combustion Institute*, 36(1):799–806.

Jorgensen, W. L., Maxwell, D. S., and Tirado-Rives, J. (1996). Development and testing of the OPLS all-atom force field on conformational energetics and properties of organic liquids. *Journal of the American Chemical Society*, 118(45):11225–11236.

Kalpathy, S. V., Poddar, N. B., Bagley, S. P., and Wornat, M. J. (2015). Reaction pathways for the growth of polycyclic aromatic hydrocarbons during the supercritical pyrolysis of n-decane, as determined from doping experiments with 1-and 2-methylnaphthalene. *Proceedings of the Combustion Institute*, 35(2):1833–1841.

Kamath, G., Robinson, J., and Potoff, J. J. (2006). Application of TraPPE-UA force field for determination of vapor–liquid equilibria of carboxylate esters. *Fluid Phase Equilibria*, 240(1):46–55.

Kashiwagi, H. and Makita, T. (1982). Viscosity of twelve hydrocarbon liquids in the temperature range 298–348 K at pressures up to 110 MPa. *International Journal of Thermophysics*, 3(4):289–305.

Kawasaki, T. and Kim, K. (2017). Identifying time scales for violation/preservation of Stokes-Einstein relation in supercooled water. *Science Advances*, 3(8):e1700399.

Kay, A. K. and B., W. (1969). Critical constants of conformed mixtures. *Journal of Physical Chemistry*, 73:3359–3366.

Keasler, S. J., Charan, S. M., Wick, C. D., Economou, I. G., and Siepmann, J. I. (2012). Transferable potentials for phase equilibria–united atom description of five-and six-membered cyclic alkanes and ethers. *The Journal of Physical Chemistry B*, 116(36):11234–11246.

Keil, F. J. (2018). Molecular modelling for reactor design. *Annual Review of Chemical and Biomolecular Engineering*, 9:201–227.

Keller, M., de Bruin, T., Matrat, M., Nicolle, A., and Catoire, L. (2019). A theoretical multiscale approach to study the initial steps involved in the chemical reactivity of soot precursors. *Energy & Fuel*, 33(10):10255–10266.

Kholghy, M. R., Eaves, N. A., Veshkini, A., and Thomson, M. J. (2019). The role of reactive PAH dimerization in reducing soot nucleation reversibility. *Proceedings of the Combustion Institute*, 37(1):1003–1011.

Kiełczyński, P., Ptasznik, S., Szalewski, M., Balcerzak, A., Wieja, K., and Rostocki, A. (2017). Thermophysical properties of rapeseed oil methyl esters (RME) at high pressures and various temperatures evaluated by ultrasonic methods. *Biomass & Bioenergy*, 107:113–121.

Kim, K.-S., Han, M. H., Kim, C., Li, Z., Karniadakis, G. E., and Lee, E. K. (2018). Nature of intrinsic uncertainties in equilibrium molecular dynamics estimation of shear viscosity for simple and complex fluids. *The Journal of Chemical Physics*, 149(4):044510.

Kim, S. (2014). Issues on the choice of a proper time step in molecular dynamics. *Physics Procedia*, 53:60–62.

Kirkwood, J. G. and Buff, F. P. (1949). The statistical mechanical theory of surface tension. *The Journal of Chemical Physics*, 17(3):338–343.

Koddermann, T., Ludwig, R., and Paschek, D. (2008). On the validity of Stokes-Einstein and Stokes-Einstein-Debye relations in ionic liquids and ionic-liquid mixtures. *ChemPhysChem*, 9(13):1851.

Kondratyuk, N., Lenev, D., and Pisarev, V. (2020a). Transport coefficients of model lubricants up to 400 MPa from molecular dynamics. *The Journal of Chemical Physics*, 152(19):191104.

Kondratyuk, N. D., Norman, G. E., and Stegailov, V. V. (2016). Self-consistent molecular dynamics calculation of diffusion in higher n-alkanes. *The Journal of Chemical Physics*, 145(20):204504.

Kondratyuk, N. D. and Pisarev, V. V. (2019). Calculation of viscosities of branched alkanes from 0.1 to 1000 MPa by molecular dynamics methods using COMPASS force field. *Fluid Phase Equilibria*, 498:151–159.

Kondratyuk, N. D., Pisarev, V. V., and Ewen, J. P. (2020b). Probing the high-pressure viscosity of hydrocarbon mixtures using molecular dynamics simulations. *The Journal of Chemical Physics*, 153(15):154502.

Kouakou, A. C., Le Mapihan, K., and Pauly, J. (2013). Solid–liquid equilibria under high pressure of pure fatty acid methyl esters. *Fuel*, 109:297–302.

Kremer, K. and Grest, G. S. (1990). Dynamics of entangled linear polymer melts: A molecular-dynamics simulation. *The Journal of Chemical Physics*, 92(8):5057–5086.

Kumar, P. (2006). Breakdown of the Stokes–Einstein relation in supercooled water. *Proceedings of the National Academy of Sciences*, 103(35):12955–12956.

Kutcherov, V., Chernoutsan, A., and Brazhkin, V. (2017). Crystallization and glass transition in crude oils and their fractions at atmospheric and high pressures. *Journal of Molecular Liquids*, 241:428–434.

Kwon, H., Lele, A., Zhu, J., McEnally, C. S., Pfefferle, L. D., Xuan, Y., and van Duin, A. C. (2020a). ReaxFF-based molecular dynamics study of bio-derived polycyclic alkanes as potential alternative jet fuels. *Fuel*, 279:118548.

Kwon, H., Shabnam, S., van Duin, A. C., and Xuan, Y. (2020b). Numerical simulations of yield-based sooting tendencies of aromatic fuels using ReaxFF molecular dynamics. *Fuel*, 262:116545.

Lapuerta, M., Armas, O., and Rodriguez-Fernandez, J. (2008). Effect of biodiesel fuels on diesel engine emissions. *Progress in energy and combustion science*, 34(2):198–223.

Lapuerta, M., Barba, J., Sediako, A. D., Kholghy, M. R., and Thomson, M. (2017). Morphological analysis of soot agglomerates from biodiesel surrogates in a coflow burner. *Journal of Aerosol Science*, 111:65–74.

Lele, A., Kwon, H., Ganeshan, K., Xuan, Y., and van Duin, A. C. (2021). ReaxFF molecular dynamics study on pyrolysis of bicyclic compounds for aviation fuel. *Fuel*, 297:120724.

Li, C. (1971). Critical temperature estimation for simple mixtures. *The Canadian Journal of Chemical Engineering*, 49(5):709–710.

Li, C., Zhao, X., Wang, A., Huber, G. W., and Zhang, T. (2015). Catalytic transformation of lignin for the production of chemicals and fuels. *Chemical Reviews*, 115(21):11559–11624.

Li, D. D. and Greenfield, M. L. (2014). Viscosity, relaxation time, and dynamics within a model asphalt of larger molecules. *The Journal of Chemical Physics*, 140(3):034507.

Li, J., Tao, J., Yan, B., Cheng, K., Chen, G., and Hu, J. (2020). Microwave reforming with char-supported nickel-cerium catalysts: A potential approach for thorough conversion of biomass tar model compound. *Applied Energy*, 261:114375.

Li, X., Zheng, M., Ren, C., and Guo, L. (2021). ReaxFF molecular dynamics simulations of thermal reactivity of various fuels in pyrolysis and combustion. *Energy & Fuels*, 35(15):11707–11739.

Li, Z. and Wang, H. (2005). Gas-nanoparticle scattering: A molecular view of momentum accommodation function. *Physical Review Letters*, 95(1):014502.

Lin, R. and Tavlarides, L. L. (2012). Thermophysical properties needed for the development of the supercritical diesel combustion technology: Evaluation of diesel fuel surrogate models. *The Journal of Supercritical Fluids*, 71:136–146.

Lindner, B., Petridis, L., Schulz, R., and Smith, J. C. (2013). Solvent-driven preferential association of lignin with regions of crystalline cellulose in molecular dynamics simulation. *Biomacromolecules*, 14(10):3390–3398.

Liu, C., Brandenburg, J. G., Valsson, O., Kremer, K., and Bereau, T. (2020). Free-energy landscape of polymer-crystal polymorphism. *Soft Matter*, 16(42):9683–9692.

Liu, C., Zhao, R., Xu, R., Egolfopoulos, F. N., and Wang, H. (2017a). Binary diffusion coefficients and non-premixed flames extinction of long-chain alkanes. *Proceedings of the Combustion Institute*, 36(1):1523–1530.

Liu, W.-J., Li, W.-W., Jiang, H., and Yu, H.-Q. (2017b). Fates of chemical elements in biomass during its pyrolysis. *Chemical Reviews*, 117(9):6367–6398.

Liu, X., Bull, C., Kleppe, A., Dowding, P., Lewtas, K., and Pulham, C. (2019). High-pressure crystallisation studies of biodiesel and methyl stearate. *CrystEngComm*, 21(30):4427–4436.

Liu, X., Li, X., Nie, F., and Guo, L. (2017c). Initial reaction mechanism of bio-oil high-temperature oxidation simulated with reactive force field molecular dynamics. *Energy & Fuels*, 31(2):1608–1619.

Liu, X., Schnell, S. K., Simon, J.-M., Kruger, P., Bedeaux, D., Kjelstrup, S., Bardow, A., and Vlugt, T. J. (2013). Diffusion coefficients from molecular dynamics simulations in binary and ternary mixtures. *International journal of thermophysics*, 34(7):1169–1196.

Lombardo, T. G., Debenedetti, P. G., and Stillinger, F. H. (2006). Computational probes of molecular motion in the lewis-wahnström model for $ortho-terphenyl$. *The Journal of Chemical Physics*, 125(17):174507.

Lowe, J. S., Lai, J. Y., Elvati, P., and Violi, A. (2015). Towards a predictive model for polycyclic aromatic hydrocarbon dimerization propensity. *Proceedings of the Combustion Institute*, 35(2):1827–1832.

Luo, C., Sommer, J.-U., Schreiner, E., Castro, I. G., Tinsley, J., and Weiss, H. (2015). Length-dependent segregation in crystallization of n-alkanes: MD simulations. *Journal of Non-Crystalline Solids*, 407:206–212.

Luque, R., Herrero-Davila, L., Campelo, J. M., Clark, J. H., Hidalgo, J. M., Luna, D., Marinas, J. M., and Romero, A. A. (2008). Biofuels: a technological perspective. *Energy & Environmental Science*, 1(5):542–564.

Lynd, L. R. and de Brito Cruz, C. H. (2010). Make way for ethanol. *Science*, 330(6008):1176–1176.

Maginn, E. J., Messerly, R. A., Carlson, D. J., Roe, D. R., and Elliott, J. R. (2018). Best practices for computing transport properties 1. Self-diffusivity and viscosity from equilibrium molecular dynamics [article v1. 0]. *Living Journal of Computational Molecular Science*, 1(1):6324.

Mallepally, R. R., Bamgbade, B. A., Rowane, A. J., Rokni, H. B., Newkirk, M. S., and McHugh, M. A. (2018). Fluid properties at high pressures and temperatures: Experimental and modelling challenges. *The Journal of Supercritical Fluids*, 134:33–40.

Mao, Q., Hou, D., Luo, K. H., and You, X. (2018). Dimerization of polycyclic aromatic hydrocarbon molecules and radicals under flame conditions. *The Journal of Physical Chemistry A*, 122(44):8701–8708.

Mao, Q., van Duin, A. C., and Luo, K. (2017). Formation of incipient soot particles from polycyclic aromatic hydrocarbons: A ReaxFF molecular dynamics study. *Carbon*, 121:380–388.

Mao, Q., Zhou, J., Luo, K. H., and Van Duin, A. C. (2019). Atomistic insights into the dynamics of binary collisions between gaseous molecules and polycyclic aromatic hydrocarbon dimers. *Physical Chemistry Chemical Physics*, 21(7):3849–3856.

Martin, M. G. and Siepmann, J. I. (1998). Transferable potentials for phase equilibria. 1. united-atom description of n-alkanes. *The Journal of Physical Chemistry B*, 102(14):2569–2577.

Matsumoto, M., Saito, S., and Ohmine, I. (2002). Molecular dynamics simulation of the ice nucleation and growth process leading to water freezing. *Nature*, 416(6879):409–413.

McEnally, C. S., Pfefferle, L. D., Atakan, B., and Kohse-Höinghaus, K. (2006). Studies of aromatic hydrocarbon formation mechanisms in flames: Progress towards closing the fuel gap. *Progress in Energy and Combustion Science*, 32(3):247–294.

McIlroy, A., McRae, G., Sick, V., Siebers, D., Westbrook, C., Smith, P., Taatjes, C., Trouve, A., Wagner, A., and Rohlfing, E. (2006). Basic research needs for clean and efficient combustion of 21st century transportation fuels. Report, DOESC (USDOE Office of Science (SC)).

Mercier, X., Carrivain, O., Irimiea, C., Faccinetto, A., and Therssen, E. (2019). Dimers of polycyclic aromatic hydrocarbons: the missing pieces in the soot formation process. *Physical Chemistry Chemical Physics*, 21(16):8282–8294.

Messerly, R. A., Knotts IV, T. A., Rowley, R. L., and Wilding, W. V. (2016). An improved approach for predicting the critical constants of large molecules with gibbs ensemble monte carlo simulation. *Fluid Phase Equilibria*, 425:432–442.

Meuwly, M. (2021). Machine learning for chemical reactions. *Chemical Reviews*.

Michelsen, H. (2017). Probing soot formation, chemical and physical evolution, and oxidation: A review of *in situ* diagnostic techniques and needs. *Proceedings of the Combustion Institute*, 36(1):717–735.

Molino, A., Chianese, S., and Musmarra, D. (2016). Biomass gasification technology: The state of the art overview. *Journal of Energy Chemistry*, 25(1):10–25.

Mondello, M. and Grest, G. S. (1997). Viscosity calculations of n-alkanes by equilibrium molecular dynamics. *The Journal of Chemical Physics*, 106(22):9327–9336.

Mondello, M., Grest, G. S., Webb III, E. B., and Peczak, P. (1998). Dynamics of n-alkanes: Comparison to rouse model. *The Journal of Chemical Physics*, 109(2):798–805.

Monti, S., Srifa, P., Kumaniaev, I., and Samec, J. S. (2018). ReaxFF simulations of lignin fragmentation on a palladium-based heterogeneous catalyst in methanol–water solution. *The Journal of Physical Chemistry Letters*, 9(18):5233–5239.

Moore, R. H., Thornhill, K. L., Weinzierl, B., Sauer, D., D'Ascoli, E., Kim, J., Lichtenstern, M., Scheibe, M., Beaton, B., and Beyersdorf, A. J. (2017). Biofuel blending reduces particle emissions from aircraft engines at cruise conditions. *Nature*, 543(7645):411–415.

Morrow, B. H. and Harrison, J. A. (2019). Vapor-liquid equilibrium simulations of hydrocarbons using molecular dynamics with long-range Lennard-Jones interactions. *Energy & Fuels*, 33(2):848–858.

Moultos, O. A., Zhang, Y., Tsimpanogiannis, I. N., Economou, I. G., and Maginn, E. J. (2016). System-size corrections for self-diffusion coefficients calculated from molecular dynamics simulations: The case of CO_2, n-alkanes, and poly (ethylene glycol) dimethyl ethers. *The Journal of Chemical Physics*, 145(7):074109.

Mueller, J. E., van Duin, A. C., and Goddard III, W. A. (2010a). Application of the ReaxFF reactive force field to reactive dynamics of hydrocarbon chemisorption and decomposition. *The Journal of Physical Chemistry C*, 114(12):5675–5685.

Mueller, J. E., van Duin, A. C., and Goddard III, W. A. (2010b). Development and validation of ReaxFF reactive force field for hydrocarbon chemistry catalyzed by nickel. *The Journal of Physical Chemistry C*, 114(11):4939–4949.

Murphy, B. M. and Xu, B. (2018). Foundational techniques for catalyst design in the upgrading of biomass-derived multifunctional molecules. *Progress in Energy and Combustion Science*, 67:1–30.

Müller-Plathe, F. (1997). A simple nonequilibrium molecular dynamics method for calculating the thermal conductivity. *The Journal of Chemical Physics*, 106(14):6082–6085.

Natti, K., Sinha, A., Hoerter, C., Andersson, P., Andersson, J., Lohmann, C., Schultz, D., Cho, N. H., and Winsor, R. (2013). Studies on the impact of 300 MPa injection pressure on engine performance, gaseous and particulate emissions. *SAE International Journal of Engines*, 6(1):336–351.

Nazarychev, V. M., Glova, A. D., Volgin, I. V., Larin, S. V., Lyulin, A. V., Lyulin, S. V., and Gurtovenko, A. A. (2021). Evaluation of thermal conductivity of organic phase-change materials from equilibrium and non-equilibrium computer simulations: Paraffin as a test case. *International Journal of Heat and Mass Transfer*, 165:120639.

Neyts, E. C. and Bogaerts, A. (2009). Numerical study of the size-dependent melting mechanisms of nickel nanoclusters. *The Journal of Physical Chemistry C*, 113(7):2771–2776.

Nie, X., Du, Z., Zhao, L., Deng, S., and Zhang, Y. (2019). Molecular dynamics study on transport properties of supercritical working fluids: Literature review and case study. *Applied Energy*, 250:63–80.

NIST (2021). https://webbook.nist.gov/chemistry/fluid/.

Nose, S. (1984). A unified formulation of the constant temperature molecular dynamics methods. *The Journal of Chemical Physics*, 81(1):511–511.

Ochoa, A., Aramburu, B., Valle, B., Resasco, D. E., Bilbao, J., Gayubo, A. G., and Castaño, P. (2017). Role of oxygenates and effect of operating conditions in the deactivation of a Ni supported catalyst during the steam reforming of bio-oil. *Green Chemistry*, 19(18):4315–4333.

Ochoa, A., Bilbao, J., Gayubo, A. G., and Castaño, P. (2020). Coke formation and deactivation during catalytic reforming of biomass and waste pyrolysis products: A review. *Renewable and Sustainable Energy Reviews*, 119:109600.

Okolie, J. A., Rana, R., Nanda, S., Dalai, A. K., and Kozinski, J. A. (2019). Supercritical water gasification of biomass: a state-of-the-art review of process parameters, reaction mechanisms and catalysis. *Sustainable Energy & Fuels*, 3(3):578–598.

Paajanen, A., Rinta-Paavola, A., and Vaari, J. (2021). High-temperature decomposition of amorphous and crystalline cellulose: reactive molecular simulations. *Cellulose*, pages 1–19.

Paajanen, A., Vaari, J., and Verho, T. (2019). Crystallization of cross-linked polyethylene by molecular dynamics simulation. *Polymer*, 171:80–86.

Palle, S. and Miller, R. S. (2007). Analysis of high-pressure hydrogen, methane, and heptane laminar diffusion flames: Thermal diffusion factor modeling. *Combustion and Flame*, 151(4):581–600.

Papavasileiou, K. D., Peristeras, L. D., Bick, A., and Economou, I. G. (2019). Molecular dynamics simulation of pure n-alkanes and their mixtures at elevated temperatures using atomistic and coarse-grained force fields. *The Journal of Physical Chemistry B*, 123(29):6229–6243.

Parrinello, M. and Rahman, A. (1981). Polymorphic transitions in single crystals: A new molecular dynamics method. *Journal of Applied physics*, 52(12):7182–7190.

Phankosol, S., Sudaprasert, K., Lilitchan, S., Aryusuk, K., and Krisnangkura, K. (2014). Estimation of surface tension of fatty acid methyl ester and biodiesel at different temperatures. *Fuel*, 126:162–168.

Pickett, L. M., Genzale, C. L., Bruneaux, G., Malbec, L.-M., Hermant, L., Christiansen, C., and Schramm, J. (2010). Comparison of diesel spray combustion in different high-temperature, high-pressure facilities. *SAE International Journal of Engines*, 3(2):156–181.

Pitz, W. J. and Mueller, C. J. (2011). Recent progress in the development of diesel surrogate fuels. *Progress in Energy and Combustion Science*, 37(3):330–350.

Plimpton, S. (1995). Fast parallel algorithms for short-range molecular dynamics. *Journal of Computational Physics*, 117(1):1–19.

Pluhackova, K., Morhenn, H., Lautner, L., Lohstroh, W., Nemkovski, K. S., Unruh, T., and Bockmann, R. A. (2015). Extension of the LOPLS-AA force field for alcohols, esters, and monoolein bilayers and its validation by neutron scattering experiments. *The Journal of Physical Chemistry B*, 119(49):15287–15299.

Poltavsky, I. and Tkatchenko, A. (2021). Machine learning force fields: Recent advances and remaining challenges. *The Journal of Physical Chemistry Letters*, 12(28):6551–6564.

Pranami, G. and Lamm, M. H. (2015). Estimating error in diffusion coefficients derived from molecular dynamics simulations. *Journal of Chemical Theory and Computation*, 11(10):4586–4592.

Prentice, I. J., Liu, X., Nerushev, O. A., Balakrishnan, S., Pulham, C. R., and Camp, P. J. (2020). Experimental and simulation study of the high-pressure behavior of squalane and poly-α-olefins. *The Journal of Chemical Physics*, 152(7):074504.

Qian, Y., Yu, L., Li, Z., Zhang, Y., Xu, L., Zhou, Q., Han, D., and Lu, X. (2018). A new methodology for diesel surrogate fuel formulation: Bridging fuel fundamental properties and real engine combustion characteristics. *Energy*, 148:424–447.

Qian, Y., Zhan, J.-H., Lai, D., Li, M., Liu, X., and Xu, G. (2016). Primary understanding of non-isothermal pyrolysis behavior for oil shale kerogen using reactive molecular dynamics simulation. *International Journal of Hydrogen Energy*, 41(28):12093–12100.

Qiu, Y., Smith, D., Boothroyd, S., Jang, H., Wagner, J., Bannan, C. C., Gokey, T., Lim, V. T., Stern, C., and Rizzi, A. (2021). Development and benchmarking of open force field v1. 0.0, the parsley small molecule force field.

Raabe, G. (2017). *Molecular Simulation Studies on Thermophysical Properties*.

Ribeiro, M. C., Pádua, A. A., and Gomes, M. F. C. (2014). Glass transition of ionic liquids under high pressure. *The Journal of Chemical Physics*, 140(24):244514.

Rosner, D., Israel, R., and La Mantia, B. (2000). "Heavy" species Ludwig–Soret transport effects in air-breathing combustion. *Combustion and Flame*, 123(4):547–560.

Roy, M. M., Wang, W., and Bujold, J. (2013). Biodiesel production and comparison of emissions of a DI diesel engine fueled by biodiesel–diesel and canola oil–diesel blends at high idling operations. *Applied Energy*, 106:198–208.

Rzoska, S. J. (2017). New challenges for the pressure evolution of the glass temperature. *Frontiers in Materials*, 4:33.

Sabbah, H., Biennier, L., Klippenstein, S. J., Sims, I. R., and Rowe, B. R. (2010). Exploring the role of PAHs in the formation of soot: Pyrene dimerization. *The Journal of Physical Chemistry Letters*, 1(19):2962–2967.

Savic, N., Rahman, M. M., Miljevic, B., Saathoff, H., Naumann, K.-H., Leisner, T., Riches, J., Gupta, B., Motta, N., and Ristovski, Z. (2016). Influence of biodiesel fuel composition on the morphology and microstructure of particles emitted from diesel engines. *Carbon*, 104:179–189.

Scalliet, C., Gnoli, A., Puglisi, A., and Vulpiani, A. (2015). Cages and anomalous diffusion in vibrated dense granular media. *Physical Review Letters*, 114(19):198001.

Schulz, F., Commodo, M., Kaiser, K., De Falco, G., Minutolo, P., Meyer, G., Andrea, D., and Gross, L. (2019). Insights into incipient soot formation by atomic force microscopy. *Proceedings of the Combustion Institute*, 37(1):885–892.

Shaddix, C., Brezinsky, K., and Glassman, I. (1997). Analysis of fuel decay routes in the high-temperature oxidation of 1-methylnaphthalene. *Combustion and Flame*, 108(1-2):139–157.

Sharifzadeh, M., Sadeqzadeh, M., Guo, M., Borhani, T. N., Konda, N. M., Garcia, M. C., Wang, L., Hallett, J., and Shah, N. (2019). The multi-scale challenges of biomass fast pyrolysis and bio-oil upgrading: Review of the state of art and future research directions. *Progress in Energy and Combustion Science*, 71:1–80.

Shi, Z., Debenedetti, P. G., and Stillinger, F. H. (2013). Relaxation processes in liquids: Variations on a theme by Stokes and Einstein. *The Journal of Chemical Physics*, 138(12):12A526.

Shumway, S. L., Clarke, A. S., and Jónsson, H. (1995). Molecular dynamics simulations of a pressure-induced glass transition. *The Journal of Chemical Physics*, 102(4):1796–1805.

Siu, S. W., Pluhackova, K., and Bockmann, R. A. (2012). Optimization of the OPLS-AA force field for long hydrocarbons. *Journal of Chemical Theory and Computation*, 8(4):1459–1470.

Steinhardt, P. J., Nelson, D. R., and Ronchetti, M. (1983). Bond-orientational order in liquids and glasses. *Physical Review B*, 28(2):784.

Stukowski, A. (2009). Visualization and analysis of atomistic simulation data with OVITO–the open visualization tool. *Modelling Simulation in Materials Science and Engineering*, 18(1):015012.

Sun, W., Huang, C., Tao, T., Zhang, F., Li, W., Hansen, N., and Yang, B. (2017a). Exploring the high-temperature kinetics of diethyl carbonate (dec) under pyrolysis and flame conditions. *Combustion and Flame*, 181:71–81.

Sun, W., Tao, T., Liao, H., Hansen, N., and Yang, B. (2019). Probing fuel-specific reaction intermediates from laminar premixed flames fueled by two C5 ketones and model interpretations. *Proceedings of the Combustion Institute*, 37(2):1699–1707.

Sun, W., Tao, T., Zhang, R., Liao, H., Huang, C., Zhang, F., Zhang, X., Zhang, Y., and Yang, B. (2017b). Experimental and modeling efforts towards a better understanding of the high-temperature combustion kinetics of c3c5 ethyl esters. *Combustion and Flame*, 185:173–187.

Sun, W., Wang, G., Li, S., Zhang, R., Yang, B., Yang, J., Li, Y., Westbrook, C. K., and Law, C. K. (2017c). Speciation and the laminar burning velocities of poly (oxymethylene) dimethyl ether 3 (POMDME3) flames: An experimental and modeling study. *Proceedings of the Combustion Institute*, 36(1):1269–1278.

Surblys, D., Matsubara, H., Kikugawa, G., and Ohara, T. (2019). Application of atomic stress to compute heat flux via molecular dynamics for systems with many-body interactions. *Physical Review E*, 99(5):051301.

Swope and William, C. (1982). A computer simulation method for the calculation of equilibrium constants for the formation of physical clusters of molecules: Application to small water clusters. *Journal of Chemical Physics*, 76(1):637–649.

Takekiyo, T., Koyama, Y., Matsuishi, K., and Yoshimura, Y. (2020). High-pressure Raman study of n-Octane up to 15 GPa. *The Journal of Physical Chemistry B*, 124(49):11189–11196.

Tarakowski, R., Malanowski, A., Rostocki, A. J., Kowalczyk, M., Modzelewski, P., Ptasznik, S., and Siegoczyński, R. M. (2015). Could RME biodiesel be potentially harmful to modern engine? solidification process in RME. *Fuel*, 146:28–32.

Thangaraja, J., Anand, K., and Mehta, P. S. (2016). Predicting surface tension for vegetable oil and biodiesel fuels. *RSC Advances*, 6(88):84645–84657.

Tolman, R. C. (1948). Consideration of the gibbs theory of surface tension. *The Journal of Chemical Physics*, 16(8):758–774.

Tribello, G. A., Giberti, F., Sosso, G. C., Salvalaglio, M., and Parrinello, M. (2017). Analyzing and driving cluster formation in atomistic simulations. *Journal of Chemical Theory and Computation*, 13(3):1317–1327.

Ungerer, P., Nieto-Draghi, C., Rousseau, B., Ahunbay, G., and Lachet, V. (2007). Molecular simulation of the thermophysical properties of fluids: From understanding toward quantitative predictions. *Journal of Molecular Liquids*, 134(1-3):71–89.

Unke, O. T., Chmiela, S., Sauceda, H. E., Gastegger, M., Poltavsky, I., Schutt, K. T., Tkatchenko, A., and Muller, K.-R. (2021). Machine learning force fields. *Chemical Reviews*.

Van, Gunsteren, W. and Berendsen, H. (1988). A leap-frog algorithm for stochastic dynamics. *Molecular Simulation*, 1:173–185.

Van Der Spoel, D., Lindahl, E., Hess, B., Groenhof, G., Mark, A. E., and Berendsen, H. J. (2005). GROMACS: fast, flexible, and free. *Journal of computational chemistry*, 26(16):1701–1718.

van Duin, A. C., Dasgupta, S., Lorant, F., and Goddard, W. A. (2001). ReaxFF: a reactive force field for hydrocarbons. *The Journal of Physical Chemistry A*, 105(41):9396–9409.

Vanommeslaeghe, K., Hatcher, E., Acharya, C., Kundu, S., Zhong, S., Shim, J., Darian, E., Guvench, O., Lopes, P., and Vorobyov, I. (2010). CHARMM general force field: A force field for drug-like molecules compatible with the CHARMM all-atom additive biological force fields. *Journal of Computational Chemistry*, 31(4):671–690.

Vashisth, A., Ashraf, C., Zhang, W., Bakis, C. E., and Van Duin, A. C. (2018). Accelerated ReaxFF simulations for describing the reactive cross-linking of polymers. *The Journal of Physical Chemistry A*, 122(32):6633–6642.

Vega, L. F. (2018). Perspectives on molecular modeling of supercritical fluids: From equations of state to molecular simulations. Recent advances, remaining challenges and opportunities. *The Journal of Supercritical Fluids*, 134:41–50.

Verlet, L. (1967). Computer "experiments" on classical fluids. I. Thermodynamical properties of Lennard-Jones molecules. *Physical Review*, 159(1):98.

Violi, A. (2004). Modeling of soot particle inception in aromatic and aliphatic premixed flames. *Combustion and Flame*, 139(4):279–287.

Violi, A., Kubota, A., Truong, T., Pitz, W., Westbrook, C., and Sarofim, A. (2002). A fully integrated kinetic monte carlo/molecular dynamics approach for the simulation of soot precursor growth. *Proceedings of the Combustion Institute*, 29(2):2343–2349.

Violi, A. and Venkatnathan, A. (2006). Combustion-generated nanoparticles produced in a benzene flame: a multiscale approach. *The Journal of Chemical Physics*, 125(5):054302.

Von Meerwall, E., Beckman, S., Jang, J., and Mattice, W. (1998). Diffusion of liquid n-alkanes: Free-volume and density effects. *The Journal of Chemical Physics*, 108(10):4299–4304.

Wang, H. (2011). Formation of nascent soot and other condensed-phase materials in flames. *Proceedings of the Combustion Institute*, 33(1):41–67.

Wang, H., Wen, K., You, X., Mao, Q., Luo, K. H., Pilling, M. J., and Robertson, S. H. (2019). Energy transfer in intermolecular collisions of polycyclic aromatic hydrocarbons with bath gases He and Ar. *The Journal of Chemical Physics*, 151(4):044301.

Wensink, E. J., Hoffmann, A. C., van Maaren, P. J., and van der Spoel, D. (2003). Dynamic properties of water/alcohol mixtures studied by computer simulation. *The Journal of Chemical Physics*, 119(14):7308–7317.

Westbrook, C. K., Pitz, W. J., and Curran, H. J. (2006). Chemical kinetic modeling study of the effects of oxygenated hydrocarbons on soot emissions from diesel engines. *The Journal of Physical Chemistry A*, 110(21):6912–6922.

Woodcock, L. V. (1971). Isothermal molecular dynamics calculations for liquid salts. *Chemical Physics Letters*, 10(3):257–261.

Xin, Y., Sung, C.-J., and Law, C. K. (2012). A mechanistic evaluation of Soret diffusion in heptane/air flames. *Combustion and Flame*, 159(7):2345–2351.

Xu, D., Lu, Y., and Luo, C. (2020). Pathway of orientational symmetry breaking in crystallization of short n-alkane droplets: A molecular dynamics study. *The Journal of Chemical Physics*, 153(8):084903.

Xue, J., Grift, T. E., and Hansen, A. C. (2011). Effect of biodiesel on engine performances and emissions. *Renewable and Sustainable Energy Reviews*, 15(2):1098–1116.

Yang, X., Duan, C., Xu, J., Liu, Y., and Cao, B. (2019). A numerical study on the thermal conductivity of $H_2O/CO_2/H_2$ mixtures in supercritical regions of water for coal supercritical water gasification system. *International Journal of Heat and Mass Transfer*, 135:413–424.

Yang, X., Zhang, M., Gao, Y., Cui, J., and Cao, B. (2021). Molecular dynamics study on viscosities of sub/supercritical n-decane, n-undecane and n-dodecane. *Journal of Molecular Liquids*, 335:116180.

Yeh, I.-C. and Hummer, G. (2004). System-size dependence of diffusion coefficients and viscosities from molecular dynamics simulations with periodic boundary conditions. *The Journal of Physical Chemistry B*, 108(40):15873–15879.

Yiannourakou, M., Ungerer, P., Lachet, V., Rousseau, B., and Teuler, J.-M. (2019). United atom force field for vapor-liquid equilibrium (VLE) properties of cyclic and polycyclic compounds from monte carlo simulations. *Fluid Phase Equilibria*, 481:28–43.

Yoon, T. J., Ha, M. Y., Lee, W. B., and Lee, Y.-W. (2018). “Two-phase” thermodynamics of the Frenkel line. *The Journal of Physical Chemistry Letters*, 9(16):4550–4554.

Yoshimura, Y., Takekiyo, T., Koyama, Y., Takaku, M., Yamamura, M., Kikuchi, N., Wakabayashi, D., Funamori, N., Matsuishi, K., and Abe, H. (2018). High-pressure glass formation of a series of 1-alkyl-3-methylimidazolium bis(trifluoromethanesulfonyl)imide homologues. *Physical Chemistry Chemical Physics*, 20(1):199–205.

Zeng, J., Cao, L., Xu, M., Zhu, T., and Zhang, J. Z. (2020). Complex reaction processes in combustion unraveled by neural network-based molecular dynamics simulation. *Nature Communications*, 11(1):1–9.

Zerze, H., Mittal, J., and McHugh, A. J. (2013). *Ab initio* crystallization of alkanes: Structure and kinetics of nuclei formation. *Macromolecules*, 46(22):9151–9157.

Zhang, L. and Greenfield, M. L. (2007). Relaxation time, diffusion, and viscosity analysis of model asphalt systems using molecular simulation. *The Journal of Chemical Physics*, 127(19):194502.

Zhang, L. and Greenfield, M. L. (2010). Rotational relaxation times of individual compounds within simulations of molecular asphalt models. *The Journal of Chemical Physics*, 132(18):184502.

Zhang, L., Han, J., Wang, H., Car, R., and Weinan, E. (2018). Deep potential molecular dynamics: a scalable model with the accuracy of quantum mechanics. *Physical Review Letters*, 120(14):143001.

Zhang, M., Lussetti, E., de Souza, L. E., and Müller-Plathe, F. (2005). Thermal conductivities of molecular liquids by reverse nonequilibrium molecular dynamics. *The Journal of Physical Chemistry B*, 109(31):15060–15067.

Zhang, T., Li, X., Qiao, X., Zheng, M., Guo, L., Song, W., and Lin, W. (2016). Initial mechanisms for an overall behavior of lignin pyrolysis through large-scale ReaxFF molecular dynamics simulations. *Energy & Fuels*, 30(4):3140–3150.

Zhang, Y., He, H., Liu, Y., Wang, Y., Huo, F., Fan, M., Adidharma, H., Li, X., and Zhang, S. (2019). Recent progress in theoretical and computational studies on the utilization of lignocellulosic materials. *Green Chemistry*, 21(1):9–35.

Zhang, Y., Otani, A., and Maginn, E. J. (2015). Reliable viscosity calculation from equilibrium molecular dynamics simulations: A time decomposition method. *Journal of Chemical Theory and Computation*, 11(8):3537–3546.

Zhang, Y., Zhang, R., Rao, L., Kim, D., and Kook, S. (2017). The influence of a large methyl ester on in-flame soot particle structures in a small-bore diesel engine. *Fuel*, 194:423–435.

Zhao, B., Yang, Z., Li, Z., Johnston, M. V., and Wang, H. (2005). Particle size distribution function of incipient soot in laminar premixed ethylene flames: effect of flame temperature. *Proceedings of the Combustion Institute*, 30(1):1441–1448.

Zhao, J., Leonid, G., and Pengfei, Y. (2020). Limit of fuel injection rate in the common rail system under ultra-high pressures. *International Journal of Automotive Technology*, 21(3):649–656.

Zhao, L., Cheng, T., and Sun, H. (2008). On the accuracy of predicting shear viscosity of molecular liquids using the periodic perturbation method. *The Journal of Chemical Physics*, 129(14):144501.

Zhao, L., Wang, X., Wang, L., and Sun, H. (2007). Prediction of shear viscosities using periodic perturbation method and OPLS force field. *Fluid Phase Equilibria*, 260(2):212–217.

Zhao, X., Luo, T., and Jin, H. (2021). A predictive model for self-, Maxwell-Stefan, and Fick diffusion coefficients of binary supercritical water mixtures. *Journal of Molecular Liquids*, 324:114735.

Zheng, M., Wang, Z., Li, X., Qiao, X., Song, W., and Guo, L. (2016). Initial reaction mechanisms of cellulose pyrolysis revealed by ReaxFF molecular dynamics. *Fuel*, 177:130–141.

Zhu, H., Zhu, S., Jia, Z., Parvinian, S., Li, Y., Vaaland, O., Hu, L., and Li, T. (2015). Anomalous scaling law of strength and toughness of cellulose nanopaper. *Proceedings of the National Academy of Sciences*, 112(29):8971–8976.

Zhu, Q., Gu, Y., Hu, L., Gaudin, T., Fan, M., and Ma, J. (2021). Shear viscosity prediction of alcohols, hydrocarbons, halogenated, carbonyl, nitrogen-containing, and sulfur compounds using the variable force fields. *The Journal of Chemical Physics*, 154(7):074502.